POLITECNICO DI TORINO

Master's Degree in Electronic Engineering

Master's Degree Thesis

Signal amplitude monitoring system for in-plant communication based on multi-source energy harvesting: design and characterization

Supervisors

Prof. Danilo DEMARCHI

Ph.D. Umberto GARLANDO

M.Sc. Stefano CALVO

M.Sc. Mattia BAREZZI

M.Sc. Federico CUM

Ph.D. Alessandro SANGINARIO

Candidate

Luca ROLLE S304803

April 2024

Abstract

Environmental sustainability has become a significant topic, especially in recent years. The consequences of the increasingly frequent extreme natural phenomena (such as domestic and international mass migrations, food insecurity related to the rise of the world population, etc.) have further highlighted the environmental situation and increased interest in the relative research and publications. Within this framework, Smart Agriculture solutions may represent a viable answer to boost productivity, improve resilience, reduce emissions and waste, and optimize human labor through the utilization of several new technologies and techniques helping to speed up the change of route in the climate-change scenario due to the crucial impact on the environment of the agricultural sector. In this perspective, this thesis work proposes an energetically self-sufficient, low-cost, and low-power system capable of evaluating the plant health status by the stem electrical impedance developed to minimize the waste of energy and water resources and the eventual chemical utilization to what is strictly necessary for every single plant's maintenance. A Plant Microbial Fuel Cell (PMFC) has been chosen to work with a photovoltaic (PV) module to achieve the energy-related goal. Thus, a PMFC-based solution has been studied and characterized in this thesis work to inspect the most suitable electrode materials combination and to retrieve information on this still-not-so-exploited energy solution. Then, the system used for the electrical plant stem impedance evaluation has been designed and developed comprising a transmitting module, a receiving device, and a microcontroller unit (MCU). The transmitting module injects a signal with a known amplitude and a plant-stem-related frequency. The receiving device exploits a peak-detector-based solution to estimate the electrical plant stem impedance module by retrieving the peak voltage of the signal sent by the transmitter and proportionally attenuated by the distance traveled along the plant stem before being read by the receiver. The microcontroller unit (MCU) has been configured to properly manage the data from the transmitter, receiver, and other eventually exploited sensors and send the results via LoRa communication protocol. The developed system has been mounted and tested on a tobacco plant, reporting strong and promising results. In particular, almost 12 hours and 20 minutes of developed Tx-plant-Rx system monitoring operation can be accomplished considering the best-performing studied PMFC as the only energy supply of the system.

Summary

Environmental sustainability has become a significant topic, especially in recent years. The consequences of the increasingly frequent extreme natural phenomena (such as domestic and international mass migrations, food insecurity related to the rise of the world population, etc.) have further highlighted the environmental situation and increased interest in the relative research and publications.

Within this framework, Smart Agriculture solutions may represent a viable answer to boost productivity, improve resilience, reduce emissions and waste, and optimize human labor through the utilization of several new technologies and techniques helping to speed up the change of route in the climate-change scenario due to the crucial impact on the environment of the agricultural sector. In this perspective, this thesis work proposes an energetically self-sufficient, low-cost, and low-power system capable of evaluating the plant health status by the stem electrical impedance developed to minimize the waste of energy and water resources and the eventual chemical utilization to what is strictly necessary for every single plant's maintenance.

A Plant Microbial Fuel Cell (PMFC) has been chosen to work with a photovoltaic (PV) module to achieve the energy-related goal. Thus, a PMFC-based solution has been studied and characterized in this thesis work to inspect the most suitable electrode materials combination and to retrieve information on this still-not-so-exploited energy solution. The results retrieved have evidenced an overall better performance of Zinc-Copper electrode chosen materials, as further underlined in previous studies. However, the presence of aluminum plates in the employed PMFC has reported strong results in terms of power performance even for the Zinc-Aluminum electrode configuration, providing an interesting base for future studies.

In parallel, the system used for the electrical plant stem impedance evaluation has been designed and developed comprising a transmitting module (Tx), a receiving device (Rx), and a microcontroller unit (MCU).

The transmitting module injects a signal with a known amplitude and a plant-stem-related frequency. The receiving device exploits a peak-detector-based solution to estimate the electrical plant stem impedance module by retrieving the peak voltage

of the signal sent by the transmitter and proportionally attenuated by the distance traveled along the plant stem before being read by the receiver. The microcontroller unit (MCU) has been configured to properly manage the data from the transmitter, receiver, and other eventually exploited sensors and send the results via LoRa communication protocol.

The developed system has been mounted and tested on a tobacco plant, reporting strong and promising results such as:

- Transmitter and receiver output frequencies are respectively inversely and directly proportional to the plant stem electrical impedance, which is growing in turn to a worsening of the plant overall health condition (for instance, lack of water). Thus it can be stated that it is possible to evaluate the plant stem electrical impedance through the examination of the receiver-specific output frequency.
- Healthy plants present a higher transmitter-related stem-specific output frequency than the one produced by damaged and near-to-end plants. In contrast, a lower receiver-related stem-specific output frequency can be evidenced in healthy plants with respect to the one retrieved in damaged plants.
- Considering the best-performing studied PMFC as the only energy supply of the system, almost 12 hours and 20 minutes of developed Tx-plant-Rx system monitoring operation can be accomplished.

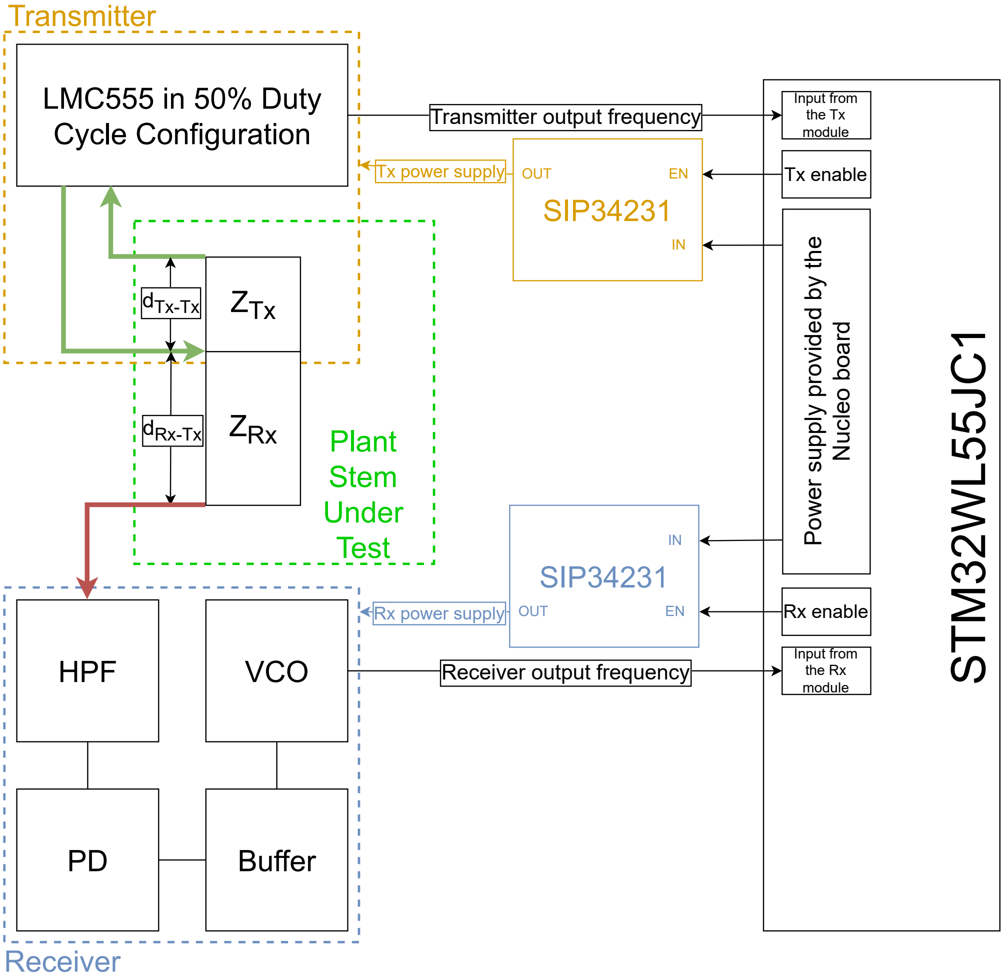

Figure 1: Schematic block diagram of the developed system: in particular, the transmitter, the receiver, the green and red surgical needles used for plant connections and their relative distances, the SIP switches, and the Nucleo-64 Development Board are highlighted.

Acknowledgements

I would like to thank Prof. Demarchi Danilo, my thesis coordinator, for the opportunity to work on such a promising and essential project characterized by a vital goal for everyone's present and future. I also wish to thank Calvo Stefano and Garlando Umberto, my thesis co-advisors, and the rest of the eLions team, in particular Barezzi Mattia, Cum Federico, and Sanginario Alessandro, for both theoretical and practical support over the past few months and their uninterrupted helpfulness. Last but not least, special thanks to my family, friends, and colleagues for tolerating and supporting me over the past few years. To everybody I have met along the way, to those who have left and those who have stayed, thank you all from the bottom of my heart.

Table of Contents

List of Tables IX

List of Figures XV

Acronyms XXX

1 Introduction 1
- 1.1 Overview . . . 1
- 1.2 Agriculture and its smart management . . . 5
- 1.3 Thesis organization . . . 12

2 Plant Microbial Fuel Cell 13
- 2.1 Overview . . . 13
- 2.2 PMFC experimental setup implementation . . . 19
- 2.3 PMFCs characterization . . . 22
  - 2.3.1 PMFC 1 characterization . . . 23
  - 2.3.2 PMFC 2 characterization . . . 27
  - 2.3.3 PMFCs comparison . . . 36
- 2.4 Conclusions . . . 43

3 Implemented System 45
- 3.1 Overview . . . 45
- 3.2 Project of the transmitting system . . . 49
- 3.3 Project of the receiving system . . . 53
  - 3.3.1 Input filter . . . 55
  - 3.3.2 Peak detector . . . 56
  - 3.3.3 Buffer . . . 59
  - 3.3.4 Voltage-controlled oscillator . . . 60

3.4 Characterization of the system 62
3.4.1 Section-specific exploited variables' nomenclature 62
3.4.2 Characterization only with instrumentation 65
3.4.3 First characterization considering the tobacco plant 72
3.4.4 Second characterization considering the tobacco plant 83
3.4.5 Third characterization considering the tobacco plant 94
3.5 Conclusions 125

4 Microcontroller Unit Implementation 129
4.1 Overview 129
4.1.1 LoRa modulation and LoRaWAN protocol 134
4.1.2 The Things Network 135
4.2 Firmware Implementation 136
4.3 Conclusions 140

5 Implementation on the actual plant 141
5.1 Overview 141
5.2 Experimental results 146
5.3 Conclusions 161

6 Conclusions 162

A Power supply versus output frequency range 163

B PMFCs registered data 166
B.1 Characterization data of the Zinc-Copper PMFC 1 167
B.2 Characterization data of the Zinc-Copper PMFC 2 176
B.3 Characterization data of the Zinc-Aluminum PMFC 2 185
B.4 Characterization data of the Copper-Aluminum PMFC 2 192

C Developed system characterization data 199
C.1 Receiver characterization without plant data 199
C.2 Transmitter characterization without plant data 209
C.3 Registered data of the first characterization with the tobacco plant 210
C.4 Registered data of the second characterization with the tobacco plant 215
C.5 Registered data of the third characterization with the tobacco plant 220

D MCU firmware implementation 230

D.0.1 Application code 234
D.0.2 The Things Network algorithm 245

Bibliography 247

List of Tables

2.1 MPP-related registered results for the Zn-Cu electrode combination of PMFC 1. 26
2.2 MPP-related registered results for the Zn-Cu electrode combination of PMFC 2. 34
2.3 MPP-related registered results for the Zn-Al electrode combination of PMFC 2. 34
2.4 MPP-related registered results for the Cu-Al electrode combination of PMFC 2. 35
2.5 MPP-related best registered not-loaded and loaded results for the Zn-Cu electrode combination of PMFC 1. 41
2.6 MPP-related best registered not-loaded and loaded results for the Zn-Cu electrode combination of PMFC 2. 42

3.1 Chosen values for the components of the transmitting device. 50
3.2 Chosen values for the components of the highpass filter of the receiver. 56
3.3 Chosen values for the components of the peak detector of the receiving device. 58
3.4 Chosen values for the components of the buffer of the receiving device. 59
3.5 Chosen values for the components of the voltage-controlled oscillator of the receiving device in the "50% Duty Cycle Oscillator" configuration [39]. 61

5.1 Exploited parameters of the experimental setup. 144
5.2 Electrical impedance modulus values (Z_{Tx} and Z_{Rx}) retrieved using the BK Precision 891 LCR meter [68, 69] on March 4$^{\text{th}}$, 2024. . . . 152

B.1 Registered data of the 1$^{\text{st}}$ characterization of the Zinc-Copper configuration of PMFC 1. 167

B.2 Registered data of the 2$^{\text{nd}}$ characterization of the Zinc-Copper configuration of PMFC 1. 168
B.3 Registered data of the 3$^{\text{rd}}$ characterization of the Zinc-Copper configuration of PMFC 1. 169
B.4 Registered data of the 4$^{\text{th}}$ characterization of the Zinc-Copper configuration of PMFC 1. 170
B.5 Registered data of the 5$^{\text{th}}$ characterization of the Zinc-Copper configuration of PMFC 1. 171
B.6 Registered data of the 6$^{\text{th}}$ characterization of the Zinc-Copper configuration of PMFC 1. 172
B.7 Registered data of the 7$^{\text{th}}$ characterization of the Zinc-Copper configuration of PMFC 1. 173
B.8 Registered data of the 8$^{\text{th}}$ characterization of the Zinc-Copper configuration of PMFC 1. 174
B.9 Registered data of the 9$^{\text{th}}$ characterization of the Zinc-Copper configuration of PMFC 1. 175
B.10 Registered data of the 1$^{\text{st}}$ characterization of the Zinc-Copper configuration of PMFC 2. 176
B.11 Registered data of the 2$^{\text{nd}}$ characterization of the Zinc-Copper configuration of PMFC 2. 177
B.12 Registered data of the 3$^{\text{rd}}$ characterization of the Zinc-Copper configuration of PMFC 2. 178
B.13 Registered data of the 4$^{\text{th}}$ characterization of the Zinc-Copper configuration of PMFC 2. 179
B.14 Registered data of the 5$^{\text{th}}$ characterization of the Zinc-Copper configuration of PMFC 2. 180
B.15 Registered data of the 6$^{\text{th}}$ characterization of the Zinc-Copper configuration of PMFC 2. 181
B.16 Registered data of the 7$^{\text{th}}$ characterization of the Zinc-Copper configuration of PMFC 2. 182
B.17 Registered data of the 8$^{\text{th}}$ characterization of the Zinc-Copper configuration of PMFC 2. 183
B.18 Registered data of the 9$^{\text{th}}$ characterization of the Zinc-Copper configuration of PMFC 2. 184
B.19 Registered data of the 1$^{\text{st}}$ characterization of the Zinc-Aluminum configuration of PMFC 2. 185
B.20 Registered data of the 2$^{\text{nd}}$ characterization of the Zinc-Aluminum configuration of PMFC 2. 186

B.21 Registered data of the 3rd characterization of the Zinc-Aluminum configuration of PMFC 2. 187

B.22 Registered data of the 4th characterization of the Zinc-Aluminum configuration of PMFC 2. 188

B.23 Registered data of the 5th characterization of the Zinc-Aluminum configuration of PMFC 2. 189

B.24 Registered data of the 6th characterization of the Zinc-Aluminum configuration of PMFC 2. 190

B.25 Registered data of the 7th characterization of the Zinc-Aluminum configuration of PMFC 2. 191

B.26 Registered data of the 1st characterization of the Copper-Aluminum configuration of PMFC 2. 192

B.27 Registered data of the 2nd characterization of the Copper-Aluminum configuration of PMFC 2. 193

B.28 Registered data of the 3rd characterization of the Copper-Aluminum configuration of PMFC 2. 194

B.29 Registered data of the 4th characterization of the Copper-Aluminum configuration of PMFC 2. 195

B.30 Registered data of the 5th characterization of the Copper-Aluminum configuration of PMFC 2. 196

B.31 Registered data of the 6th characterization of the Copper-Aluminum configuration of PMFC 2. 197

B.32 Registered data of the 7th characterization of the Copper-Aluminum configuration of PMFC 2. 198

C.1 Results of the plant-less instrumentation-only receiver-related characterization process exploiting an input 1-kHz sine waveform with peak-to-peak amplitude ranging from 100 mV to 200 mV. 199

C.2 Results of the plant-less instrumentation-only receiver-related characterization process exploiting an input 1-kHz sine waveform with peak-to-peak amplitude ranging from 210 mV to 500 mV. 200

C.3 Results of the plant-less instrumentation-only receiver-related characterization process exploiting an input 10-kHz sine waveform with peak-to-peak amplitude ranging from 100 mV to 300 mV. 201

C.4 Results of the plant-less instrumentation-only receiver-related characterization process exploiting an input 10-kHz sine waveform with peak-to-peak amplitude ranging from 310 mV to 500 mV. 202

C.5 Results of the plant-less instrumentation-only receiver-related characterization process exploiting an input 50-kHz sine waveform with peak-to-peak amplitude ranging from 100 mV to 300 mV. 203
C.6 Results of the plant-less instrumentation-only receiver-related characterization process exploiting an input 50-kHz sine waveform with peak-to-peak amplitude ranging from 310 mV to 500 mV. 204
C.7 Results of the plant-less instrumentation-only receiver-related characterization process exploiting an input 100-kHz sine waveform with peak-to-peak amplitude ranging from 100 mV to 300 mV. 205
C.8 Results of the plant-less instrumentation-only receiver-related characterization process exploiting an input 100-kHz sine waveform with peak-to-peak amplitude ranging from 310 mV to 500 mV. 206
C.9 Results of the plant-less instrumentation-only receiver-related characterization process exploiting an input 150-kHz sine waveform with peak-to-peak amplitude ranging from 100 mV to 300 mV. 207
C.10 Results of the plant-less instrumentation-only receiver-related characterization process exploiting an input 150-kHz sine waveform with peak-to-peak amplitude ranging from 310 mV to 500 mV. 208
C.11 Results of the plant-less instrumentation-only transmitter-related characterization process. 209
C.12 Results of the 1st characterization process with the tobacco plant and setting d_{Tx-Tx} to 1 cm. 210
C.13 Results of the 1st characterization process with the tobacco plant and setting d_{Tx-Tx} to 2 cm. 210
C.14 Results of the 1st characterization process with the tobacco plant and setting d_{Tx-Tx} to 3 cm. 211
C.15 Results of the 1st characterization process with the tobacco plant and setting d_{Tx-Tx} to 4 cm. 211
C.16 Results of the 1st characterization process with the tobacco plant and setting d_{Tx-Tx} to 5 cm. 212
C.17 Results of the 1st characterization process with the tobacco plant and setting d_{Tx-Tx} to 6 cm. 212
C.18 Results of the 1st characterization process with the tobacco plant and setting d_{Tx-Tx} to 7 cm. 213
C.19 Results of the 1st characterization process with the tobacco plant and setting d_{Tx-Tx} to 8 cm. 213
C.20 Results of the 1st characterization process with the tobacco plant and setting d_{Tx-Tx} to 9 cm. 214

C.21 Results of the 1st characterization process with the tobacco plant and setting d_{Tx-Tx} to 10 cm. 214
C.22 Results of the 2nd characterization process with the tobacco plant and setting d_{Tx-Tx} to 1 cm. 215
C.23 Results of the 2nd characterization process with the tobacco plant and setting d_{Tx-Tx} to 2 cm. 215
C.24 Results of the 2nd characterization process with the tobacco plant and setting d_{Tx-Tx} to 3 cm. 216
C.25 Results of the 2nd characterization process with the tobacco plant and setting d_{Tx-Tx} to 4 cm. 216
C.26 Results of the 2nd characterization process with the tobacco plant and setting d_{Tx-Tx} to 5 cm. 217
C.27 Results of the 2nd characterization process with the tobacco plant and setting d_{Tx-Tx} to 6 cm. 217
C.28 Results of the 2nd characterization process with the tobacco plant and setting d_{Tx-Tx} to 7 cm. 218
C.29 Results of the 2nd characterization process with the tobacco plant and setting d_{Tx-Tx} to 8 cm. 218
C.30 Results of the 2nd characterization process with the tobacco plant and setting d_{Tx-Tx} to 9 cm. 219
C.31 Results of the 2nd characterization process with the tobacco plant and setting d_{Tx-Tx} to 10 cm. 219
C.32 Frequencies and peak voltage results of the 3rd characterization process with the tobacco plant and setting d_{Tx-Tx} to 1 cm. 220
C.33 Electrical impedance module results of the 3rd characterization process with the tobacco plant and setting d_{Tx-Tx} to 1 cm. 220
C.34 Frequencies and peak voltage results of the 3rd characterization process with the tobacco plant and setting d_{Tx-Tx} to 2 cm. 221
C.35 Electrical impedance module results of the 3rd characterization process with the tobacco plant and setting d_{Tx-Tx} to 2 cm. 221
C.36 Frequencies and peak voltage results of the 3rd characterization process with the tobacco plant and setting d_{Tx-Tx} to 3 cm. 222
C.37 Electrical impedance module results of the 3rd characterization process with the tobacco plant and setting d_{Tx-Tx} to 3 cm. 222
C.38 Frequencies and peak voltage results of the 3rd characterization process with the tobacco plant and setting d_{Tx-Tx} to 4 cm. 223
C.39 Electrical impedance module results of the 3rd characterization process with the tobacco plant and setting d_{Tx-Tx} to 4 cm. 223

C.40 Frequencies and peak voltage results of the 3rd characterization process with the tobacco plant and setting d_{Tx-Tx} to 5 cm. 224
C.41 Electrical impedance module results of the 3rd characterization process with the tobacco plant and setting d_{Tx-Tx} to 5 cm. 224
C.42 Frequencies and peak voltage results of the 3rd characterization process with the tobacco plant and setting d_{Tx-Tx} to 6 cm. 225
C.43 Electrical impedance module results of the 3rd characterization process with the tobacco plant and setting d_{Tx-Tx} to 6 cm. 225
C.44 Frequencies and peak voltage results of the 3rd characterization process with the tobacco plant and setting d_{Tx-Tx} to 7 cm. 226
C.45 Electrical impedance module results of the 3rd characterization process with the tobacco plant and setting d_{Tx-Tx} to 7 cm. 226
C.46 Frequencies and peak voltage results of the 3rd characterization process with the tobacco plant and setting d_{Tx-Tx} to 8 cm. 227
C.47 Electrical impedance module results of the 3rd characterization process with the tobacco plant and setting d_{Tx-Tx} to 8 cm. 227
C.48 Frequencies and peak voltage results of the 3rd characterization process with the tobacco plant and setting d_{Tx-Tx} to 9 cm. 228
C.49 Electrical impedance module results of the 3rd characterization process with the tobacco plant and setting d_{Tx-Tx} to 9 cm. 228
C.50 Frequencies and peak voltage results of the 3rd characterization process with the tobacco plant and setting d_{Tx-Tx} to 10 cm. 229
C.51 Electrical impedance module results of the 3rd characterization process with the tobacco plant and setting d_{Tx-Tx} to 10 cm. 229

D.1 Summary of the exploited pins on the employed NUCLEO-WL55JC1 STM32WL Nucleo-64 development board [40, 53, 54, 55]. 232

List of Figures

1 Schematic block diagram of the developed system: in particular, the transmitter, the receiver, the green and red surgical needles used for plant connections and their relative distances, the SIP switches, and the Nucleo-64 Development Board are highlighted. iii

1.1 Monthly globally averaged mole fraction (measure of atmospheric concentration), in 1984-2021 in the top row and the growth rates representing increases in successive annual means of mole fractions for three of the main GHGs (CO_2, CH_4 and C_2O) in the bottom row are reported [1]. 2

1.2 Local surface temperature variations between 2022 and the 1991–2020 average [1]. 2

1.3 The black curve represents the global mean sea level (GMSL) evolution in the 1993-2022 time span with uncertainty related to the satellite elevation highlighted by the grey area, while the three horizontal blue lines reports the average trends over three consecutive periods [1]. 3

1.4 Synthetic summary about internal population displacements triggered by disasters where in particular it is reported the share of weather-related disaster displacements and the most affected countries in 2022 [2]. 4

1.5 Pesticides use over the 1990–2021 period considering world agricultural use [3]. 5

1.6 Nutrients use over the 1990–2021 period considering world agricultural use [3]. 6

1.7 Food production GHG emissions contribution over the global GHGs emitted in the atmosphere [4, 5, 6]. 7

1.8 Agriculture and food production impacts on the environment [6]. . . 8

1.9 Emissions share (in $CO_2 - equivalent$) of agrifood systems on a worldwide scale averaged on the 1990–2021 period [3]. 9

1.10 Actual data and projection of world population and its annual growth rate in the 1700-2100 time span [7]. 9
1.11 Smart farming exploited relationships overview [9]. 10
1.12 Applications and services for Smart Agriculture [10]. 11

2.1 This plot is courtesy of the National Renewable Energy Laboratory, Golden, CO. and it reports the efficiencies of different photovoltaic cells employed in different operating fields and manufactured with diverse techniques, processes and materials. 14
2.2 On the top, plot of the energy sources involved over time in a continuous multi-source energy harvesting system with mechanical, thermal and solar energy, while at the bottom, different structures combining together piezoelectric and triboelectric energy generators [22]. 15
2.3 Single-chamber PMFC power generation structure and mechanisms [28]. 17
2.4 Several schematic illustration of different PMFC structures such as the plant-MFC with vascular plants in (a), the macrophyte PMFC in (b), the constructed wetland MFC (CW–MFC) in (c) and the bryophyte MFC with vascular-tissue-less plants in (d) [30]. 18
2.5 Materials exploited as electrodes in the PMFCs. 19
2.6 Employed PMFC structure exploiting three electrodes with the zinc-plated mesh grid electrode on top, the aluminum plates electrode in the middle and the copper helix wire at the bottom, each with their own correspondent external link. 20
2.7 Zoom of the wires connected to the exploited electrodes (white wire associated to the zinc mesh grid, brown wire related to the copper spiral wire and red wire linked to the aluminum plate) and exiting through a thereafter-sealed hole at the bottom of the pot in PMFC 2. 21
2.8 PMFCs at the time of the first characterization where PMFC 2 is on the foreground while PMFC 1 is in the background. 22
2.9 Evolution of the open-circuit voltage V_{OC} over time for the Zn-Cu electrode combination of PMFC 1. 23
2.10 Characterization results in terms of R-V curves for the Zn-Cu electrode combination of PMFC 1. 24
2.11 Characterization results in terms of R-I curves for the Zn-Cu electrode combination of PMFC 1. 24
2.12 Characterization results in terms of I-V curves for the Zn-Cu electrode combination of PMFC 1. 25

2.13 Characterization results in terms of V-P curves for the Zn-Cu electrode combination of PMFC 1. 26
2.14 Evolution of the open-circuit voltage V_{OC} over time for all of the PMFC 2 possible electrode combinations (Zn-Cu, Zn-Al, and Cu-Al). 27
2.15 Characterization results in terms of R-V curves for the Zn-Cu electrode combination of PMFC 2. 28
2.16 Characterization results in terms of R-V curves for the Zn-Al electrode combination of PMFC 2. 28
2.17 Characterization results in terms of R-V curves for the Cu-Al electrode combination of PMFC 2. 29
2.18 Characterization results in terms of R-I curves for the Zn-Cu electrode combination of PMFC 2. 29
2.19 Characterization results in terms of R-I curves for the Zn-Al electrode combination of PMFC 2. 30
2.20 Characterization results in terms of R-I curves for the Cu-Al electrode combination of PMFC 2. 30
2.21 Characterization results in terms of I-V curves for the Zn-Cu electrode combination of PMFC 2. 31
2.22 Characterization results in terms of I-V curves for the Zn-Al electrode combination of PMFC 2. 31
2.23 Characterization results in terms of I-V curves for the Cu-Al electrode combination of PMFC 2. 32
2.24 Characterization results in terms of V-P curves for the Zn-Cu electrode combination of PMFC 2. 32
2.25 Characterization results in terms of V-P curves for the Zn-Al electrode combination of PMFC 2. 33
2.26 Characterization results in terms of V-P curves for the Cu-Al electrode combination of PMFC 2. 33
2.27 Comparison between the open-circuit output voltages V_{OC} of each electrode material pair configuration. 36
2.28 Comparison between the maximum generated power-related curves of each electrode material pair configuration. 37
2.29 Evolution of the PMFC-2-related voltage across the 56-kΩ resistive load over time. 38
2.30 Zoom of the evolution of the PMFC-2-related voltage across the 56-kΩ resistive load over time. 38
2.31 Evolution of the PMFC-1-related voltage across the 56-kΩ resistive load over time. 39

2.32 Zoom of the evolution of the PMFC-1-related voltage across the 56-kΩ resistive load over time. 39
2.33 Comparison between the 56-kΩ-related voltage curves of both the Zn-Cu configurations. 40
2.34 Comparison between the generated power-related curves of both the Zn-Cu configurations, even considering the loaded results. 41
2.35 Comparison between the open-circuit voltage curves of both the Zn-Cu configurations, even considering the loaded results. 42
2.36 PMFCs at the time of the last characterization where PMFC 2 is on the foreground while PMFC 1 is in the background. 44

3.1 Functional block diagram of the LMC555 from the LMC555 datasheet [39]. 47
3.2 Schematic of the transmitting module based on the "50% Duty Cycle Oscillator" configuration reported at page 16 of the LMC555 datasheet [39]. 49
3.3 Zoom on the connection between transmitter (the green needles) and receiver (the red needle) and the plant stem. 51
3.4 Transmitting module with power supply jumper cables at the top in red and black, output with a white cable on the right side and two jumpers at both ends of the resistor R_{plant} at the bottom in green and violet. 52
3.5 Basic schematic of the receiving module. 53
3.6 Receiver module with power supply jumper cables at the top in red and black, input through a green wire on the left and output with a yellow jumper on the right. 54
3.7 Schematic of the highpass filter exploited in the receiving module [20]. 55
3.8 Basic scheme of the implemented peak detector exploited in the receiving module. 56
3.9 Schematic of the implemented buffer exploited in the receiving module. 59
3.10 Schematic of the voltage-controlled oscillator of the receiving module based on the "50% Duty Cycle Oscillator" configuration reported at page 16 of the LMC555 datasheet [39]. 60
3.11 Experimental setup with exploited variables highlighted according to the employed nomenclature convention. 64
3.12 Plot of the absolute frequency error between the Equation 3.1 expected frequency and the experimentally-obtained output frequency. 66
3.13 Plot of the relative frequency error between the Equation 3.1 expected frequency and the experimentally-obtained output frequency. 66

3.14 Plot of both the Equation 3.1 expected frequency and the actual experimentally-obtained one. 67

3.15 Plot of the relation between the input peak-to-peak voltage evaluated after the highpass filter V_{pp-in} and the one set by the 33220A waveform generator [47] $V_{pp-in-instr}$ put as input of the receiving system. 68

3.16 Plot of the relation between the input maximum voltage evaluated after the highpass filter V_{max-in} and the one measured after the buffer $V_{max-out}$ of the receiving system. 69

3.17 Plot of the relation between the absolute variation of the maximum voltage across the peak detector ΔV_{max} and the input peak-to-peak voltage set by the 33220A waveform generator [47] $V_{pp-in-instr}$. . . . 69

3.18 Plot of the relation between the input peak-to-peak voltage set by the 33220A waveform generator [47] $V_{pp-in-instr}$ and the maximum voltage stored in the peak detector capacitor $V_{max-out}$. 70

3.19 Plot of the relationship between the input of the voltage-controlled oscillator $V_{max-out}$ and its output frequency f_{out-Rx}. 70

3.20 Plot of the input-output relationship of the receiving system. 71

3.21 Plot of the relationship between the input of the peak detector V_{pp-in} and the voltage-controlled oscillator output frequency (thus receiver output frequency) f_{out-Rx}. 71

3.22 Zoom on the surgical needles employed in the characterization of the system related to a living plant with green needles related to the transmitter and the red needle connected as input of the receiver. . 72

3.23 Zoom from another point of view on the surgical needles employed in the characterization of the system related to a living plant with green needles related to the transmitter and the red needle connected as input of the receiver. 73

3.24 Situation of the plant stem under investigation few moments after the end of the characterization process of the implemented system. . 74

3.25 Evolution of the transmitting output frequency f_{no-Rx} varying the distance d_{Tx-Tx} over the stem length between the two needles related to R_{plant}. 75

3.26 Plot of the evolution of the maximum voltage detected and stored downstream the peak detector $V_{max-out}$ changing time for time the relative distance over the stem length d_{Tx-Tx} between the two needles related to R_{plant} and fixing for each curve the relative distance d_{Rx-Tx} over the stem length. 76

3.27 Zoom on the damages left on an healthy new tobacco plant stem due to the characterization process after 10 days without performed measurements. 77

3.28 Plot of the evolution of the maximum voltage detected and stored downstream the peak detector $V_{max-out}$ changing time for time the relative distance d_{Rx-Tx} over the stem length and fixing for each curve the relative distance over the stem length d_{Tx-Tx} between the two needles related to the extremities of R_{plant}. 78

3.29 Evolution of the output peak voltage of the peak detector $V_{max-out}$ varying both the relative distances d_{Tx-Tx} and d_{Rx-Tx} over the plant stem length. 79

3.30 Plot of the relationship between the output frequency of the receiving module f_{out-Rx} varying the output peak voltage $V_{max-out}$ detected upstream the voltage-controlled oscillator for each value of the relative distance d_{Tx-Tx}. 80

3.31 Plot of the relationship between the output frequency of the receiving module f_{out-Rx} varying the output peak voltage $V_{max-out}$ detected upstream the voltage-controlled oscillator for each value of the relative distance d_{Rx-Tx}. 80

3.32 Evolution of the receiver's output frequency f_{out-Rx} varying the relative distance d_{Tx-Tx} for each value of the relative distance d_{Rx-Tx}. 81

3.33 Evolution of the receiver's output frequency f_{out-Rx} varying the relative distance d_{Rx-Tx} for each value of the relative distance d_{Tx-Tx}. 81

3.34 Evolution of the output frequency of the receiver f_{out-Rx} varying both the relative distances d_{Tx-Tx} and d_{Rx-Tx} over the plant stem length. 82

3.35 Trend of the attenuation the receiver-related input signal is subjected to in terms of the output frequency of the receiver f_{out-Rx} varying the relative distance d_{Rx-Tx} over the plant stem length. 82

3.36 Trend of the attenuation the receiver-related input signal is subjected to in terms of the output frequency of the receiver f_{out-Rx} varying the relative distance d_{Tx-Tx} over the plant stem length. 83

3.37 Tobacco plant utilized for the characterization with both transmitter and receiver modules. 84

3.38 Zoom on the surgical needles employed in the characterization of the system related to a living tobacco plant. 85

3.39 Evolution of the transmitting output frequency f_{no-Rx} varying the distance d_{Tx-Tx} over the stem length between the two needles related to R_{plant}. 86

3.40 Graph of the evolution of the maximum voltage detected downstream the peak detector $V_{max-out}$ changing time for time the relative distance over the stem length d_{Tx-Tx} and fixing the relative distance d_{Rx-Tx} over the stem length for each curve. 87
3.41 Evolution of the maximum voltage detected by the peak detector $V_{max-out}$ in relationship with the relative distance d_{Rx-Tx} over the stem length and fixing for each curve the relative distance over the stem length d_{Tx-Tx}. 88
3.42 Evolution of the output peak voltage $V_{max-out}$ varying both the relative distances d_{Tx-Tx} and d_{Rx-Tx} over the second plant stem length. 89
3.43 Relationship between the output frequency of the receiving module f_{out-Rx} changing the peak detector output $V_{max-out}$ for each value of the relative distance between both the needles of the transmitter d_{Tx-Tx}. 90
3.44 Relationship between the receiving-module output frequency f_{out-Rx} varying the peak detector output $V_{max-out}$ for each value of the relative distance over the stem length d_{Rx-Tx}. 90
3.45 Evolution of the receiver's output frequency f_{out-Rx} varying the distance d_{Tx-Tx} and fixing the relative length d_{Rx-Tx} from time to time on the second plant. 91
3.46 Evolution of the receiver's output frequency f_{out-Rx} varying the relative distance d_{Rx-Tx} and fixing the relative length d_{Tx-Tx} from time to time on the second plant. 92
3.47 Evolution of the output frequency of the receiver f_{out-Rx} varying both the relative distances d_{Tx-Tx} and d_{Rx-Tx} over the second plant stem length. 92
3.48 Trend of the attenuation the receiver-related input signal is subjected to in terms of the output frequency of the receiver f_{out-Rx} varying the relative distance d_{Rx-Tx} over the plant stem length. 93
3.49 Trend of the attenuation the receiver-related input signal is subjected to in terms of the output frequency of the receiver f_{out-Rx} varying the relative distance d_{Tx-Tx} over the plant stem length. 93
3.50 Evolution of the transmitting output frequency f_{no-Rx} changing over time the distance d_{Tx-Tx} over the stem length between the two needles related to R_{plant}. 95
3.51 Evolution of the transmitter-related electrical impedance Z_{no-Rx} at different frequencies changing over time the distance over the stem length between the transmitter-related two needles d_{Tx-Tx}. 96

3.52 Evolution of the d_{Tx-Tx}-related electrical impedance Z_{Tx} evaluated at 1 kHz in relationship with the relative distance d_{Tx-Tx} and fixing for each curve the relative distance over the stem length d_{Rx-Tx}. . . 97
3.53 Evolution of the d_{Tx-Tx}-related electrical impedance Z_{Tx} evaluated at 10 kHz in relationship with the relative distance d_{Tx-Tx} and fixing for each curve the relative distance over the stem length d_{Rx-Tx}. . . 97
3.54 Evolution of the d_{Tx-Tx}-related electrical impedance Z_{Tx} evaluated at 100 kHz in relationship with the relative distance d_{Tx-Tx} and fixing for each curve the relative distance over the stem length d_{Rx-Tx}. 98
3.55 Evolution of the d_{Tx-Tx}-related electrical impedance Z_{Tx} evaluated at 1 kHz in relationship with the relative distance d_{Rx-Tx} and fixing for each curve the relative distance over the stem length d_{Tx-Tx}. . . 98
3.56 Evolution of the d_{Tx-Tx}-related electrical impedance Z_{Tx} evaluated at 10 kHz in relationship with the relative distance d_{Rx-Tx} and fixing for each curve the relative distance over the stem length d_{Tx-Tx}. . . 99
3.57 Evolution of the d_{Tx-Tx}-related impedance Z_{Tx} evaluated at 100 kHz in relationship with the relative distance d_{Rx-Tx} and fixing for each curve the relative distance over the stem length d_{Tx-Tx}. 99
3.58 Evolution of the output transmitter-related frequency f_{out-Tx} in relationship with the relative distance d_{Rx-Tx} and fixing for each curve the relative distance over the stem length d_{Tx-Tx}. 100
3.59 Evolution of the output transmitter-related frequency f_{out-Tx} in relationship with the relative distance d_{Tx-Tx} and fixing for each curve the relative distance over the stem length d_{Rx-Tx}. 100
3.60 Evolution of the peak detector output voltage $V_{max-out}$ changing time for time the relative distance d_{Tx-Tx} and fixing the relative distance d_{Rx-Tx} for each curve. 101
3.61 Evolution of the peak detector detected output $V_{max-out}$ in relationship with the relative distance d_{Rx-Tx} and fixing for each curve the relative distance over the stem length d_{Tx-Tx}. 103
3.62 Evolution of the d_{Rx-Tx}-related electrical impedance Z_{Rx} evaluated at 1 kHz in relationship with the relative distance d_{Tx-Tx} and fixing for each curve the relative distance over the stem length d_{Rx-Tx}. . . 104
3.63 Evolution of the d_{Rx-Tx}-related electrical impedance Z_{Rx} evaluated at 10 kHz in relationship with the relative distance d_{Tx-Tx} and fixing for each curve the relative distance over the stem length d_{Rx-Tx}. . . 105
3.64 Evolution of the d_{Rx-Tx}-related electrical impedance Z_{Rx} evaluated at 100 kHz in relationship with the relative distance d_{Tx-Tx} and fixing for each curve the relative distance over the stem length d_{Rx-Tx}.105

3.65 Evolution of the d_{Rx-Tx}-related electrical impedance Z_{Rx} evaluated at 1 kHz in relationship with the relative distance d_{Rx-Tx} and fixing for each curve the relative distance over the stem length d_{Tx-Tx}. . . 106

3.66 Evolution of the d_{Rx-Tx}-related electrical impedance Z_{Rx} evaluated at 10 kHz in relationship with the relative distance d_{Rx-Tx} and fixing for each curve the relative distance over the stem length d_{Tx-Tx}. . . 106

3.67 Evolution of the d_{Rx-Tx}-related electrical impedance Z_{Rx} evaluated at 100 kHz in relationship with the relative distance d_{Rx-Tx} and fixing for each curve the relative distance over the stem length d_{Tx-Tx}.107

3.68 Graphical representation of the output peak voltage $V_{max-out}$ varying both the relative distances d_{Tx-Tx} and d_{Rx-Tx}. 108

3.69 Relationship between the output frequency of the receiving module f_{out-Rx} changing the peak detector output $V_{max-out}$ for each value of the relative distance d_{Tx-Tx}. 109

3.70 Relationship between the receiving-module output frequency f_{out-Rx} varying the peak detector output $V_{max-out}$ for each value of the relative distance over the stem length d_{Rx-Tx}. 109

3.71 Plot of the receiver's output frequency f_{out-Rx} varying the distance d_{Tx-Tx} and fixing the relative length d_{Rx-Tx} from time to time on the second plant. 110

3.72 Plot of the receiver's output frequency f_{out-Rx} varying the relative distance d_{Rx-Tx} and fixing the relative length d_{Tx-Tx} from time to time on the second plant. 110

3.73 Plot of the output frequency of the receiver f_{out-Rx} varying both the relative distances d_{Tx-Tx} and d_{Rx-Tx}. 111

3.74 Plot of the receiver's output frequency f_{out-Rx} over receiver-related electrical impedance Z_{Rx} value at 1 kHz fixing the relative length d_{Rx-Tx} from time to time on the second plant. 112

3.75 Plot of the receiver's output frequency f_{out-Rx} over receiver-related impedance Z_{Rx} value at 10 kHz fixing the relative length d_{Rx-Tx} from time to time on the second plant. 112

3.76 Plot of the receiver's output frequency f_{out-Rx} over receiver-related electrical impedance Z_{Rx} value at 100 kHz fixing the relative length d_{Rx-Tx} from time to time on the second plant. 113

3.77 Plot of the receiver's output frequency f_{out-Rx} over receiver-related electrical impedance Z_{Rx} value at 1 kHz fixing the relative length d_{Tx-Tx} from time to time on the second plant. 113

3.78 Plot of the receiver's output frequency f_{out-Rx} over receiver-related electrical impedance Z_{Rx} value at 10 kHz fixing the relative length d_{Tx-Tx} from time to time on the second plant. 114

3.79 Plot of the receiver's output frequency f_{out-Rx} over receiver-related impedance Z_{Rx} value at 100 kHz fixing the relative length d_{Tx-Tx} from time to time on the second plant. 114

3.80 Relationship between the transmitter-related output frequency f_{out-Tx} and the receiver-related output frequency f_{out-Rx} varying the relative distance d_{Rx-Tx} over the plant stem length. 115

3.81 Relationship between the transmitter-related output frequency f_{out-Tx} and the receiver-related output frequency f_{out-Rx} varying the relative distance d_{Tx-Tx} over the plant stem length. 115

3.82 Trend of the attenuation the receiver-related input signal is subjected to in terms of the output frequency of the receiver f_{out-Rx} varying the relative distance d_{Rx-Tx} over the plant stem length. 116

3.83 Trend of the attenuation the receiver-related input signal is subjected to in terms of the output frequency of the receiver f_{out-Rx} varying the relative distance d_{Tx-Tx} over the plant stem length. 116

3.84 Trend of the attenuation the receiver-related input signal is subjected to in terms of the output frequency of the transmitter f_{out-Tx} varying the relative distance d_{Rx-Tx} over the plant stem length. 117

3.85 Trend of the attenuation the receiver-related input signal is subjected to in terms of the output frequency of the transmitter f_{out-Tx} varying the relative distance d_{Tx-Tx} over the plant stem length. 117

3.86 Evolution of the attenuation the receiver-related input signal is subjected to in relation with the receiver-related electrical impedance Z_{Rx} evaluated at 1 kHz and varying the relative distance d_{Rx-Tx} over the plant stem length. 118

3.87 Evolution of the attenuation the receiver-related input signal is subjected to in relation with the receiver-related electrical impedance Z_{Rx} evaluated at 10 kHz and varying the relative distance d_{Rx-Tx} over the plant stem length. 119

3.88 Evolution of the attenuation the receiver-related input signal is subjected to in relation with the receiver-related electrical impedance Z_{Rx} evaluated at 100 kHz and varying the relative distance d_{Rx-Tx} over the plant stem length. 119

3.89 Evolution of the attenuation the receiver-related input signal is subjected to in relation with the receiver-related electrical impedance Z_{Rx} evaluated at 1 kHz and varying the relative distance d_{Tx-Tx} over the plant stem length. 120

3.90 Evolution of the attenuation the receiver-related input signal is subjected to in relation with the receiver-related electrical impedance Z_{Rx} evaluated at 10 kHz and varying the relative distance d_{Tx-Tx} over the plant stem length. 120

3.91 Evolution of the attenuation the receiver-related input signal is subjected to in relation with the receiver-related impedance Z_{Rx} evaluated at 100 kHz and varying the relative distance d_{Tx-Tx} over the plant stem length. 121

3.92 Evolution of the attenuation the receiver-related input signal is subjected to in relation with the transmitter-related electrical impedance Z_{Tx} evaluated at 1 kHz and varying the relative distance d_{Rx-Tx} over the plant stem length. 121

3.93 Evolution of the attenuation the receiver-related input signal is subjected to in relation with the transmitter-related impedance Z_{Tx} evaluated at 10 kHz and varying the relative distance d_{Rx-Tx} over the plant stem length. 122

3.94 Evolution of the attenuation the receiver-related input signal is subjected to in relation with the transmitter-related electrical impedance Z_{Tx} evaluated at 100 kHz and varying the relative distance d_{Rx-Tx} over the plant stem length. 122

3.95 Evolution of the attenuation the receiver-related input signal is subjected to in relation with the transmitter-related electrical impedance Z_{Tx} evaluated at 1 kHz and varying the relative distance d_{Tx-Tx} over the plant stem length. 123

3.96 Evolution of the attenuation the receiver-related input signal is subjected to in relation with the transmitter-related electrical impedance Z_{Tx} evaluated at 10 kHz and varying the relative distance d_{Tx-Tx} over the plant stem length. 123

3.97 Evolution of the attenuation the receiver-related input signal is subjected to in relation with the transmitter-related electrical impedance Z_{Tx} evaluated at 100 kHz and varying the relative distance d_{Tx-Tx} over the plant stem length. 124

3.98 Comparison of the three-characterization-produced results in terms of transmitter output frequency without considering the receiver in the experimental setup f_{no-Rx} over the relative distance d_{Tx-Tx}. . . 125

3.99 Comparison of the three scatter plots related respectively to the electrical impedance Z_{Rx} at 1 kHz (red results), the electrical impedance Z_{Rx} at 10 kHz (green plots) and the electrical impedance Z_{Rx} at 100 kHz (blue measurements) in relation with the receiver-related output frequency f_{out-Rx}. 127

4.1 Top view of the STM32WL55JC1 development board. 130
4.2 Bottom view of the STM32WL55JC1 development board. 131
4.3 Scan of the pinout of the STM32WL55JC1 Nucleo-64 development board from its leaflet comprised in the commercial package [55]. . . 132
4.4 Classification in terms of power consumption and communication range of several wireless technologies [56]. 134
4.5 Representation of the typical LoRaWAN architecture [56]. 135
4.6 Schematic block diagram of the complete system: in particular, the transmitter, the receiver, the green and red surgical needles (as depicted in Figure 3.3) and their relative distances, the SIP switches and the Nucleo-64 Development Board are highlighted. 137
4.7 Schematic flowchart of the behavior of the developed setup. 139
4.8 Application-specific data log displayed in The Things Network's "Live Data" tab. 140

5.1 LoRa-based WAPPSEN sensor end node block scheme [60]. 142
5.2 CMWX1ZZABZ-078 LoRaWAN module block scheme [61]. 143
5.3 Experimental setup located in the PIC4SeR thesis students' room. . 144
5.4 Zoom on the experimental setup which comprehends the WAPPSEN system (comprising the TEROS 21 Gen 2 sensor properly installed into the soil in the plant pot [64, 66]) on the leftmost part of the rack (in the red circle) and the CPX200D bench-type power supply unit [48] on its rightmost part (in the brown circle), while this latter is connected to this thesis developed system on its left (in the green circle), which in turn is mounted on the tobacco plant previously exploited in Section 3.4.4 and Section 3.4.5. 145
5.5 Receiver-related output evolution from January 19th, 2024 to February 23rd, 2024. 146
5.6 Transmitter-related output evolution from January 19th, 2024 to February 23rd, 2024. 146
5.7 Soil water potential evolution from January 19th, 2024 to February 23rd, 2024. 147

5.8 Soil temperature evolution from January 19th, 2024 to February 23rd, 2024. 147
5.9 Zoom on the watering effect on receiver-related output evolution. . 148
5.10 Zoom on the watering effect on transmitter-related output evolution. 148
5.11 Zoom on the watering effect on soil water potential evolution. . . . 149
5.12 Zoom on the watering effect on soil temperature evolution. 149
5.13 Employed plant condition after the 35-day-long monitoring period from January 19th, 2024 to February 23rd, 2024. 150
5.14 Employed plant condition four days after the watering event performed on February 26th, 2024 (thus on March 1st, 2024). 151
5.15 Comparison between the receiver-related output retrieved from this thesis' developed system and the receiver-related electrical impedance modulus values Z_{Rx} evaluated exploiting the BK Precision 891 LCR meter [68, 69]. 153
5.16 Comparison between the transmitter-related output retrieved from this thesis' developed system and the transmitter-related electrical impedance modulus values Z_{Tx} evaluated exploiting the BK Precision 891 LCR meter [68, 69]. 153
5.17 Receiver-related output evolution from March 8th, 2024 to March 19th, 2024. 154
5.18 Transmitter-related output evolution from March 8th, 2024 to March 19th, 2024. 154
5.19 Soil water potential evolution from March 8th, 2024 to March 19th, 2024. 155
5.20 Soil water potential evolution from March 8th, 2024 to March 19th, 2024. 155
5.21 Zoom on the watering effect on receiver-related output evolution. . 157
5.22 Zoom on the watering effect on transmitter-related output evolution. 157
5.23 Zoom on the watering effect on soil water potential evolution. . . . 158
5.24 Zoom on the watering effect on soil temperature evolution. 158
5.25 Employed plant condition just few moments before the watering event performed on March 15th, 2024. 159
5.26 Employed plant condition three days after the watering event performed on March 15th, 2024 (thus on March 18th, 2024). 160

A.1 Exploited LTspice model according to the developed receiver (see Section 3.3). 164

A.2 Plot of the output frequency f_{out-Rx} for each power supply studied levels V_{supply}. 165
A.3 Bar plot of the output frequency ranges for each power supply studied levels V_{supply}. 165

D.1 Exploited STM32WL55JC1 pins in the integrated development environment STM32CubeIDE [53, 54]. 232

Acronyms

AC
Alternating Current
ADC
Analog-to-Digital Converter
AEM
Anion Exchange Membrane
API
Application Programming Interface
ARR
Auto-Reload Register

C
Capacitor
CCR
Capture-Compare Register
CISC
Complex Instruction Set Computer
CMOS
Complementary Metal Oxide Semiconductor
CPU
Central Processing Unit

DAC
Digital-to-Analog Converter
DC
Direct Current
DSS
Decision Support System

E
Energy
EH
Energy Harvesting

FAO
Food and Agriculture Organization of the United Nations
FC
Fuel Cell
FEC
Forward Error Correction

GBW
Gain-BandWidth product
GHG
Greenhouse Gas
GMDAC
Global Migration Data Analysis Centre
GMSL
Global Mean Sea Level
GPIO
General Purpose I/O

HAL
Hardware Abstraction Layer
HPF
Highpass Filter
HTTP
HyperText Transfer Protocol

I
Current
IC
Input Capture
IDE
Integrated Development Environment
IDMC
Internal Displacement Monitoring Centre

IOM	International Organization for Migration
IoT	Internet of Things
LoRa	Long Range Protocol
LoRaWAN	Long Range Wide Area Network
LPF	Lowpass Filter
LPWAN	Low Power Wide Area Network
MAC	Medium Access Control
MCU	Microcontroller Unit
MFC	Microbial Fuel Cell
MOSFET	Metal Oxide Semiconductor Field Effect Transistor
MPP	Maximum Power Point
MPPT	Maximum Power Point Tracking
MPU	Memory Protection Unit
MQTT	Message Queuing Telemetry Transport
NDVI	Normalized Difference Vegetation Index
nMOS	n-type Metal Oxide Semiconductor
NoC	Network-on-Chip

NVIC
Nested Vectored Interrupt Controller

OC
Output Compare
OCV
Open Circuit Voltage

P
Power
PCB
Printed Circuit Board
PEM
Proton Exchange Membrane
PD
Peak Detector
PMFC
Plant Microbial Fuel Cell
pMOS
p-type Metal Oxide Semiconductor
PMS
Power Management System
PV
Photovoltaic
PVD
Programmable Voltage Detector

R
Resistor
RAM
Random Access Memory
RISC
Reduced Instruction Set Computer
RO
Ring Oscillator
ROM
Read-Only Memory

RF
Radio Frequency
RFEH
Radio Frequency Energy Harvesting
Rx
Receiver

SiP
System-in-Package
SIP
Single In-Line Package
SoC
System-on-Chip
SRAM
Static Random Access Memory
SWP
Soil Water Potential

TTN
The Things Network
Tx
Transmitter

UAV
Unmanned Aerial Vehicle

V
Voltage
VCO
Voltage Controlled Oscillator
VCR
Voltage Controlled Resistor

WMO
World Meteorological Organization
WSN
Wireless Sensor Network

Chapter 1

Introduction

1.1 Overview

In the last few years, the social awareness about the environmental sustainability of human actions has increased due to the increasingly frequent extreme natural phenomena that have occurred all over the world.

According to the WMO State of the Global Climate report 2022 [1], extreme weather and climate events came in various forms, from record-breaking heatwaves in Europe and China to extensive flooding in Pakistan and extreme and continuous drought in East Africa particularly.

In addition, as highlighted in Figure 1.1, Figure 1.2 and Figure 1.3, the increase of both the concentration and growth rate of greenhouse gases (GHGs) and the consequent rise of the global mean temperature and sea level (and its ever-increasing rising rate too) [1] unfortunately involves the need to consider these up-to-date so-called anomalies as more and more frequent events.

These extreme events can all be united by the same socioeconomic consequences, such as the increase of weather-and-climate-related deaths, food insecurity, mass migrations, and billions of dollars in loss and damage, which affect the social fabric balance and international relationships. To be aware of the proportion of these phenomenons, it is enough to consider just the internal population displacement due to natural disasters: in fact, according to the latest report of the Internal Displacement Monitoring Center (IDMC) [2], more than half of all the 60.9 million new internal displacements registered in 2022 is owed to the necessity to have to deal

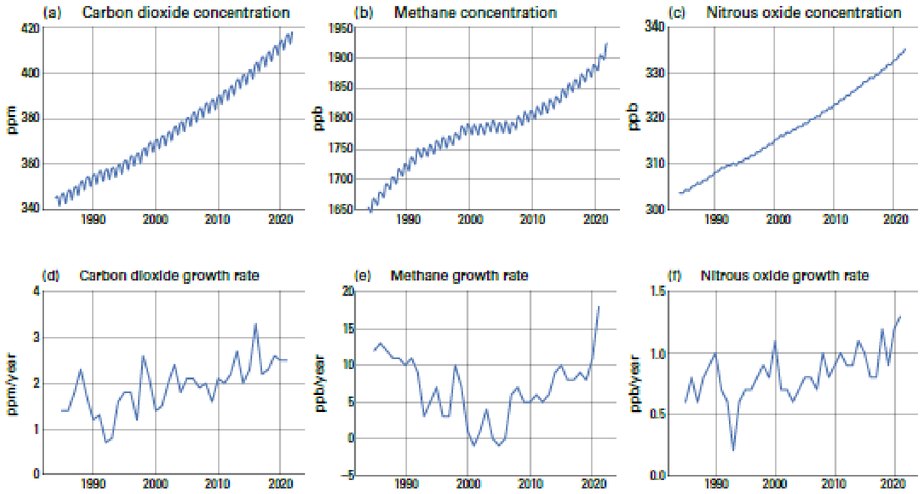

Figure 1.1: Monthly globally averaged mole fraction (measure of atmospheric concentration), in 1984-2021 in the top row and the growth rates representing increases in successive annual means of mole fractions for three of the main GHGs (CO_2, CH_4 and C_2O) in the bottom row are reported [1].

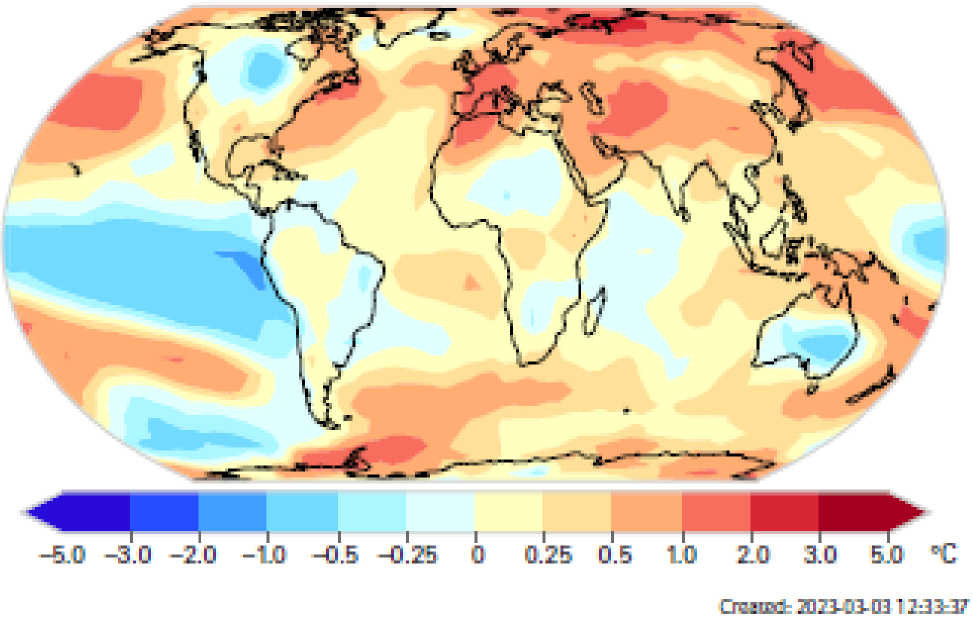

Created: 2023-03-03 12:33:37

Figure 1.2: Local surface temperature variations between 2022 and the 1991–2020 average [1].

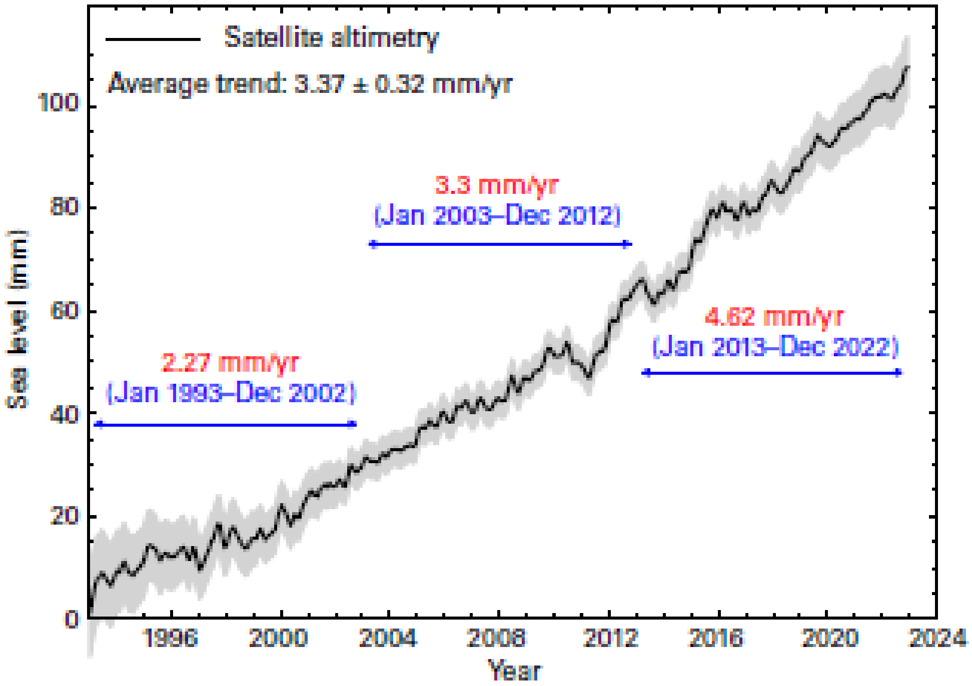

Figure 1.3: The black curve represents the global mean sea level (GMSL) evolution in the 1993-2022 time span with uncertainty related to the satellite elevation highlighted by the grey area, while the three horizontal blue lines reports the average trends over three consecutive periods [1].

with the actual or probable disasters and consequences of natural hazards setting a new record in the last decade, as highlighted in Figure 1.4. These population displacements, for example, imply the adoption by the governments of policies and actions to face at first the emergency phase to provide the basic needs of the environmentally displaced person and then the subsequent new arrangements and accommodations, inevitably spending economic and financial resources and consequently influencing the future economic and social policies of an entire country. Now considering also international mass migrations and the ever-increasing frequency of these disasters, it is clear that these numbers may unfortunately have a rising trend in the future if no action to face the environmental problem is taken into account.

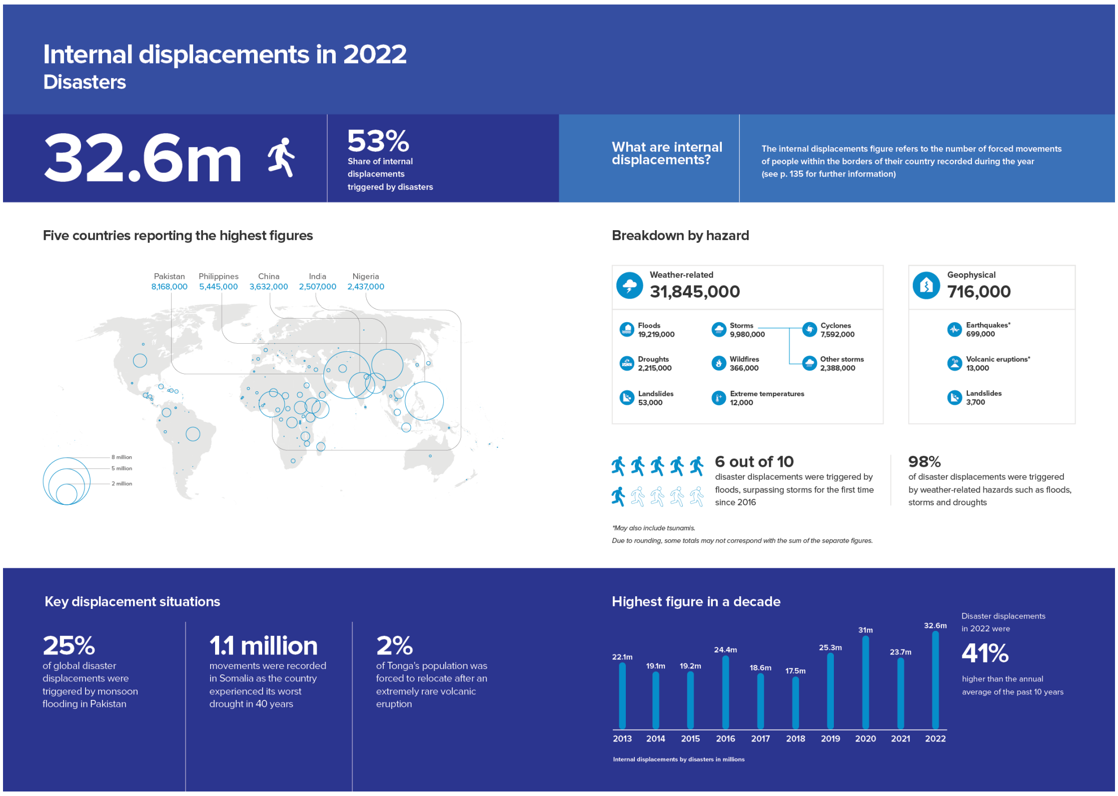

Internal displacements in 2022
Disasters

32.6m

53%
Share of internal displacements triggered by disasters

What are internal displacements?

The internal displacements figure refers to the number of forced movements of people within the borders of their country recorded during the year (see p. 135 for further information)

Five countries reporting the highest figures

Breakdown by hazard

Weather-related	31,845,000
Floods	19,219,000
Storms	9,980,000
Cyclones	7,592,000
Other storms	2,388,000
Droughts	2,215,000
Wildfires	366,000
Landslides	53,000
Extreme temperatures	12,000

Geophysical	716,000
Earthquakes*	699,000
Volcanic eruptions*	13,000
Landslides	3,700

6 out of 10
disaster displacements were triggered by floods, surpassing storms for the first time since 2016

98%
of disaster displacements were triggered by weather-related hazards such as floods, storms and droughts

*May also include tsunamis.
Due to rounding, some totals may not correspond with the sum of the separate figures.

Key displacement situations

25%
of global disaster displacements were triggered by monsoon flooding in Pakistan

1.1 million
movements were recorded in Somalia as the country experienced its worst drought in 40 years

2%
of Tonga's population was forced to relocate after an extremely rare volcanic eruption

Highest figure in a decade

Disaster displacements in 2022 were
41%
higher than the annual average of the past 10 years

Figure 1.4: Synthetic summary about internal population displacements triggered by disasters where in particular it is reported the share of weather-related disaster displacements and the most affected countries in 2022 [2].

1.2 Agriculture and its smart management

Like any other anthropic phenomenon, the intensive land use due by the agricultural sector is responsible for numerous actions which consequences are also impactful on human everyday life: for example, pesticides and fertilizers still-increasing overuse (as reported in Figure 1.5 and Figure 1.6) and water resources waste may lead to desertification, watershed and atmospheric contamination, and resultant acid rain phenomena influencing routines, diets and global socioeconomic situation [3].

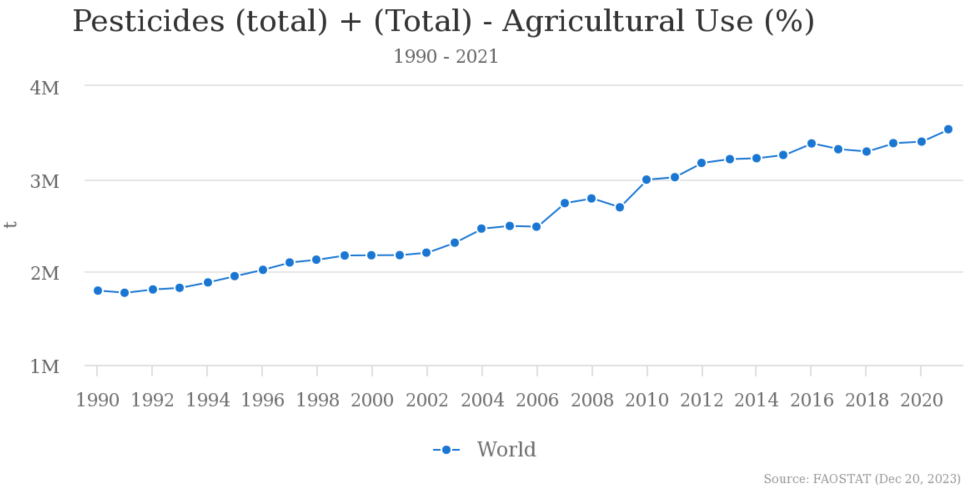

Figure 1.5: Pesticides use over the 1990–2021 period considering world agricultural use [3].

As highlighted in Figure 1.7, this topic can be analyzed in particular considering the share of GHG emissions from food production over the global emissions [4, 5]: in fact, around a quarter of the global GHGs released in the atmosphere are caused by food production spatially concentrated in the half of the world's habitable land that is dedicated for agriculture purposes [6] in charge of more than three-fourths of global eutrophication (namely ocean and freshwater pollution) and more than three-fifths of the global demand of freshwater, as noted in Figure 1.8.

Focusing in particular on the agrifood sector (which namely takes into account food primary production, its distribution, and household consumption), it is evident the significant impact on emissions share of the actions directly related to the agricultural land, as reported in Figure 1.9. Even if it can be highlighted a downward trend concerning agricultural-related emissions over the last thirty years [3], other agrifood indicators should be and have to be streamlined, for instance, starting from livestock and pre- and post-production contribution on the overall agrifood-related emission.

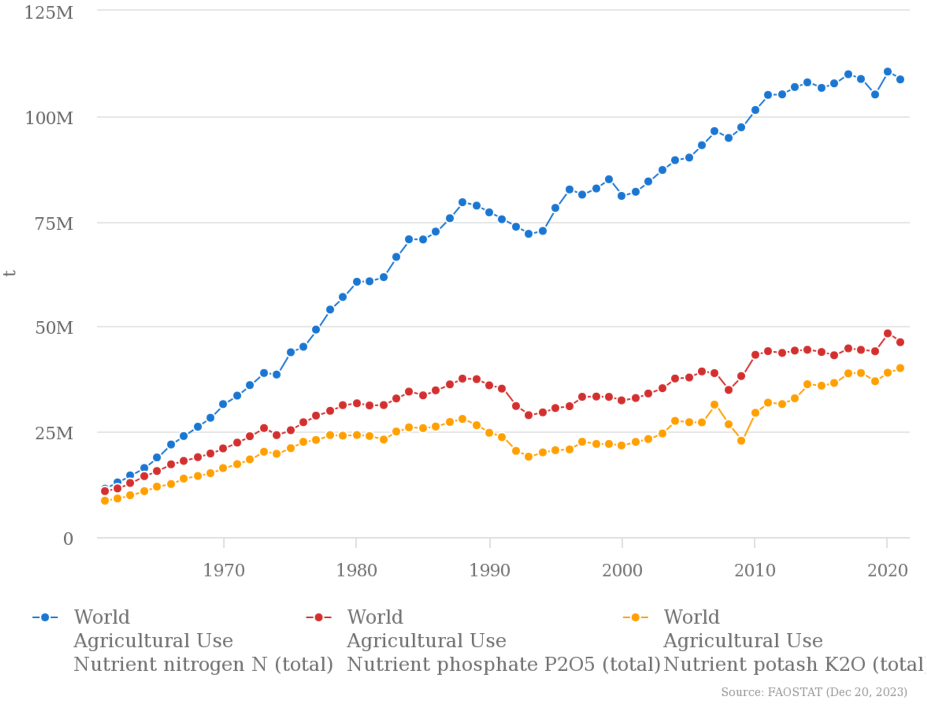

Source: FAOSTAT (Dec 20, 2023)

Figure 1.6: Nutrients use over the 1990–2021 period considering world agricultural use [3].

Therefore, also considering the ever-higher food demand due to the still-increasing world population [7] as reported in Figure 1.10, it is clear the need for a change of direction in the way of thinking the management of the agricultural sector to reduce its impact on the environment and to make it more sustainable: for this purpose the studies about new technologies and techniques employed in the so-called Smart Agriculture field have led to a wide range of different deployable solutions.

The goals of Smart Agriculture are to boost productivity, improve resilience, reduce emissions, and optimize human labor through the utilization of technologies such as Wireless Sensor Networks (WSNs), Long Range Wide Area Network (LoRaWAN), and Internet of Things (IoT) to satisfy the ever-increasing need of food related to the ever-increasing world hunger due to extreme weather phenomena too and to speed up the change of route in the climate-change scenario.

For instance, a shortlist of actually-employed hardware components exploited for Smart Agriculture applications in order to help farmers' work and to improve yields quality and quantity has been reported in Gzar, Mahmood, and Abbas' survey [8] and in the studies conducted by Prakash, Singh, Gupta, and Lohan [9]: in

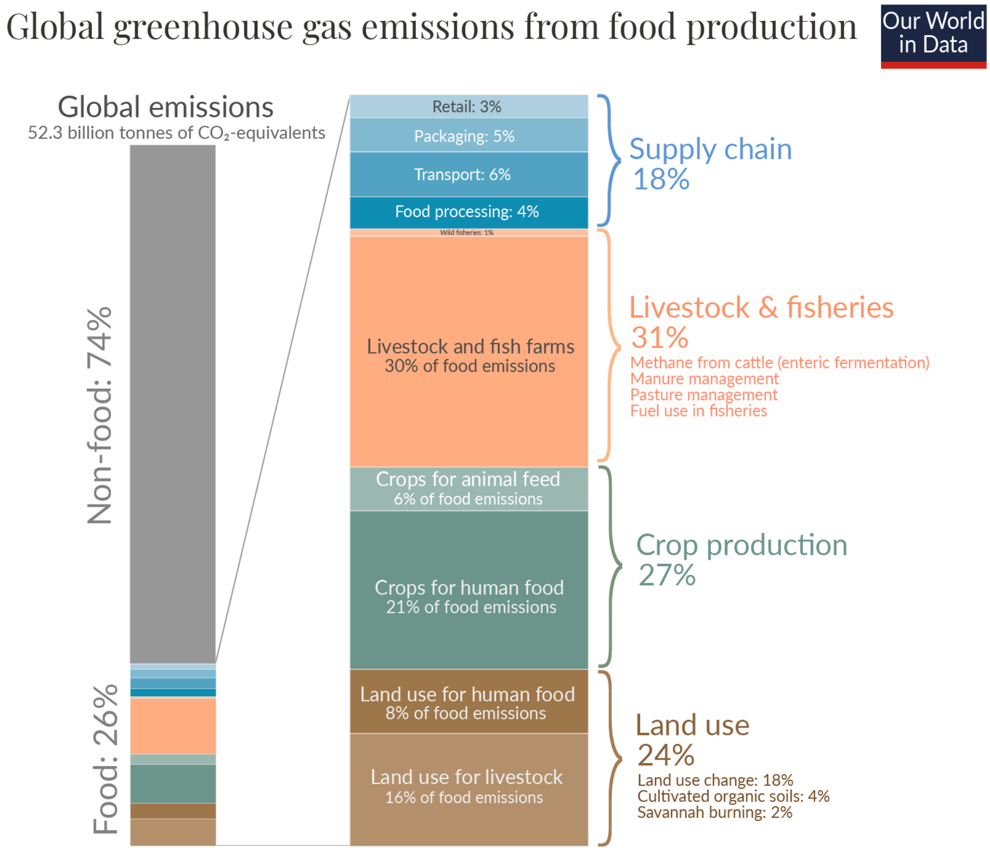
Global greenhouse gas emissions from food production

Data source: Joseph Poore & Thomas Nemecek (2018). Reducing food's environmental impacts through producers and consumers. Published in *Science*.
Licensed under CC-BY by the author Hannah Ritchie (Nov 2022).

Figure 1.7: Food production GHG emissions contribution over the global GHGs emitted in the atmosphere [4, 5, 6].

particular, noteworthy systems are open-source electronics platform like Arduino UNO developed by Arduino, pocket-sized computer such as Raspberry Pi and Beaglebone (the latter developed by Texas Instruments) and sensors employed to evaluate valuable parameters such as humidity of the air, temperature, soil moisture, pH level and gas concentrations, each of which can rely on a network of devices and/or on softwares required for IoT implementation like protocols such as MQTT (Message Queuing Telemetry Transport), HTTP (HyperText Transfer Protocol), LoRa (Long Range) and WiFi, platforms in order to view and analyze data from embedded IoT-based devices such as ThinkSpeak and may be exploited in both indoor and outdoor applications, impacting agriculture sector significantly all over the world [8, 9].

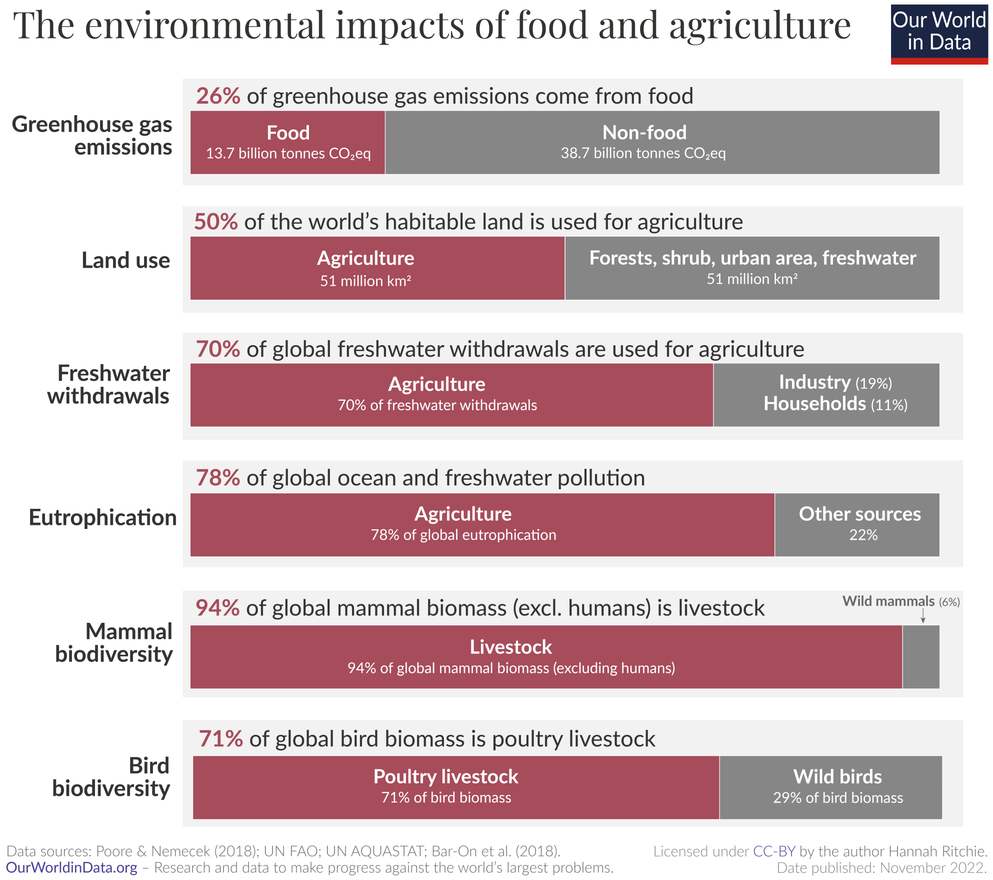

Data sources: Poore & Nemecek (2018); UN FAO; UN AQUASTAT; Bar-On et al. (2018).
OurWorldinData.org – Research and data to make progress against the world's largest problems.

Licensed under CC-BY by the author Hannah Ritchie.
Date published: November 2022.

Figure 1.8: Agriculture and food production impacts on the environment [6].

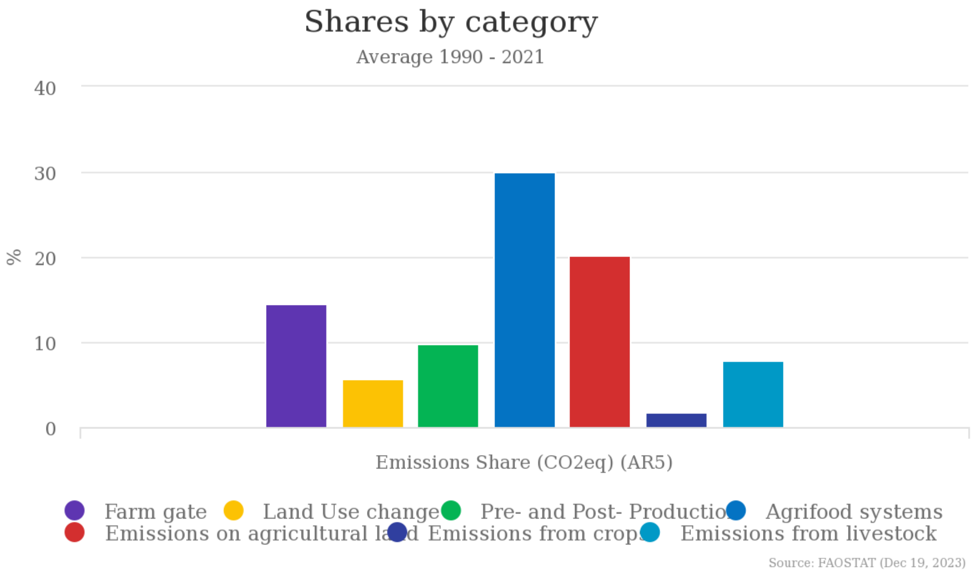

Figure 1.9: Emissions share (in $CO_2 - equivalent$) of agrifood systems on a worldwide scale averaged on the 1990–2021 period [3].

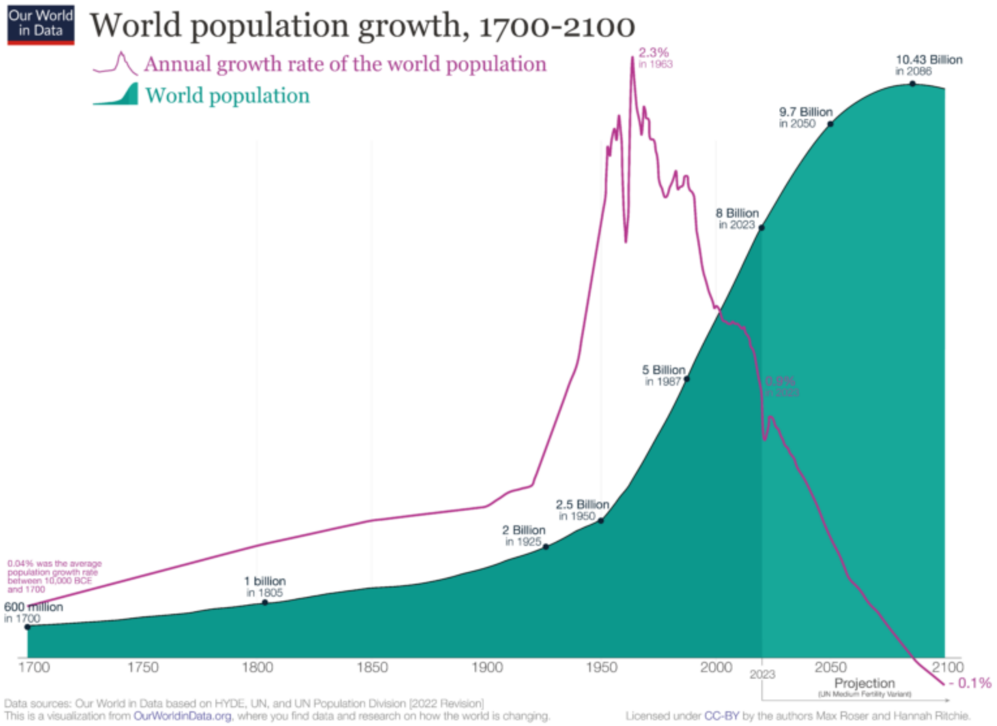

Figure 1.10: Actual data and projection of world population and its annual growth rate in the 1700-2100 time span [7].

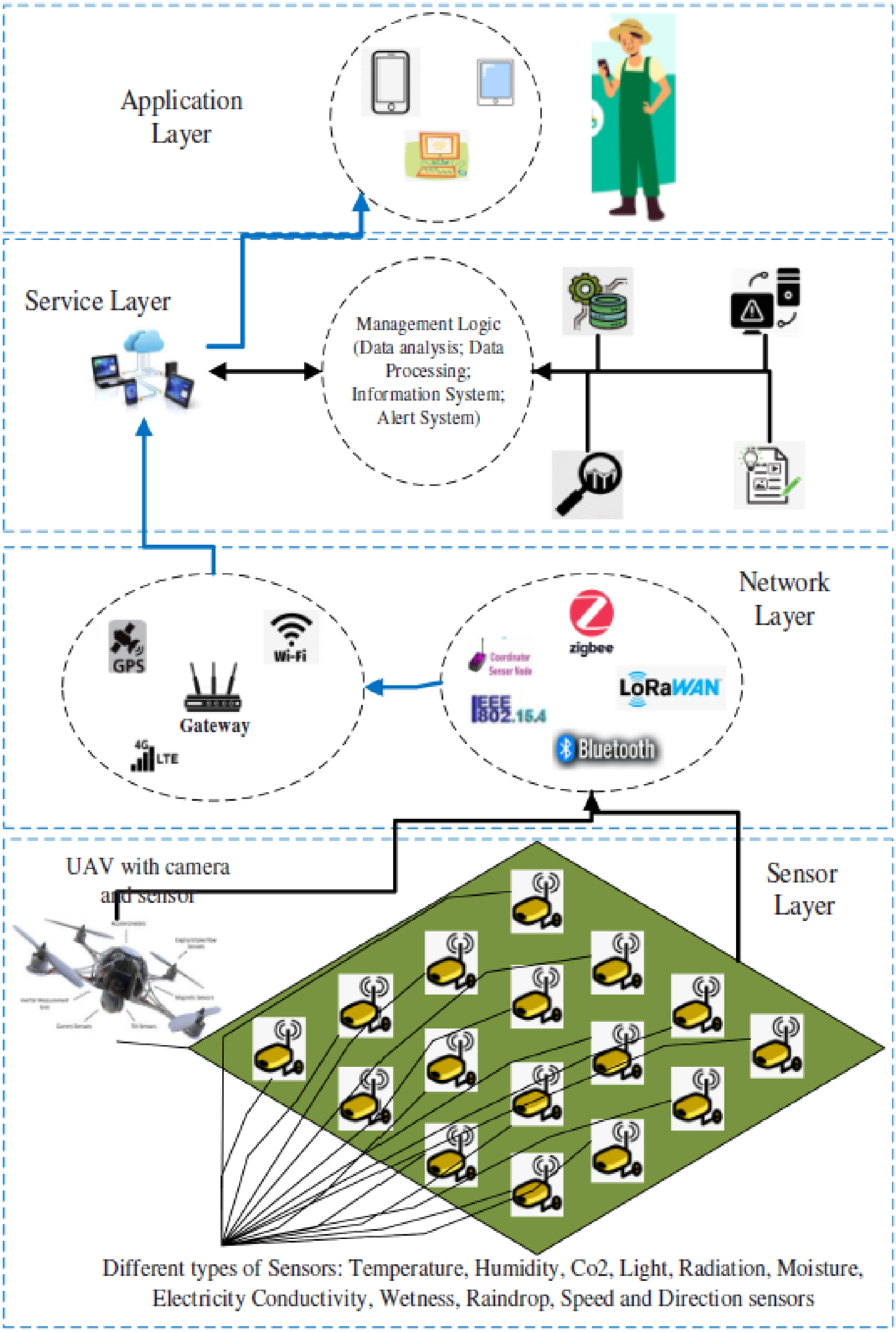

Figure 1.11: Smart farming exploited relationships overview [9].

According to the analysis reviewed by Namana et al. [10], several IoT solutions for Smart Agriculture applications have been exploited in particular for what concerns irrigation monitoring (improving different irrigation techniques such as surface irrigation, sprinkle irrigation, and drip irrigation), fertilizer monitoring based for example on normalized difference vegetation index (NDVI) fertilization approach (thus exploiting aerial/satellite images to monitor the crop nutrient levels), soil monitoring where IoT sensors can be even employed for soil mapping, crop disease and pest monitoring (exploiting devices such as UAVs, field sensors and/or remote sensing satellites), yield monitoring to, for example, identify the right moment for harvesting, and weather monitoring as depicted in Figure 1.12.

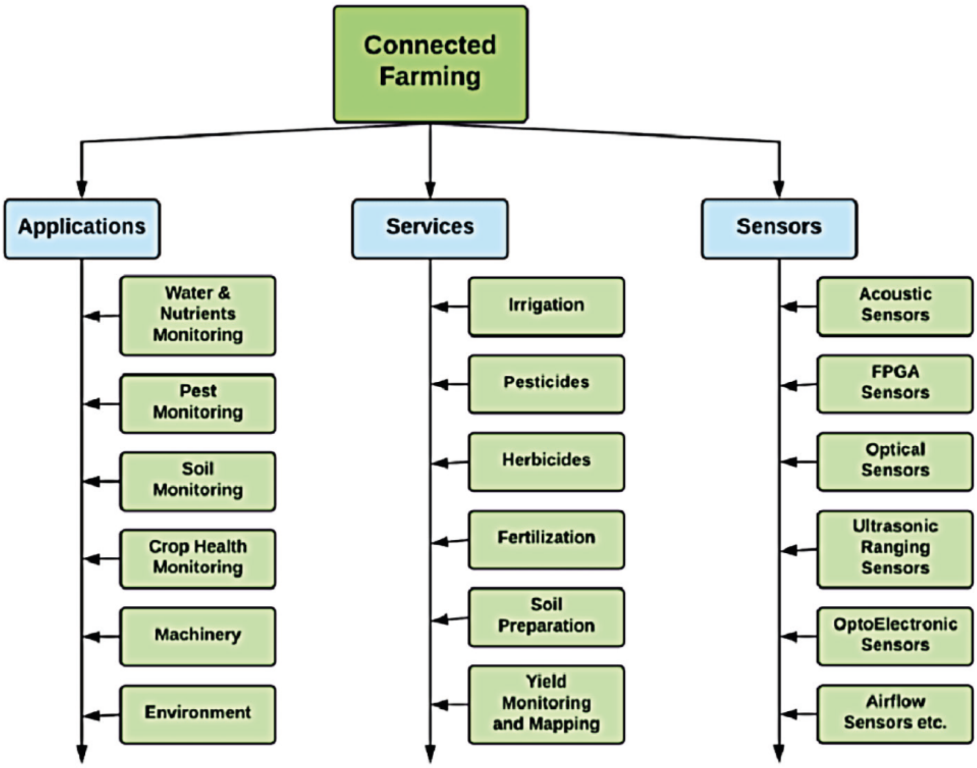

Figure 1.12: Applications and services for Smart Agriculture [10].

Moreover, with the increase of interest and publications on these solutions [9, 10], many actual implementations have been developed and then studied: for instance, in the same aforementioned Namana et al. work [10], few IoT devices actually employed for Smart Agriculture applications to help farmers have been reported such as the Yuktix Green Sense (an off-grid remote monitoring analytics solution exploiting a solar-powered long-range wireless device for irrigation, crop and disease monitoring), the Agrela Ecosystems PheNode (a customizable phenotyping device integrated with several wireless sensors), the Agrila (a smart sensor station for Smart Agriculture purposes with multiple sensors integrated), the Fasal (an IoT-based data-driven smart farming device), the Arable Mark 2 (an infield sensing and data capture IoT device), the Exabit RobotiX (an infield device installed in order to sense soil conditions, environmental conditions and upload the data into its own cloud server), and several UAV-based solutions in order to track crop growth, increase crop yield and improve agriculture techniques and overall outcome performing monitoring tasks from an aerial point of view.

In this particular case, the solution presented in this thesis has been developed to minimize the waste of energy and water resources and the eventual chemical utilization to what is strictly necessary for each single plant's maintenance: to achieve this and taking a cue from results discussed in several past studies [11, 12, 13, 14, 15, 16], an energetically self-sufficient system capable of evaluating the plant health status by the stem electrical impedance has been developed. It has even been designed to permit the sharing through a LoRa-based communication of the measurements made to other network components to take appropriate actions on a single plant and/or a whole field.

1.3 Thesis organization

This thesis is divided in several chapters as follows:

- In Chapter 1, a brief overview of the actual global situation and a glimpse of this thesis topic have been presented.
- In Chapter 2, an implementation of a Plant Microbial Fuel Cell (PMFC) will be introduced, and the results obtained will be discussed.
- In Chapter 3, the components of the developed system of this thesis project will be explained in detail and characterized.
- In Chapter 4, the firmware implementation and the microcontroller (MCU) configuration will be presented.
- In Chapter 5, the experimental setup comprising the developed system will be mounted and tested, and the results will be discussed.
- In Chapter 6, the conclusions and possible future implementations will be presented.

Chapter 2

Plant Microbial Fuel Cell

2.1 Overview

As previously presented in Section 1.2, this thesis' developed solution is to design a system capable of evaluating the plant health status by the stem electrical impedance analysis. In particular, considering the possible dimensions and layout of a cultivation field, a wired power network to supply each plant-mounted monitoring system may be impractical and difficult to maintain. Therefore, a completely autonomous system in terms of energy supply that is able to perform wireless communication is the most suitable solution.

One of the most employed energy-supply-related options for energetically self-sufficient devices is by using photovoltaic (PV) cells: these exploit the physical phenomenon named photovoltaic effect which consists in the generation of electrical power in a semiconductor material (usually a silicon-based p-n junction) exposed to a light source. Light radiation in the form of photons excites electron-hole pairs in a specific region of the p-n junction named depletion region, where then the pairs are spatially separated through an electric field and drifted to the electrodes, generating a DC current, which then flows through the load, and the rest of the circuit. Furthermore, PV cells are a mature technology with a long lifetime and a reliable DC output [17, 18, 19]. In addition, PV cells can be applied in several fields as long as a light source is present due to their scalability since the relation between their surface area and output power is directly proportional with an efficiency ranging from 13% to 47.6% depending on the manufacturing process, on the field of application and on the materials utilized to build the cell, according to the National Renewable Energy Laboratory (NREL) report depicted in Figure 2.1.

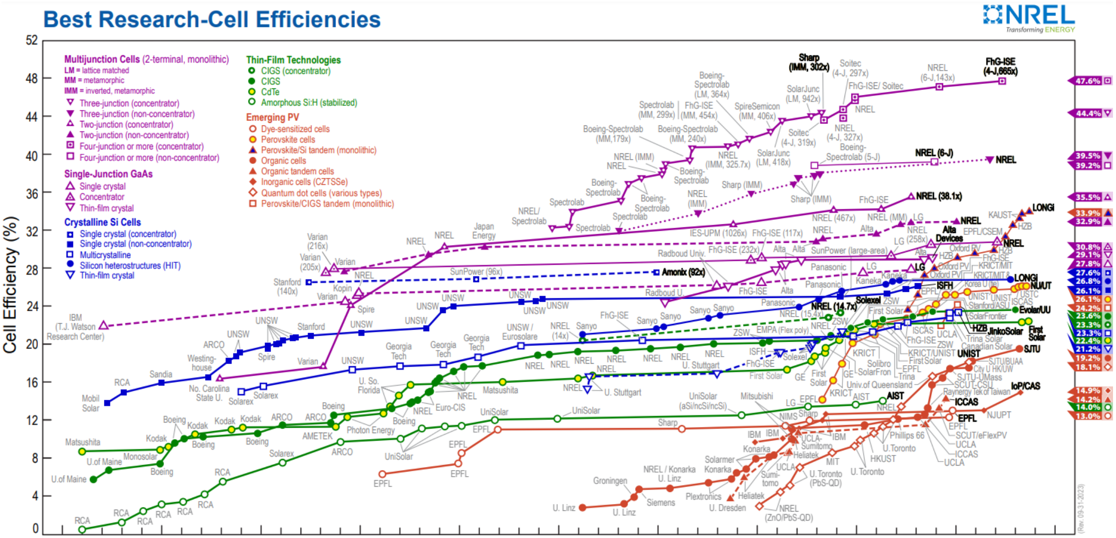

Figure 2.1: This plot is courtesy of the National Renewable Energy Laboratory, Golden, CO. and it reports the efficiencies of different photovoltaic cells employed in different operating fields and manufactured with diverse techniques, processes and materials.

Relatively new alternative options that can be employed to harvest energy and subsequently provide power to small systems can be identified in radio-frequency energy harvesting (RFEH) systems, mechanical energy harvesting systems, thermoelectric and bio-electrochemical systems [18, 19, 20, 21, 22].

As mentioned in the work of Rahman and Kader [23], RFEH can be a viable option, especially to encounter the energy constraints of the devices part of ever greater WSNs. RFEH systems are able to generate an electrical output starting from electromagnetic energy, and thus, they can be used, for example, to supply low-power electronic systems.

However, as also highlighted in Altug's Master's Degree Thesis [18] and by Serdijn, Mansano, and Stoopman's study [24], RF energy harvesting is quite a challenge to be employed since it is characterized by a relatively low power density. It is also highly dependent on the nearness of the radiation source (and on any of its variations). At the same time, the design and the project of the interface between the electromagnetic fields and the electronic circuitry can be very challenging.

Concerning mechanical energy harvesting systems, it is possible to consider several options such as electromagnetic, electrostatic, piezoelectric, and triboelectric harvesting systems [18, 19, 25, 22]. They differ from each other by inspecting the harvesting principle exploited: in particular, electromagnetic harvesting is based on electromagnetic induction phenomena modeled by Faraday's induction law, while electrostatic, piezoelectric, and triboelectric harvesting systems, respectively, rely on electrostatic induction, on direct (or converse) piezoelectric effects (exploiting the straightforward relation between stress applied to a suitable material and the subsequent density of charge, or vice-versa) [18, 19, 22, 25] and finally on the triboelectric effect which is a type of contact electrification on which certain materials become electrically charged after they come into frictional contact with a different material [19, 22, 25]. As reported in Figure 2.2, different combinations of different harvesting principles are permitted such as an integration of flexible piezoelectric and triboelectric generators in the same system [22].

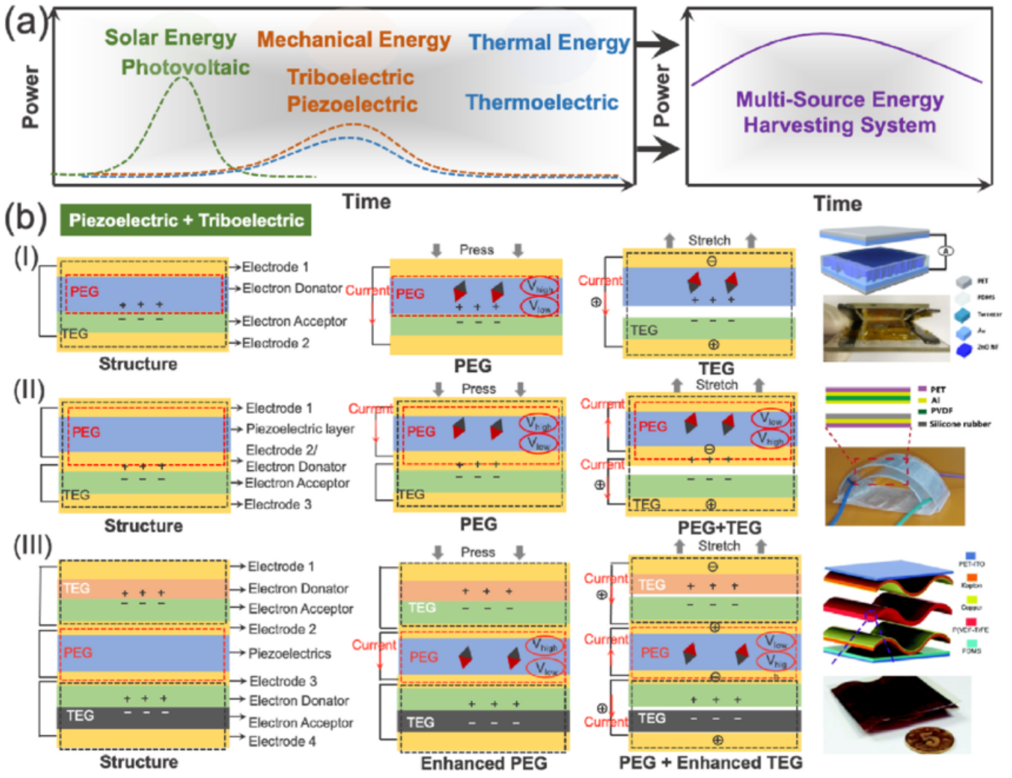

Figure 2.2: On the top, plot of the energy sources involved over time in a continuous multi-source energy harvesting system with mechanical, thermal and solar energy, while at the bottom, different structures combining together piezoelectric and triboelectric energy generators [22].

Regarding thermoelectric harvesting systems, the basic principle is the Seebeck effect, which states that a temperature gradient applied on certain electrically conductive materials generates a voltage [26]. As reported in Snyder's work [26], the charge carriers in the material start to move more freely, preferentially from the hot part to the cold one, resulting in an electrostatic potential. These thermoelectric energy harvesting systems are fascinating, particularly for bio-medical and/or wearable applications, due to the possibility of exploiting body heat to energize low-power devices. However, the omnipresence of temperature gradients and heat flows in natural and anthropical environments makes this one of the most exciting energy harvesting options for small-sized devices [18, 26, 21].

In this specific case, a continuous renewable energy system is needed to fulfill the energy demand and the sustainability goal: in this scenario, a system based on solar panels only could not be enough due to the scarceness of light during the night and in bad weather conditions in particular, thus a Plant Microbial Fuel Cell (PMFC) has been exploited to satisfy the energy demand of the system when needed due to the possibility to obtain energy through the plant organic waste [27], especially considering the field of application in which the developed system is designed to be applied, making the PMFC-based solution the more suitable in this specific study case in tandem with the solar panels. In addition, the greater ease of usage and installation and the lower cost compared to the energy harvesting systems mentioned above are features coherent with the low-cost and low-power characteristics required for this thesis' developed system.

A Plant Microbial Fuel Cell (PMFC) is considered a bio-electrochemical renewable source of energy based on the Fuel Cell (FC) system. It exploits microorganisms to produce bio-electricity made from the organic matter accumulated near the roots of a plant. Bacteria in the so-called rhizosphere behave like catalysts to convert plant-derived scrap (called rhizodeposits) released in the soil into bio-electricity [28].

Similarly to an actual FC, a PMFC is essentially based on a structure composed by an anode region (where the oxidation takes place) and a cathode region (where instead the reduction occurs) separated by an eventual membrane that allows only the permeate of the cations in case of a Proton Exchange Membrane (PEM) or anions in case of an Anion Exchange Membrane (AEM) forcing the electrons derived by the anodic oxidation reaction to flow through an external load, as represented in Figure 2.3.

As also highlighted in Angelini's Master's Degree Thesis [27] referencing Rabaey and Verstraete's work [29], a fermentation-based way of metabolism of the bacteria accumulated in the rhizosphere of the plant is needed to generate an electric current, thus an anaerobic region in which at least the anode should be located is required.

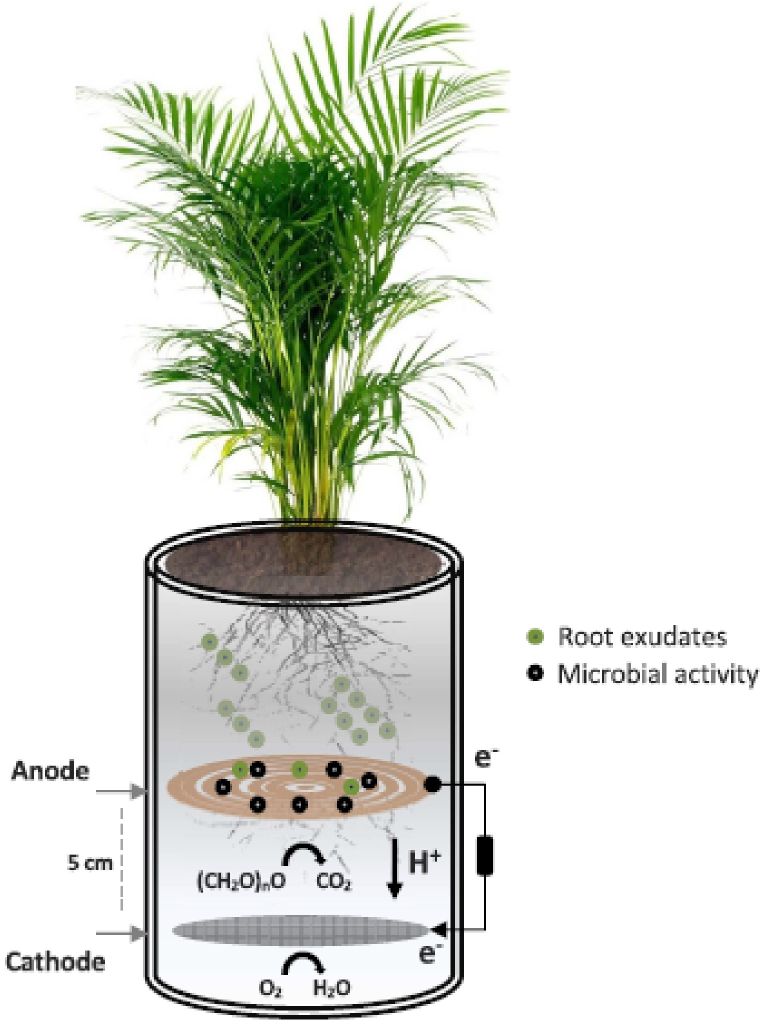

Figure 2.3: Single-chamber PMFC power generation structure and mechanisms [28].

Therefore, as stated in Altug's work [18] and in the review carried out by Kabutey et al. [30], different designs of the PMFC can be implemented exploiting several combinations of materials as electrodes and different structure configurations: in fact, each variety of cultivation may need a specific combination of electrode materials and structure related for instance to the microorganisms involved in the redox reaction, to the composition of the rhizodeposits released in the soil and other factors linked to the site where the PMFC is implemented as further underlined in Figure 2.4.

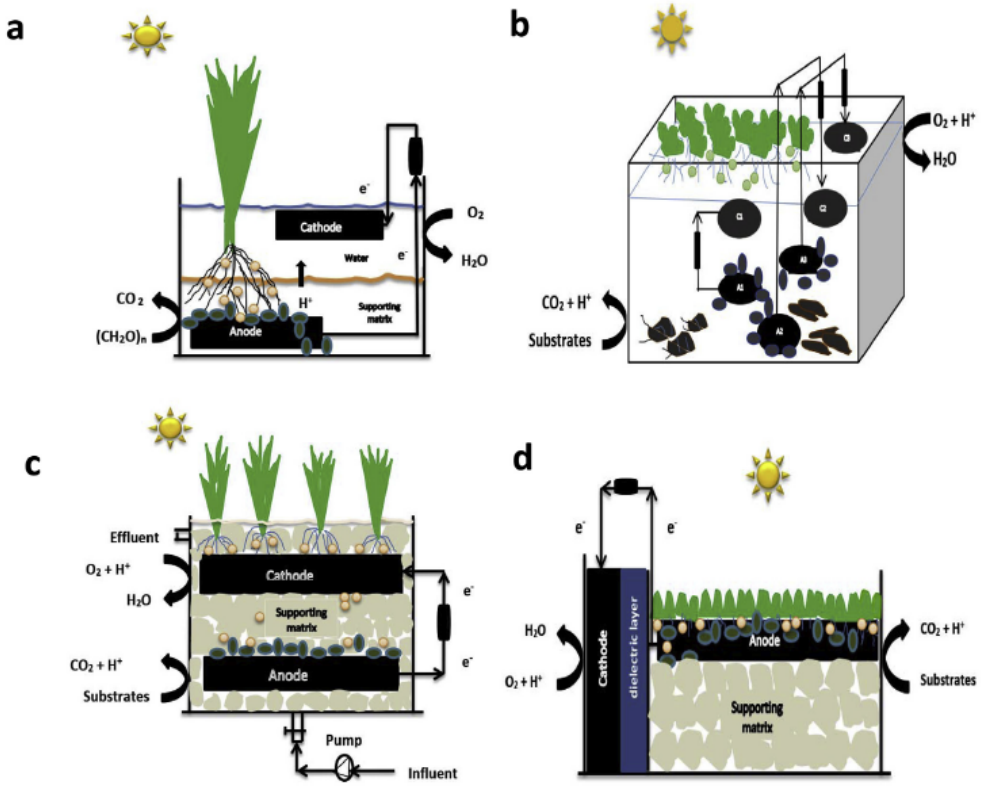

Figure 2.4: Several schematic illustration of different PMFC structures such as the plant-MFC with vascular plants in (a), the macrophyte PMFC in (b), the constructed wetland MFC (CW–MFC) in (c) and the bryophyte MFC with vascular-tissue-less plants in (d) [30].

2.2 PMFC experimental setup implementation

For this thesis, two PMFCs have been built exploiting tobacco (Nicotiana tabacum L.) as plants for the cells' realization. Tobacco has been selected since it is a C3-class plant (a three-carbon compound as the first photosynthesis product) [31] that presents a fully-sequenced genome, a relatively short maturation period (even in a protected and closed environment such as a laboratory), and due to the availability of the grown crops in the laboratory.

The structure implemented is based on the single-chamber design setup employing three different materials as metal electrodes due to their low cost, high electrical conductivity, and availability [18]:

- Aluminum (Al) in the form of an aluminum plate depicted in Figure 2.5a.
- Copper (Cu) as a copper wire helix shown in Figure 2.5b.
- Zinc (Zn) as a zinc mesh grid portrayed in Figure 2.5c.

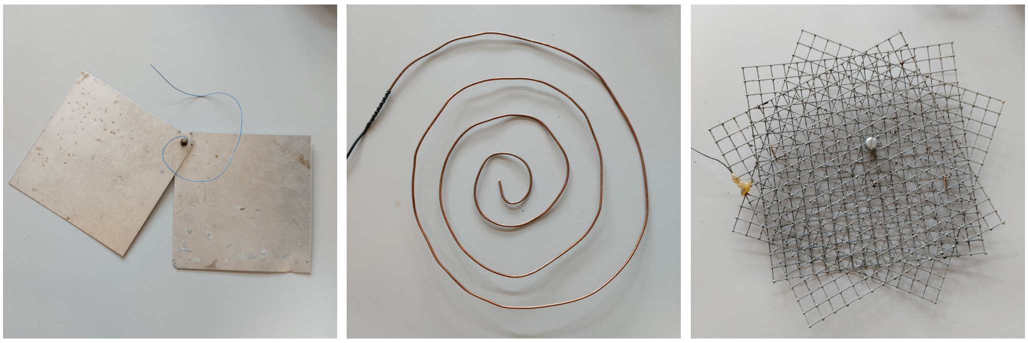

(a) Aluminum plates. **(b)** Copper wire helix. **(c)** Zinc mesh grid.

Figure 2.5: Materials exploited as electrodes in the PMFCs.

In particular, the tobacco plant for the from-now-on-called PMFC 1 was sown two days before the one exploited for the from-now-on-called PMFC 2 (September 13th, 2023 vs. September 15th, 2023): then both plants were watered twice a week with a liter of water each until after this thesis project.

Another difference can be identified in the electrode materials since the PMFC 1 only presents a zinc mesh grid and a copper wire helix from top to bottom, while the PMFC 2 takes into account three electrodes as depicted in Figure 2.6, from above downward a zinc-plated wire mesh, an aluminum plate and finally a copper wire spiral at the bottom of the plant pot: thus three different pairs of electrodes have been studied in PMFC 2 (Zinc-Copper, Zinc-Aluminum, and Copper-Aluminum) as opposed to only one in PMFC 1 (Zinc-Copper). In Figure 2.7, a zoom on the electrode-sourced wires exploited to connect the PMFC with an external feasible load has been depicted. In particular, it is referred to PMFC 2 since three wires are present, each one related to a specific electrode. For thoroughness, the potting soil exploited is the same for both the PMFCs and it is a common universal potting soil organic mix of peat moss, sand, and minerals such as perlite and vermiculite able to provide the plant enough nutrients such as nitrogen (N), phosphorous (P) and potassium (K) to sustain its growth.

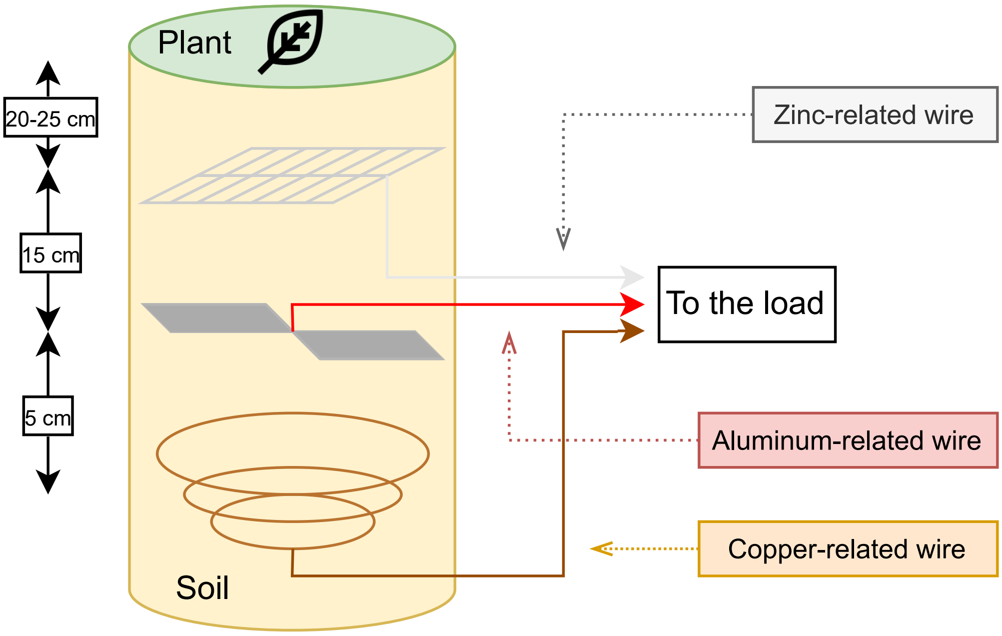

Figure 2.6: Employed PMFC structure exploiting three electrodes with the zinc-plated mesh grid electrode on top, the aluminum plates electrode in the middle and the copper helix wire at the bottom, each with their own correspondent external link.

Figure 2.7: Zoom of the wires connected to the exploited electrodes (white wire associated to the zinc mesh grid, brown wire related to the copper spiral wire and red wire linked to the aluminum plate) and exiting through a thereafter-sealed hole at the bottom of the pot in PMFC 2.

2.3 PMFCs characterization

Figure 2.8: PMFCs at the time of the first characterization where PMFC 2 is on the foreground while PMFC 1 is in the background.

After having waited until November 2$^{\text{nd}}$, 2023 to let both plants grow by watering them twice a week (as in Figure 2.8), the characterization of each pair of electrodes of both PMFCs have been performed on a two-week basis to have a piece of more comprehensive knowledge about the PMFC electrodes conditions and their performances over time: this analysis may permit to find the most suitable electrodes combination for the on-field applications.

The characterization consists of an open-circuit voltage measurement of each pair of electrodes and an indirect evaluation of the current flowing through well-known resistors as a load by measuring the voltage drop across them. During the characterization process of a specific pair of electrodes, the other electrode-related not-used wires are free-floating. All the measurements were done after a watering event, organized in a table, and plotted in several R-V, R-I, I-V, and P-V curves. Within this framework, a Fluke 115 True RMS multimeter [32] from Fluke has been employed for each characterization process performed at the Pierluigi Civera laboratory inside the DET department of the Politecnico di Torino. The resistor exploited set ranges from 120 Ω to 1 MΩ.

The retrieved characterization data have been further reported in Appendix B for completeness.

2.3.1 PMFC 1 characterization

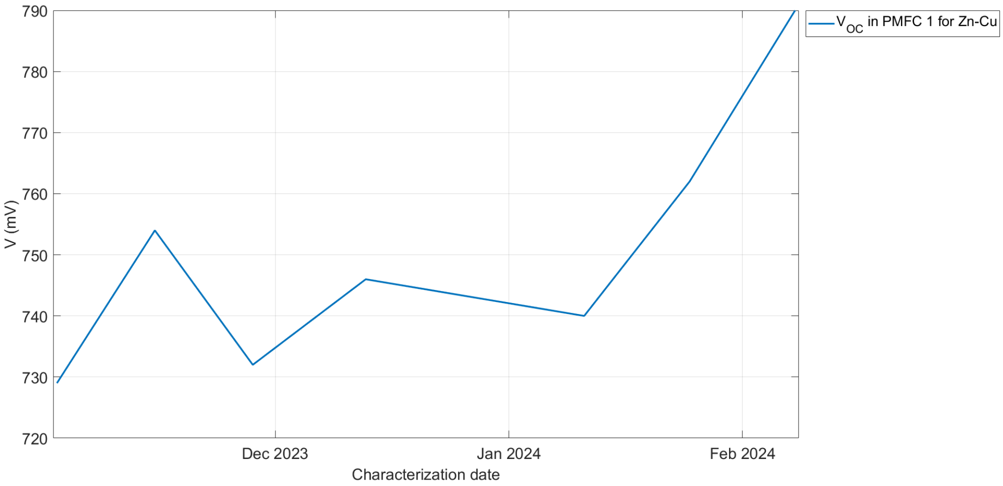

Figure 2.9: Evolution of the open-circuit voltage V_{OC} over time for the Zn-Cu electrode combination of PMFC 1.

As mentioned before in Section 2.3, an open-circuit voltage measurement has been done. In particular, the evolution of the open-circuit voltage V_{OC} over the several characterization processes made during the experimental period has been described in Figure 2.9: it is evident the overall increasing trend of the open-circuit voltage V_{OC} over time which is related to the plant growth and subsequently to its ever-increasing photosynthetic capacity and thus the following rhizodeposition process.

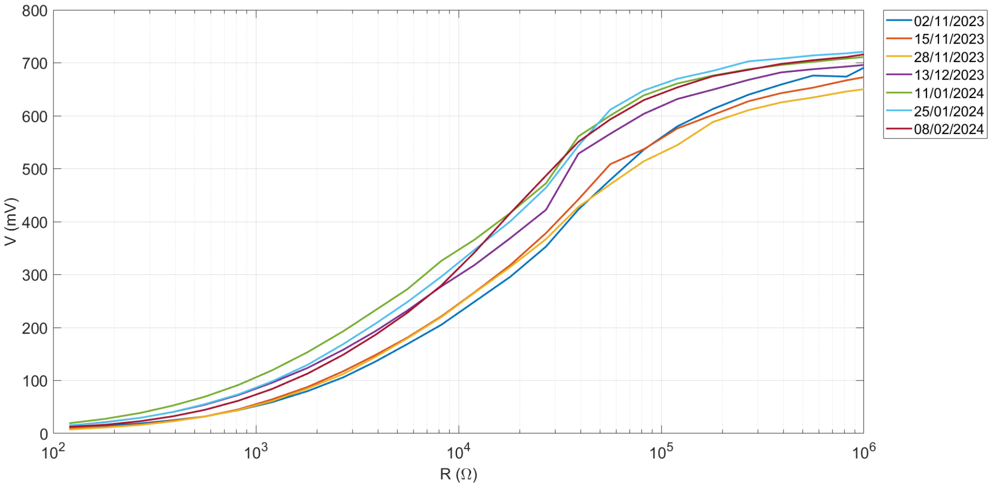

Figure 2.10: Characterization results in terms of R-V curves for the Zn-Cu electrode combination of PMFC 1.

The evolution over time of the output voltage related to the Zinc-Copper electrode combination of PMFC 1 in relation to different resistive loads has been depicted in Figure 2.10. It is noticeable an up-shifting phenomenon of the voltage-related curves over the growth of the tobacco plant exploited in PMFC 1: in fact, the plant tends to release more rhizodeposits in the soil as it grows, in parallel to the higher photosynthetic process rate. Therefore, since the PMFC current generation is directly proportional to the presence of bacteria accumulated in the rhizosphere, the previously underlined up-shifting phenomenon can be expected.

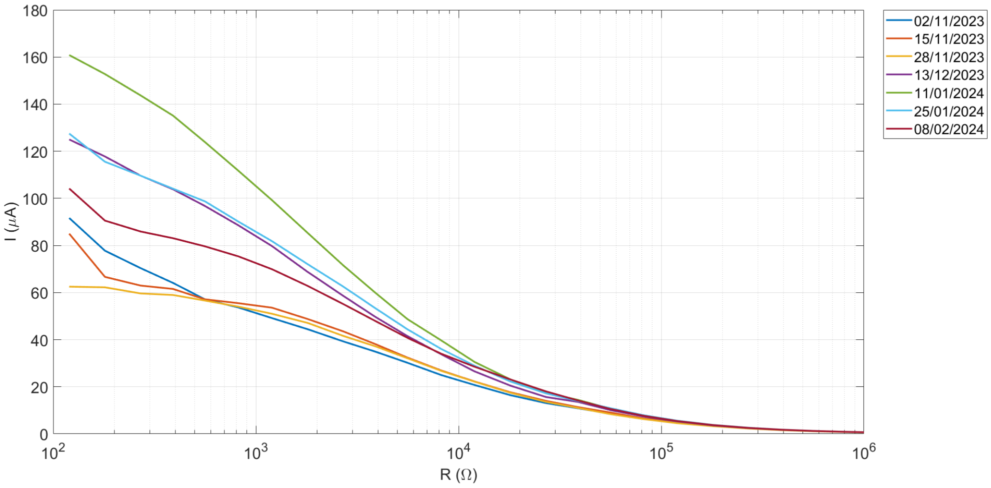

Figure 2.11: Characterization results in terms of R-I curves for the Zn-Cu electrode combination of PMFC 1.

The assumptions done about Figure 2.10 can be transposed on the results depicted in Figure 2.11 where the evolution over time of the output current related to the Zinc-Copper electrode combination of PMFC 1 in relation with different resistive loads has been plotted: according to the Ohm's law, current and voltage are directly proportional, thus a consequent up-shifting phenomenon can be expected remembering the considerations reported in Figure 2.10.

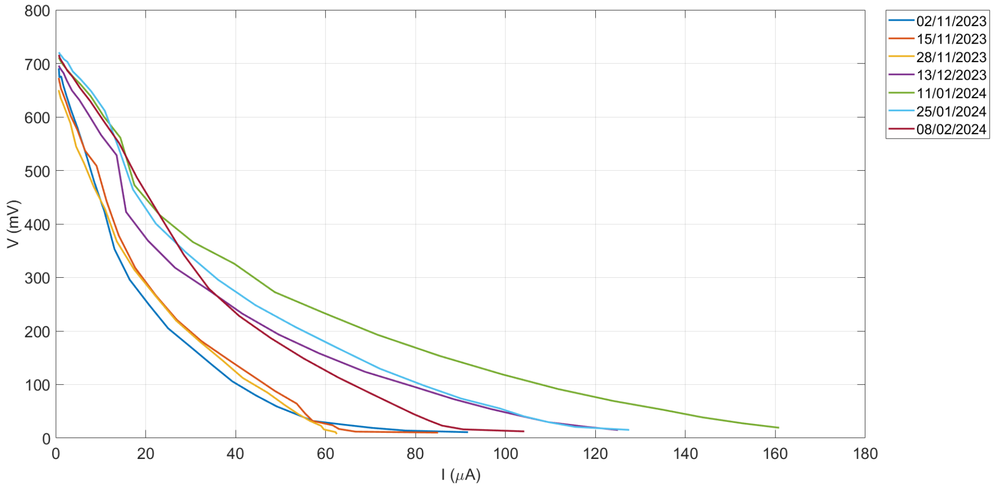

Figure 2.12: Characterization results in terms of I-V curves for the Zn-Cu electrode combination of PMFC 1.

The characterization results discussed before concerning both Figure 2.10 and Figure 2.11 can be further analyzed by inspecting the I-V curves presented in Figure 2.12: it is evident a higher output power in turn to the plant growth, coherently to what has been previously assumed in Figure 2.10 and Figure 2.11. Still focusing on the generated output power provided by the Zinc-Copper electrode combination of PMFC 1, in Figure 2.13 the generated output power behavior in relation to the output voltage of PMFC 1 has been reported highlighting the maximum power point (MPP) retrieved for each characterization result: it is noticeable that most of the registered maximum power points are around 200 mV - 300 mV, coherently to what has been retrieved in Angelini's work [27].

For the sake of completeness, the registered maximum power points have been reported in Table 2.1 where, for each characterization process carried out, P_{MPP} is the output power at the maximum power point (MPP), V_{MPP} is the respective output voltage at the maximum power point (MPP) and $\frac{V_{MPP}}{V_{OC}}$ is the relative share in percentage of the maximum output power evaluated at the characterization-specific maximum power point P_{MPP} with respect to the correspondent open-circuit voltage V_{OC}: in particular, inspecting the $\frac{V_{MPP}}{V_{OC}}$ ratio values it can be evidenced

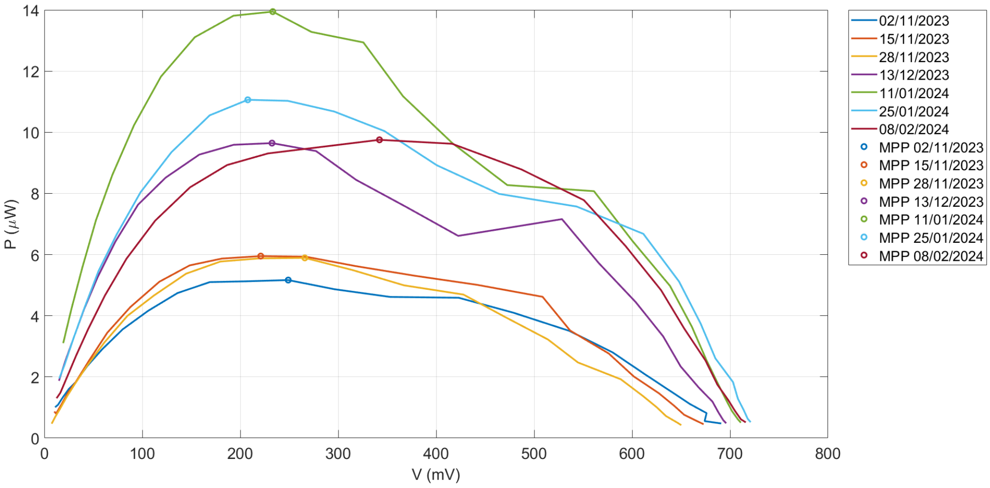

Figure 2.13: Characterization results in terms of V-P curves for the Zn-Cu electrode combination of PMFC 1.

that the output voltage measured at the maximum power point V_{MPP} stands at around 27% - 43% (thus a 35% average value), coherently to the results registered in Angelini's performed evaluations [27].

Characterization number	P_{MPP} (μW)	V_{MPP} (mV)	$\frac{V_{MPP}}{V_{OC}}$ (%)
#1	5.167	249	34.16
#2	5.951	220.9	29.3
#3	5.892	265.9	36.33
#4	9.645	232.4	31.15
#5	13.944	233.2	31.51
#6	11.061	207.7	27.26
#7	9.753	342.1	43.3

Table 2.1: MPP-related registered results for the Zn-Cu electrode combination of PMFC 1.

2.3.2 PMFC 2 characterization

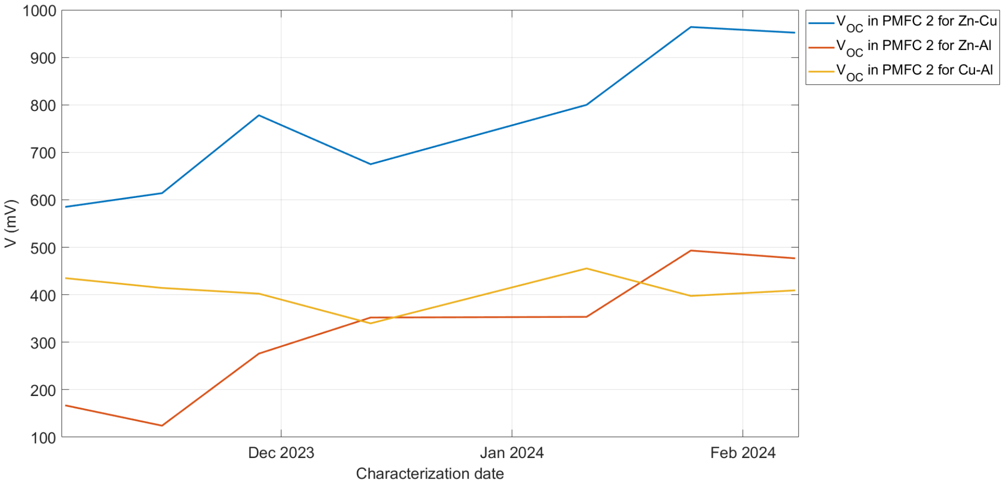

Figure 2.14: Evolution of the open-circuit voltage V_{OC} over time for all of the PMFC 2 possible electrode combinations (Zn-Cu, Zn-Al, and Cu-Al).

In Figure 2.14, the overall increasing trend of the open-circuit voltage V_{OC} over time previously explained in Section 2.3.1 can be underlined, in particular for the Zinc-Copper and Zinc-Aluminum electrode-material configurations. In contrast, the Copper-Aluminum electrode combination presents a relatively constant V_{OC} curve over time, leading to hypothesize an extremely low correlation between V_{OC} and plant growth for this specific electrode couple. Another evident result reported in Figure 2.14 is related to the registered V_{OC} values: the wide voltage gap between the Zinc-Copper curve and the others is noticeable.

In parallel to the results discussed in Section 2.3.1, the R-V plots reported in Figure 2.15, Figure 2.16, and Figure 2.17 present the same up-shifting phenomenon described in Section 2.3.1, thus the same considerations made above can be assumed, in particular for the Zinc-Copper and Zinc-Aluminum electrode-material configurations. Further support can be found in the results depicted in Figure 2.18, Figure 2.19, and Figure 2.20, where the output current evolution over different resistive loads for each PMFC 2 possible electrode-pair configuration has been plotted.

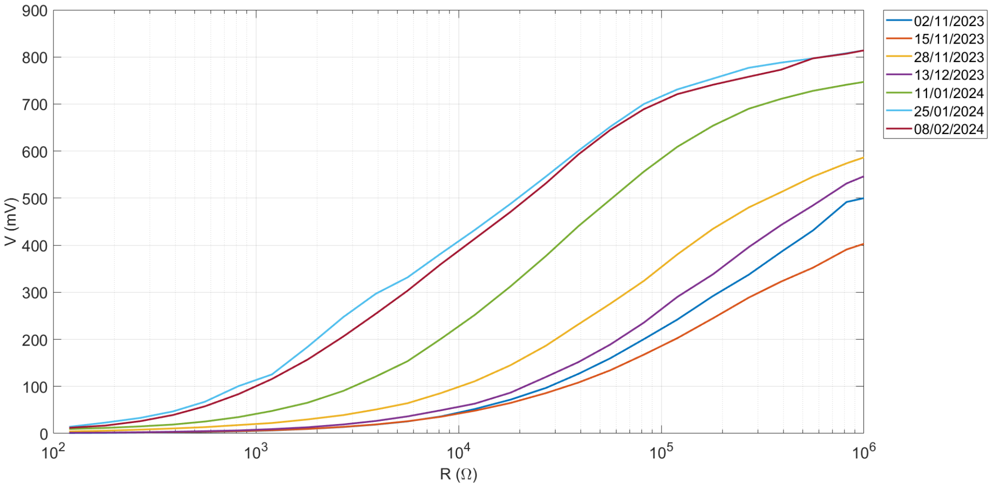

Figure 2.15: Characterization results in terms of R-V curves for the Zn-Cu electrode combination of PMFC 2.

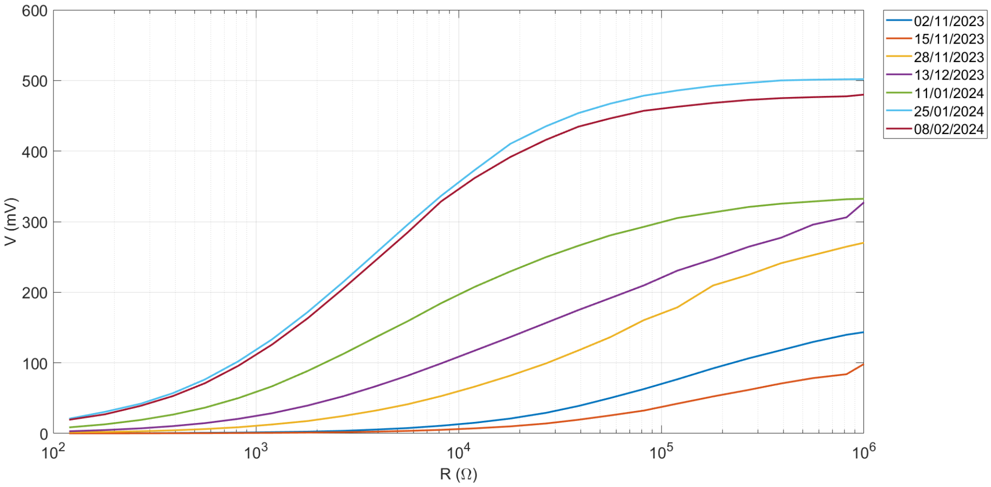

Figure 2.16: Characterization results in terms of R-V curves for the Zn-Al electrode combination of PMFC 2.

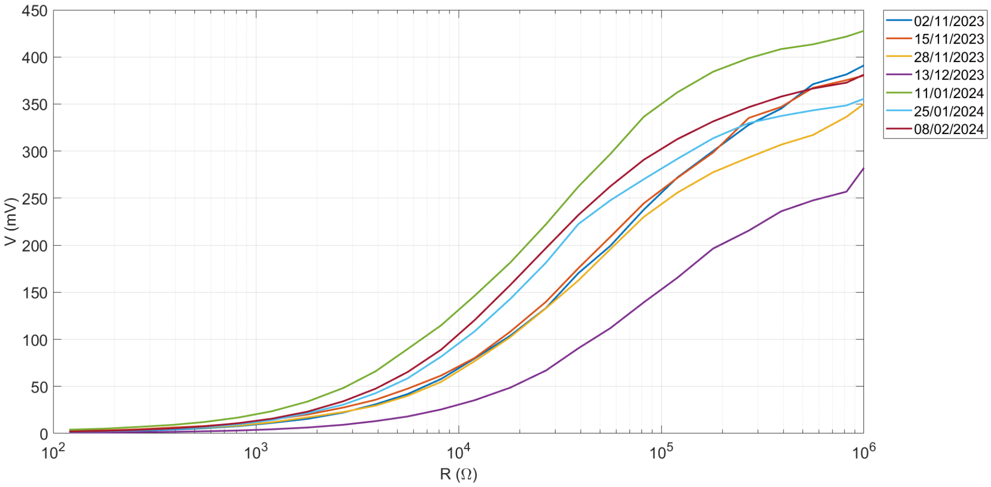

Figure 2.17: Characterization results in terms of R-V curves for the Cu-Al electrode combination of PMFC 2.

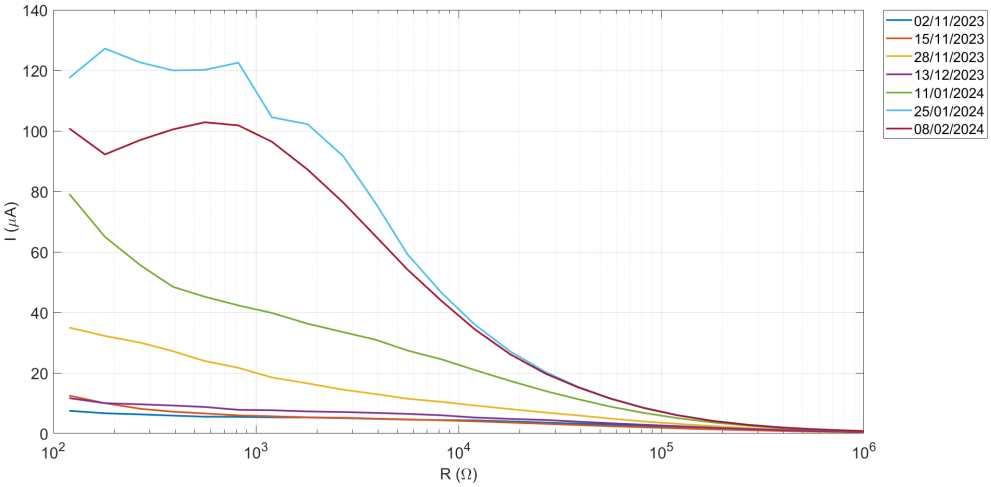

Figure 2.18: Characterization results in terms of R-I curves for the Zn-Cu electrode combination of PMFC 2.

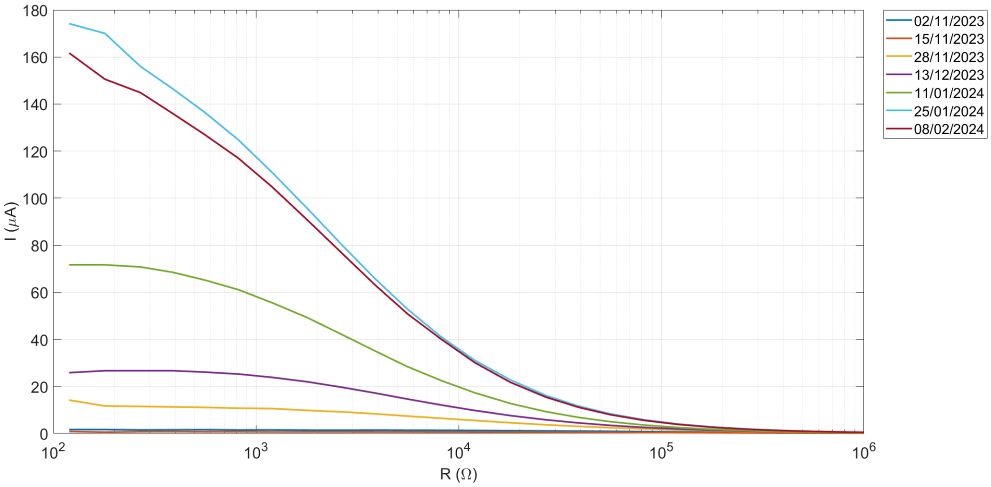

Figure 2.19: Characterization results in terms of R-I curves for the Zn-Al electrode combination of PMFC 2.

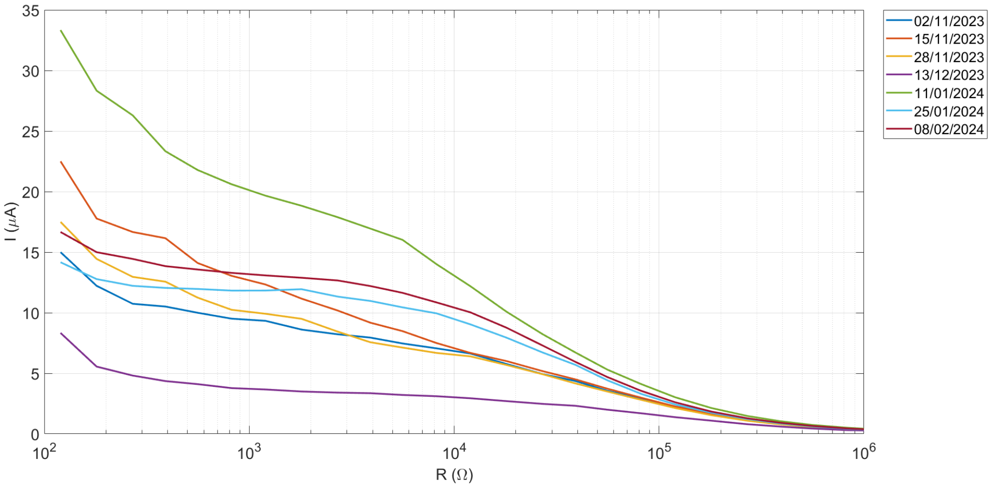

Figure 2.20: Characterization results in terms of R-I curves for the Cu-Al electrode combination of PMFC 2.

In Figure 2.21, Figure 2.22, and Figure 2.23, further support for the increase of the output power of each electrode combination in turn to the plant growth can be highlighted (albeit much less evident in the Copper-Aluminum case), coherently to the R-V and R-I results previously shown and discussed.

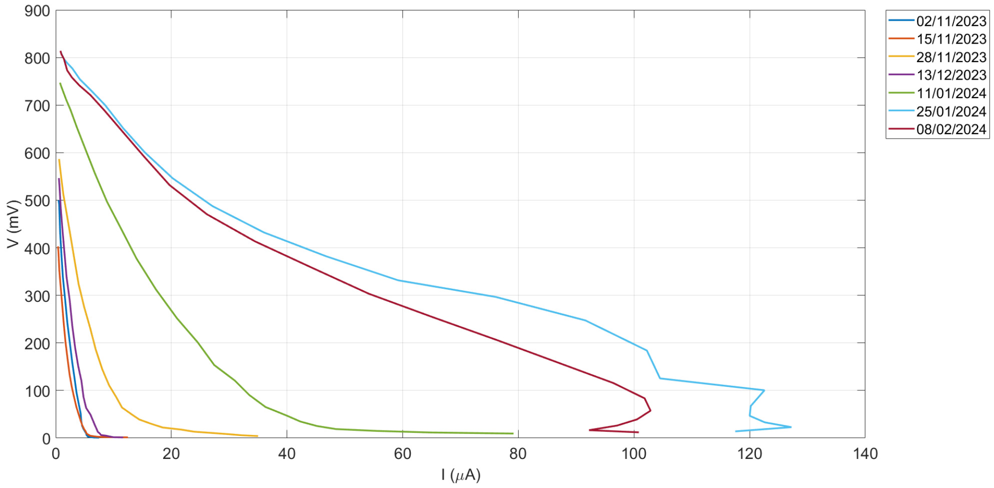

Figure 2.21: Characterization results in terms of I-V curves for the Zn-Cu electrode combination of PMFC 2.

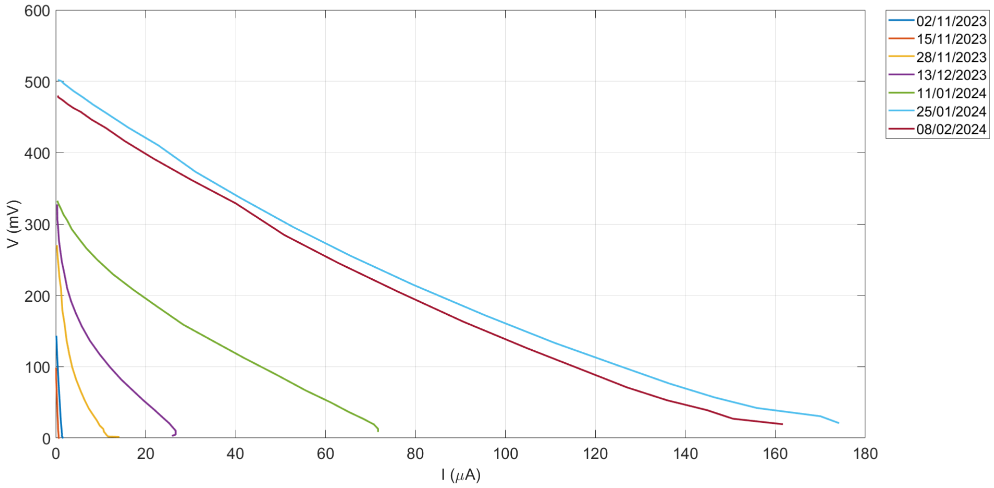

Figure 2.22: Characterization results in terms of I-V curves for the Zn-Al electrode combination of PMFC 2.

In parallel to the discussion done in Section 2.3.1, the generated output power behavior in relation to the output voltage of each possible electrode combination of PMFC 2 has been plotted in Figure 2.24, Figure 2.25, and Figure 2.26 highlighting the maximum power point (MPP) retrieved for each characterization process.

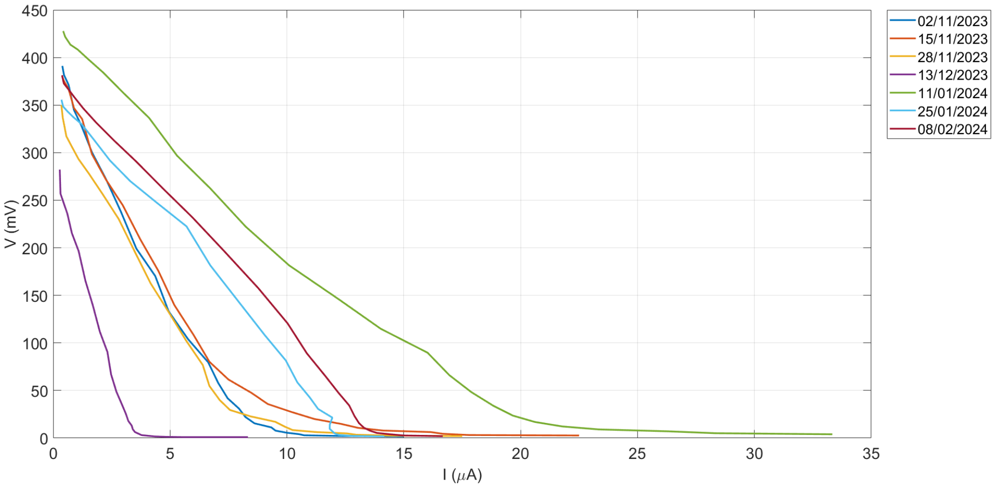

Figure 2.23: Characterization results in terms of I-V curves for the Cu-Al electrode combination of PMFC 2.

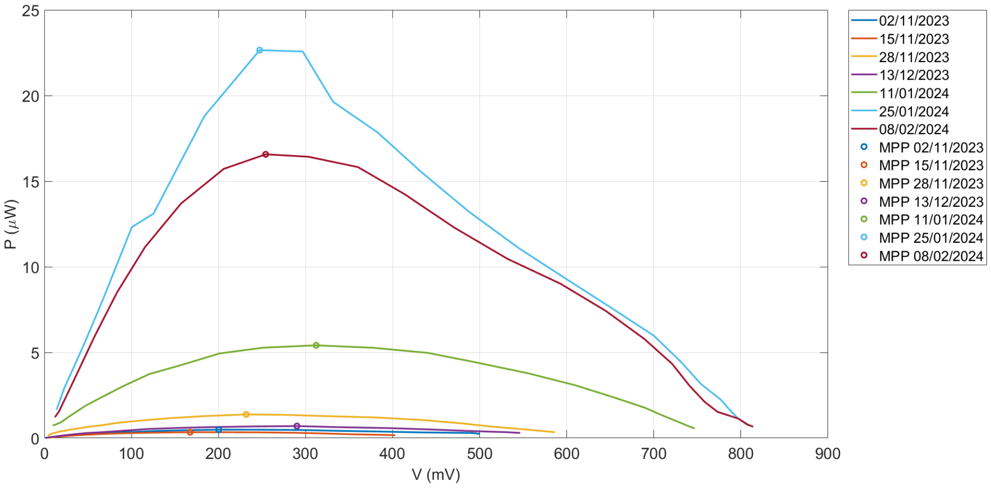

Figure 2.24: Characterization results in terms of V-P curves for the Zn-Cu electrode combination of PMFC 2.

It is noticeable that most of the retrieved maximum power points for the Zinc-Copper electrode configuration are in the 200 mV - 300 mV output voltage range, coherently to what has been registered in Angelini's work [27] and in Section 2.3.1. In contrast, the aluminum-included electrode combinations (for instance, Zinc-Aluminum and Copper-Aluminum) present a downshift of the maximum-power-point-related output voltage range, respectively around 50 mV - 200 mV and around 140 mV - 220 mV. Another significant result can be underlined considering the maximum output power of each electrode combination: in particular, it can be

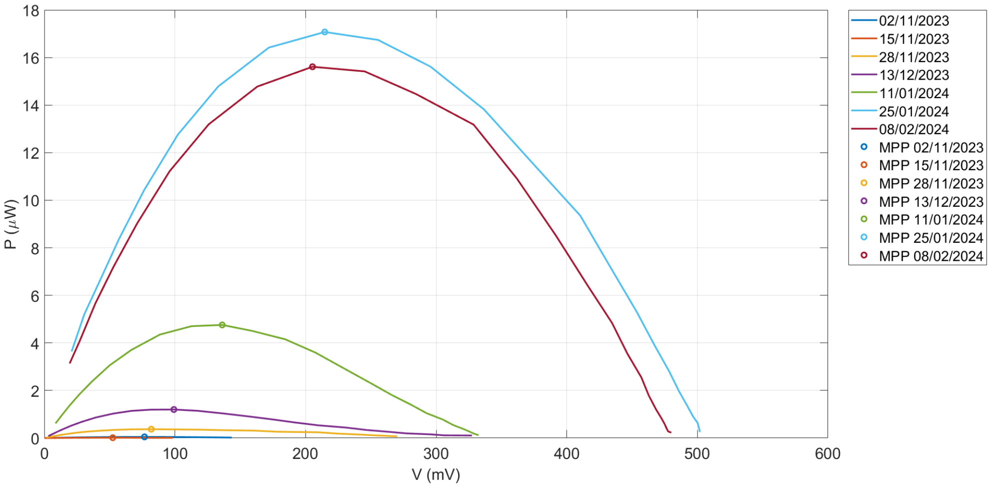

Figure 2.25: Characterization results in terms of V-P curves for the Zn-Al electrode combination of PMFC 2.

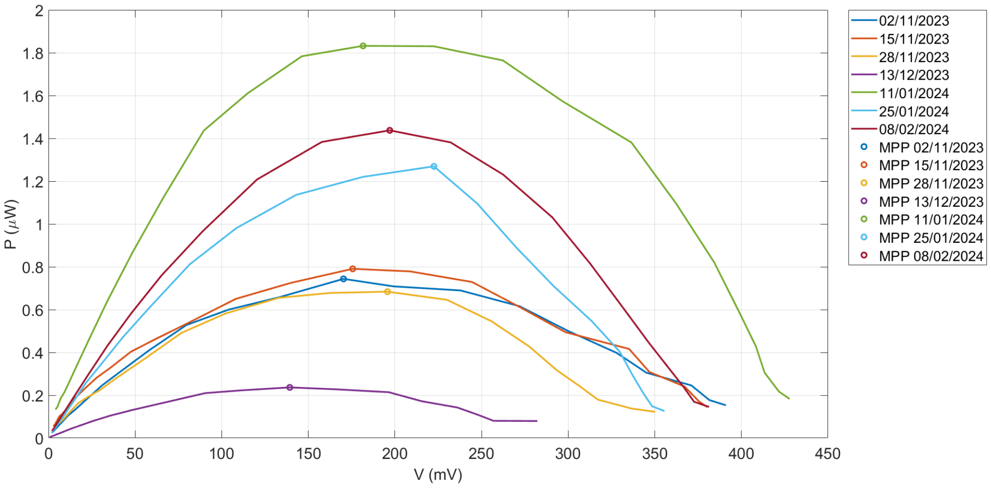

Figure 2.26: Characterization results in terms of V-P curves for the Cu-Al electrode combination of PMFC 2.

evidenced an higher generated output power from the zinc-included electrode pairs with respect to the Copper-Aluminum results. However, the Zinc-Copper choice seems to be a better option with respect to the Zinc-Aluminum one in terms of generated output power.

The results of the PMFC 2 viable electrode pairs power characterization have been reported in Table 2.2, Table 2.3, and Table 2.4 where, for each characterization process carried out, P_{MPP} is the output power at the maximum power point (MPP),

V_{MPP} is the respective output voltage at the maximum power point (MPP) and $\frac{V_{MPP}}{V_{OC}}$ is the relative share in percentage of the maximum output power evaluated at the characterization-specific maximum power point P_{MPP} with respect to the correspondent open-circuit voltage V_{OC}. In this case, the $\frac{V_{MPP}}{V_{OC}}$ ratio evaluations related to the Zinc-Copper, Zinc-Aluminum, and Copper-Aluminum electrode pairs of PMFC 2, respectively, stand at 26% - 43%, 28% - 46%, and 39% - 55%, confirming the almost 35% average value retrieved in Section 2.3.1 and in Angelini's work [27] for what concerns the Zinc-Copper case.

Characterization number	P_{MPP} (μW)	V_{MPP} (mV)	$\frac{V_{MPP}}{V_{OC}}$ (%)
#1	0.489	200.3	34.24
#2	0.342	167.4	27.26
#3	1.379	231.9	29.81
#4	0.701	290.1	42.98
#5	5.415	312.2	39.03
#6	22.651	247.3	25.65
#7	16.569	254.2	26.7

Table 2.2: MPP-related registered results for the Zn-Cu electrode combination of PMFC 2.

Characterization number	P_{MPP} (μW)	V_{MPP} (mV)	$\frac{V_{MPP}}{V_{OC}}$ (%)
#1	0.049	76.7	45.93
#2	0.015	52.4	42.19
#3	0.373	81.9	29.67
#4	1.200	99.2	28.18
#5	4.757	136.2	38.54
#6	17.073	214.7	43.54
#7	15.610	205.3	43.07

Table 2.3: MPP-related registered results for the Zn-Al electrode combination of PMFC 2.

Characterization number	P_{MPP} (μW)	V_{MPP} (mV)	$\frac{V_{MPP}}{V_{OC}}$ (%)
#1	0.744	170.3	39.15
#2	0.791	175.6	42.38
#3	0.684	195.7	48.65
#4	0.237	139.3	41.01
#5	1.832	181.6	39.88
#6	1.269	222.5	55.97
#7	1.437	197	48.14

Table 2.4: MPP-related registered results for the Cu-Al electrode combination of PMFC 2.

2.3.3 PMFCs comparison

Regarding the open-circuit output voltages V_{OC} of each electrode configuration reported in Figure 2.27, it is noticeable that the zinc-based combinations present an overall higher V_{OC} with respect to the Copper-Aluminum electrode pair, implying the supposed uselessness of the aluminum plates in the PMFC.

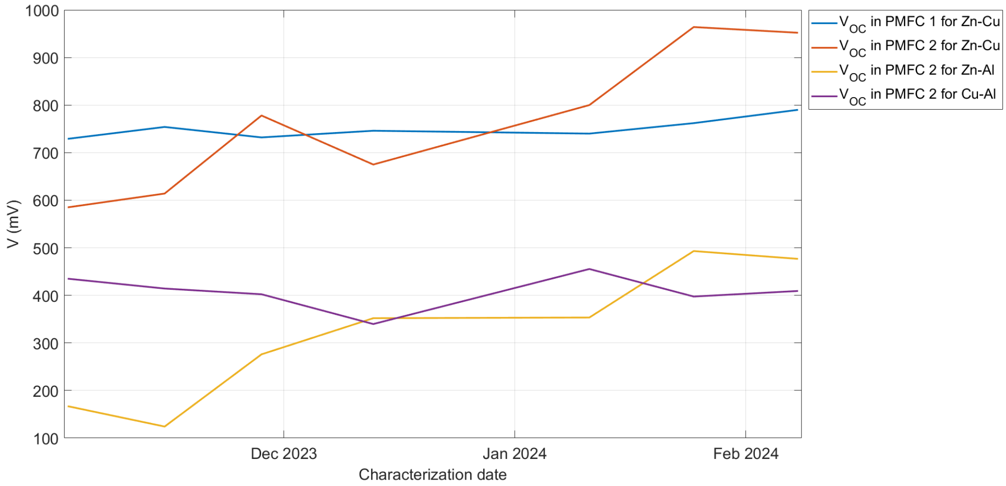

Figure 2.27: Comparison between the open-circuit output voltages V_{OC} of each electrode material pair configuration.

However, inspecting the results listed in Table 2.1, Table 2.2, Table 2.3, and Table 2.4, it can be evidenced that the presence of the aluminum plates seems to improve and enhance the Zinc-Copper electrode pair performances in terms of generated output power in PMFC 2 with respect to the results related to the same electrode materials in PMFC 1. Moreover, the Zinc-Aluminum electrode combination provides a generated maximum output power comparable to the PMFC 1 maximum power level, as further depicted in Figure 2.28.

Therefore, the results previously retrieved and discussed for each electrode material couple lead to considering the zinc-based configurations most suitable in terms of generated output power, particularly the Zinc-Copper electrode materials pair.

Within this framework, the experimental setup has been modified by neglecting the aluminum-based electrode (leaving the respective external connection wire as free-floating) in PMFC 2 and applying a 56-kΩ resistive load between the Zinc-Copper electrodes of PMFC 2 to evaluate the degradation in terms of performances between the loaded Zinc-Copper electrodes of PMFC 2 and the other not-loaded Zinc-Copper electrodes of PMFC 1.

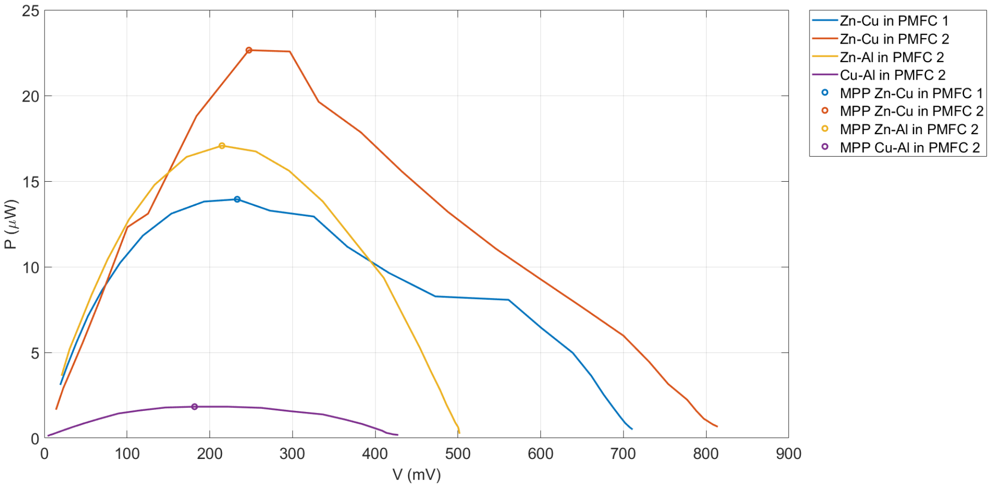

Figure 2.28: Comparison between the maximum generated power-related curves of each electrode material pair configuration.

The 56-kΩ resistive load has been arbitrarily chosen since it is associated with a 10-μA current (again arbitrarily chosen) in the Zinc-Copper configuration of PMFC 2 according to the latter 7th characterization process performed on February 8th, 2024.

In this connection, a 34411A bench-type multimeter from Agilent Technologies Inc. (now Keysight) [33] with its associated LabVIEW script (exploited to read and register the multimeter output over time) has been employed to retrieve the loaded electrodes data, while the characterization process exploited to compare the loaded and not-loaded Zinc-Copper electrodes performance has been performed utilizing the Fluke 115 True RMS multimeter [32] from Fluke.

After a 13-day-long measurement period from February 8th, 2024 to February 21st, 2024, the over-time evolution of the PMFC-2-related voltage across the 56-kΩ resistive load has been depicted in Figure 2.29 and Figure 2.30. Several daily output voltage oscillations can be particularly highlighted in correspondence to the presence of sunlight and related to the circadian cycle. The enhanced photosynthetic process during the daytime can justify this behavior since it leads to a higher release of rhizodeposits in the soil. Moreover, the watering events have been further underlined to evidence their effect on the generated voltage. A rapid increase in the output voltage can be noticed right after the watering events.

On February 21st, 2024, the Zinc-Copper combination of the previously-not-loaded PMFC 1 has been loaded with a 56-kΩ resistive load. In this connection, a 34401A

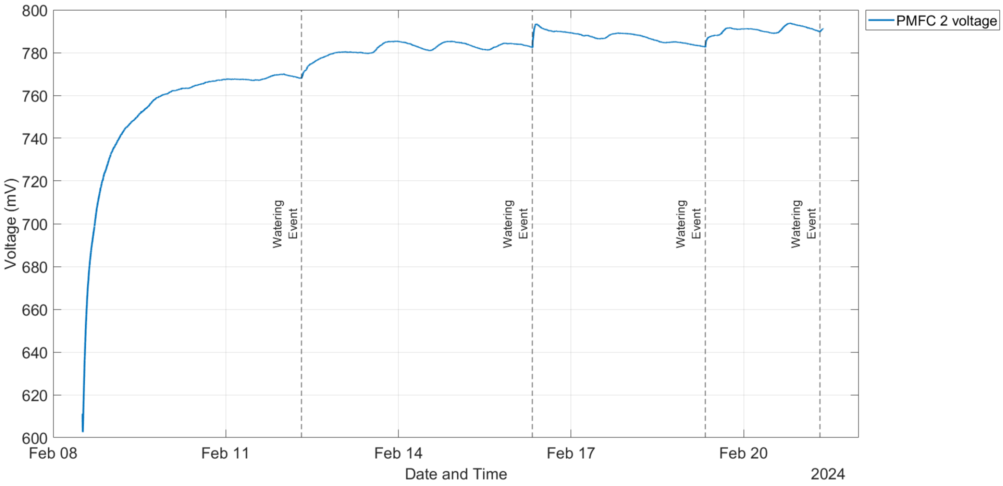

Figure 2.29: Evolution of the PMFC-2-related voltage across the 56-kΩ resistive load over time.

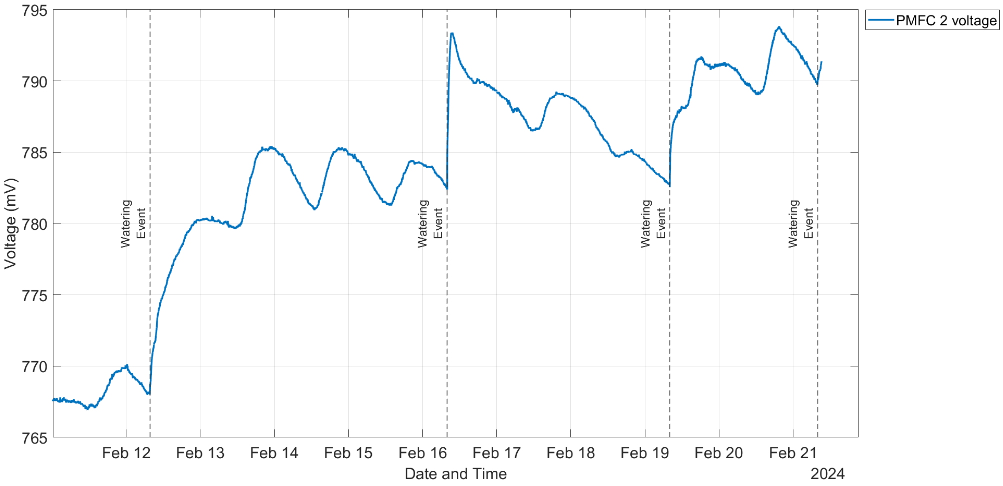

Figure 2.30: Zoom of the evolution of the PMFC-2-related voltage across the 56-kΩ resistive load over time.

bench-type multimeter from Agilent Technologies Inc. (now Keysight) [34] with its associated LabVIEW script has been employed to retrieve the loaded electrodes data, while the rest of the experimental setup has been maintained as before. Thus, a 34411A bench-type multimeter [33] and the Fluke 115 True RMS multimeter [32] have been exploited respectively to monitor the PMFC 2 output voltage and to characterize both the PMFCs.

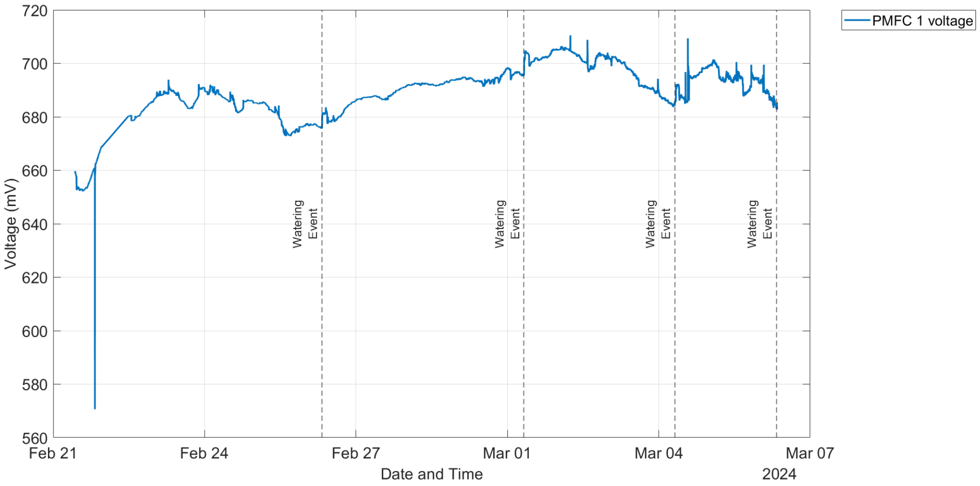

Figure 2.31: Evolution of the PMFC-1-related voltage across the 56-kΩ resistive load over time.

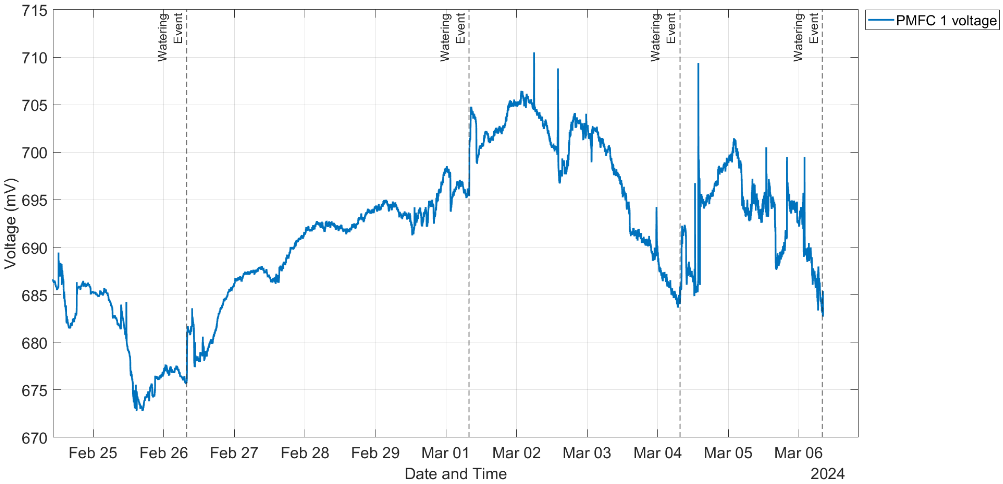

Figure 2.32: Zoom of the evolution of the PMFC-1-related voltage across the 56-kΩ resistive load over time.

The results of the 13-day-long monitoring experiment from February 21st, 2024 to March 6th, 2024 have been reported in Figure 2.31 and Figure 2.32. The same considerations made in Figure 2.29 and Figure 2.30 have been considered valid and verified, albeit less evident than before.

For the sake of completeness, the comparison of the over-time evolution of both the PMFC-related voltage across the 56-kΩ resistive load has been depicted in Figure 2.33. The PMFC-1-related voltage results are significantly lower than the PMFC-2-related ones: the presence of the aluminum plates may be related to these results coherently to what has been previously mentioned.

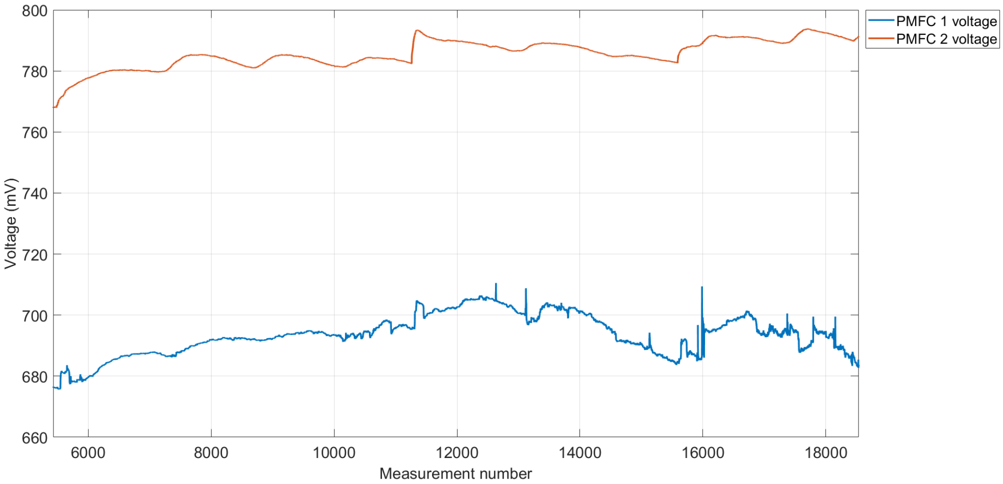

Figure 2.33: Comparison between the 56-kΩ-related voltage curves of both the Zn-Cu configurations.

In parallel to the monitoring of the over-time evolution of both the PMFC-related voltage across the 56-kΩ resistive load, two characterization processes have been performed on February 21st, 2024 and March 6th, 2024 on both the employed PMFCs. In particular, in Figure 2.34, both the 7th and 8th characterization process power-related curves have been depicted and compared with the best performance result of each Zinc-Copper electrode materials combination of both the PMFCs retrieved among the first seven characterization processes (for instance, the 5th and 6th characterization process results for, respectively, the PMFC 1 and PMFC 2 Zinc-Copper configurations) previously exposed and described in Section 2.3.1 and Section 2.3.2. For what concerns the PMFC 1 results, it can be evidenced a significant increase of power performance between the 56-kΩ-load-related result (retrieved on March 6th) and the previous unloaded outcomes (registered on January 11th and February 21st). The same considerations can be confirmed taking into account both the loaded curve (retrieved on January 25th) and unloaded power-related results (registered on February 21st and March 6th) of PMFC 2. Focusing on the best PMFC-specific power-related performance (for instance, the March-6th-related curves for both the PMFCs), it is evident that the PMFC 2 results almost double the PMFC 1 ones in terms of power generation (around 51 μW versus 28 μW), corroborating the assumption which states the Zinc-Copper electrode materials of PMFC 2 as the best-performing solution among the ones studied in this thesis work. The aforementioned power-related results have been reported in Table 2.5 and Table 2.6 for, respectively, PMFC 1 and PMFC 2.

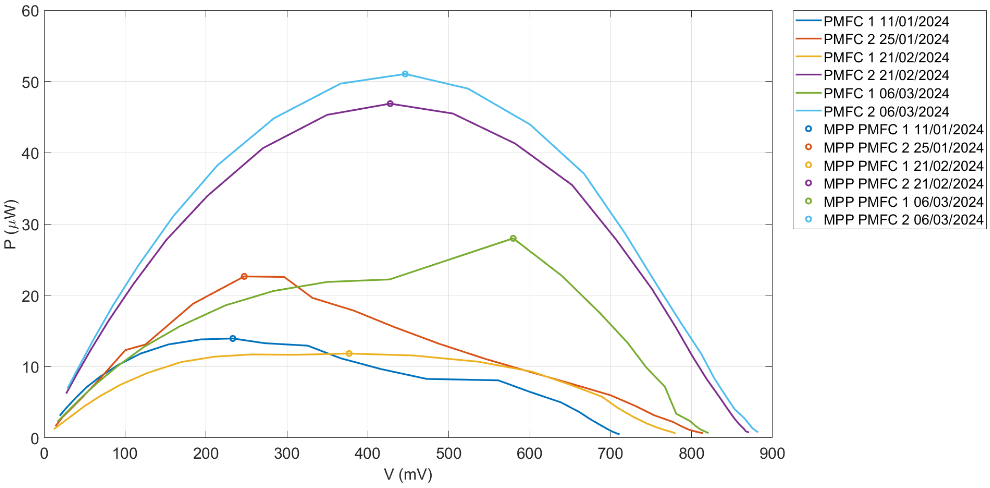

Figure 2.34: Comparison between the generated power-related curves of both the Zn-Cu configurations, even considering the loaded results.

Characterization number	P_{MPP} (μW)	V_{MPP} (mV)	$\frac{V_{MPP}}{V_{OC}}$ (%)	PMFC 1 configuration
#5	13.944	233.2	31.51	Not-loaded
#8	11.832	376.8	44.33	Not-loaded
#9	27.995	579.6	70.17	Loaded

Table 2.5: MPP-related best registered not-loaded and loaded results for the Zn-Cu electrode combination of PMFC 1.

Characterization number	P_{MPP} (μW)	V_{MPP} (mV)	$\frac{V_{MPP}}{V_{OC}}$ (%)	PMFC 2 configuration
#6	22.651	247.3	25.65	Not-loaded
#8	46.883	427.6	48.89	Loaded
#9	51.050	446.2	50.48	Loaded

Table 2.6: MPP-related best registered not-loaded and loaded results for the Zn-Cu electrode combination of PMFC 2.

For thoroughness, the evolution of the open-circuit voltage curves of both the Zinc-Copper configurations (even considering the results reported in Section 2.3.1 and Section 2.3.2) has been depicted in Figure 2.35.

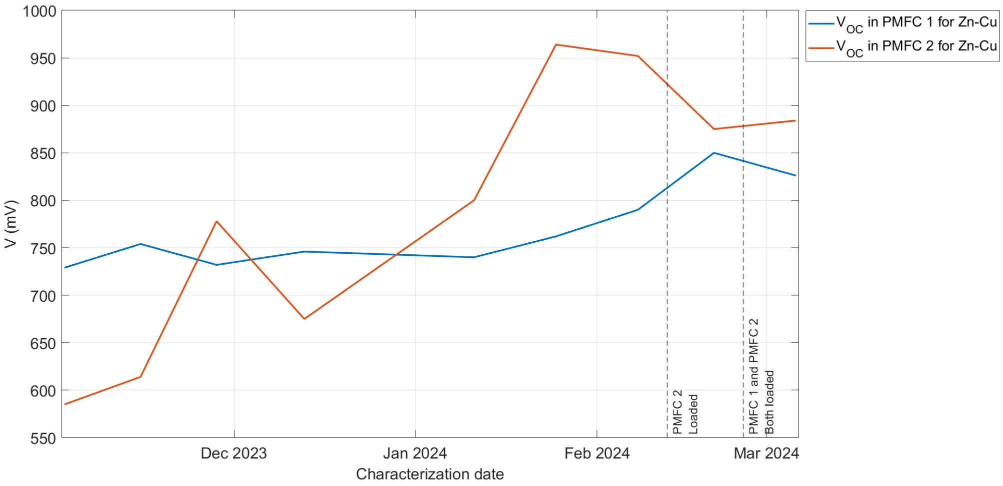

Figure 2.35: Comparison between the open-circuit voltage curves of both the Zn-Cu configurations, even considering the loaded results.

2.4 Conclusions

In the previous Section 2.3, several characterization processes have been performed on the experimental setup described in Section 2.2 to find the best-performing electrode materials pair among three viable combinations (Zinc-Copper, Zinc-Aluminum, and Copper-Aluminum) employed in a single-chamber PMFC structure exploiting two tobacco plants (Nicotiana tabacum L.). In the end, zinc-based configurations have presented good results, particularly the Zinc-Copper electrode couples. Among these latter, the one mounted on PMFC 2 provides the best overall performance in generated power, implying a performance improvement probably related to the aluminum presence in the PMFC 2 structure with respect to aluminum-less PMFC 1 configuration, almost doubling the output generated power. Thus, further analysis of the effect of aluminum plates in Zinc-Copper-based PMFCs may be needed.

Figure 2.36: PMFCs at the time of the last characterization where PMFC 2 is on the foreground while PMFC 1 is in the background.

Chapter 3

Implemented System

3.1 Overview

As reported in Chapter 1, Smart Agriculture can have various and different implementations to achieve its primary goals, such as boosting productivity, improving resilience, reducing emissions, and optimizing human labor by exploiting new technologies.

Within this framework, this thesis project wants to propose an alternative evolution of previous works exposed in Marta Chiarillo's Master Thesis [20] and in Stefano Calvo's Master Thesis [19], and based on Garlando et al. and Motto Ros et al. recently published studies [11, 12, 35].

As reported in Garlando et al. studies [11, 12], a Smart Agriculture application of great interest consists of evaluating the plant's health status by considering the environmental conditions as well as the internal parameters of a plant. Taking into account only the external factors such as soil humidity level and temperature and relying solely on them to achieve the application aim may lead to an incorrect or not-so-precise estimation of the plant's health status due to the natural complexity of this goal.

Therefore, it is evident that the correct measurement and interpretation of the internal parameters of a plant can be a game changer in order to improve plant's health status estimation [11, 12].

One of the internal parameters that can be directly evaluated is the stem electrical impedance. According to Motto Ros et al. results [35], injecting a signal characterized by a known amplitude inside a plant stem and retrieving it from another point of the same plant stem, it is possible to notice an attenuation in the received signal amplitude with respect to the injected one that can be associated with a conductive behavior of the plant stem which may imply a stem electrical impedance proportional to the distance traveled by the injected signal along the employed stem. Therefore, retrieving and evaluating the attenuation experienced by a previously injected signal with a known amplitude through, for example, the maximum value of the received signal thanks to a peak detector can be an excellent way to estimate the correspondent plant stem electrical impedance.

Several studies have inspected and verified the relation between the plant's health status and its related electrical impedance. Garlando et al. [13, 14] have studied, analyzed, and evidenced a relation between the stem electrical impedance and the need for a watering event for the in-vivo over-time-monitored plant. Also, Bar-On et al. [15] have performed studies on the evaluation of stem electrical impedance behavior, while Borges et al. [16] have exploited bio-electric impedance spectroscopy to monitor the plant's health status and to detect plant diseases early.

In Chiarillo's work [20], a system composed of a receiving (Rx) and a transmitting (Tx) part has been developed and tested to perform health monitoring of a plant by measuring the stem electrical impedance after an evaluation of signal previously injected inside the stem. In particular:

- The transmitting side responsible for the 50% duty cycle square-wave signal injection at the top of the plant stem is composed of a power block that supplies energy to a signal generation block based on a single-ended type ring oscillator (RO).

- The receiving counterpart of the system is responsible for retrieving at the bottom of the plant stem the signal sent by the transmitter and influenced by the stem-related bio-electrical impedance, and it is comprised of a signal-conditioning module and a microcontroller unit (MCU): the first module is built on a TLV7011 [36] from Texas Instruments as an inverting threshold comparator with hysteresis prefaced by a highpass filter (HPF) and a digital potentiometer AD5272 [37] from Analog Devices exploited as feedback, while the latter is STM32F401RE [38] from STMicroelectronics mounting on a Nucleo-F401RE as development board. The STM32F401RE is also responsible for the power supply of the rest of the system [20].

The digital-based reading method of the electrical-impedance-related frequency has been employed to avoid the microcontroller analog peripherals that are very sensitive to power voltage oscillations and whose usage leads to an increase in the overall power consumption [12]. In addition, the absence of analog-to-digital converters (ADCs) and the exploitation of timers permit the reduction of power consumption, as well as cost and overall complexity in developing the system.

Even in this thesis project, as in Chiarillo's one [20], the developed system has been designed to be a low-cost and low-power device in which both the transmitting and receiving part have been developed to be two distinct and separated systems and where no analog-to-digital converters are involved simplifying the overall system and reducing the power consumption.

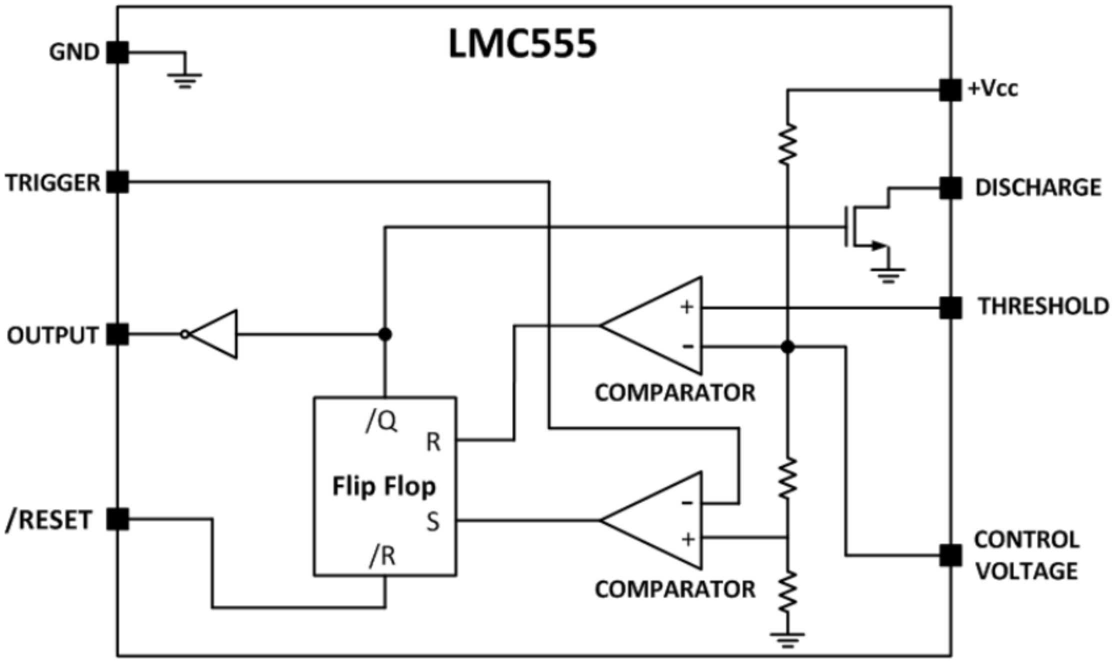

Figure 3.1: Functional block diagram of the LMC555 from the LMC555 datasheet [39].

However, as previously stated, the system designed for this thesis project has been developed as an alternative evolution of the state-of-the-art device. Main differences and characteristics can be identified in:

- The whole system has been projected considering the implementation of a 1.8 V power supply to reduce power consumption as much as possible even if the system is entirely fully-functional also with a 3.3 V power supply (as in Chiarillo's work [20]), therefore each component has been chosen considering 1.8 V as the voltage level of the power supply (further explanations about the 1.8-V power supply choice are reported in Appendix A).
- Under the same conditions of electrical characteristics and available packages, each component has been chosen in terms of ready availability and cost-per-component to work towards developing a real low-cost system.
- Chiarillo's receiving device [20] has been projected to exploit the amplitude of the peak-to-peak voltage of the received signal to evaluate the stem electrical impedance. In contrast, the newly implemented system uses a peak detector, which extracts the peak value of the first-injected-and-then-received signal, which has been attenuated by traveling along the plant stem.
- The microcontroller employed to take care of the output frequency of both the transmitting side and the receiving side in this thesis project is the STM32WL55JC1 [40] from STMicroelectronics instead of the STM32F401RE [38] used in Chiarillo's work [20] to exploit the LoRa protocol and to integrate our system in a previously implemented LoRaWAN network by the department team.

In the following Section 3.2 and Section 3.3, a more detailed analysis of the developed system will be presented, while in Section 3.4 and Section 3.5, the results of the characterization of the system will be discussed.

3.2 Project of the transmitting system

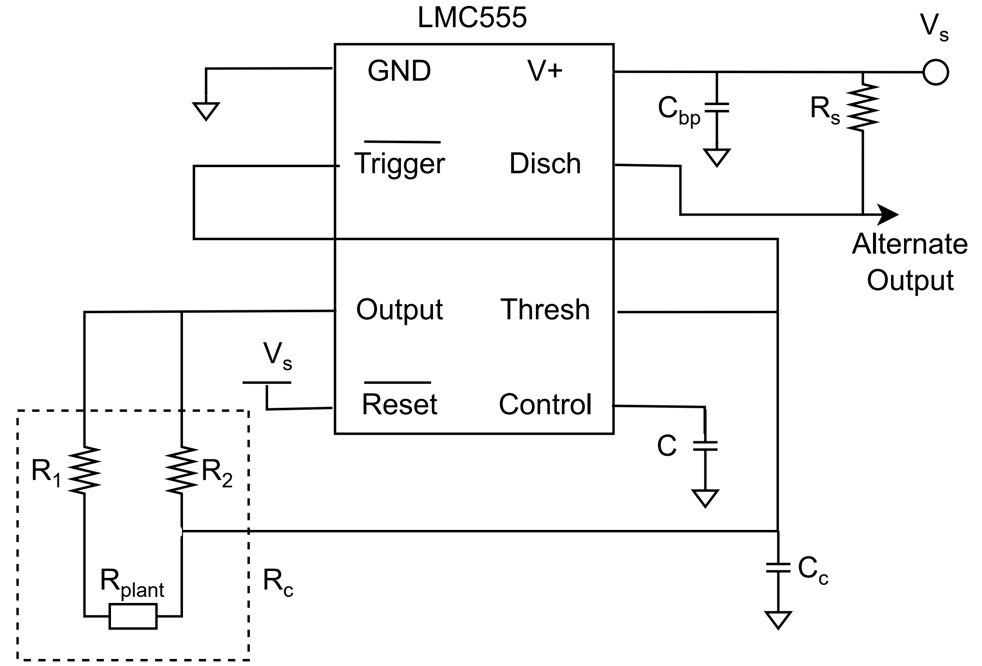

Figure 3.2: Schematic of the transmitting module based on the "50% Duty Cycle Oscillator" configuration reported at page 16 of the LMC555 datasheet [39].

The transmitting system is made up of an LMC555 CMOS timer [39] (which internal functional block scheme is represented in Figure 3.1) in a configuration similar to the one named "50% Duty Cycle Oscillator" and reported at page 16 of the LMC555 datasheet [39], as highlighted in Figure 3.2 and Figure 3.4. The choice of the LMC555 component has been led by its instant availability in the laboratory and its suitability for the needed work since it has been used in previous studies of the team [11, 12] in the same field of interest.

$$f_{datasheet} = \frac{1}{1.4 R_c C_c} \tag{3.1}$$

At the design stage, it has been decided to size the transmitter to make it work in the range between 50 kHz and 200 kHz according to the exploited frequency range reported in Chiarillo's work [20] referring to previous studies [11, 13, 14, 15]: for this reason, Equation 3.1 reported at page 16 of the LMC555 datasheet [39] has been exploited to choose the suitable values of the resistors and the capacitor. Focusing on the resistor R_c depicted in Figure 3.2, in order to find a suitable value for R_1 and R_2, R_{plant} has been neglected and substituted alternatively with a short circuit and an open circuit to evaluate respectively the highest and the lowest frequency limit exploiting Equation 3.2: in fact, when R_{plant} is associated to a short-circuit situation (thus to an almost-zero resistance value), R_1 and R_2 can be considered in parallel therefore adjusting the maximum frequency value, while when R_{plant} is associated to an open-circuit configuration (thus to a very high resistance value), R_2 implies a reduction of the current in the load therefore setting the minimum frequency value, similar to what has been done for the system designed in Garlando et al. work [11].

The value of the bypass capacitor C_{bp} has been chosen to be 100 nF to mitigate the effect of low-frequency noise and to provide a more stable power supply for the transmitter. At the same time, for the pull-up resistor R_s an 8.2-kΩ resistor has been picked to behave as a pull-up when needed: referring to Figure 3.1, it can be noticed that the primary purposes of the pull-up resistor R_s are to provide high output voltage and to limit the current that could sink in the discharge-pin-related n-type MOSFET when it is active. At the control input pin of the LMC555 [39], a capacitor C has been selected to reduce oscillation on the alternate output (from which the actual output of the transmitter module is taken), forcing the control pin to maintain a quite constant value as reference input voltage of the threshold comparators reported in the functional block diagram depicted in Figure 3.1. As underlined in Section 3.1, the power supply V_s considered at the design stage is equal to 1.8 V in order to reduce power consumption. All the chosen values are reported in Table 3.1.

$$R_c = \begin{cases} R_1 || R_2 & \text{for highest frequency limit evaluation} \\ R_2 & \text{for lowest frequency limit evaluation} \end{cases} \tag{3.2}$$

Component	Chosen value
R_s	8.2 $k\Omega$
R_1	1 $k\Omega$
R_2	3.3 $k\Omega$
C_c	4.7 nF
C_{bp}	100 nF
C	67 nF

Table 3.1: Chosen values for the components of the transmitting device.

When it is used, the transmitting module is connected to the plant through two surgical needles (like the ones employed for subcutaneous medical applications) inserted through the plant stem as depicted in Figure 3.3 and Figure 3.4. These exploited 1-cm-long 0.4-mm-diameter-wide stainless-steel surgical needles have been chosen since they provide good bio-compatibility and resistance to deterioration [12].

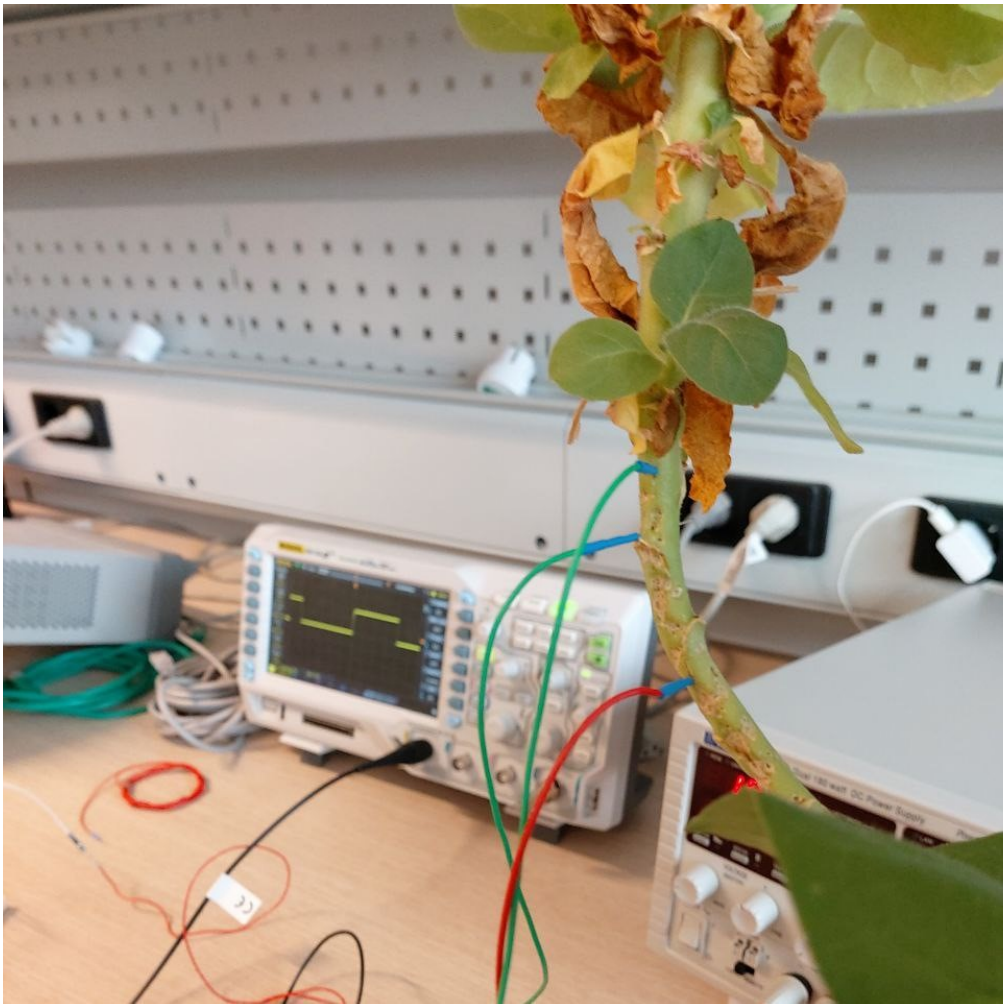

Figure 3.3: Zoom on the connection between transmitter (the green needles) and receiver (the red needle) and the plant stem.

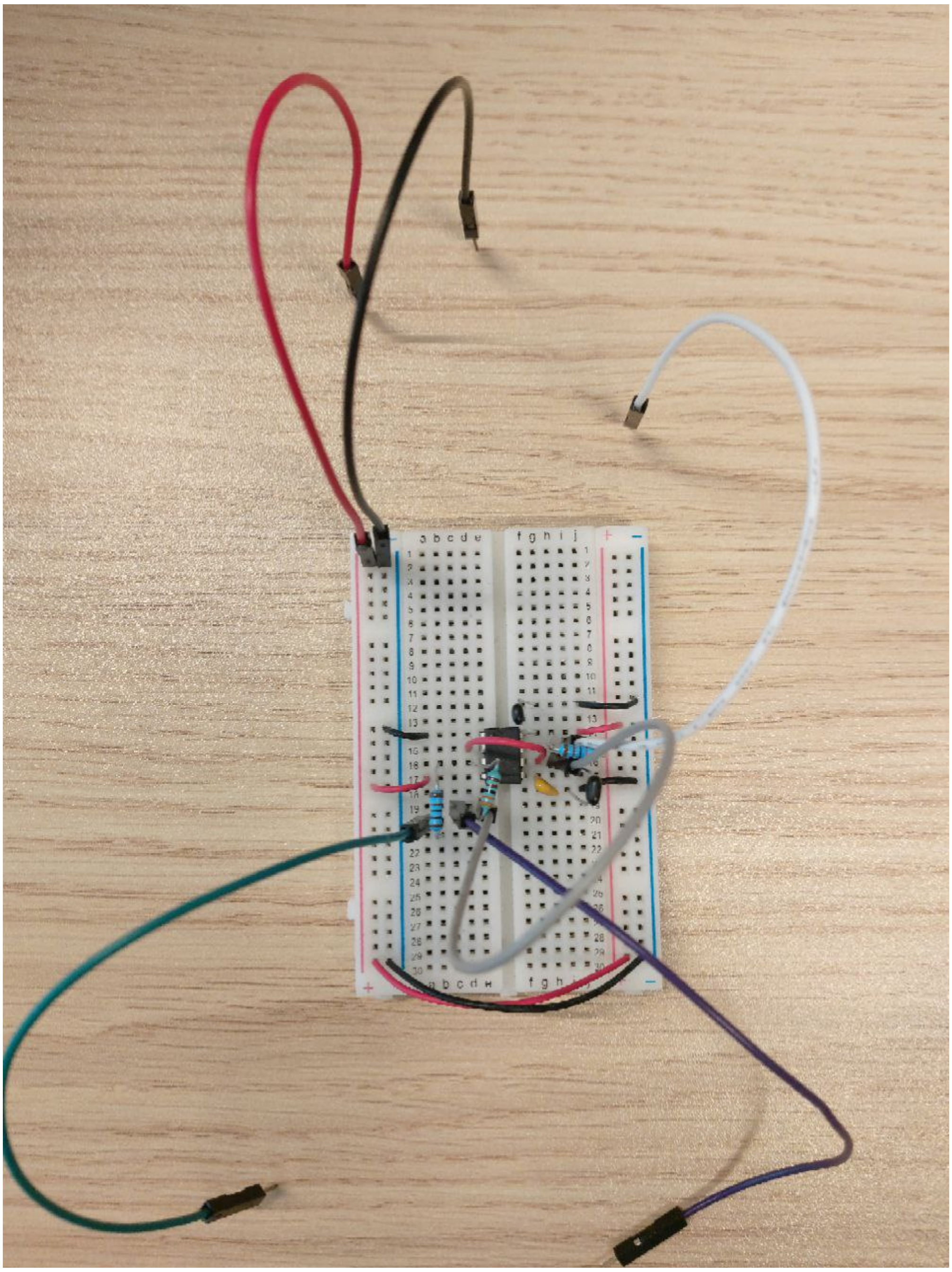

Figure 3.4: Transmitting module with power supply jumper cables at the top in red and black, output with a white cable on the right side and two jumpers at both ends of the resistor R_{plant} at the bottom in green and violet.

3.3 Project of the receiving system

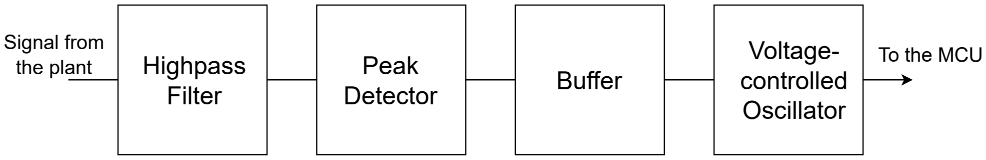

Figure 3.5: Basic schematic of the receiving module.

For what concerns the receiving system (reported in Figure 3.5 and depicted in Figure 3.6), it can be analyzed by inspecting each component on its own:

- Input highpass filter (HPF)
- Peak detector (PD)
- Buffer
- Voltage-controlled oscillator (VCO)

In the following sections, each component exploited in the receiving module will be explained in details. The microcontroller (MCU) characteristics and firmware will be explained in Chapter 4.

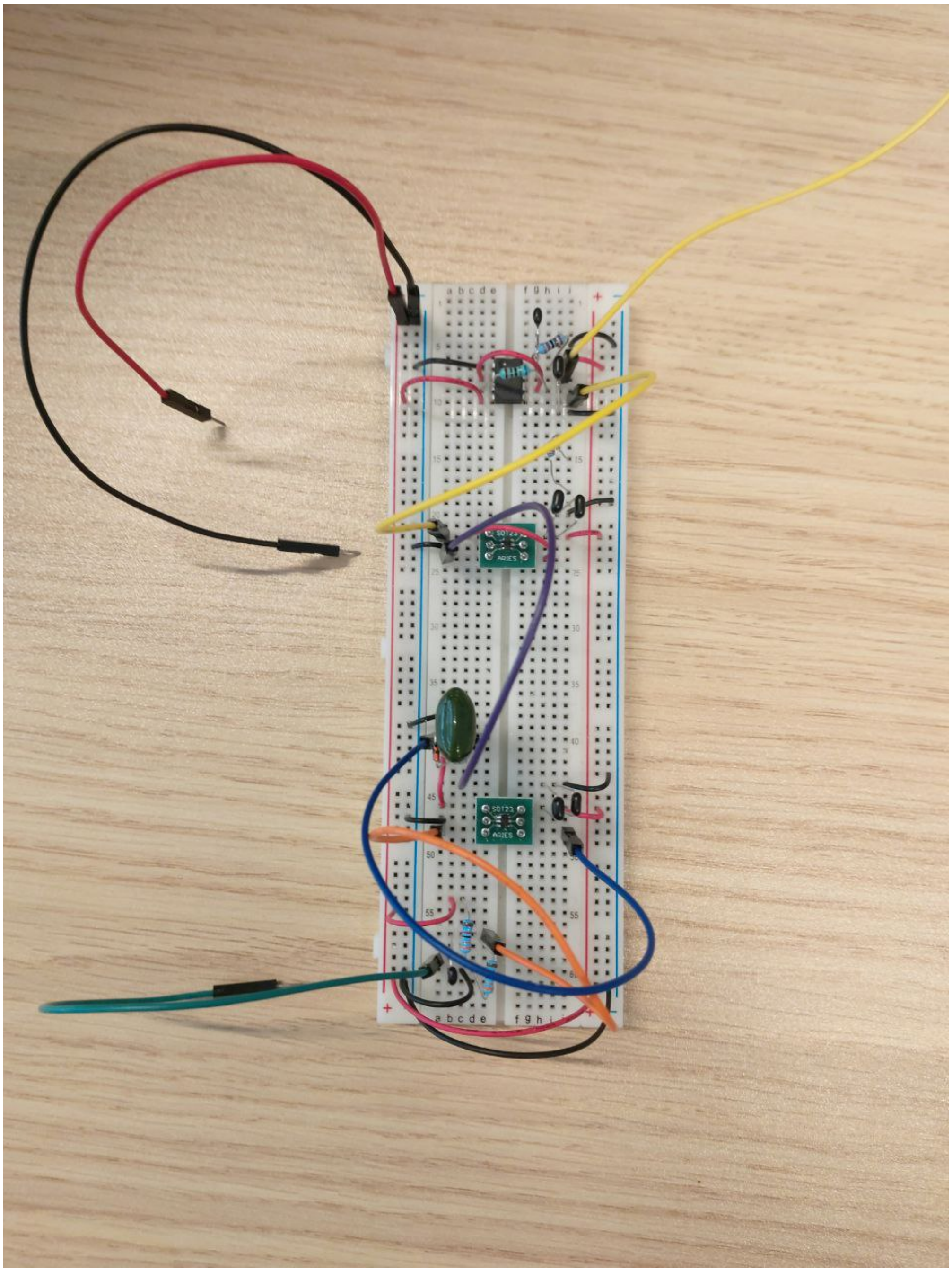

Figure 3.6: Receiver module with power supply jumper cables at the top in red and black, input through a green wire on the left and output with a yellow jumper on the right.

3.3.1 Input filter

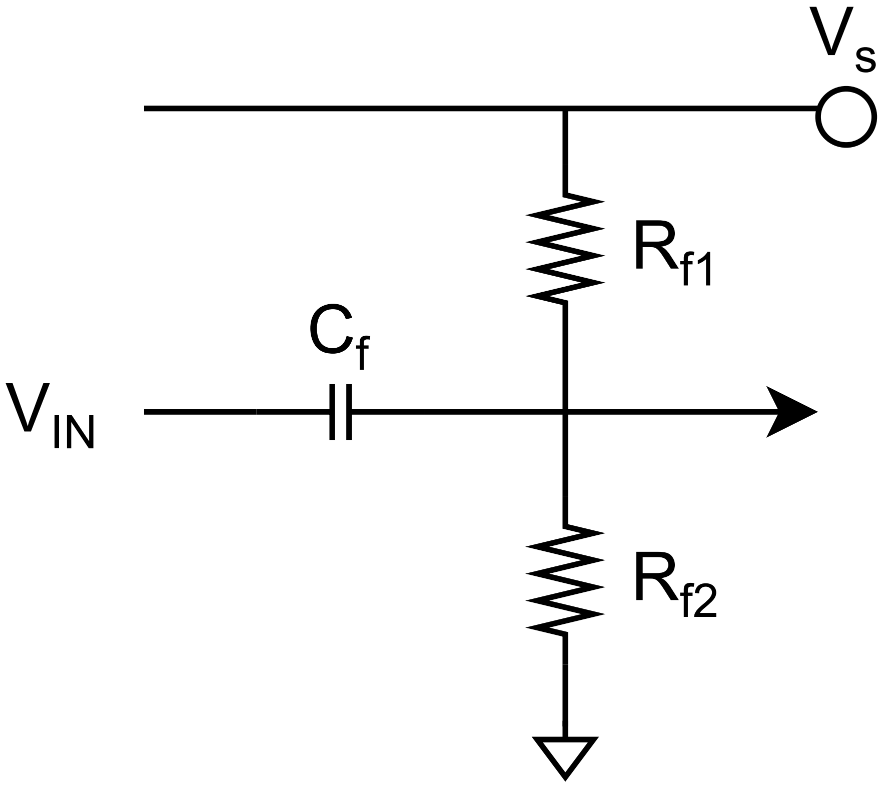

Figure 3.7: Schematic of the highpass filter exploited in the receiving module [20].

The highpass filter employed in this project (which schematic is highlighted in Figure 3.7) is the same explained on page 35 of Chiarillo's work [20] since its main function is to filter out the environmental noise from the input signal coming from the plant stem V_{IN}. Therefore, R_{f1}, R_{f2} and C_f have been chosen in order to present the cut-off frequency $f_{cut-off}$ around 10 kHz. Moreover, R_{f1} and R_{f2} have been imposed to be of the same nominal value to set the bias point at half the supply voltage, assuring an always-positive signal as peak detector input. As highlighted in Section 3.1, the power supply V_s considered at the design stage is equal to 1.8 V.

$$f_{cut-off} = \frac{1}{2\pi(R_{f1}||R_{f2})C_f} \tag{3.3}$$

The relation employed to size the components is reported in Equation 3.3, and the selected values are grouped in Table 3.2.

Component	Chosen value
R_{f1}	$33\ k\Omega$
R_{f2}	$33\ k\Omega$
C_f	$1\ nF$

Table 3.2: Chosen values for the components of the highpass filter of the receiver.

3.3.2 Peak detector

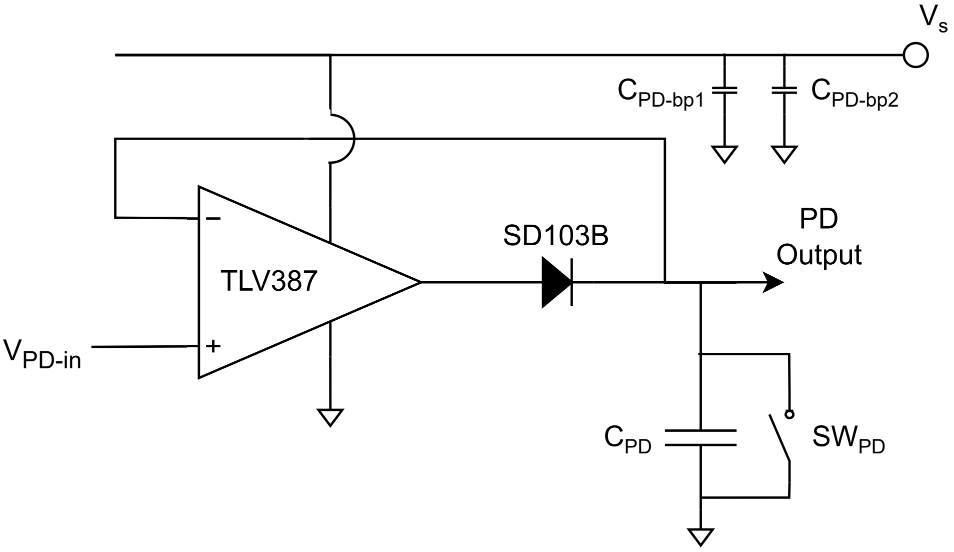

Figure 3.8: Basic scheme of the implemented peak detector exploited in the receiving module.

A peak detector (PD) is a circuit able to detect the maximum value of an input signal (precisely, its peak value) and store it until a reset condition has been met. As explained in Kelley and Alonso's article [41], there are several kinds of even-commercial peak detectors implemented as improvements of an elementary and minimal peak detector scheme (reported in Figure 3.8).

The design of a peak-detector-based receiving module has been decided to meet the low-power consumption requirement previously exposed in Section 3.1, particularly avoiding the exploitation of analog-to-digital converters.

In the most straightforward peak detector scheme reported in Figure 3.8, the capacitor C_{PD} is charged to the input peak value through the diode by the applied input voltage: if a higher peak is detected on the input, then C_{PD} is charged to the new peak value until the system reset condition (through the control of the discharge switch SW_{PD}) is met and the capacitor is discharged: in the proposed positive-peak-detector configuration, the diode is forward biased only if the applied input signal is higher than the actual voltage level stored in C_{PD}, otherwise it is reverse biased, and the capacitor retains its previously stored value (until a forced discharge of C_{PD} in turn to the SW_{PD} activation is triggered or a higher-than-actual peak value at the input is detected).

However, according to Calvo et al. considerations [42], changes in plant health status require time, allowing the registration of significant variations by performing the plant stem electrical impedance measurement only a few times per hour and thus influencing the components selection and design.

Therefore, due to the just mentioned very loose time constraints that this thesis' developed system has to take into account, the cost of each component, and the results of preliminary tests exploited during the project, several modifications have been done at the design stage (always remember the 1.8 V voltage supply design constraint previously reported in Section 3.1 and discussed more in detail in Appendix A):

- First, a TLV9041 [43] from Texas Instruments has been chosen due to its ultra-low supply voltage, low cost, unity-gain stability, and low quiescent current as exploited operational amplifier. However, after few preliminary tests, it has been substituted with the actually employed TLV387 [44] from Texas Instruments since TLV9041 has presented a gain-bandwidth product (GBW) around 350 kHz (page 9 of the datasheet [43]), so low it originally affected the peak detector worsening its behavior since distortion problems have been highlighted at relatively low frequencies around 35 kHz.

- To decouple the employed operational amplifier from the power supply, two bypass capacitors C_{PD-bp1} and C_{PD-bp2} have been placed between the power supply V_s and the ground reference.

- The main reason that has led the choice of the SD103B diode [45] from Vishay as employed diode in the peak detector scheme is the really low voltage drop when active since it is a small signal Schottky diode with a forward voltage drop equal to 370 mV at 20 mA as forward current (page 2 of the datasheet [45]). In the preliminary tests, while awaiting for the

SD103B delivery, some measurements have been done by using a bigger-forward-voltage-drop diode, the 1N4148 [46] from Diodes Incorporated, due to its instant availability, confirming the effectiveness of the SD103B choice (further verified with subsequent tests with the SD103B diode).

- The sizing of the output peak detector capacitor C_{PD} has been done considering the applicable voltage range on the $V_{control}$ input of the LMC555-based voltage-controlled oscillator [39]: in fact, considering 1.8 V as power supply, the maximum permissible $V_{control}$ at the LMC555 input pin is around 1.4 V (pages 4-5 of the datasheet [39]). Thus, bearing in mind the maximum output current of the TLV387 [44], the forward current of the SD103B diode [45], the speculated working input frequencies of tens of kHz and the highlighted amplitude of the input signal V_{PD-in} ranging from 200 mV to 500 mV (page 36 of Chiarillo's thesis [20]) and shifted up due to the input highpass filter by $\frac{1}{2}V_s$ (note Section 3.3.1), a 470-nF ceramic capacitor has been selected.
- A low-side nMOS-based switch (as SW_{PD} in Figure 3.8) was initially intended to force the discharge of the capacitor C_{PD} through a 100-Ω resistor in turn to the activation of a control signal sourced from a microcontroller. However, after few preliminary tests, it became evident that since a ceramic capacitor has been exploited for C_{PD}, an explicit switch SW_{PD} to discharge C_{PD} may be neglected due to the very low retention of the ceramic capacitor and in particular due to the loose time constraints that this thesis' developed system needs to meet (which permit a complete discharge of the employed ceramic capacitor C_{PD} without the implementation of a switch) allowing to reduce overall costs due to less components exploitation.

The selected values for the components of the peak detector are grouped in Table 3.3, remembering that the supply voltage V_s is set at 1.8 V at the design stage to reduce overall system power consumption (further information reported in Appendix A).

Component	Chosen value
C_{PD-bp1}	$1\ \mu F$
C_{PD-bp2}	$100\ nF$
C_{PD}	$470\ nF$

Table 3.3: Chosen values for the components of the peak detector of the receiving device.

3.3.3 Buffer

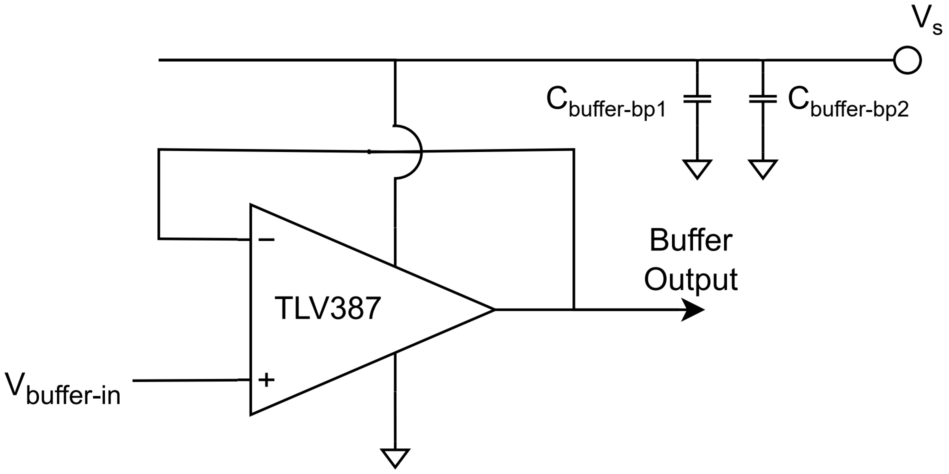

Figure 3.9: Schematic of the implemented buffer exploited in the receiving module.

An operational amplifier in a buffer configuration as represented in Figure 3.9 has been implemented to decouple the output of the peak detector and the control input $V_{control}$ of the LMC555-based voltage-controlled oscillator [39] making the buffer output to follow its input $V_{buffer-in}$. The presence of the buffer has been required due to the low-impedance nature of the LMC555 $V_{control}$ pin [39] that would have permitted the discharge of the peak detector output capacitor C_{PD} through it. Moreover, two bypass capacitors $C_{buffer-bp1}$ and $C_{buffer-bp2}$ have been placed between the supply voltage V_s and the ground reference to decouple the employed TLV387 [44] and the power supply. The TLV387 operational amplifier has been exploited since it can support a buffer operation due to the unity-gain stability [44] and its instant availability (since it is used for the peak detector too as highlighted in Section 3.3.2). The chosen values for the buffer components are listed in Table 3.4, remembering that the supply voltage V_s is set at 1.8 V at the design stage to reduce overall system power consumption (further explanations about the 1.8-V power supply choice are reported in Appendix A).

Component	Chosen value
$C_{buffer-bp1}$	1 μF
$C_{buffer-bp2}$	100 nF

Table 3.4: Chosen values for the components of the buffer of the receiving device.

3.3.4 Voltage-controlled oscillator

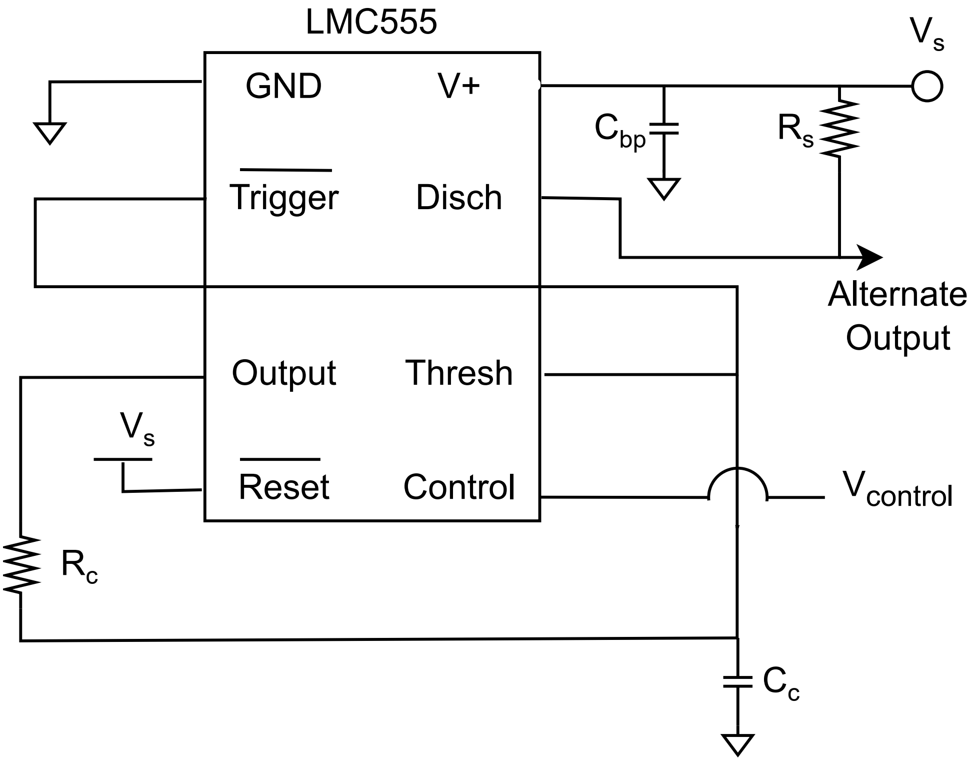

Figure 3.10: Schematic of the voltage-controlled oscillator of the receiving module based on the "50% Duty Cycle Oscillator" configuration reported at page 16 of the LMC555 datasheet [39].

A voltage-controlled oscillator (VCO) is an electronic device whose output is an oscillating signal with a frequency strictly related to the input control voltage. In particular, as highlighted in Section 3.4, the exploited "50% Duty Cycle Oscillator" configuration reported on page 16 of the LMC555 datasheet [39] as represented in Figure 3.10 is characterized by an inverse relationship between the input control voltage $V_{control}$ sourcing from the buffer output (note Section 3.3.3) and the frequency of the output oscillating signal extracted from alternate output pin (which is then sent to the exploited microcontroller to be finally analyzed and dispatched through LoRa communication protocol).

Due to the configuration employed in this project, the oscillating output signal is a 50%-duty-cycle square-wave signal ranging from 0 V and V_s (in our case, at the design stage, it is equal to 1.8 V) with a frequency controlled by the input control voltage $V_{control}$.

As done in Section 3.2, a bypass capacitor C_{bp} has been exploited to decouple the voltage-controlled oscillator from the supply voltage and the resistor R_s has been utilized as a pull-up resistor, while according to the Equation 3.1 and assuming the voltage-controlled oscillator to work around 20 kHz (actually around 22 kHz), the sizing of the resistor R_c and the capacitor C_c has been done.

The chosen values for the components of the designed voltage-controlled oscillator are listed in Table 3.5, remembering that the supply voltage V_s is set at 1.8 V at the design stage to reduce overall system power consumption.

Component	Chosen value
R_s	8.2 $k\Omega$
R_c	6.8 $k\Omega$
C_c	4.7 nF
C_{bp}	100 nF

Table 3.5: Chosen values for the components of the voltage-controlled oscillator of the receiving device in the "50% Duty Cycle Oscillator" configuration [39].

3.4 Characterization of the system

In the following sections, each component previously projected has undergone several characterizations to verify their behavior before the actual installation and the results will be exposed in Section 3.4.2, Section 3.4.3 and Section 3.4.4. No microcontroller has been assessed at this stage and its implementation will be discussed in Chapter 4. All the characterization procedures have taken place under the 1.8 V voltage supply case for each component. The registered characterization data have been further reported in Appendix C for thoroughness.

3.4.1 Section-specific exploited variables' nomenclature

To simplify the following discussion, some definitions that will be adopted in further sections have been listed, even referring to the conceptual block scheme reported in Figure 3.11. In particular, organizing the exploited variables in relation to the type of characterization in which they have been employed:

- Characterization only with instrumentation (Section 3.4.2)
  - R_{plant}: as reported in Figure 3.2, it is the resistance value associated to the plant stem and related to the transmitter output frequency according to Equation 3.1.
  - $f_{in-instr}$: frequency of the input voltage $V_{pp-in-instr}$ upstream the receiver.
  - f_{out-Rx}: output frequency evaluated downstream the receiving system.
  - V_{pp-in}: peak-to-peak voltage evaluated downstream the highpass filter (HPF) and thus upstream the peak detector (PD).
  - $V_{pp-in-instr}$: peak-to-peak voltage set by the exploited waveform generator and put as input of the receiving system and thus upstream the highpass filter (HPF).
  - V_{max-in}: maximum voltage level detected downstream the highpass filter (HPF) and thus upstream the peak detector (PD).
  - $V_{max-out}$: maximum voltage level detected downstream the buffer after the peak detector (PD) and thus upstream the voltage-controlled oscillator (VCO).
  - ΔV_{max}: variation between V_{max-in} and $V_{max-out}$, therefore in different terms $\Delta V_{max} = V_{max-out} - V_{max-in}$.

- Characterizations considering the tobacco plant (Section 3.4.3, Section 3.4.4 and Section 3.4.5)
  - d_{Tx-Tx}: relative distance between the two transmitter-related surgical needles and incrementing by moving towards the plant roots (thus evaluated by placing the start value in correspondence of Point A in Figure 3.11 and the end value in Point B in Figure 3.11, and considering $d_{Tx-Tx} \geq 0$ implying Point B always after Point A in the direction towards the roots).
  - d_{Rx-Tx}: relative distance between the second transmitter-related surgical needle and the receiver-related surgical needle and incrementing by moving towards the plant roots (thus evaluated by placing the start value in correspondence of Point B in Figure 3.11 and the end value in Point C in Figure 3.11, and considering $d_{Rx-Tx} \geq 0$ implying Point C always after Point B in the direction towards the roots).
  - f_{no-Rx}: transmitter-related output frequency without considering the presence of the the receiver system in the experimental setup.
  - f_{out-Tx}: transmitter-related output frequency taking into account the presence of the receiver system in the experimental setup.
  - f_{out-Rx}: output frequency evaluated downstream the receiver system.
  - $V_{max-out}$: maximum voltage level detected downstream the buffer after the peak detector (PD) and thus upstream the voltage-controlled oscillator (VCO).
  - Z_{no-Rx}: transmitter-related electrical impedance evaluated between the two surgical needles of the transmitter module without considering the presence of the receiver system in the experimental setup.
  - Z_{Tx}: transmitter-related electrical impedance evaluated between the two surgical needles of the transmitter module taking into account the presence of the receiver system in the experimental setup (thus between Point A and Point B in Figure 3.11).
  - Z_{Rx}: receiver-related electrical impedance evaluated between the second transmitter-related surgical needle and the receiver-related surgical needle (thus between Point B and Point C in Figure 3.11).

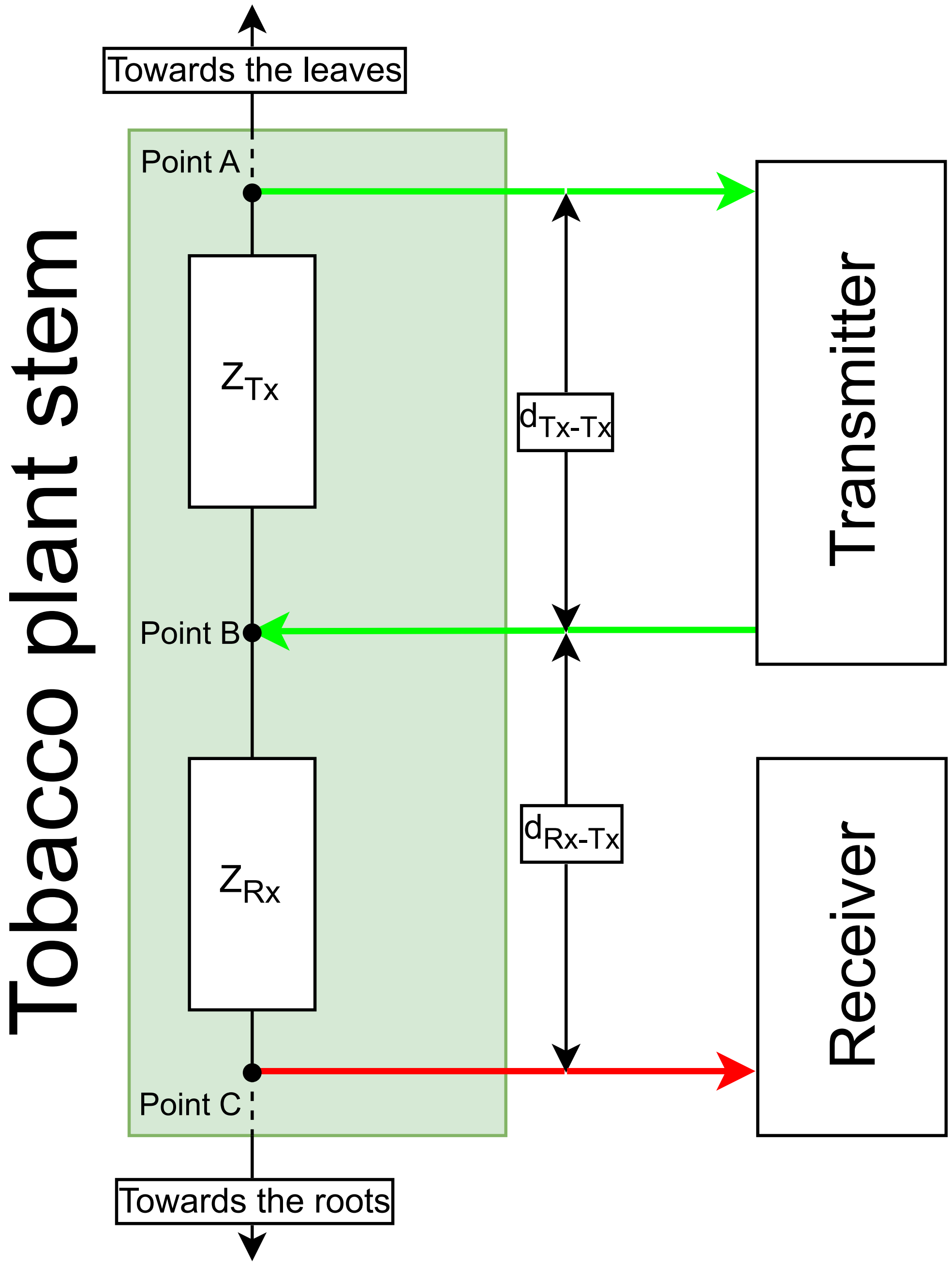

Figure 3.11: Experimental setup with exploited variables highlighted according to the employed nomenclature convention.

3.4.2 Characterization only with instrumentation

In this section, both the transmitting module and the receiving device have been studied and characterized by only exploiting laboratory instrumentation. Within this framework, a 33220A 20 MHz arbitrary waveform generator [47] from Agilent Technologies Inc. (now Keysight) has taken the place of the plant during the system characterization, while a CPX200D bench-type power supply unit [48] from Aim-TTi Instruments and a DS1104Z-S Plus digital oscilloscope [49] from Rigol have been respectively employed as DC source provider and measurement display.

This characterization took place in the afternoon at the PIC4SeR laboratories on December 6^{th}, 2023.

Transmitting module characterization

To characterize the transmitting module, a set of known resistors ranging from 120 Ω to 1 MΩ have been inserted in the place of R_{plant} in Figure 3.2 with the connections as reported in Figure 3.3 and Figure 3.4.

As exposed in Section 3.2, the transmitting module components have been selected to satisfy an output oscillating frequency range from 50 kHz to 200 kHz exploiting the Equation 3.1 reported at page 16 of the LMC555 datasheet [39]: in particular, the selected R_c and C_c values should correspond to a 46-kHz-to-198-kHz output frequency range according to the Equation 3.1.

However, the experimentally-derived transmitting output frequency range has highlighted a narrower band swinging from 39.68 kHz to 118.3 kHz: this unpredictable behavior has been attributed after several tests to an internal implementation of the LMC555 [39] working at low supply voltage. The tests have taken place under the 1.8 V supply test condition exploiting CPX200D [48] and DS1104Z-S Plus [49].

Trying to overcome this issue, in Figure 3.12 and Figure 3.13, an absolute and relative frequency error analysis have been done to find some relationship that may help to understand, notice, and eventually compensate this behavior, while in Figure 3.14 both the expected and the actual experimentally-obtained frequencies have been plotted.

Focusing on Figure 3.12, Figure 3.13 and Figure 3.14, it is evident that for relatively low R_{plant} values (below 10 kΩ) the error tends to increase moving towards even-lower resistance values, while it seems to decrease shifting to higher resistance values: these tendencies have found feedback in the output frequency issue previously highlighted in this section.

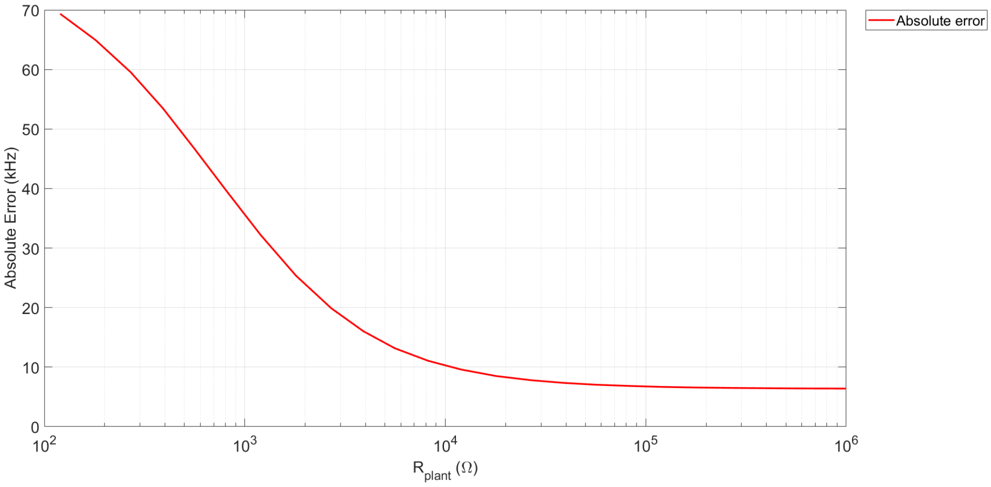

Figure 3.12: Plot of the absolute frequency error between the Equation 3.1 expected frequency and the experimentally-obtained output frequency.

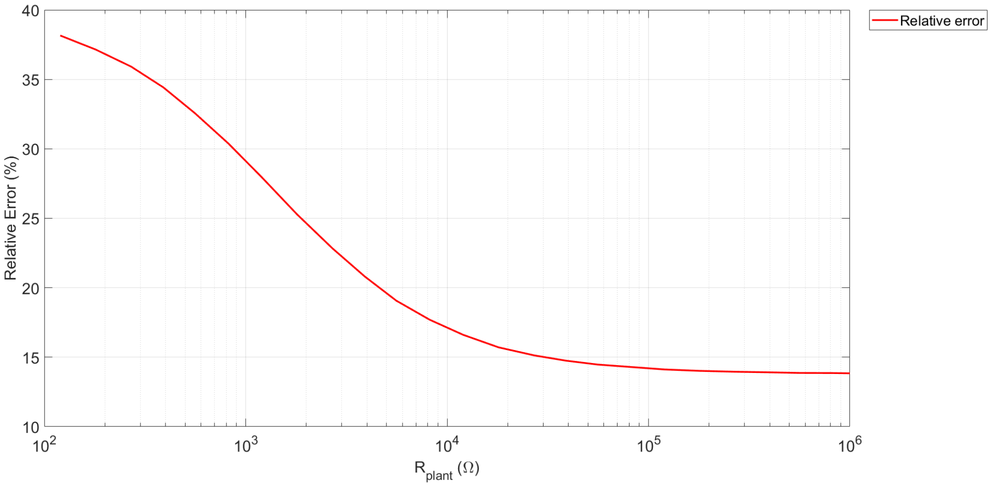

Figure 3.13: Plot of the relative frequency error between the Equation 3.1 expected frequency and the experimentally-obtained output frequency.

The results reported in Figure 3.12, Figure 3.13, and Figure 3.14 have been provided in this thesis to be of any assistance to whoever may utilize the LMC555 [39] in similar configurations. In order to compensate this previously-not-known behavior, a solution may be to eventually employ high-value resistors (at least a more-than-100-kΩ resistor) for R_c if it is possible where both absolute and relative errors seem to be relatively stable, linear and constant and therefore easier to be compensated.

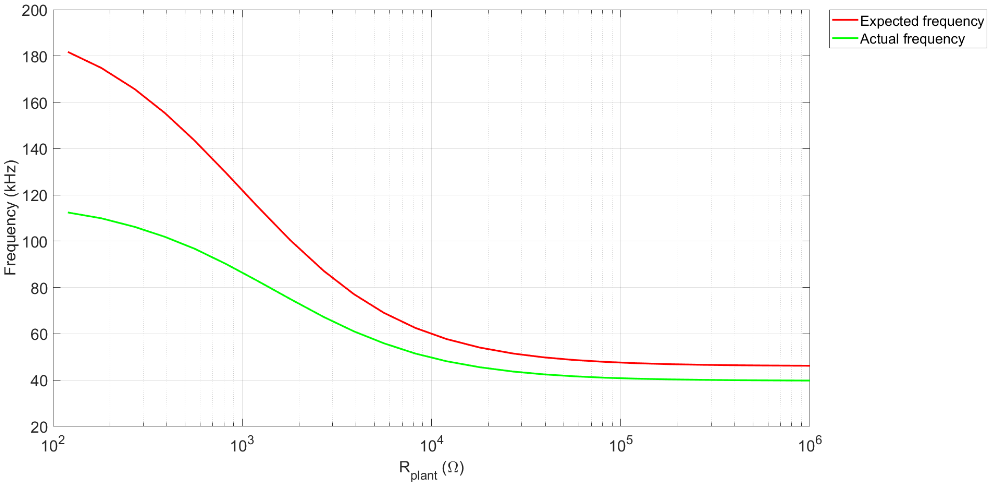

Figure 3.14: Plot of both the Equation 3.1 expected frequency and the actual experimentally-obtained one.

Receiving module characterization

For what concerns the receiving module characterization, the parameters of the 33220A waveform generator [47] have been set to generate a fixed-frequency variable-amplitude sine-wave signal to be inserted in the place of the plant as input of the receiver as reported in Figure 3.3, Figure 3.5 and Figure 3.6.

The measurements have been performed for several values of input signal frequency (1 kHz, 10 kHz, 50 kHz, 100 kHz, and 150 kHz) and a peak-to-peak input voltage ranging from 100 mV to 500 mV by a 10-mV step.

To characterize the input highpass filter previously handled in Section 3.3.1 and verify its behavior, in Figure 3.15 the relation between the input peak-to-peak voltage evaluated downstream the highpass filter (and thus upstream the peak detector) V_{pp-in} and the peak-to-peak voltage set by the 33220A waveform generator [47] $V_{pp-in-instr}$ put as input of the receiving system (and thus upstream the highpass filter) has been plotted: the quite linear relationship for input signal frequencies higher than 10 kHz is verified even if it is noticeable a slight attenuation in the 10-kHz case, while the 1-kHz input signal results to be strongly attenuated remaining relatively constant over the measurements, as expected.

For what concerns the peak detector (reference to Section 3.3.2), a first analysis has considered the relationship between the maximum voltage upstream the peak detector V_{max-in} and the maximum voltage downstream the buffer (and thus upstream the voltage-controlled oscillator) $V_{max-out}$: neglecting in the discussion

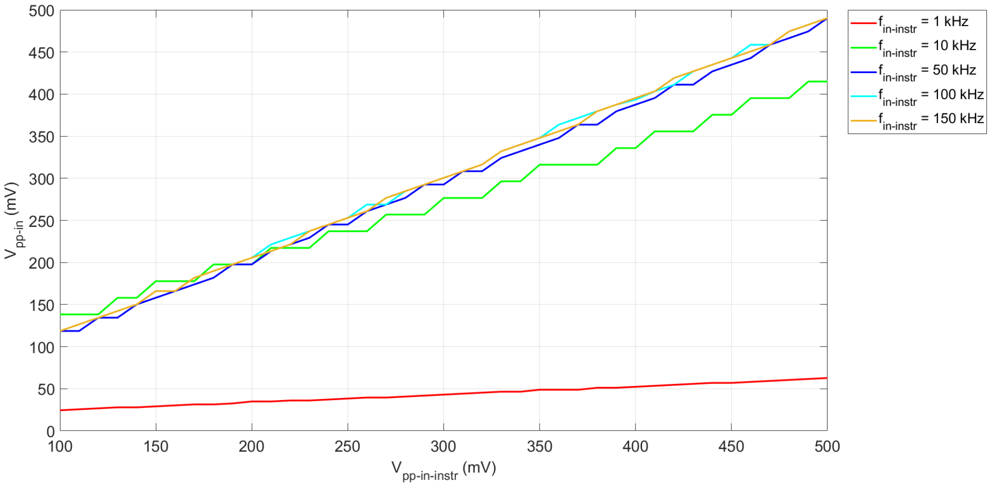

Figure 3.15: Plot of the relation between the input peak-to-peak voltage evaluated after the highpass filter V_{pp-in} and the one set by the 33220A waveform generator [47] $V_{pp-in-instr}$ put as input of the receiving system.

the expected behavior of the 1-kHz wave (strongly attenuated by the highpass filtering action), Figure 3.16 has highlighted an expected quite direct linear relation but affected by a downshift and a reduction in the slope of the linear trends while increasing the input frequency. Thus, a further investigation has been done exploiting the absolute value of the variation ΔV_{max} between $V_{max-out}$ and V_{max-in} in relation to the input peak-to-peak voltage $V_{pp-in-instr}$ set upstream the receiver on the 33220A waveform generator [47]. The results have been collected in Figure 3.17. It has been highlighted a drift phenomenon mainly increasing the input frequency and secondarily increasing the input peak-to-peak voltage. Thus, to reduce the measurement errors related to this drift phenomenon, a good advice may be to adjust the system to work primarily with more minor input frequencies and lower peak-to-peak-amplitude input signals.

For the sake of completeness, the relationship between the input peak-to-peak signal $V_{pp-in-instr}$ and the maximum voltage value downstream the buffer $V_{max-out}$ has been plotted in Figure 3.18: both the drift phenomenon previously noticed and the strong attenuation of the 1-kHz input signal due to the highpass filter are present and highlighted.

In order to characterize the voltage-controlled oscillator previously treated in Section 3.3.4, the relationship between the output frequency f_{out-Rx} and the maximum voltage evaluated downstream the buffer (thus upstream the voltage-controlled oscillator) $V_{max-out}$ has been reported in Figure 3.19: an inverse linear dependency

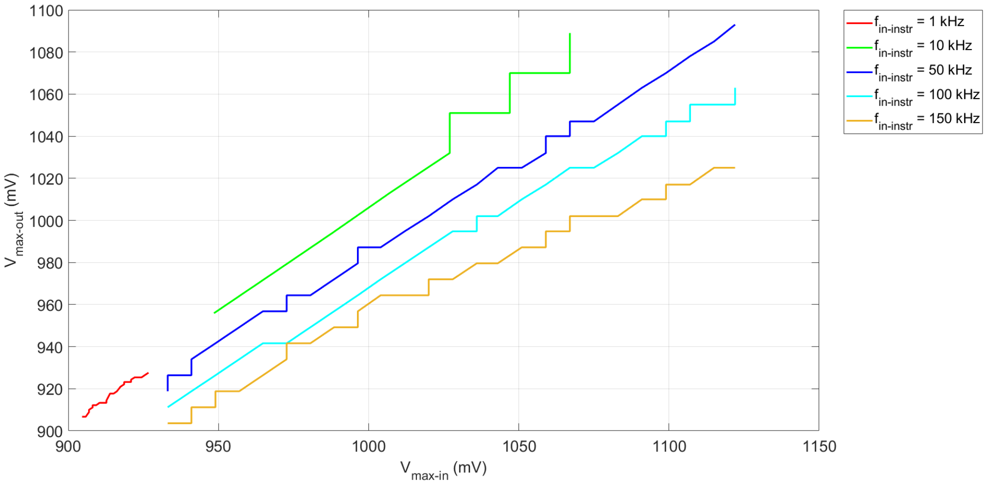

Figure 3.16: Plot of the relation between the input maximum voltage evaluated after the highpass filter V_{max-in} and the one measured after the buffer $V_{max-out}$ of the receiving system.

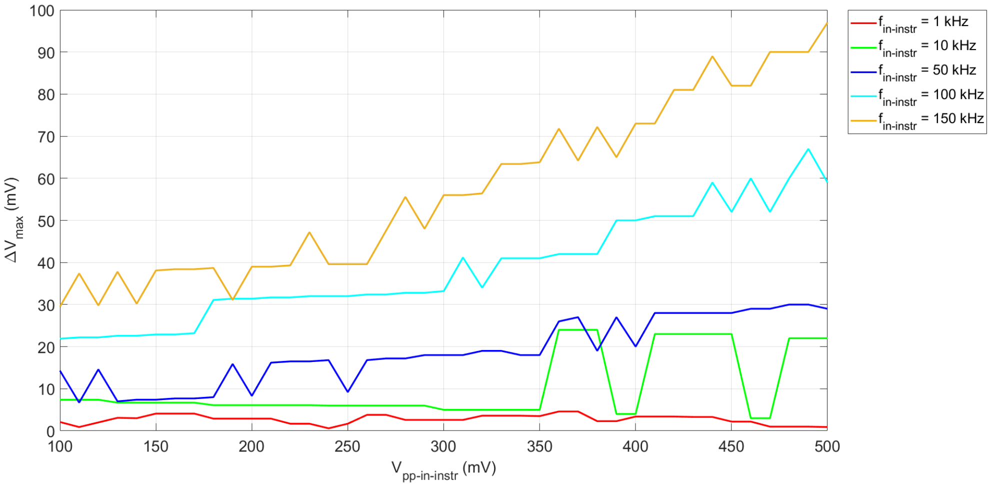

Figure 3.17: Plot of the relation between the absolute variation of the maximum voltage across the peak detector ΔV_{max} and the input peak-to-peak voltage set by the 33220A waveform generator [47] $V_{pp-in-instr}$.

has been highlighted withstanding a strong attenuation for the 1-kHz input and slightly up-shifted 10-kHz linear case.

In Figure 3.20, an overall input-output characterization of the receiving system has been reported: as expected by considering the previous characterization, an inverse linear relation, a strongly attenuated result related to the 1-kHz input signal and

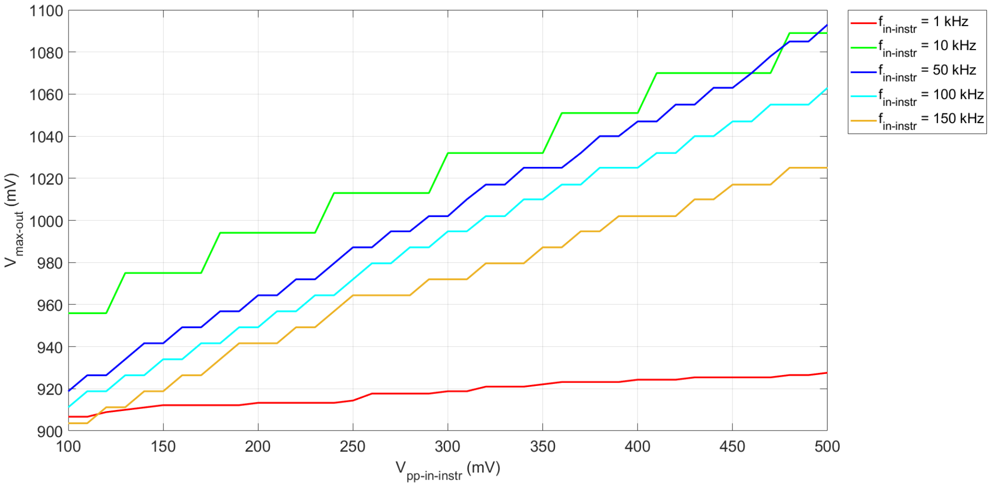

Figure 3.18: Plot of the relation between the input peak-to-peak voltage set by the 33220A waveform generator [47] $V_{pp-in-instr}$ and the maximum voltage stored in the peak detector capacitor $V_{max-out}$.

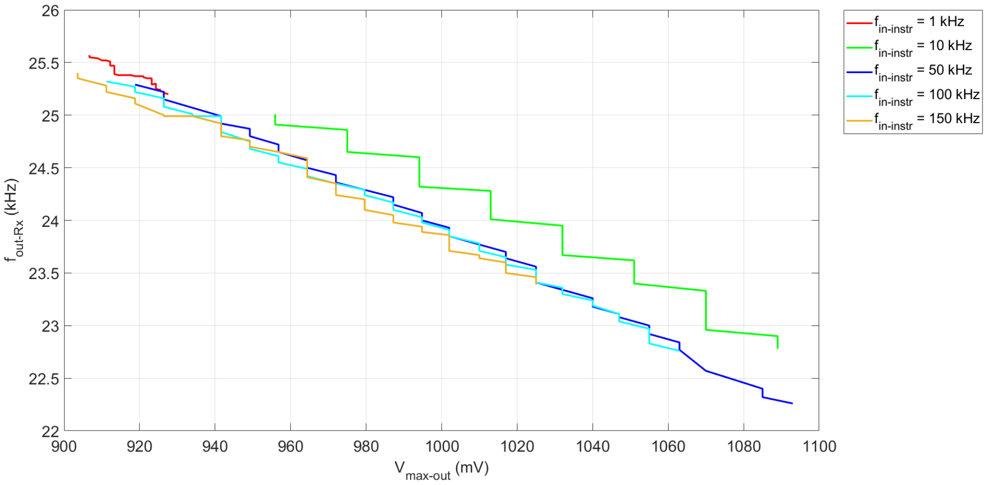

Figure 3.19: Plot of the relationship between the input of the voltage-controlled oscillator $V_{max-out}$ and its output frequency f_{out-Rx}.

slight drift in output frequency f_{out-Rx} due to the increase of the peak-to-peak input voltage $V_{pp-in-instr}$ have been highlighted.

For the sake of completeness, in Figure 3.21 it has been highlighted the relationship between the peak-to-peak value of the input voltage of the peak detector and the output frequency of the receiving module: still, an inverse linear relation and substantial attenuation of the 1-kHz input signal have been reported.

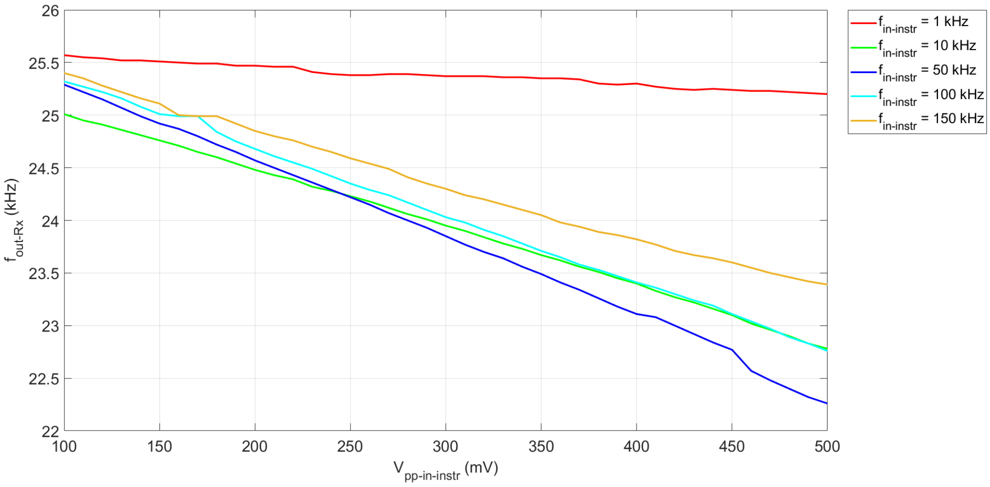

Figure 3.20: Plot of the input-output relationship of the receiving system.

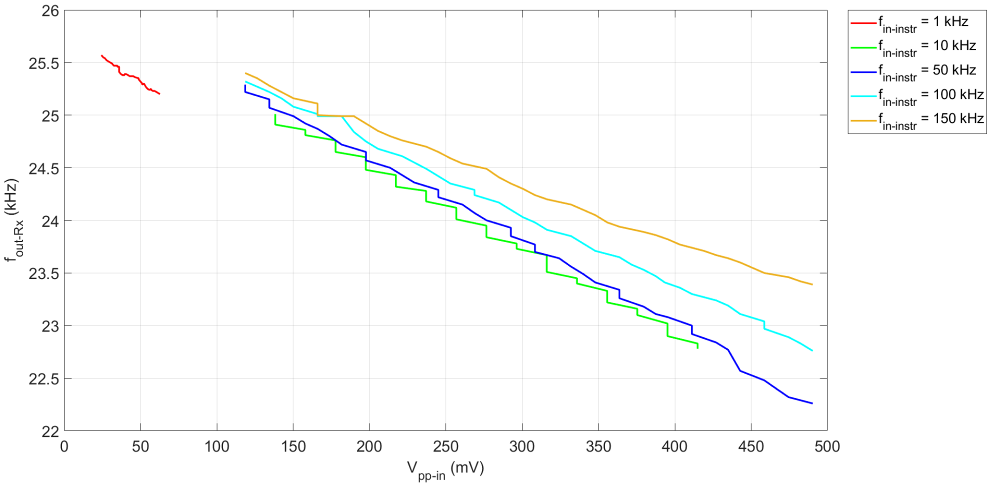

Figure 3.21: Plot of the relationship between the input of the peak detector V_{pp-in} and the voltage-controlled oscillator output frequency (thus receiver output frequency) f_{out-Rx}.

3.4.3 First characterization considering the tobacco plant

In this section, the characterization of both the transmitting module and the receiving device have been exploited employing a 6-7 months old tobacco plant (Nicotiana tabacum L.) whose stem diameter is around 1.146497 cm: the tobacco stem under question is the one reported in Figure 3.3.

The measurements of both the receiver-related and transmitter-related output frequencies and the maximum peak voltage downstream the peak detector have been performed considering variable the distance d_{Tx-Tx} between the two transmitter-related needles (the green needles in Figure 3.3) and then the relative distance d_{Rx-Tx} between the last transmitter-related needle (the bottom green needle in Figure 3.3) and the input of the receiving module (the red needle in Figure 3.3), as reported in Figure 3.22 and Figure 3.23.

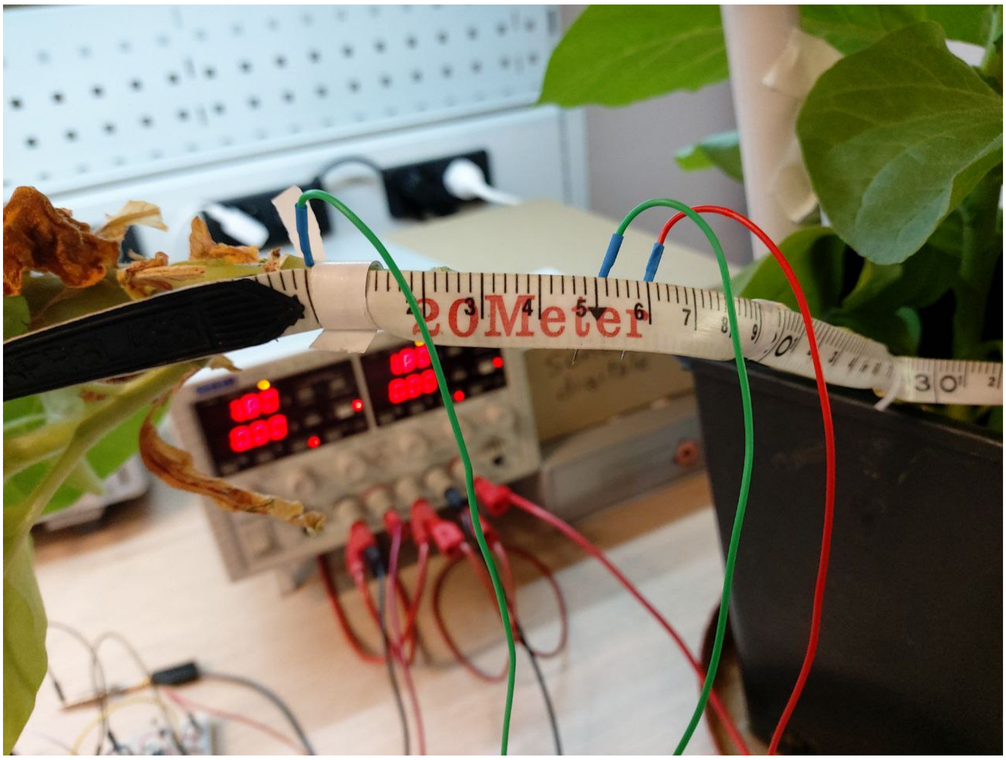

Figure 3.22: Zoom on the surgical needles employed in the characterization of the system related to a living plant with green needles related to the transmitter and the red needle connected as input of the receiver.

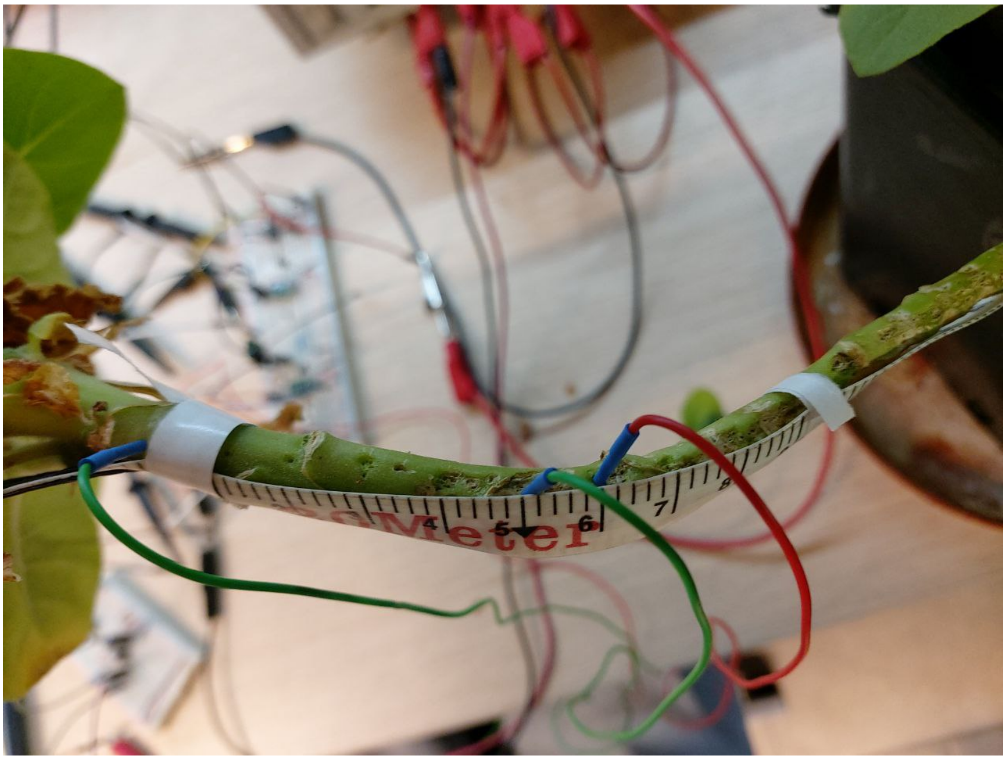

Figure 3.23: Zoom from another point of view on the surgical needles employed in the characterization of the system related to a living plant with green needles related to the transmitter and the red needle connected as input of the receiver.

This characterization took place in the late afternoon at the PIC4SeR laboratories on November 30th, 2023: it is essential to highlight that the employed tobacco plant stem has reached the end of its life just after the characterization as reported in Figure 3.24, therefore it is acceptable to consider the following results as characterizing a near-to-end tobacco plant.

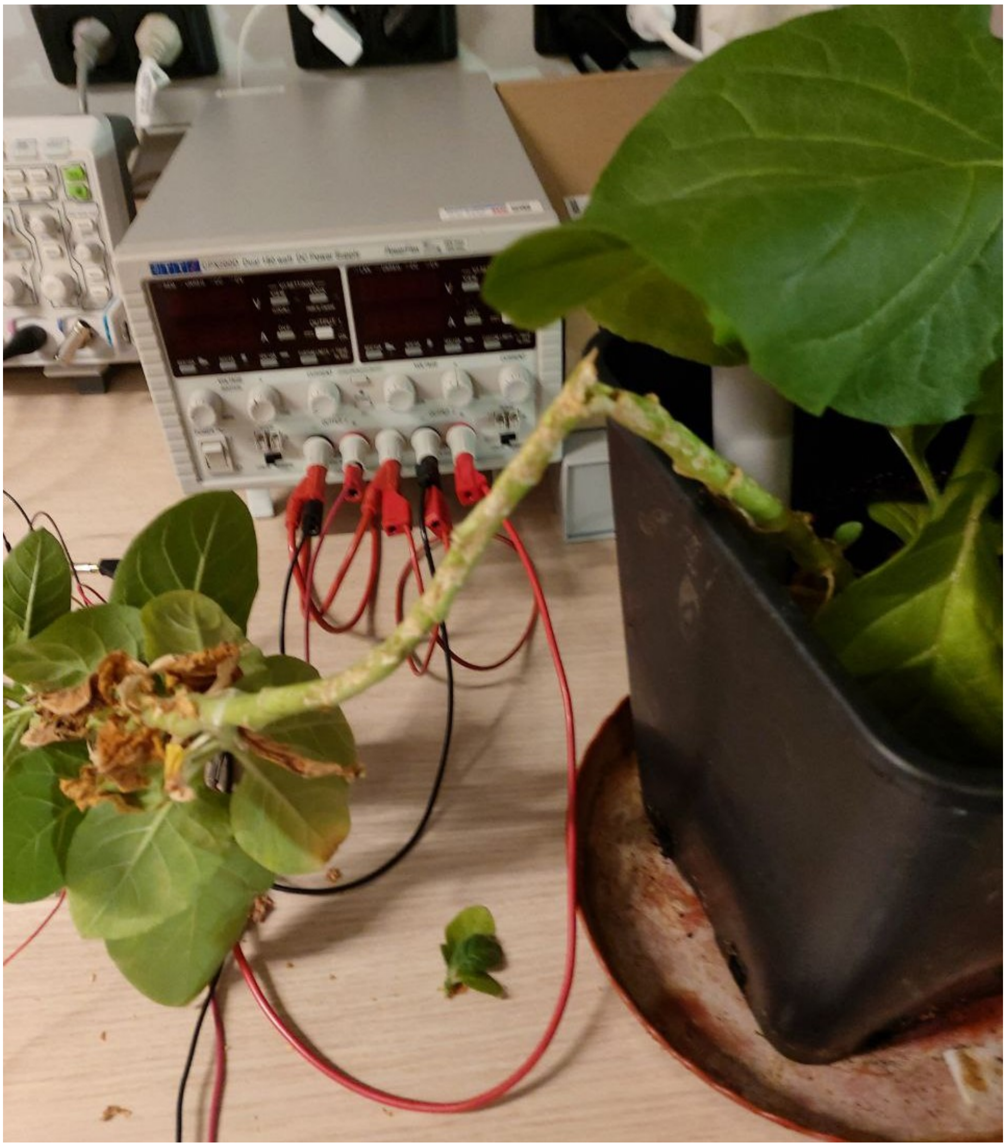

Figure 3.24: Situation of the plant stem under investigation few moments after the end of the characterization process of the implemented system.

In the following measurements, the CPX200D bench-type power supply unit [48] and the DS1104Z-S Plus digital oscilloscope [49] have been exploited.

Transmitting module characterization

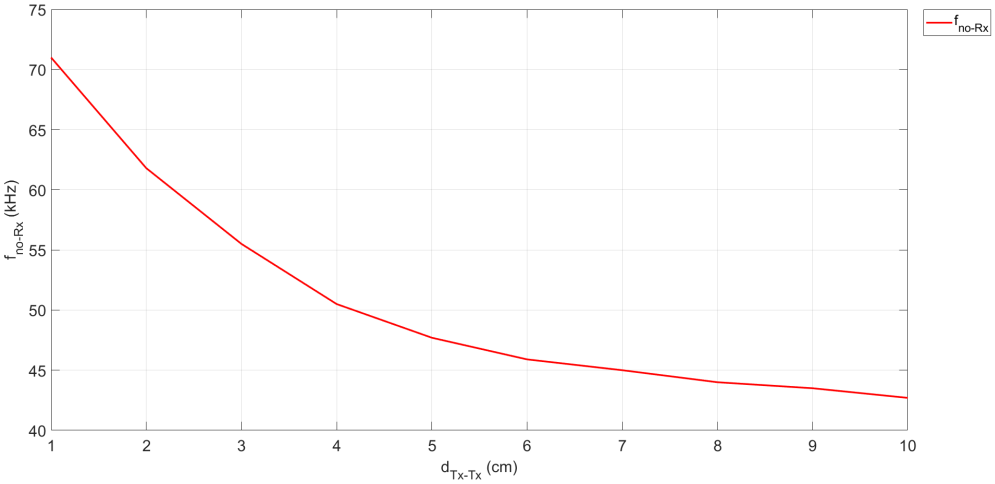

Figure 3.25: Evolution of the transmitting output frequency f_{no-Rx} varying the distance d_{Tx-Tx} over the stem length between the two needles related to R_{plant}.

As reported in Figure 3.25, it has been evidenced an inversely proportional relationship of the output frequency of the transmitting module (without considering the receiving side in the experimental setup) f_{no-Rx} by increasing the relative distance d_{Tx-Tx} between the two surgical needles employed to build both the extremities of the plant-stem-based resistor R_{plant} which sets itself in series to R_1 and then in parallel to R_2 remembering Figure 3.2. This behavior is coherent with the expected results since the scale-up of the relative distance between the transmitter-related needles d_{Tx-Tx} leads to an increase of R_{plant} value, thus to a lower output transmitting frequency f_{no-Rx} according to the Equation 3.1 and the Equation 3.2.

Complete system characterization

In this section, both the transmitting device and the receiving module have been considered in the characterization: in fact, both of the systems have been connected to the aforementioned 6-7 months old tobacco plant as highlighted in Figure 3.3, Figure 3.22 and Figure 3.23.

As reported in Figure 3.26, the peak value of the voltage evaluated at the output of the peak detector (more precisely, downstream the buffer and thus upstream the voltage-controlled oscillator) $V_{max-out}$ tends to increase by growing the relative distance between the two transmitter-related exploited surgical needles d_{Tx-Tx}: this trend is consistent with the behavior highlighted in Figure 3.18 since increasing the relative distance d_{Tx-Tx} and therefore increasing the value of R_{plant} and thus

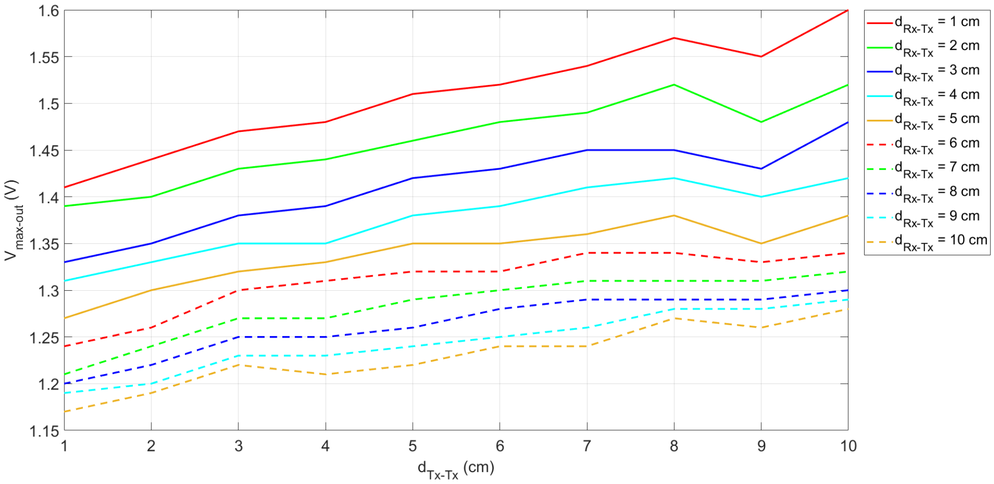

Figure 3.26: Plot of the evolution of the maximum voltage detected and stored downstream the peak detector $V_{max-out}$ changing time for time the relative distance over the stem length d_{Tx-Tx} between the two needles related to R_{plant} and fixing for each curve the relative distance d_{Rx-Tx} over the stem length.

decreasing the value of transmitter-sourced frequency leads to a slight increase of the peak voltage downstream the peak detector $V_{max-out}$ while considering constant the distance between the last transmitter-related needle and the receiver-related needle d_{Rx-Tx}. This behavior is even more justified considering the effect of the transmitter output frequency slight downshift as the predominant process with respect to the attenuation consequences introduced by the relative distance d_{Rx-Tx}.

It is essential to notice that varying the distance between the last transmitter-related needle and the receiver-related needle d_{Rx-Tx}, the peak voltage downstream the peak detector $V_{max-out}$ shifts down in turn to an increase in d_{Rx-Tx}. The main variation in $V_{max-out}$ has been experimented to be due to the rise of the relative distance d_{Rx-Tx}: the most significant delta in $V_{max-out}$ values over the variation of d_{Tx-Tx} is around 190 mV identified on the case where d_{Rx-Tx} has been imposed equal to 1 cm, while the most significant delta related to the variation of d_{Rx-Tx} is around 320 mV for the d_{Tx-Tx} case correspondent to the 10-cm measurement, as reported in Figure 3.28. These results imply a stronger dependence of the maximum peak detector output voltage $V_{max-out}$ on the relative distance between the last transmitter-related needle and the receiver-related needle d_{Rx-Tx} over the stem length and a less reliance on the relative distance d_{Tx-Tx} between the transmitter-related needles.

Another noticeable result in Figure 3.28 is the increasing density of measurements while increasing the relative distance d_{Tx-Tx}, presumably because of the extension and the consequences of the characterization procedure on the plant stem jointly with its characteristics moving towards the roots (thus increasing both the relative distances d_{Tx-Tx} and d_{Rx-Tx}): in fact, the time length required to perform the characterization in partnership with the damages of the plant stem introduced by the process (for instance, scar tissues due to the insertion and removal of the employed surgical needles over the stem length depicted in Figure 3.27) and with the ever-decreasing level of freshness moving towards the roots may imply a sort of stabilization and concentration of the results obtained thus improving the similarities in their evolution over time and over the plant-stem length.

Figure 3.27: Zoom on the damages left on an healthy new tobacco plant stem due to the characterization process after 10 days without performed measurements.

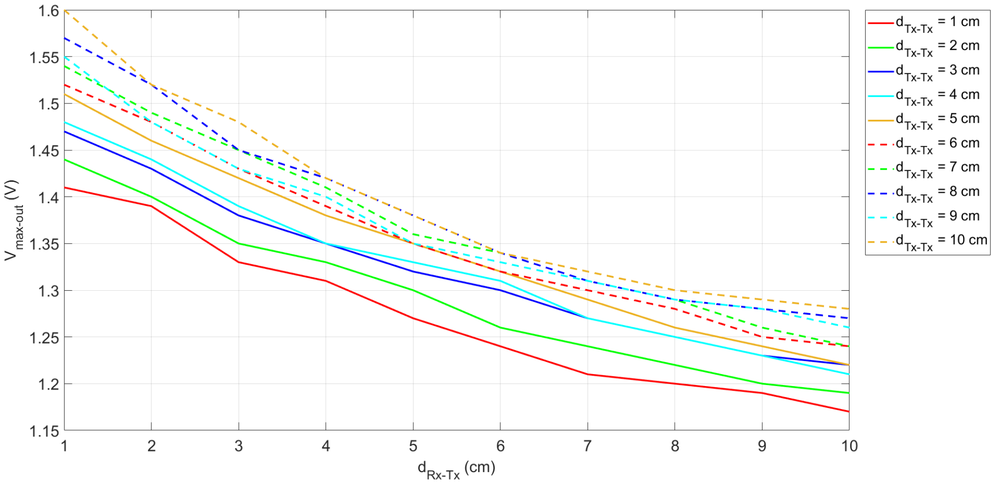

Figure 3.28: Plot of the evolution of the maximum voltage detected and stored downstream the peak detector $V_{max-out}$ changing time for time the relative distance d_{Rx-Tx} over the stem length and fixing for each curve the relative distance over the stem length d_{Tx-Tx} between the two needles related to the extremities of R_{plant}.

In particular in Figure 3.28, a more manifest (albeit still minimal and tending-to-linear) inversely proportional relationship between the peak output value of $V_{max-out}$ and the relative lapse of distance d_{Rx-Tx} has been evidenced: in fact, the grow up of the distance d_{Rx-Tx} implies an increasing trend of the attenuation suffered by the signal injected by the transmitter in the plant stem through the transmitter-related needles and detected by the receiver side from the plant stem.

In order to represent graphically the evolution of the output peak voltage $V_{max-out}$ in terms of the relative distances d_{Tx-Tx} and d_{Rx-Tx}, Figure 3.29 has been produced.

In order to represent graphically the evolution of the output peak voltage $V_{max-out}$ in terms of the relative distances d_{Tx-Tx} and d_{Rx-Tx}, Figure 3.29 has been produced.

In Figure 3.30, the relationship between the output frequency evaluated downstream the voltage-controlled oscillator (thus downstream the entire receiver system) f_{out-Rx} and the detected maximum output voltage of the peak detector $V_{max-out}$ has been highlighted: a negative-slope linear relation has been evidenced since this kind of dependency has been highlighted as the input-output characteristic of the LMC555-based voltage-controlled oscillator [39], as also noticeable in Figure 3.19.

Varying the relative lapse of distance from both the transmitter-related needles over the stem length d_{Tx-Tx}, the voltage-controlled oscillator characteristics in Figure 3.30 tend to be downshifted in terms of output frequency of the receiver side f_{out-Rx}

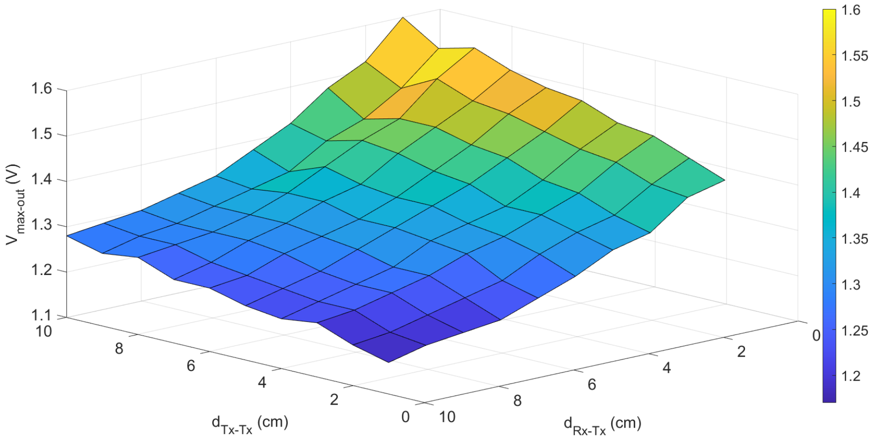

Figure 3.29: Evolution of the output peak voltage of the peak detector $V_{max-out}$ varying both the relative distances d_{Tx-Tx} and d_{Rx-Tx} over the plant stem length.

in turn to an increase of the distance d_{Tx-Tx}: remembering the relationship exposed in Figure 3.25, this result can be deduced since increasing the relative distance d_{Tx-Tx} the transmitter-derived frequency tends to be lowered. Therefore, even the signal detected by the receiver side will be characterized by a lower frequency, thus shifting down (even though slightly) the output frequency of the receiver side f_{out-Rx}.

On the other hand, varying the relative lapse of distance d_{Rx-Tx} over the stem length, the voltage-controlled oscillator characteristics in Figure 3.31 tend to be upshifted in terms of output frequency of the receiver side f_{out-Rx} in turn to an increase of the distance d_{Rx-Tx}. This result can be predicted by considering the relationship between the output of the PD $V_{max-out}$ and the input of the peak detector V_{max-in} reported in Figure 3.16: in fact, making the relative distance d_{Rx-Tx} wider, the detected input signal of the receiver results ever-more attenuated implying a lower peak detector output voltage $V_{max-out}$ and therefore a higher output frequency of the receiver's voltage-controlled oscillator f_{out-Rx}.

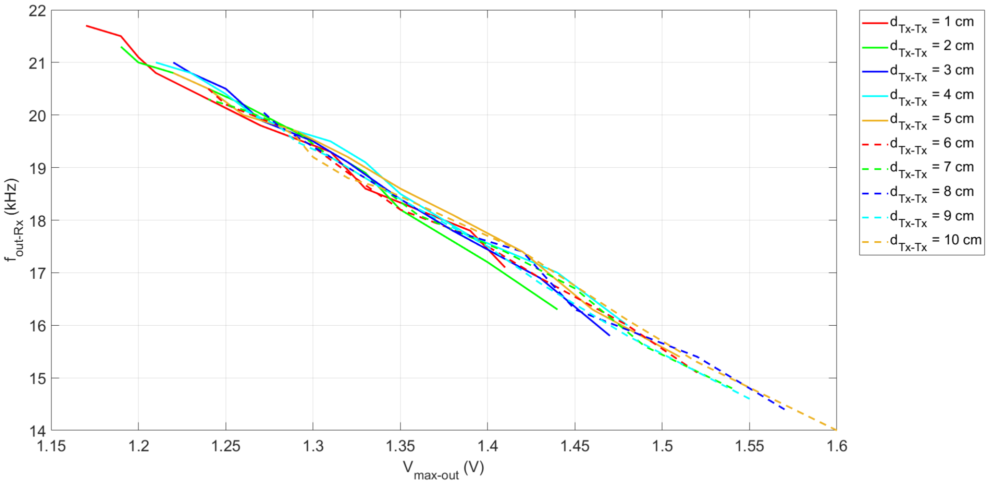

Figure 3.30: Plot of the relationship between the output frequency of the receiving module f_{out-Rx} varying the output peak voltage $V_{max-out}$ detected upstream the voltage-controlled oscillator for each value of the relative distance d_{Tx-Tx}.

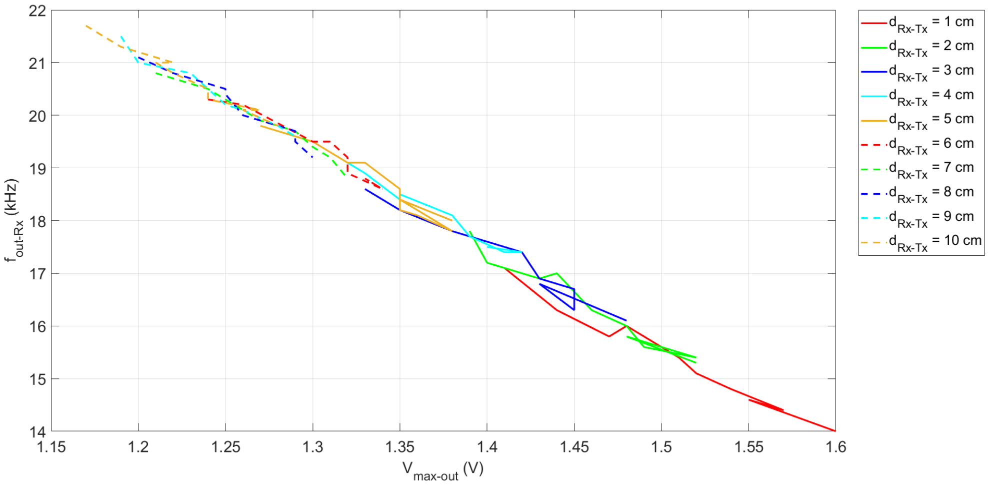

Figure 3.31: Plot of the relationship between the output frequency of the receiving module f_{out-Rx} varying the output peak voltage $V_{max-out}$ detected upstream the voltage-controlled oscillator for each value of the relative distance d_{Rx-Tx}.

Further evidence of the relationship between the output frequency of the receiving module f_{out-Rx} and the relative distance d_{Tx-Tx} has been highlighted in Figure 3.32: here it has been further evidenced the low dependence of the output of the peak detector $V_{max-out}$ (and thus of the output frequency f_{out-Rx}) on the relative distance d_{Tx-Tx} reported in Figure 3.26.

On the other hand, in Figure 3.33 the relationship exposed in Figure 3.28 finds further evidence taking into account the inverse linear dependency between the output peak voltage of the peak detector $V_{max-out}$ and the output frequency of the entire receiver side (thus downstream the voltage-controlled oscillator) f_{out-Rx}.

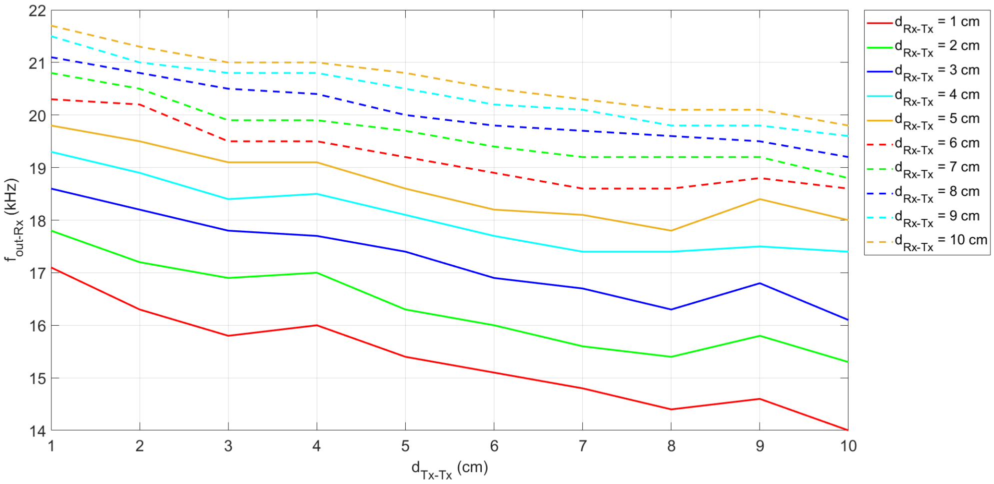

Figure 3.32: Evolution of the receiver's output frequency f_{out-Rx} varying the relative distance d_{Tx-Tx} for each value of the relative distance d_{Rx-Tx}.

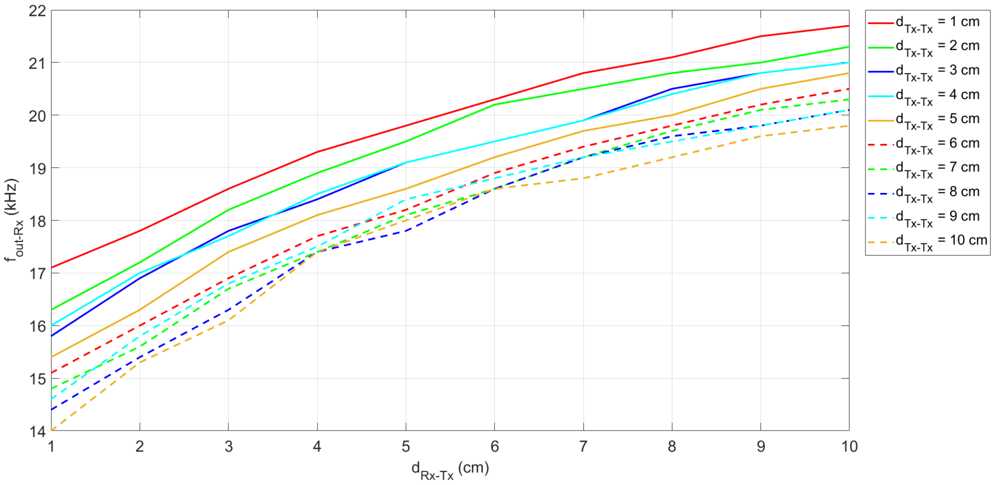

Figure 3.33: Evolution of the receiver's output frequency f_{out-Rx} varying the relative distance d_{Rx-Tx} for each value of the relative distance d_{Tx-Tx}.

For the sake of completeness, in order to represent graphically the evolution of the receiver output frequency f_{out-Rx} in terms of the relative distances d_{Tx-Tx} and d_{Rx-Tx} over the plant stem length, Figure 3.34 has been produced.

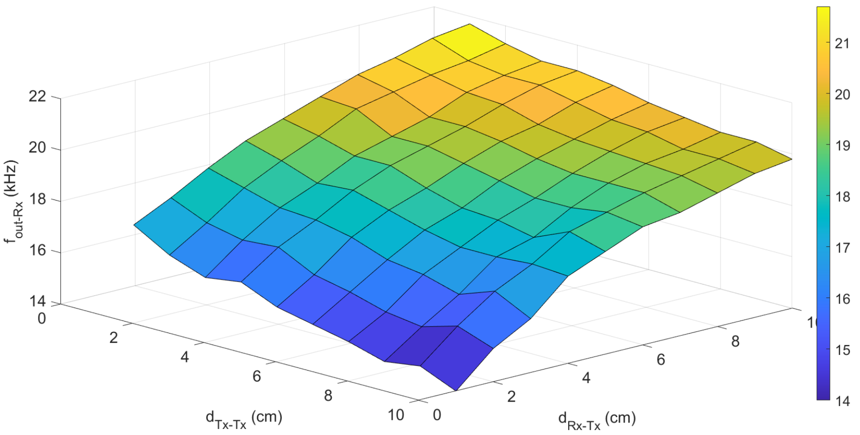

Figure 3.34: Evolution of the output frequency of the receiver f_{out-Rx} varying both the relative distances d_{Tx-Tx} and d_{Rx-Tx} over the plant stem length.

For thoroughness, in both Figure 3.35 and Figure 3.36, the attenuation applied to the receiver input signal has been plotted in relation to respectively the relative distances d_{Rx-Tx} and d_{Tx-Tx}: these curves' behavior is coherent with the results discussed before in this section.

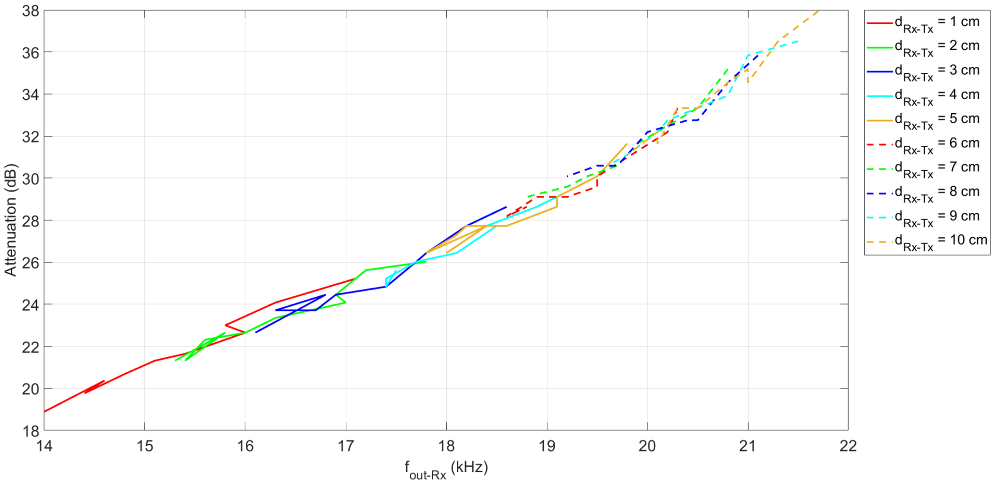

Figure 3.35: Trend of the attenuation the receiver-related input signal is subjected to in terms of the output frequency of the receiver f_{out-Rx} varying the relative distance d_{Rx-Tx} over the plant stem length.

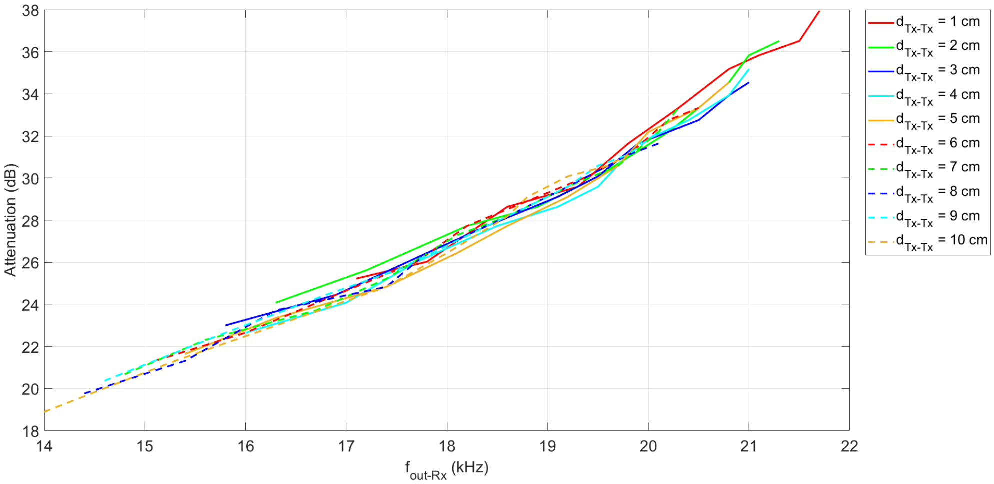

Figure 3.36: Trend of the attenuation the receiver-related input signal is subjected to in terms of the output frequency of the receiver f_{out-Rx} varying the relative distance d_{Tx-Tx} over the plant stem length.

3.4.4 Second characterization considering the tobacco plant

In order to have further knowledge of the developed system behavior, more characterizations have been done: in particular, in this section, the plant exploited for this purpose is a tobacco plant (Nicotiana tabacum L.) sown on the middle of September 2023 and transplanted in a smaller pot on December 6th, 2023. When the characterization took place (January 8th, 2024), the analyzed tobacco plant stem diameter was around 0,796178 cm.

The measurements of both transmitter and receiver modules have been performed in the same manner as the first characterization of the Tx-plant-Rx system reported in Section 3.4.3: the tobacco plant under test is the one depicted in Figure 3.37 and Figure 3.38.

As already mentioned, this characterization took place in the late forenoon and early afternoon at the Pierluigi Civera laboratory inside the DET department of the Politecnico di Torino on January 8th, 2024: in contrast to the tobacco plant exploited in Section 3.4.3, the this-section-employed plant stem has not presented any near-to-end signs, therefore the following results can be associated to a growing and healthy tobacco plant.

In the following measurements, the DP832A bench-type power supply unit [50] from Rigol and the MSO5014 digital oscilloscope [51] from Rigol have been exploited.

Figure 3.37: Tobacco plant utilized for the characterization with both transmitter and receiver modules.

Figure 3.38: Zoom on the surgical needles employed in the characterization of the system related to a living tobacco plant.

Transmitting module characterization

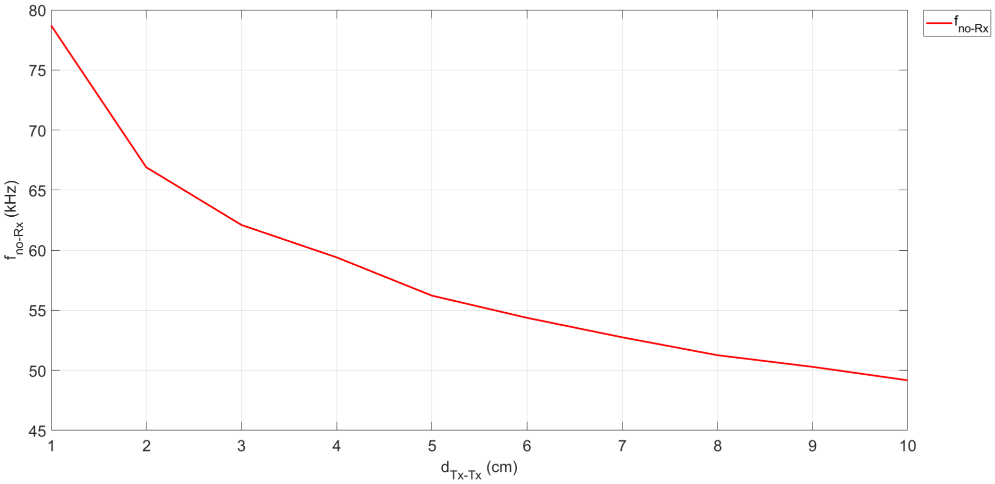

Figure 3.39: Evolution of the transmitting output frequency f_{no-Rx} varying the distance d_{Tx-Tx} over the stem length between the two needles related to R_{plant}.

As previously pointed out in Section 3.4.3 an expected inversely proportional relationship of the output frequency of the transmitting module (without considering the receiving side in the experimental setup) f_{no-Rx} by increasing the relative distance d_{Tx-Tx} between the two surgical needles employed to build both the extremities of the plant-stem-based resistor R_{plant} has been evidenced in Figure 3.39: however, an up-shift of the frequency range can be noticed in this latter characterization with respect to the previous one. This behavior might be related to the age of the plant: in fact, as previously highlighted in Section 3.4.4, the tobacco plant employed for this second characterization is at least 3 months younger than the other one and presents a healthier structure, moisture content, look and overall condition.

Complete system characterization

As previously done in Section 3.4.3, both the transmitting device and the receiving module have been considered in this section's characterization taking into account the tobacco plant depicted in Figure 3.37 and Figure 3.38 and described in Section 3.4.4.

As reported in Figure 3.40, the peak value of the voltage evaluated downstream the peak detector $V_{max-out}$ tends to increase by growing the relative distance d_{Tx-Tx} coherently to what has been previously highlighted in Section 3.4.3. However, in this second characterization process, the curves present a narrower bandwidth of measurements on equal terms of relative distance d_{Rx-Tx}, a less-linear behavior (in

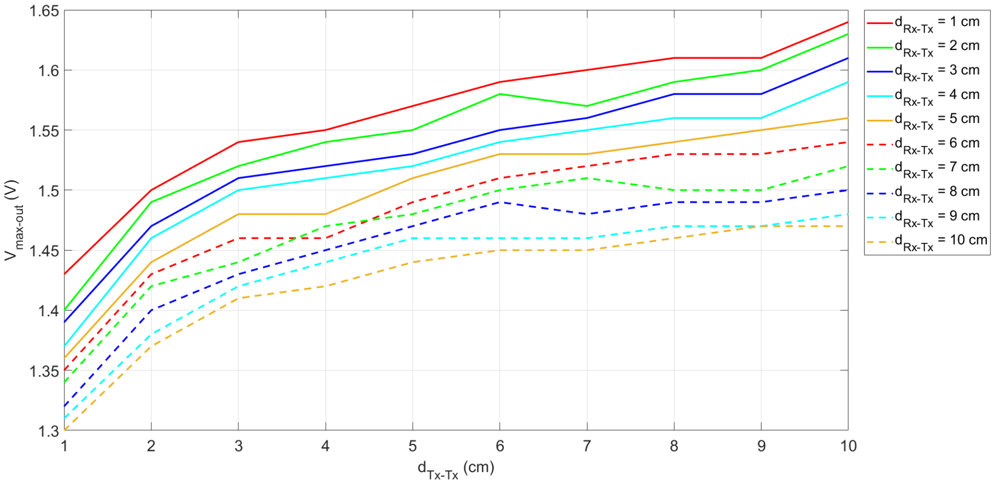

Figure 3.40: Graph of the evolution of the maximum voltage detected downstream the peak detector $V_{max-out}$ changing time for time the relative distance over the stem length d_{Tx-Tx} and fixing the relative distance d_{Rx-Tx} over the stem length for each curve.

particular, presenting a root-kind grow over the stem length) and result slightly up-drifted: these characteristics can be even more justified considering the effect of the transmitter output frequency slight downshift as predominant process with respect to the attenuation consequences introduced by the relative distance d_{Rx-Tx} as already evidenced in Section 3.4.3 and may be related to the higher value of freshness and moisture content of the tobacco plant exploited in this characterization with respect to the plant stem utilized in the previous one used in Section 3.4.3, especially distancing away from the roots and moving towards the leaves on the top and for low values of the relative distance d_{Tx-Tx} and thus of the plant-stem-introduced resistance R_{plant}.

It is relevant to notice that in comparison with the results obtained in Section 3.4.3, the stronger dependence of the maximum peak detector output voltage $V_{max-out}$ on the relative distance d_{Tx-Tx} and the less reliance on the relative distance d_{Rx-Tx} have been evidenced: in contrast to the correspondent results of the previous characterization, the most significant delta in $V_{max-out}$ values over the variation of d_{Tx-Tx} is around 230 mV identified on the case where d_{Rx-Tx} has been imposed equal to 2 cm, while the most significant delta related to the variation of d_{Rx-Tx} is around 170 mV for the d_{Tx-Tx} case correspondent to the 10-cm measurement, therefore implying a stronger dependence of the maximum peak detector output voltage $V_{max-out}$ on the transmitter-related relative distance d_{Tx-Tx} and a less reliance on the receiver-related relative distance d_{Rx-Tx} over the stem length, even though a much slighter difference in this second employed plant stem can be underlined. However, without considering low d_{Tx-Tx} values, it is possible to notice the relatively constant (in particular, slightly increasing) $V_{max-out}$ behavior on the distance d_{Tx-Tx} formerly highlighted in Section 3.4.3, finding analogies with the previous Tx-plant-Rx system characterization and then to newly assume the previously stated stronger dependence of $V_{max-out}$ on the distance d_{Rx-Tx} and thus its less reliability on d_{Tx-Tx} variations even for this results.

Precisely as previously described in Section 3.4.3, the points that have just been made can be furthermore verified by inspecting the Figure 3.41 where however, even considering the expected slight up displacement of the curves (strictly related to the aforementioned slight up-shift), it can be evidenced that especially in turn to small values of d_{Tx-Tx}, the peak voltage gap between a curve and the next one increases: the probable causes previously hypothesized in Section 3.4.3 are still considered in this case as causative factors.

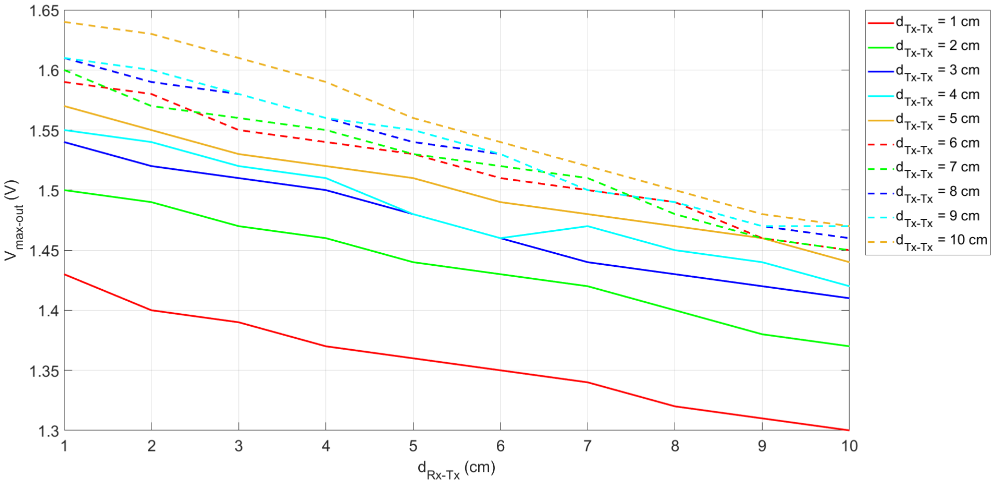

Figure 3.41: Evolution of the maximum voltage detected by the peak detector $V_{max-out}$ in relationship with the relative distance d_{Rx-Tx} over the stem length and fixing for each curve the relative distance over the stem length d_{Tx-Tx}.

In parallel to what it has been underlined in Section 3.4.3, the negative proportional relationship between the peak output value of $V_{max-out}$ and the relative lapse of distance over the stem length d_{Rx-Tx} has been evidenced in Figure 3.41: however in this second case, an even more linear behavior has been obtained with respect to the previous characterization result.

For thoroughness, in order to represent graphically the evolution of the output peak voltage $V_{max-out}$ in terms of the relative distances d_{Tx-Tx} and d_{Rx-Tx}, the Figure 3.42 has been produced evidencing a more marked uniformity in the results due to the evaluations previously explained.

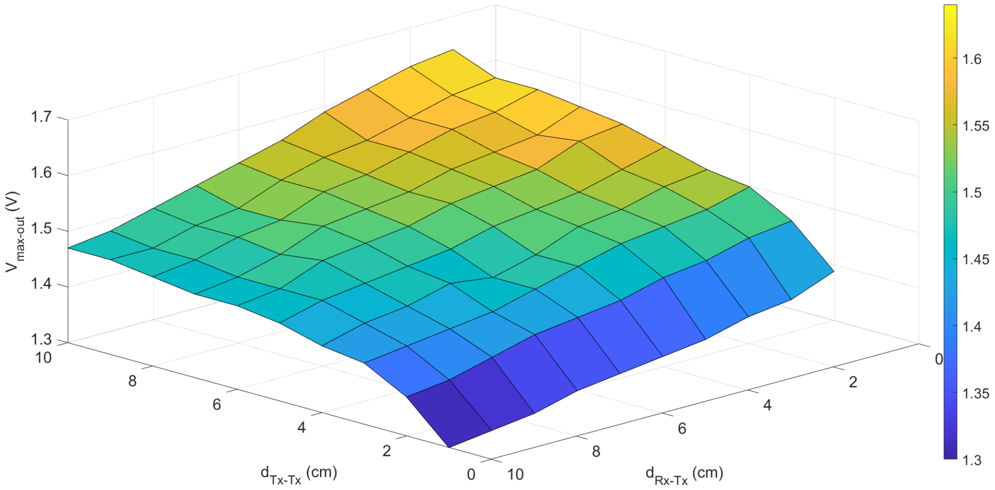

Figure 3.42: Evolution of the output peak voltage $V_{max-out}$ varying both the relative distances d_{Tx-Tx} and d_{Rx-Tx} over the second plant stem length.

Inspecting the curves depicted in Figure 3.43, the negative-slope linear relationship (albeit less uniform and more dispersed varying the relative distance d_{Tx-Tx}) between the output frequency of the entire receiver system f_{out-Rx} and the detected maximum output voltage of the peak detector $V_{max-out}$ has been furthermore verified: as emphasized in Section 3.4.3, this kind of dependency has been also highlighted as the input-output characteristic of the LMC555-based voltage-controlled oscillator [39]. However, coherently to the curves-gap-related behavior aforementioned in Figure 3.41, it is noticeable significant displacements for the low-d_{Tx-Tx}-derived curves with respect to the high-d_{Tx-Tx}-derived ones, especially underlined considering the 1-cm d_{Tx-Tx} case, but other considerations made in the first characterization are still evidenced.

Coherently to the aforementioned second-characterization-related considerations with respect to the ones enlightened in Section 3.4.3, the voltage-controlled oscillator curves in Figure 3.44 result less linear for smaller d_{Tx-Tx} values and globally more dispersed, even though the up-shifting phenomenon underlined in Figure 3.31 and the previously-enlightened negative-slope linear relation derived from the exploitation of the LMC555-based voltage-controlled oscillator [39] are still noticeable, especially moving towards higher d_{Tx-Tx} values.

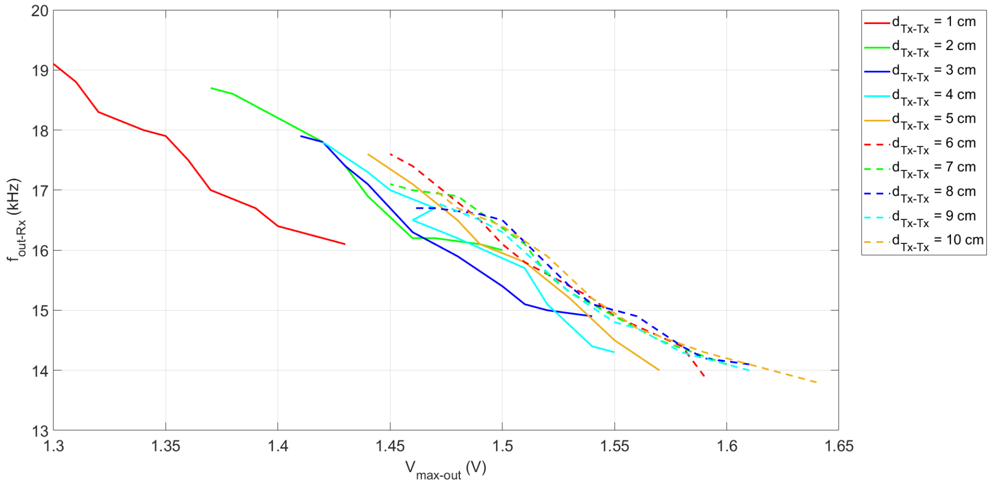

Figure 3.43: Relationship between the output frequency of the receiving module f_{out-Rx} changing the peak detector output $V_{max-out}$ for each value of the relative distance between both the needles of the transmitter d_{Tx-Tx}.

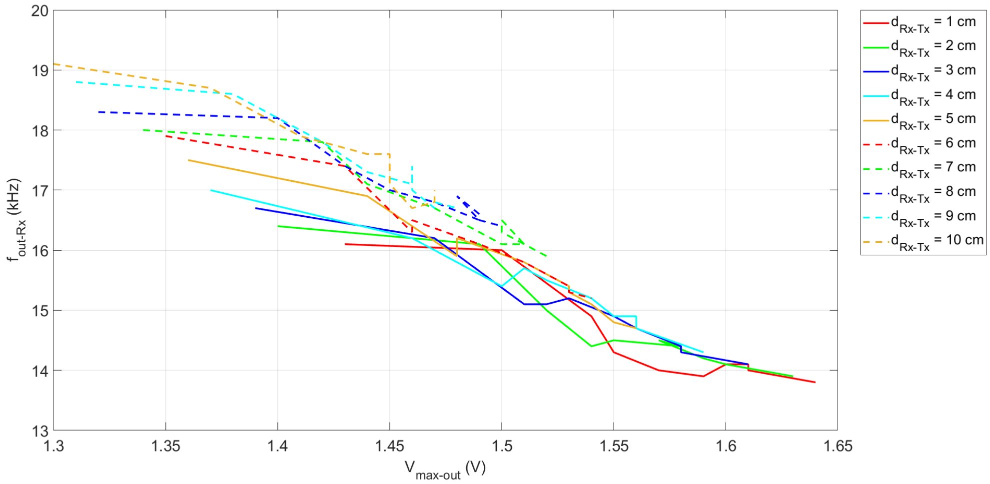

Figure 3.44: Relationship between the receiving-module output frequency f_{out-Rx} varying the peak detector output $V_{max-out}$ for each value of the relative distance over the stem length d_{Rx-Tx}.

For what concerns the relationship between the output frequency of the receiving module f_{out-Rx} and the relative distance between both the needles of the transmitter d_{Tx-Tx}, the strong dependence of the peak detector output $V_{max-out}$ (and thus of the output frequency f_{out-Rx}) on the relative distance d_{Tx-Tx} has been depicted in Figure 3.45: however, just coherently to the $V_{max-out}$ curves reported in Figure 3.40, a sort of negative-root-like behavior can be particularly noticed locally in the region around low values of d_{Tx-Tx} and a globally narrower receiver's output frequency bandwidth (especially for low values of d_{Rx-Tx}) with respect to the correspondent result in Section 3.4.3 has been underlined, again coherently to the curves previously described in Figure 3.40.

Moreover, exactly how it has been explained in Section 3.4.3, the relationship depicted in Figure 3.46 can be expected taking into account the curves reported in Figure 3.41 and the inverse linear dependency between the peak detector output $V_{max-out}$ and the output frequency of the entire receiver side f_{out-Rx}: however, remembering the hypothesis aforementioned in this section, it can be highlighted a higher level of dispersion of the measurements with respect to the ones performed in Section 3.4.3.

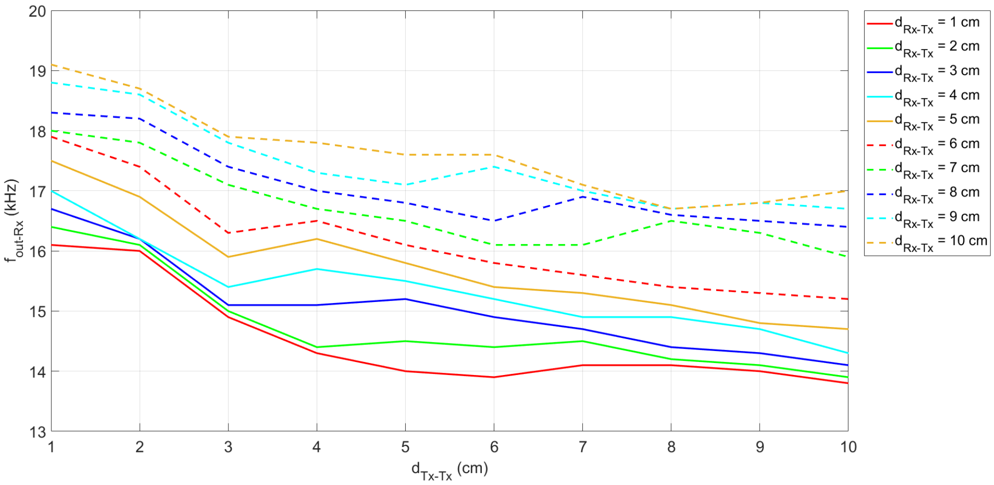

Figure 3.45: Evolution of the receiver's output frequency f_{out-Rx} varying the distance d_{Tx-Tx} and fixing the relative length d_{Rx-Tx} from time to time on the second plant.

For the sake of completeness, in order to represent graphically the evolution of the output frequency of the receiving module f_{out-Rx} in terms of the relative distances d_{Tx-Tx} and d_{Rx-Tx} over the plant stem length, Figure 3.47 has been plotted and reported: it can be highlighted a less uniform behavior, especially by varying the relative distance between the two transmitter-related employed surgical needles.

For thoroughness, in both Figure 3.48 and Figure 3.49 the attenuation applied to the receiver input signal has been plotted respectively over the relative distances d_{Rx-Tx} and d_{Tx-Tx}: this behavior is coherent with the aforementioned conclusions.

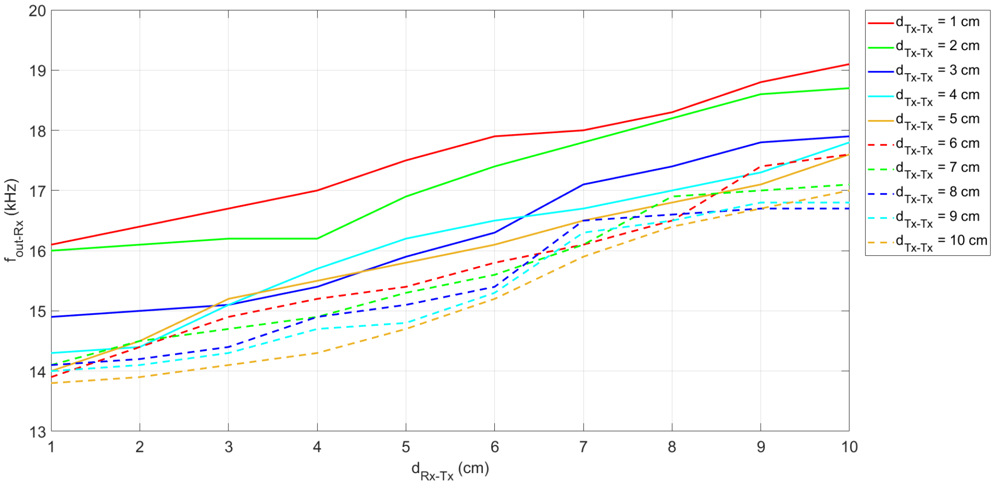

Figure 3.46: Evolution of the receiver's output frequency f_{out-Rx} varying the relative distance d_{Rx-Tx} and fixing the relative length d_{Tx-Tx} from time to time on the second plant.

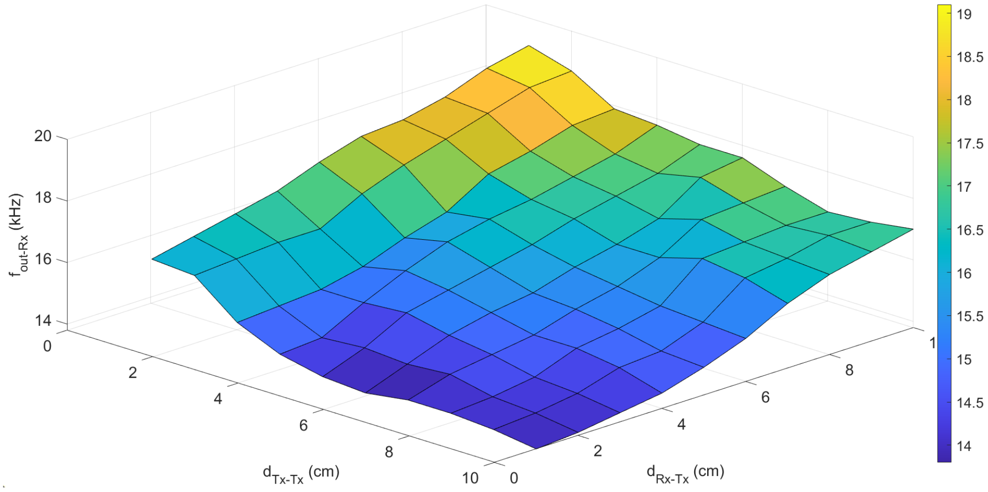

Figure 3.47: Evolution of the output frequency of the receiver f_{out-Rx} varying both the relative distances d_{Tx-Tx} and d_{Rx-Tx} over the second plant stem length.

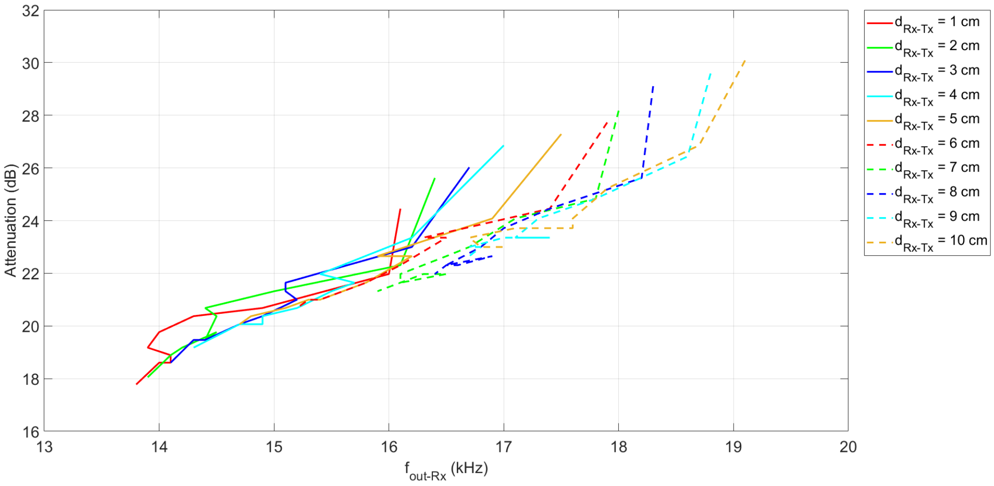

Figure 3.48: Trend of the attenuation the receiver-related input signal is subjected to in terms of the output frequency of the receiver f_{out-Rx} varying the relative distance d_{Rx-Tx} over the plant stem length.

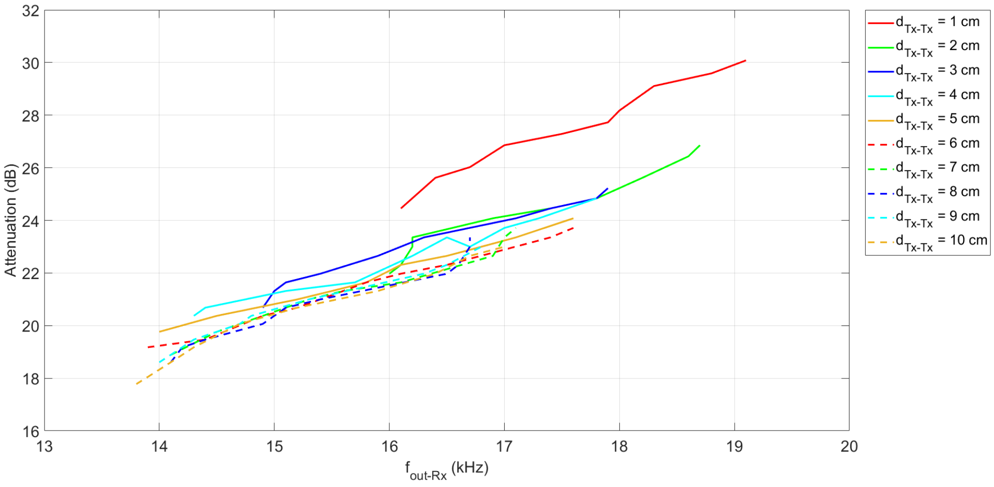

Figure 3.49: Trend of the attenuation the receiver-related input signal is subjected to in terms of the output frequency of the receiver f_{out-Rx} varying the relative distance d_{Tx-Tx} over the plant stem length.

3.4.5 Third characterization considering the tobacco plant

In this section, the same tobacco plant (Nicotiana tabacum L.) previously exploited in Section 3.4.4 has been utilized once again to characterize the developed system: however, in this case, an electrical impedance evaluation performed through the utilization of a 4294A precision impedance analyzer [52] from Agilent Technologies Inc. (now Keysight) has been deployed in the same manner of both the first and the second characterization of the Tx-plant-Rx system described in Section 3.4.3 and Section 3.4.4 in addition to the same kind of measurements deployed in previous sections exploiting the DP832A as power supply unit [50] and the MSO5014 as digital oscilloscope [51]. Furthermore, in this more-detailed-than-before characterization process, even the variation of the transmitter-related output frequency considering the receiver in the experimental setup f_{out-Tx} over the relative distances d_{Tx-Tx} and d_{Rx-Tx} has been registered since considering the plant stem associated only to a resistance-related quantity is quite limiting. In fact, it behaves in different ways at different frequencies, implying the use of the more appropriate concept of electrical impedance and necessitating the investigation of the relation between the transmitter-related output frequency f_{out-Tx} and the receiver-related one f_{out-Rx}.

Due to the high number of needed measurements and to the relatively time-consuming mechanism employed to perform the electrical-impedance-related results with the 4294A impedance analyzer [52] and its associated LabVIEW script (exploited to read more easily the output of the impedance analyzer), this third characterization has required to be spread over two days (in particular, from the morning of January 10th, 2024 to the late evening of January 11th, 2024 at the Pierluigi Civera laboratory inside the DET department of the Politecnico di Torino) consequently including some breaks in the evaluation process (for instance, one from January 10th, 2024 late evening to January 11th, 2024 morning and then a mid-day one on January 11th, 2024).

It is essential to highlight that since only a short period of time (for instance, two days) has elapsed between the second and third characterization process, the tobacco plant stem under test has still presented some damages due to the previous characterization. Moreover, due to the time length of the here-employed characterization process, it is conceivable to assume that the stress applied on the plant may have been less with respect to the previous characterizations, slightly influencing the results in a way that will be further pointed out upon the comparisons reported in Section 3.5.

Transmitting module characterization

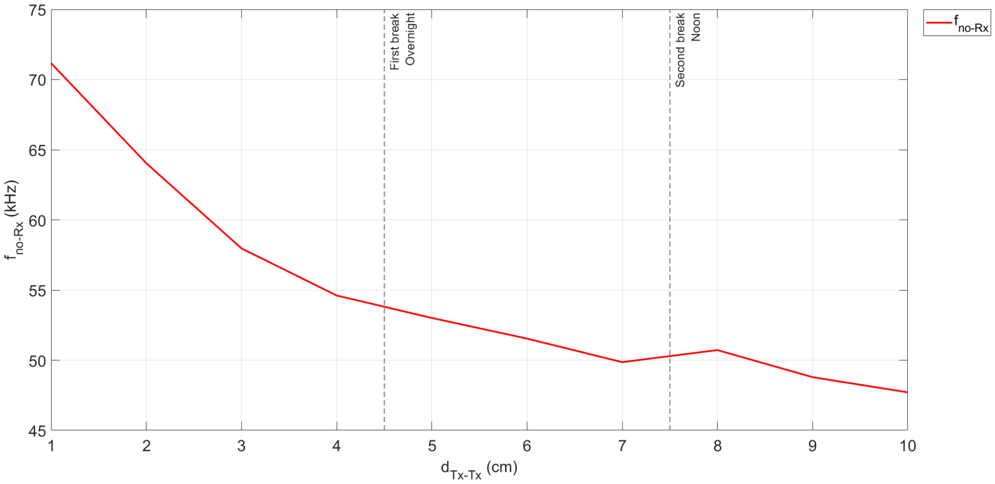

Figure 3.50: Evolution of the transmitting output frequency f_{no-Rx} changing over time the distance d_{Tx-Tx} over the stem length between the two needles related to R_{plant}.

In Figure 3.50, the same expected inversely proportional relationship of the transmitter-related output frequency (neglecting the receiving side in the experimental setup) f_{no-Rx} varying the relative distance d_{Tx-Tx} has been again noticed. Nevertheless, some differences can be detected with respect to both the previous characterizations:

- It can be noticed an overall downshift of the curve with respect to the one described in Section 3.4.4 still remaining above the correspondent curve exposed in Section 3.4.3: this result may be related to the effect of the damages left on the tobacco plant stem by the second characterization process performed quite recently on the same plant supporting the hypothesized relation between the overall plant stem condition and the transmitter-related output frequency aforementioned in Section 3.4.4.

- Focusing on the results just before and immediately after both the two breaks in the characterization process, it is evident how the mid-day break seems to permit a higher recovery rate in relation to the aforementioned assumption, while no significant variations seem to be implied by the first overnight break. This result may be related to the plant circadian rhythm responsible of electrical impedance variations.

In support of the relationship reported in Figure 3.50, it is possible to consider the evolution of the transmitter-related electrical impedance without considering the receiver module in the experimental setup Z_{no-Rx} over the relative distance d_{Tx-Tx} between the two surgical needles associated to R_{plant} plotted in Figure 3.51: it is noticeable the direct relation between the electrical impedance trends Z_{no-Rx} and the transmitter-related output frequency f_{no-Rx} since an increase in the electrical impedance value implies a decrease in the transmitter output frequency according to Equation 3.1. In addition, a further effect of the breaks in the measurement process can be underlined, especially for the electrical impedance curve evaluated at 1 kHz.

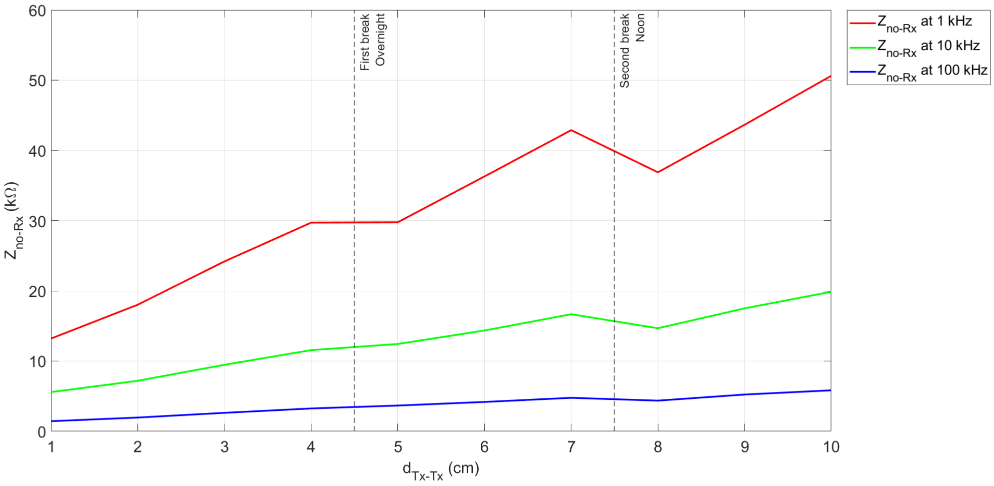

Figure 3.51: Evolution of the transmitter-related electrical impedance Z_{no-Rx} at different frequencies changing over time the distance over the stem length between the transmitter-related two needles d_{Tx-Tx}.

For thoroughness, the relationship between the d_{Tx-Tx}-related electrical impedance Z_{Tx} and both the relative distances d_{Tx-Tx} and d_{Rx-Tx} fixing for each point the other not-varying distance has been depicted in Figure 3.52, Figure 3.53, and Figure 3.54 where d_{Rx-Tx} is the fixed distance for each case for the electrical impedance values respectively retrieved at 1 kHz, 10 kHz, and 100 kHz through the use of the 4294A precision impedance analyzer [52] and in Figure 3.55, Figure 3.56, and Figure 3.57 where instead d_{Tx-Tx} is the fixed distance for each considered case, again exploiting the 4294A precision impedance analyzer [52] to retrieve the electrical impedance values respectively at 1 kHz, 10 kHz, and 100 kHz.

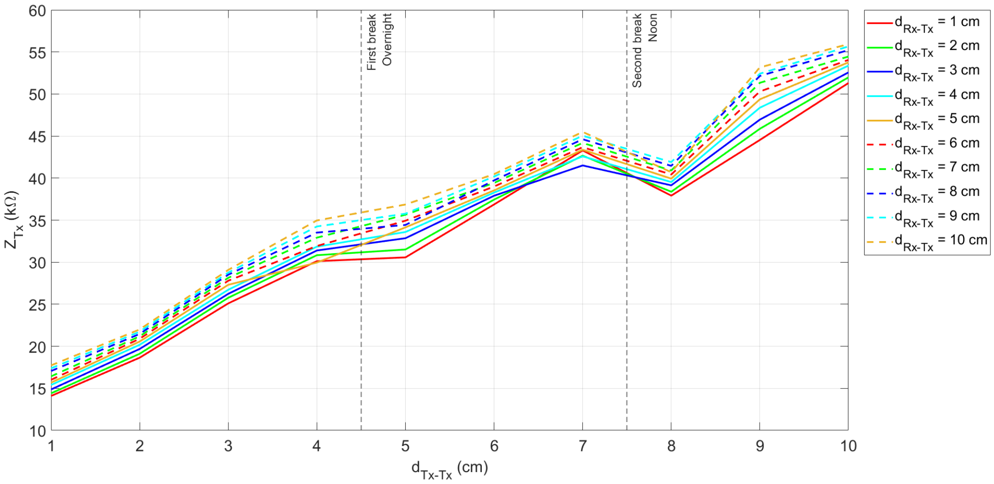

Figure 3.52: Evolution of the d_{Tx-Tx}-related electrical impedance Z_{Tx} evaluated at 1 kHz in relationship with the relative distance d_{Tx-Tx} and fixing for each curve the relative distance over the stem length d_{Rx-Tx}.

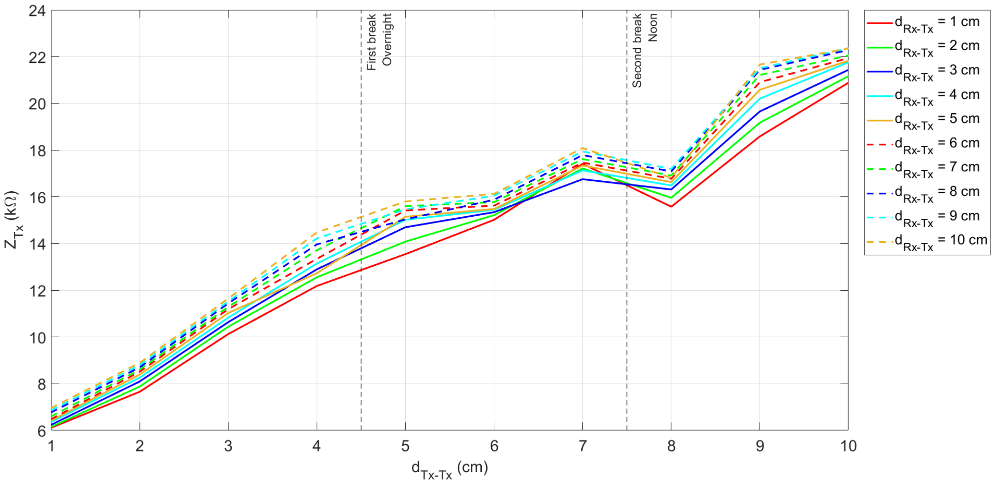

Figure 3.53: Evolution of the d_{Tx-Tx}-related electrical impedance Z_{Tx} evaluated at 10 kHz in relationship with the relative distance d_{Tx-Tx} and fixing for each curve the relative distance over the stem length d_{Rx-Tx}.

From these plots above, it is evident the expected stronger dependence of the electrical impedance Z_{Tx} over the relative distance d_{Tx-Tx} variation with respect to the one over the receiver-related distance d_{Rx-Tx}. In fact, these latter report a relatively constant (slightly increasing) trend, while it can be evidenced a much more increasing linear behavior neglecting the breaks consequences, even coherently to the results depicted in Figure 3.58 and Figure 3.59: a further proof of the

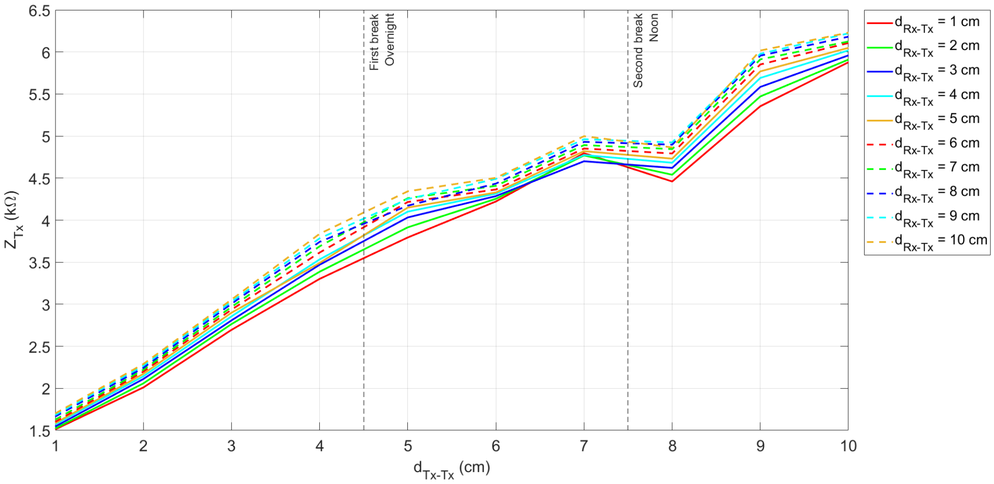

Figure 3.54: Evolution of the d_{Tx-Tx}-related electrical impedance Z_{Tx} evaluated at 100 kHz in relationship with the relative distance d_{Tx-Tx} and fixing for each curve the relative distance over the stem length d_{Rx-Tx}.

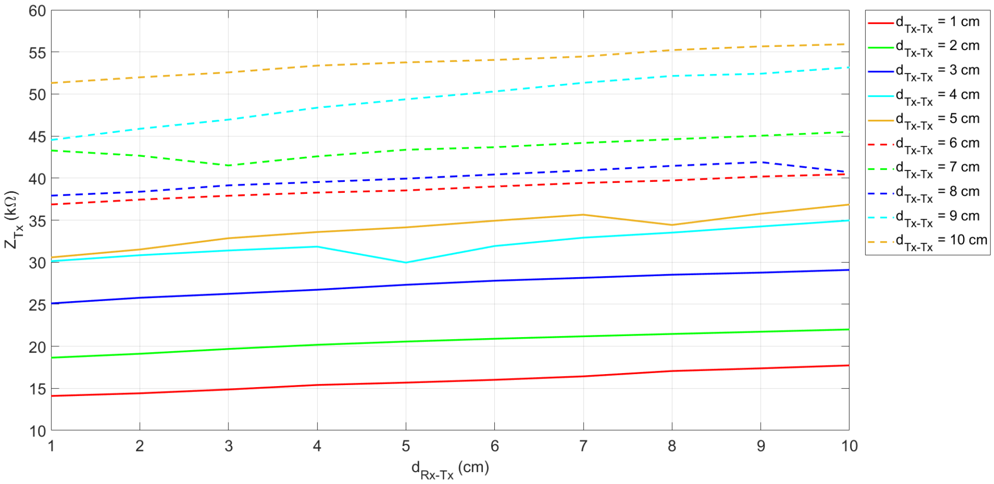

Figure 3.55: Evolution of the d_{Tx-Tx}-related electrical impedance Z_{Tx} evaluated at 1 kHz in relationship with the relative distance d_{Rx-Tx} and fixing for each curve the relative distance over the stem length d_{Tx-Tx}.

just mentioned level of dependency between Z_{Tx} and both d_{Tx-Tx} and d_{Rx-Tx} can be highlighted by inspecting the highly-dependent inverse relationship over d_{Tx-Tx}-related distance variation as opposed to the response to the d_{Rx-Tx} change over the stem length.

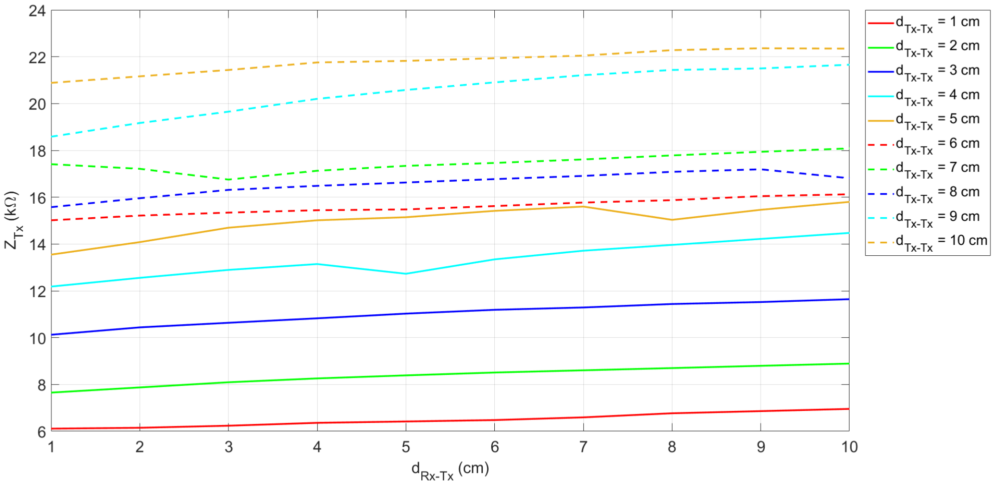

Figure 3.56: Evolution of the d_{Tx-Tx}-related electrical impedance Z_{Tx} evaluated at 10 kHz in relationship with the relative distance d_{Rx-Tx} and fixing for each curve the relative distance over the stem length d_{Tx-Tx}.

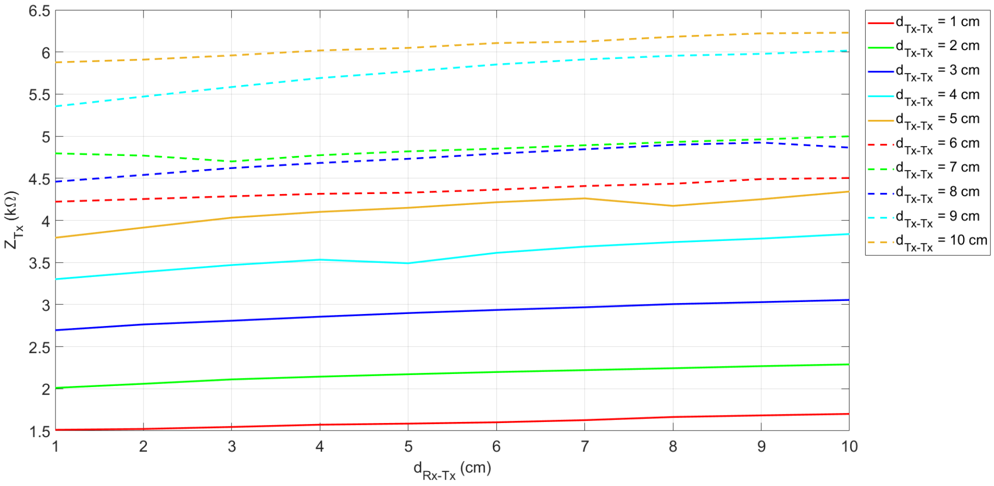

Figure 3.57: Evolution of the d_{Tx-Tx}-related impedance Z_{Tx} evaluated at 100 kHz in relationship with the relative distance d_{Rx-Tx} and fixing for each curve the relative distance over the stem length d_{Tx-Tx}.

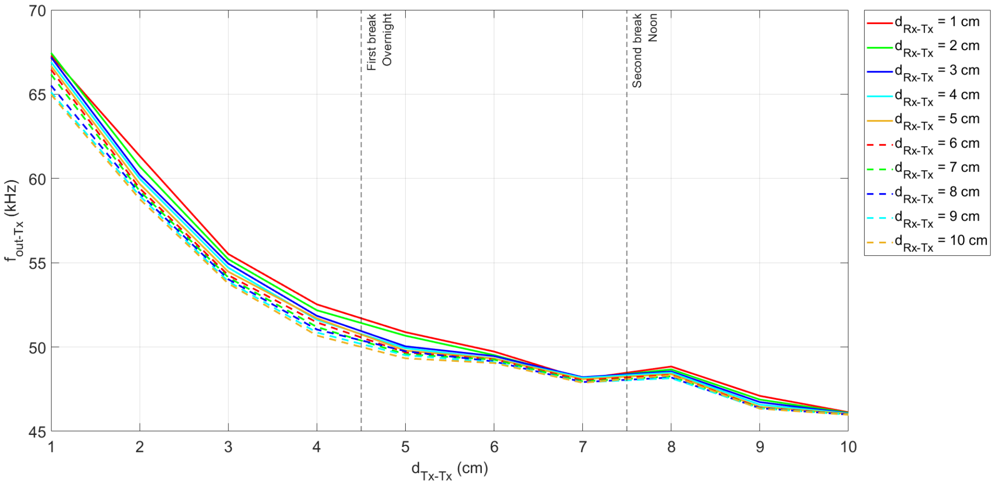

Figure 3.58: Evolution of the output transmitter-related frequency f_{out-Tx} in relationship with the relative distance d_{Rx-Tx} and fixing for each curve the relative distance over the stem length d_{Tx-Tx}.

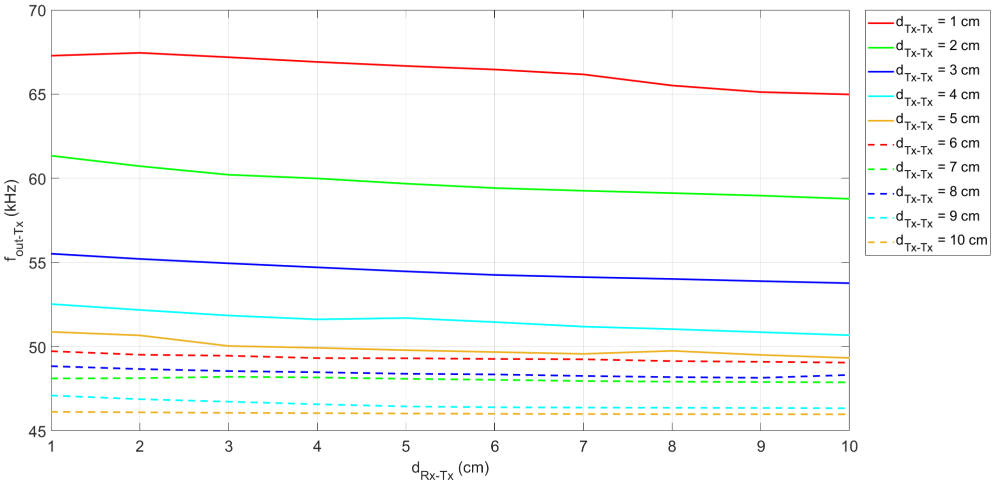

Figure 3.59: Evolution of the output transmitter-related frequency f_{out-Tx} in relationship with the relative distance d_{Tx-Tx} and fixing for each curve the relative distance over the stem length d_{Rx-Tx}.

Complete system characterization

In parallel with the analysis performed in Section 3.4.3 and Section 3.4.4, both the transmitter and the receiver have been considered in this section's characterization taking into account the tobacco plant depicted in Figure 3.37 and Figure 3.38.

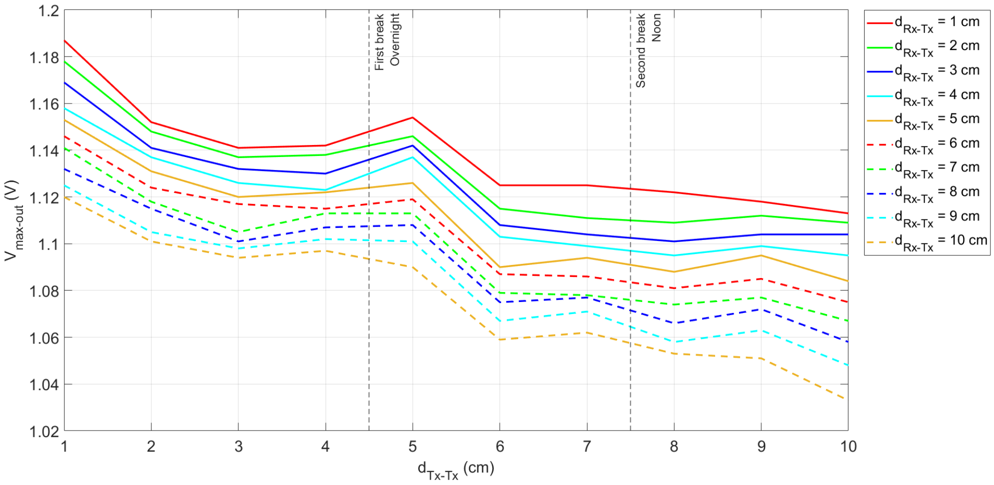

Figure 3.60: Evolution of the peak detector output voltage $V_{max-out}$ changing time for time the relative distance d_{Tx-Tx} and fixing the relative distance d_{Rx-Tx} for each curve.

In contrast to what has been highlighted in Section 3.4.3 and Section 3.4.4, the voltage peak value detected by the peak detector $V_{max-out}$ tends to decrease by incrementing the relative distance d_{Tx-Tx} as depicted in Figure 3.60. Even if this trend appears to be incoherent with respect to the previous characterization results, the curves reported in Figure 3.60 present a much narrower bandwidth (up to half of the previous) on equal terms of relative distance d_{Rx-Tx}, a negative-root-kind trend similar to the one reported in Section 3.4.4 (even if it is reducing instead of growing over the stem length) and result slightly down-drifted: these characteristics can be justified considering the effects of the transmitter output frequency slight downshift underlined in Figure 3.50 and of the attenuation consequences introduced by the relative distance d_{Rx-Tx} as quite balanced for high values of the relative distance d_{Tx-Tx}, while for low values of the relative distance d_{Tx-Tx} the predominant process seems to be the attenuation related to the plant stem (instead of the transmitter output frequency slight downshift which has been assumed to be dominant in the previous characterization correspondent results). Another probable causative factor may be related to the damage and scar tissues inflicted on the plant stem and still not healed enough, placing this third characterization in a hybrid situation between the previous ones.

In parallel with the considerations reported in Section 3.4.4, the slightly stronger dependence of the maximum peak detector output voltage $V_{max-out}$ on the relative distance d_{Tx-Tx} and the less reliance on the relative distance d_{Rx-Tx} have been already verified: in particular, the most significant delta in $V_{max-out}$ values over the variation of d_{Tx-Tx} is around 87 mV identified on the case where d_{Rx-Tx} has been imposed equal to 10 cm, while the most significant delta of the variation of d_{Rx-Tx} is around 80 mV for the d_{Tx-Tx} case correspondent to the 10-cm measurement, therefore implying again a stronger dependence of the maximum peak detector output voltage $V_{max-out}$ on the relative distance between the relative distance d_{Tx-Tx} between the transmitter-related needles and a less reliance on the last transmitter-related needle and the receiver-related needle d_{Rx-Tx} over the stem length, although an even much thinner difference between the peak voltage gap can be noticed making the two deltas quite comparable (87 mV vs 80 mV). Nevertheless, precisely as done earlier in Section 3.4.4, considering the very narrow difference between the two aforementioned deltas and their relatively small values and neglecting the effect of the breaks, it is possible to notice a sort of stabilization of the $V_{max-out}$ curves implying a probable more constant evolution from then on and therefore finding analogies with both of the previous Tx-plant-Rx system characterization and then to confirm again the previously stated stronger dependence of $V_{max-out}$ on the distance d_{Rx-Tx} and thus its less reliability on d_{Tx-Tx} variations, even for this characterization results.

Focusing on the measurements just before and immediately after the breaks, it can be noticed an increase in the peak voltage after the first overnight break and a temporary slowing down of the aforementioned decreasing rate around the second noon break (this latter is also coherent with the negative-root-like behavior previously underlined) introducing probable further evidence of the assumption for which the increase of the peak detector peak voltage (thus of the decrease of the receiver output frequency f_{out-Rx}) may be related to the overall status condition of a healthier and less-stressed plant stem.

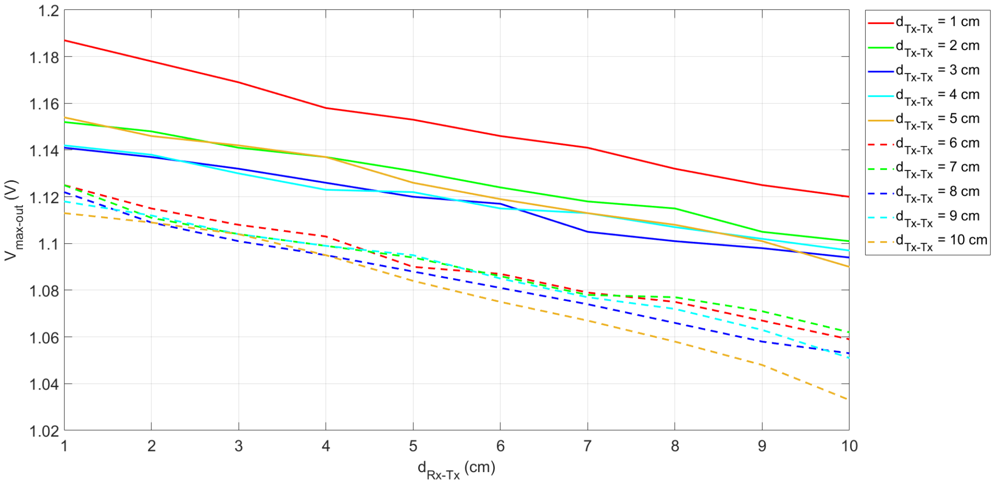

Figure 3.61: Evolution of the peak detector detected output $V_{max-out}$ in relationship with the relative distance d_{Rx-Tx} and fixing for each curve the relative distance over the stem length d_{Tx-Tx}.

As highlighted in the previous characterizations, a negative proportional trend has once more expressed the relationship between the detected output value of $V_{max-out}$ and the relative lapse of distance d_{Rx-Tx} in Figure 3.61, but in this last case, few significant results may be worth to be underlined:

- The enhanced linearity previously pointed out in Section 3.4.4 is still evidenced.
- Due to the previously observed decreasing trend depicted in Figure 3.60, the order of the curves represented in Figure 3.61 results to be inverted considering as key value the relative distance d_{Tx-Tx} with respect to the results of the previous characterizations down-drifting by increasing the relative distance d_{Tx-Tx}: in fact, the curve related to the 1-cm d_{Tx-Tx} case is associated with the highest peak voltage values over the d_{Rx-Tx} length, while in the past characterization the same considered case has been related to the lowest peak voltage values.
- The effect of the breaks can be easily remarked since, in correspondence of the first break, it can be noticed an overlap of the 5-cm d_{Tx-Tx} curve (performed after the first break) on both the 3-cm and 4-cm d_{Tx-Tx} cases (conducted before the first break) especially for small d_{Rx-Tx} values: the same behavior can be observed around the second reported break where it can be noticed an overlap of both the 8-cm and 9-cm d_{Tx-Tx} curves (performed after the second break) on the 7-cm d_{Tx-Tx} case (performed before the second break).

- Even if the order inversion of the curves, the ever-increasing density of the curves in turn to an increase of the d_{Tx-Tx} value is still observed: the probable causes previously hypothesized in Section 3.4.3 and Section 3.4.4 are still considered in this case as causative factors.

All of the aforementioned considerations find a further justification by inspecting Figure 3.62, Figure 3.63, and Figure 3.64 where the decrease of the output detected peak voltage $V_{max-out}$ in turn to an increase of the relative distance d_{Rx-Tx} can be associated to an increase of the receiver-related electrical impedance Z_{Rx} coherently to what has been previously reported in Figure 3.60, while in Figure 3.65, Figure 3.66, and Figure 3.67 can be identified a further explanation for the behavior exposed in Figure 3.28 underlining the rising linear electrical impedance Z_{Rx} trend with respect to the still linear, but decreasing evolution of $V_{max-out}$ by varying the distance d_{Rx-Tx} over the stem length, as expected according to the aforementioned assumptions.

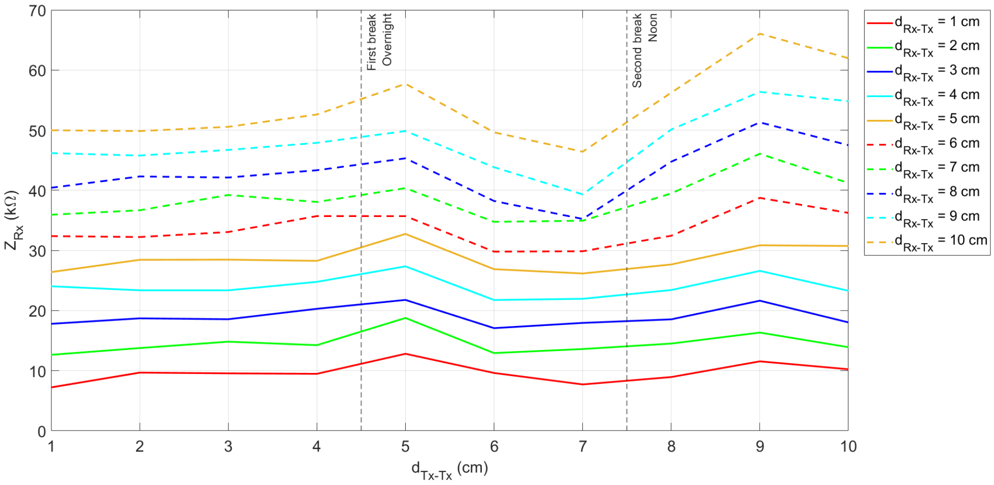

Figure 3.62: Evolution of the d_{Rx-Tx}-related electrical impedance Z_{Rx} evaluated at 1 kHz in relationship with the relative distance d_{Tx-Tx} and fixing for each curve the relative distance over the stem length d_{Rx-Tx}.

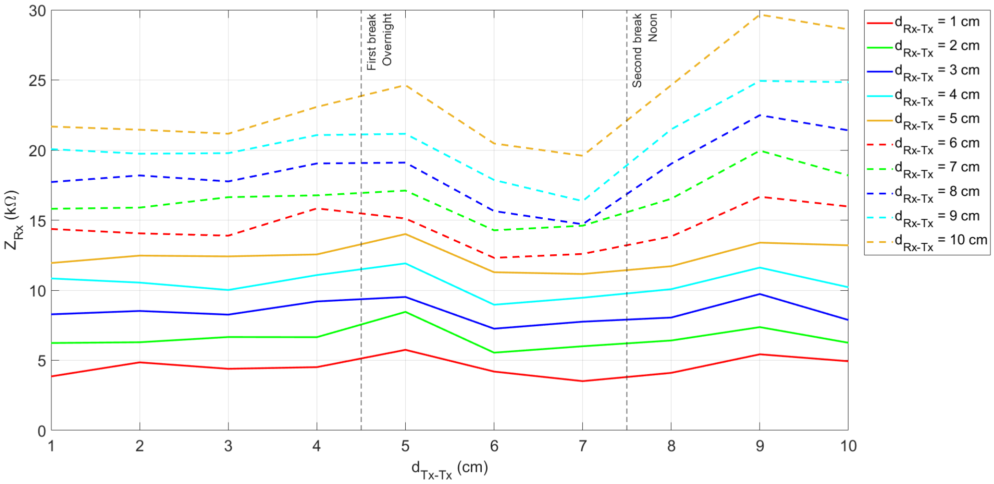

Figure 3.63: Evolution of the d_{Rx-Tx}-related electrical impedance Z_{Rx} evaluated at 10 kHz in relationship with the relative distance d_{Tx-Tx} and fixing for each curve the relative distance over the stem length d_{Rx-Tx}.

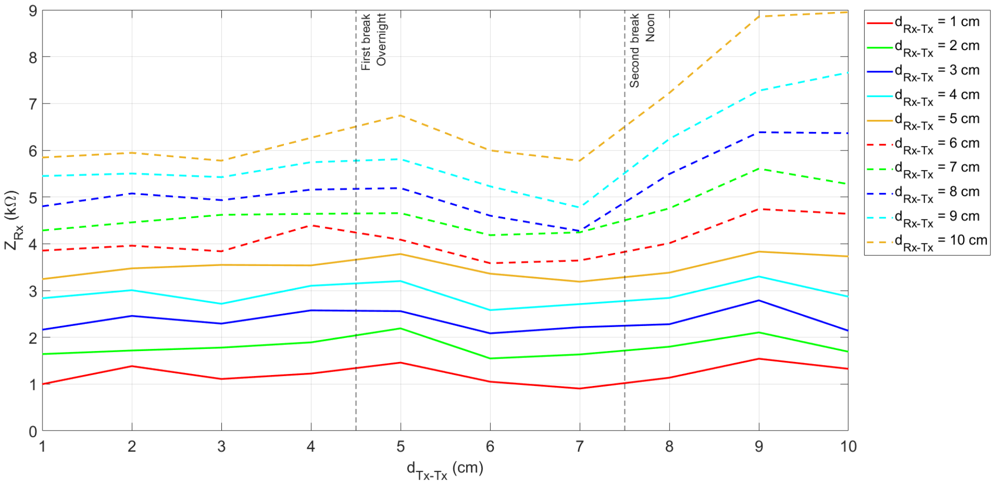

Figure 3.64: Evolution of the d_{Rx-Tx}-related electrical impedance Z_{Rx} evaluated at 100 kHz in relationship with the relative distance d_{Tx-Tx} and fixing for each curve the relative distance over the stem length d_{Rx-Tx}.

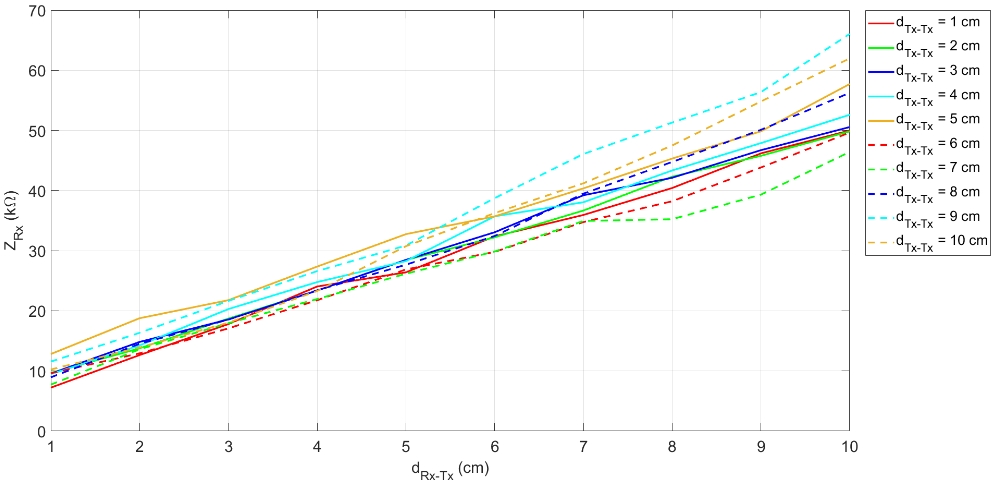

Figure 3.65: Evolution of the d_{Rx-Tx}-related electrical impedance Z_{Rx} evaluated at 1 kHz in relationship with the relative distance d_{Rx-Tx} and fixing for each curve the relative distance over the stem length d_{Tx-Tx}.

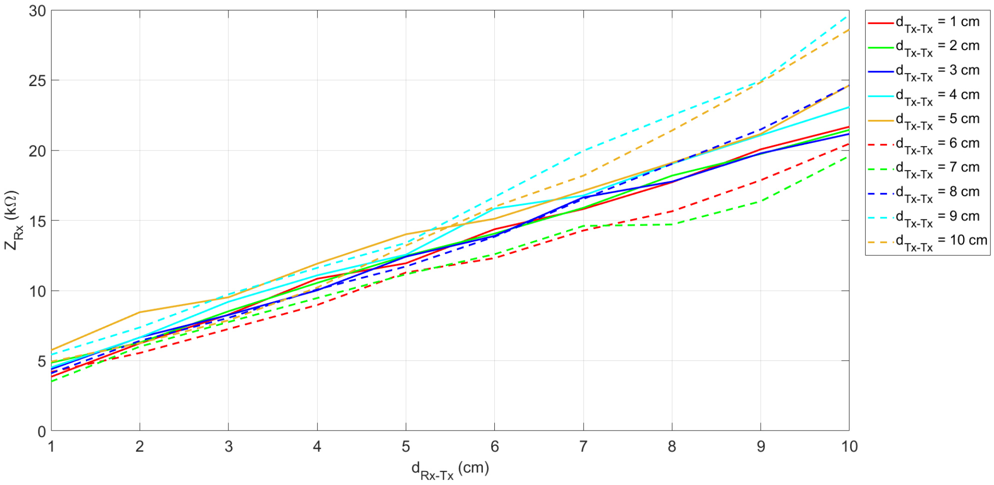

Figure 3.66: Evolution of the d_{Rx-Tx}-related electrical impedance Z_{Rx} evaluated at 10 kHz in relationship with the relative distance d_{Rx-Tx} and fixing for each curve the relative distance over the stem length d_{Tx-Tx}.

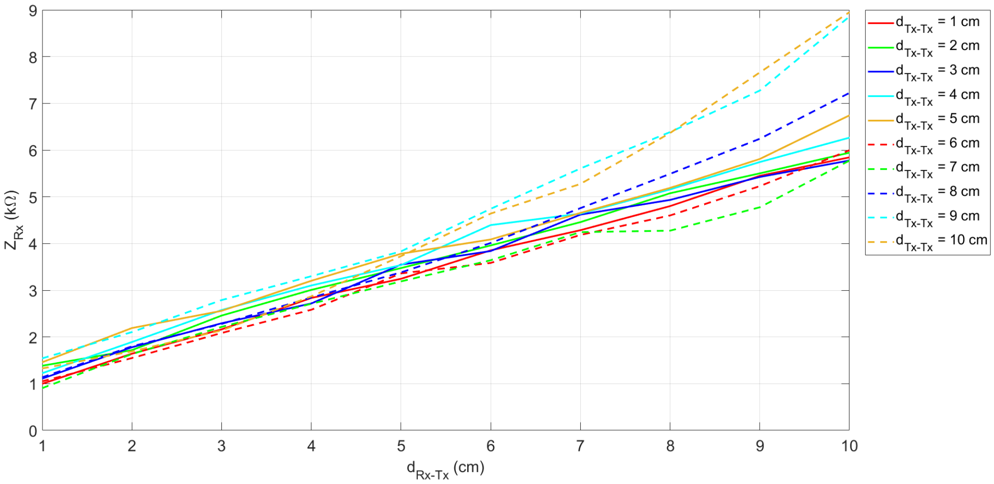

Figure 3.67: Evolution of the d_{Rx-Tx}-related electrical impedance Z_{Rx} evaluated at 100 kHz in relationship with the relative distance d_{Rx-Tx} and fixing for each curve the relative distance over the stem length d_{Tx-Tx}.

Analyzing more in detail the receiver-related electrical impedance Z_{Rx} curves, it results furthermore evident a stronger dependence of the electrical impedance value Z_{Rx} in turn to d_{Rx-Tx} variations with respect to the one in response to d_{Tx-Tx} changes: in fact, the electrical impedance values range over d_{Rx-Tx} results much wider than the other one related to d_{Tx-Tx} variations where the curves seem to be quite constant over d_{Tx-Tx} changes, coherently with the assumptions made in the previous characterizations.

For the sake of completeness, to explain the trend of the output peak voltage $V_{max-out}$ in terms of both the relative distances d_{Tx-Tx} and d_{Rx-Tx}, Figure 3.68 has been produced evidencing an even-more uniform appearance (albeit the values in correspondence of the breaks) due to the evaluations previously explained.

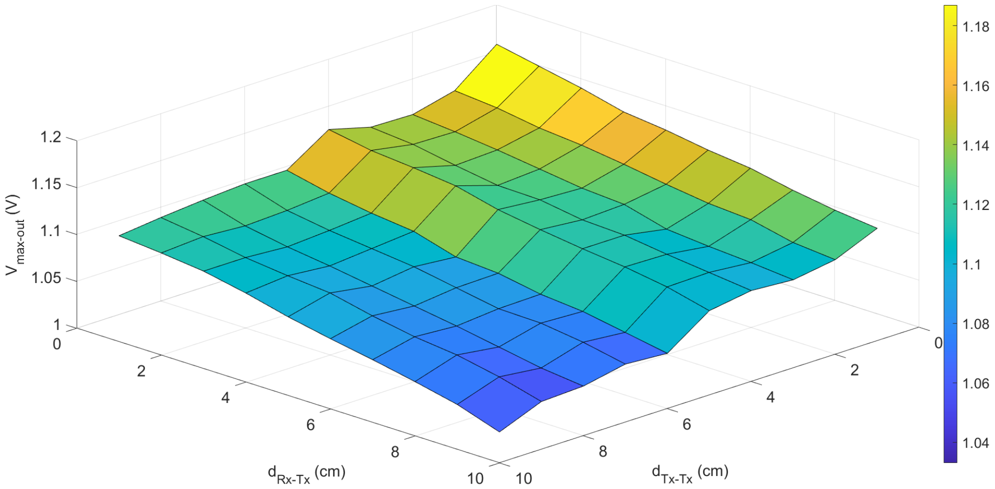

Figure 3.68: Graphical representation of the output peak voltage $V_{max-out}$ varying both the relative distances d_{Tx-Tx} and d_{Rx-Tx}.

The negative-slope linear relationship between the output frequency of the entire receiver system f_{out-Rx} and the detected maximum output voltage $V_{max-out}$ has been furthermore verified in Figure 3.69: this dependency is coherent with the input-output characteristic of the LMC555-based voltage-controlled oscillator [39]. Nevertheless, the inversion in the order of the curves underlined describing the Figure 3.61 is strictly related to the curve position associated to each d_{Tx-Tx} value in Figure 3.69. At the same time, other considerations made in the previous characterization are still evidenced.

The same considerations exposed in the previous characterizations (negative-slope linear relation and up-shifting phenomenon due to the d_{Rx-Tx}-related attenuation) have been further underlined for what concerns the receiver-specific output curves reported in Figure 3.70 noticing an overall up-drift of the results, coherently to the aforementioned assumption for which higher transmitter output frequency and lower receiver output frequency f_{out-Rx} are related to a healthier plant stem condition.

Coherently to the curves reported in Figure 3.60 and Figure 3.61, the relationship respectively depicted in Figure 3.71 and Figure 3.72 can be expected exploiting the inversely proportional linear relation associated to the input-output characteristic of the LMC555-based voltage-controlled oscillator [39] previously highlighted in Section 3.4.2.

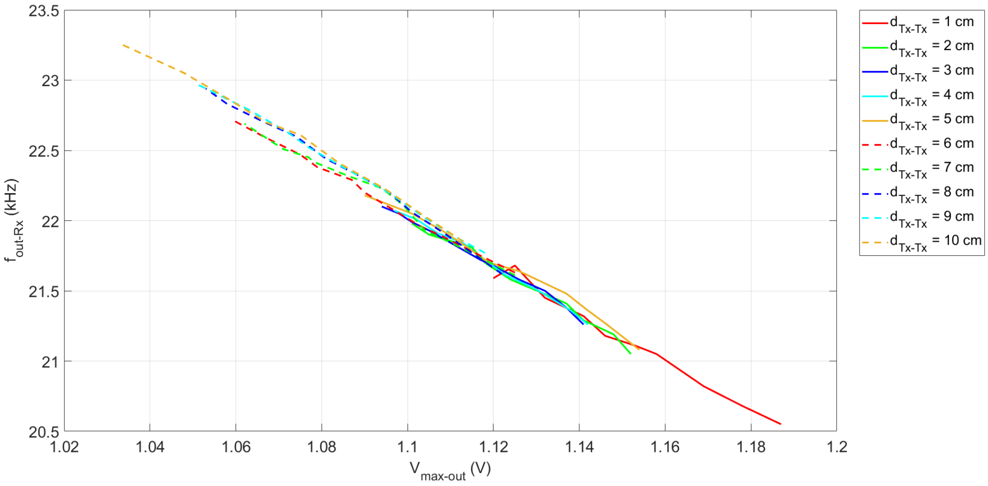

Figure 3.69: Relationship between the output frequency of the receiving module f_{out-Rx} changing the peak detector output $V_{max-out}$ for each value of the relative distance d_{Tx-Tx}.

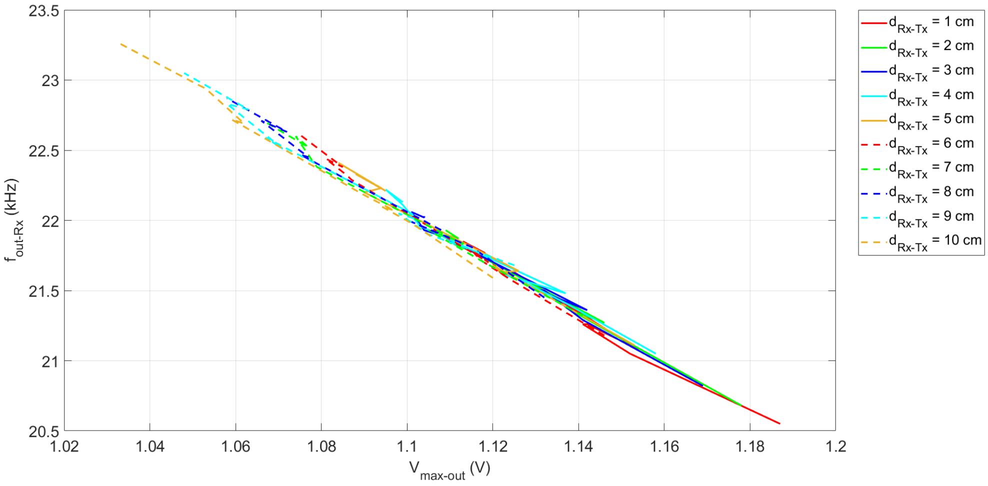

Figure 3.70: Relationship between the receiving-module output frequency f_{out-Rx} varying the peak detector output $V_{max-out}$ for each value of the relative distance over the stem length d_{Rx-Tx}.

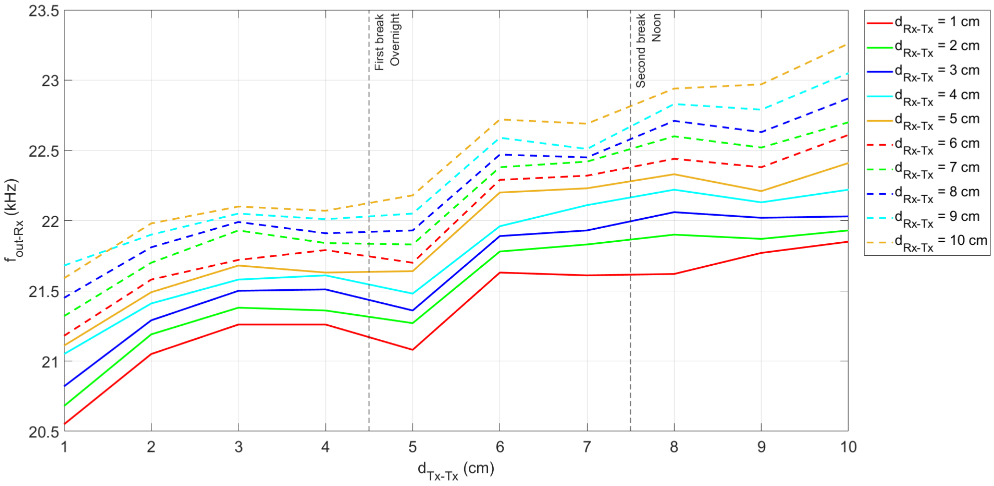

Figure 3.71: Plot of the receiver's output frequency f_{out-Rx} varying the distance d_{Tx-Tx} and fixing the relative length d_{Rx-Tx} from time to time on the second plant.

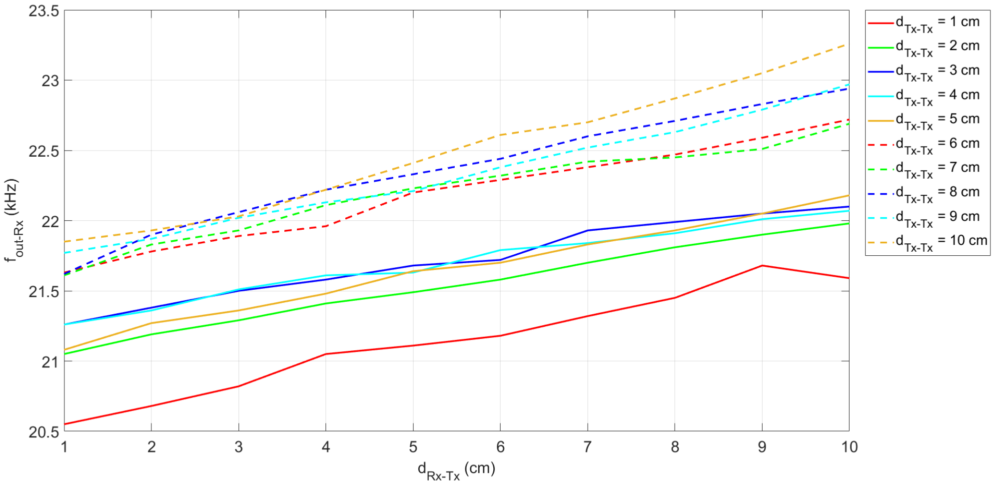

Figure 3.72: Plot of the receiver's output frequency f_{out-Rx} varying the relative distance d_{Rx-Tx} and fixing the relative length d_{Tx-Tx} from time to time on the second plant.

For thoroughness, in order to represent graphically the evolution of the output frequency of the receiving module f_{out-Rx} in terms of the relative distances d_{Tx-Tx} and d_{Rx-Tx} over the plant stem length, Figure 3.73 has been depicted.

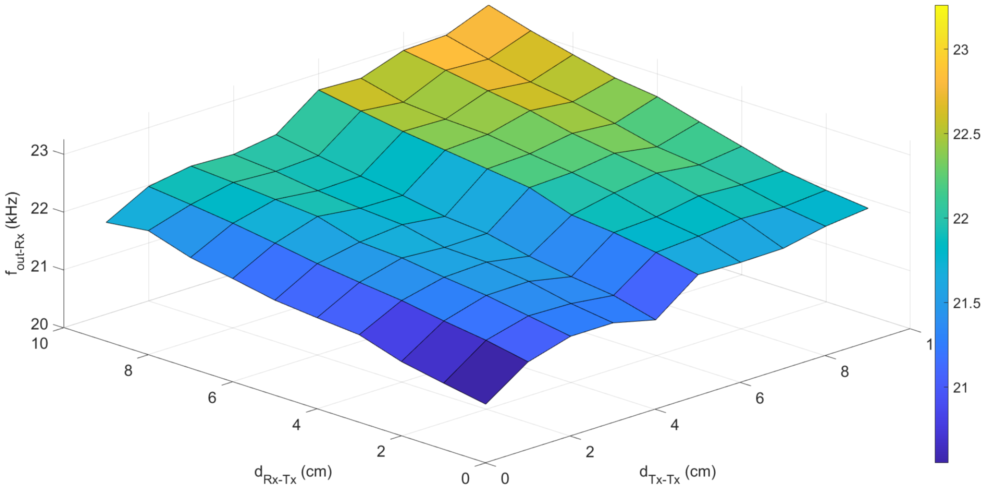

Figure 3.73: Plot of the output frequency of the receiver f_{out-Rx} varying both the relative distances d_{Tx-Tx} and d_{Rx-Tx}.

Focusing on the relation between the receiver output frequency f_{out-Rx} and the receiver-related electrical impedance Z_{Rx}, Figure 3.74, Figure 3.75 and Figure 3.76 have been plotted: it is noticeable an overall rising trend of d_{Rx-Tx} curves as expected since the electrical impedance value Z_{Rx} increases in turn to a d_{Rx-Tx} rise. Moreover, the higher the Z_{Rx} value, the lower the detected maximum voltage by the peak detector $V_{max-out}$, thus implying a higher output frequency f_{Rx}.

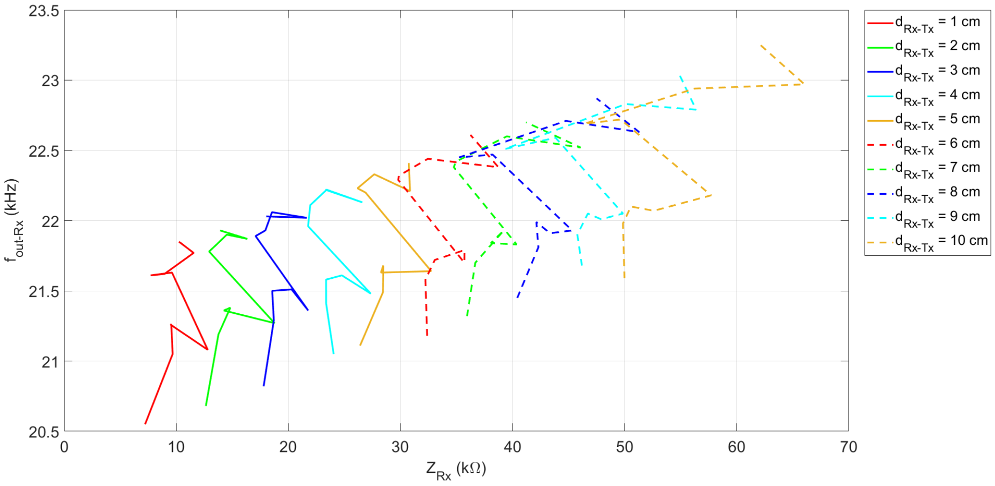

Figure 3.74: Plot of the receiver's output frequency f_{out-Rx} over receiver-related electrical impedance Z_{Rx} value at 1 kHz fixing the relative length d_{Rx-Tx} from time to time on the second plant.

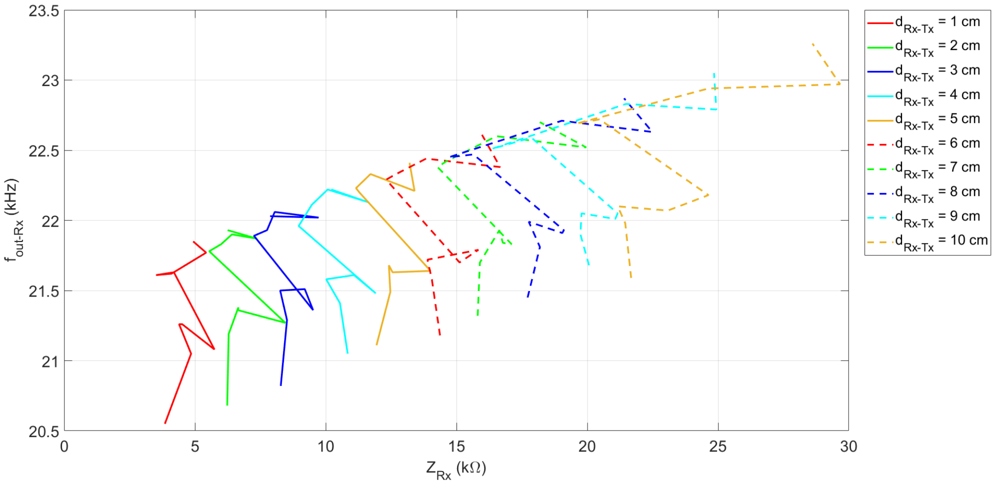

Figure 3.75: Plot of the receiver's output frequency f_{out-Rx} over receiver-related impedance Z_{Rx} value at 10 kHz fixing the relative length d_{Rx-Tx} from time to time on the second plant.

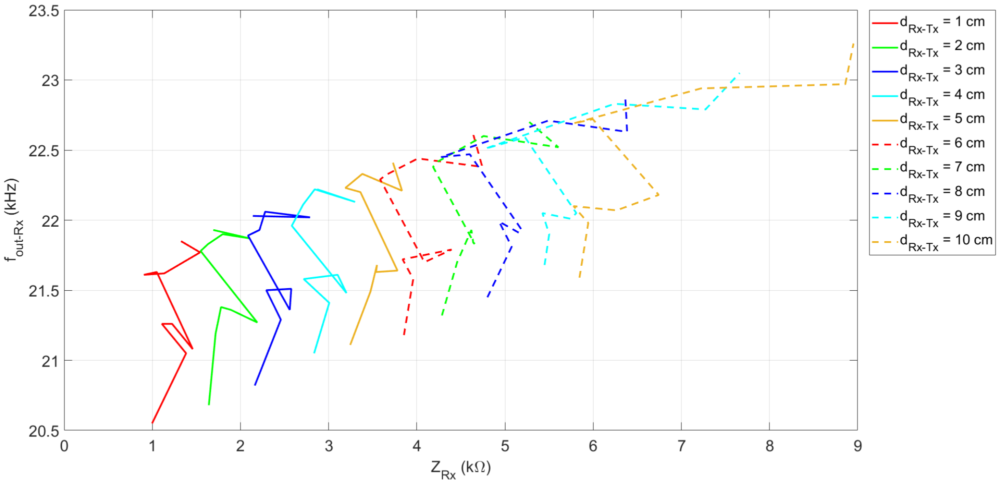

Figure 3.76: Plot of the receiver's output frequency f_{out-Rx} over receiver-related electrical impedance Z_{Rx} value at 100 kHz fixing the relative length d_{Rx-Tx} from time to time on the second plant.

For the sake of completeness, another rising (albeit quite linear in this case) trend has been pointed out in Figure 3.77, Figure 3.78 and Figure 3.79: however, the position of each d_{Tx-Tx} curve in the just-mentioned plots are probably influenced by the breaks since they are not locally in ascending order in terms of d_{Tx-Tx} values (even if globally on the rise in turn of d_{Tx-Tx} increase).

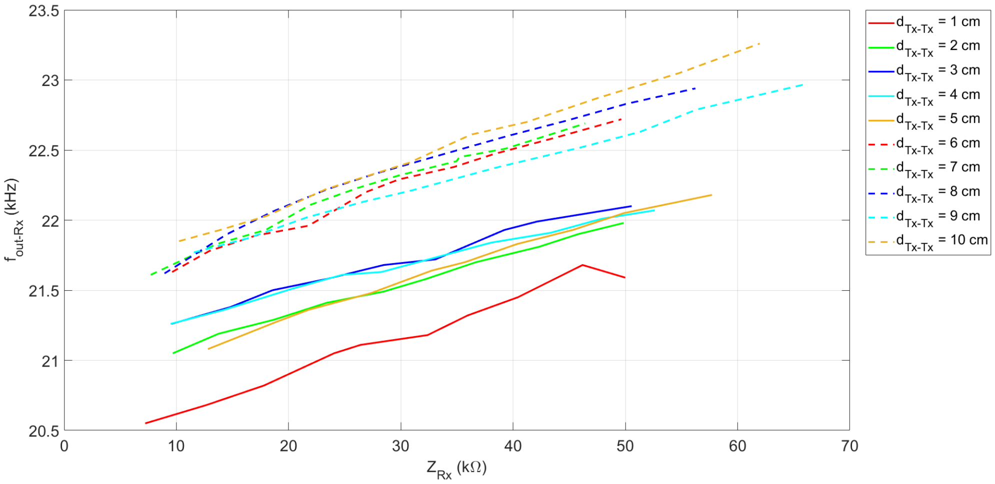

Figure 3.77: Plot of the receiver's output frequency f_{out-Rx} over receiver-related electrical impedance Z_{Rx} value at 1 kHz fixing the relative length d_{Tx-Tx} from time to time on the second plant.

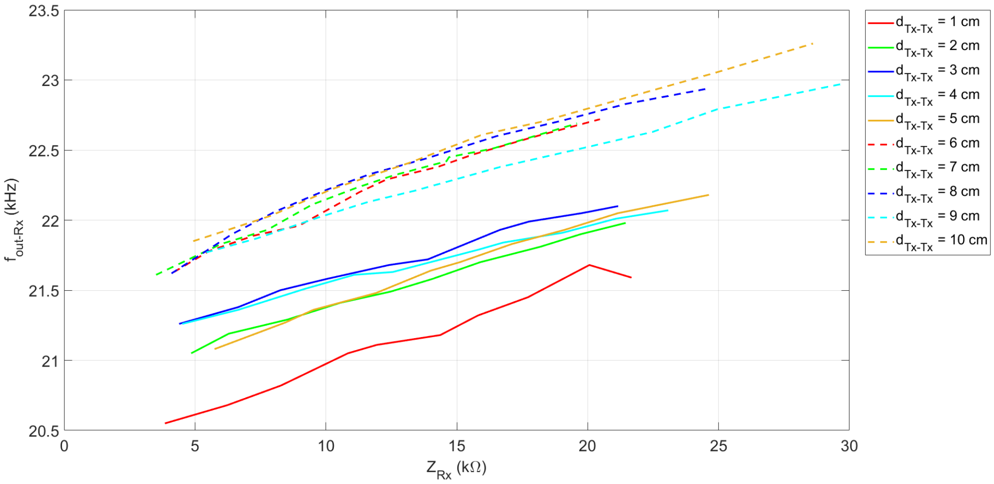

Figure 3.78: Plot of the receiver's output frequency f_{out-Rx} over receiver-related electrical impedance Z_{Rx} value at 10 kHz fixing the relative length d_{Tx-Tx} from time to time on the second plant.

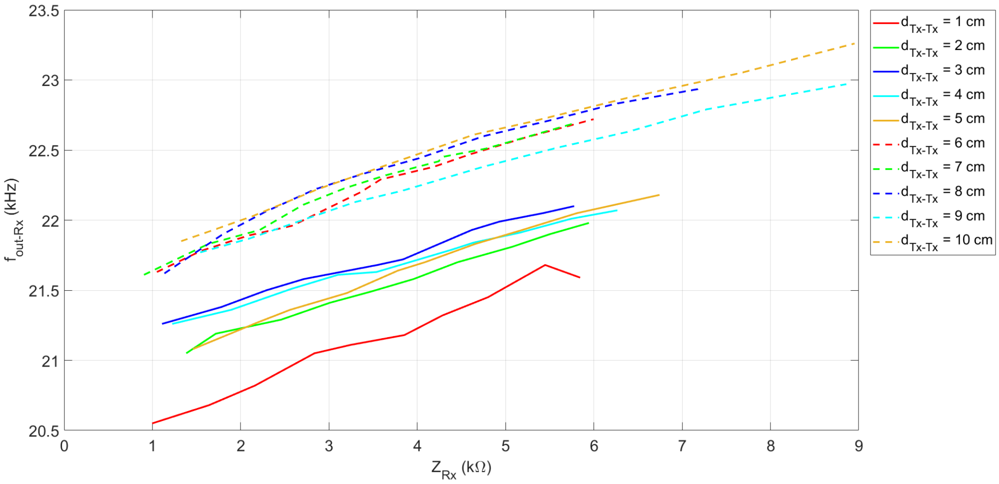

Figure 3.79: Plot of the receiver's output frequency f_{out-Rx} over receiver-related impedance Z_{Rx} value at 100 kHz fixing the relative length d_{Tx-Tx} from time to time on the second plant.

For the sake of completeness, in Figure 3.80 and Figure 3.81 the relation between the transmitter-related output frequency f_{out-Tx} and the receiver-related output frequency f_{out-Rx} respectively in terms of the relative distances d_{Rx-Tx} and d_{Tx-Tx}: it can be evidenced a behavior consistent with the aforementioned results for what concerns the evolution of the output frequencies f_{out-Rx} and f_{out-Tx} in response to relative distances variations d_{Rx-Tx} and d_{Tx-Tx}.

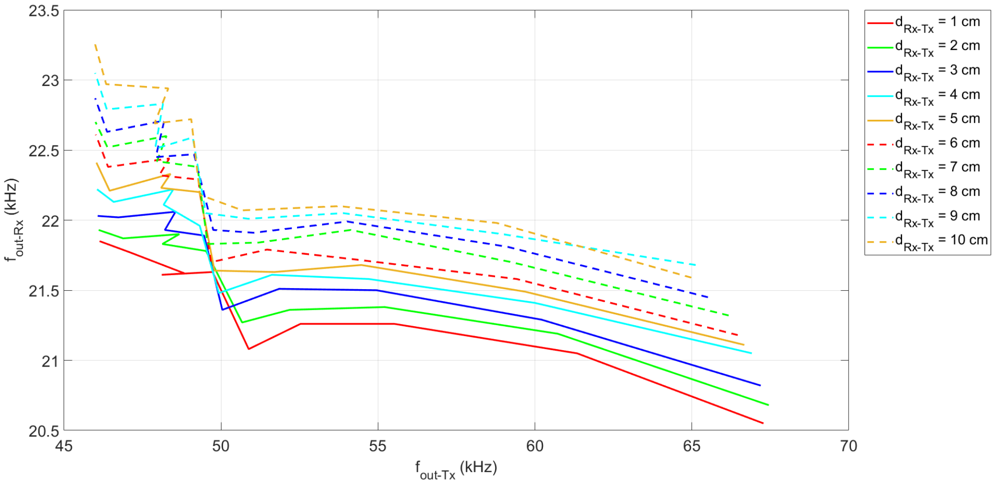

Figure 3.80: Relationship between the transmitter-related output frequency f_{out-Tx} and the receiver-related output frequency f_{out-Rx} varying the relative distance d_{Rx-Tx} over the plant stem length.

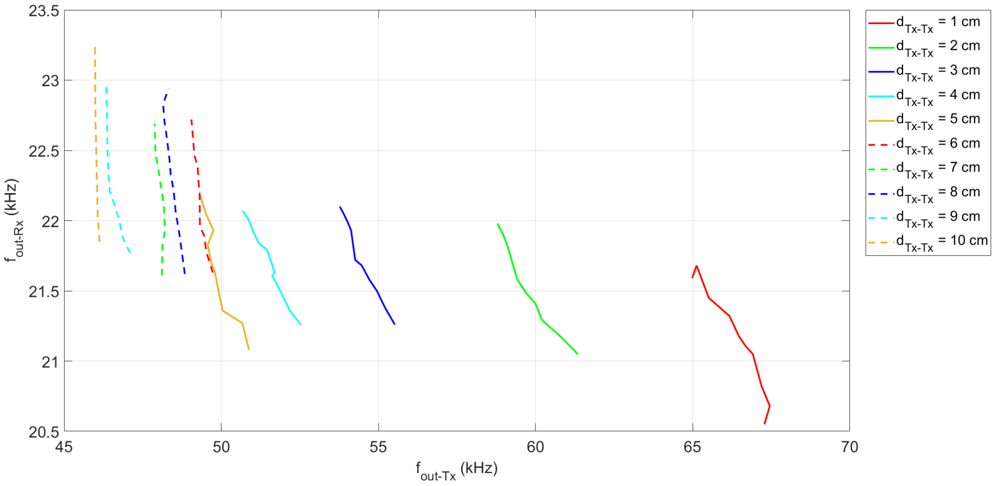

Figure 3.81: Relationship between the transmitter-related output frequency f_{out-Tx} and the receiver-related output frequency f_{out-Rx} varying the relative distance d_{Tx-Tx} over the plant stem length.

In parallel to what has been done in the previous characterizations, the attenuation applied to the receiver input signal has been analyzed, supporting the previously reported third characterization results: in Figure 3.82 and Figure 3.83 it has been considered in relation with the receiver-related output frequency f_{out-Rx}, while in Figure 3.84 and Figure 3.85 it has been studied in connection with the transmitter-related output frequency f_{out-Tx} in turn to d_{Rx-Tx} and d_{Tx-Tx} variations.

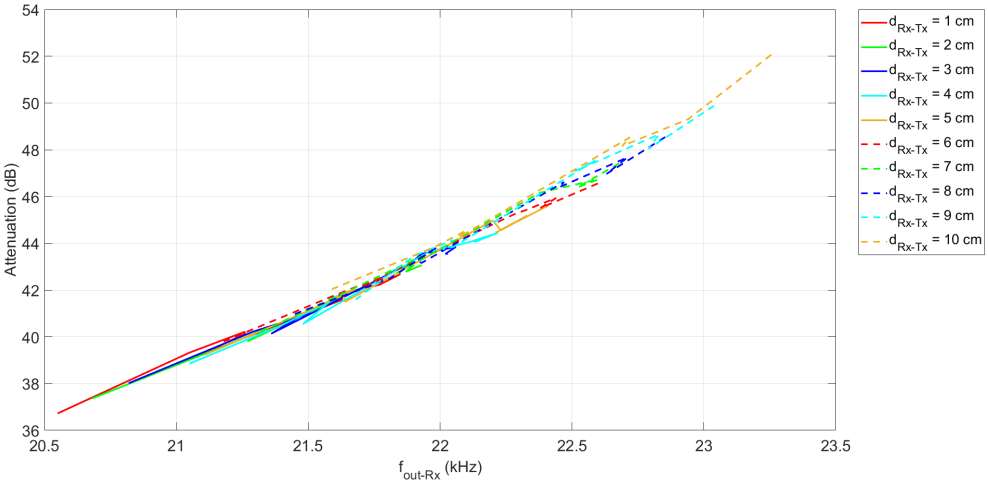

Figure 3.82: Trend of the attenuation the receiver-related input signal is subjected to in terms of the output frequency of the receiver f_{out-Rx} varying the relative distance d_{Rx-Tx} over the plant stem length.

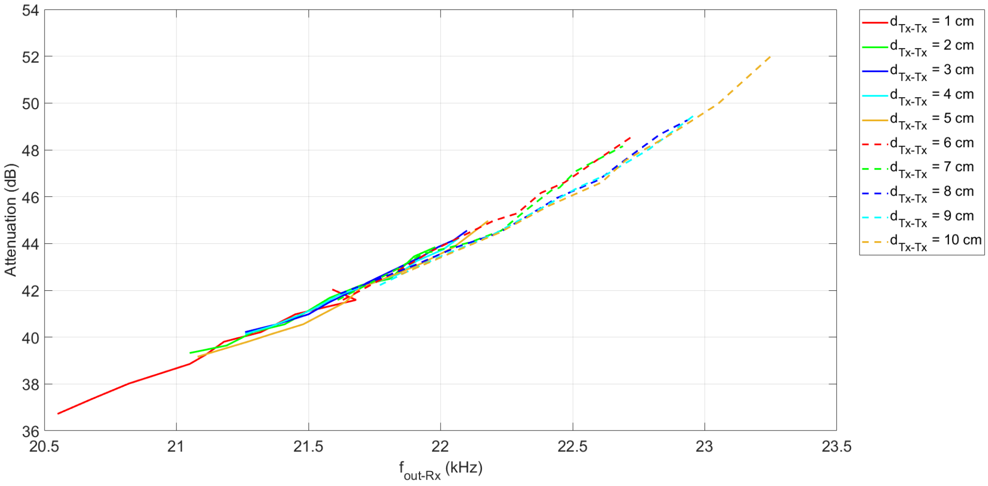

Figure 3.83: Trend of the attenuation the receiver-related input signal is subjected to in terms of the output frequency of the receiver f_{out-Rx} varying the relative distance d_{Tx-Tx} over the plant stem length.

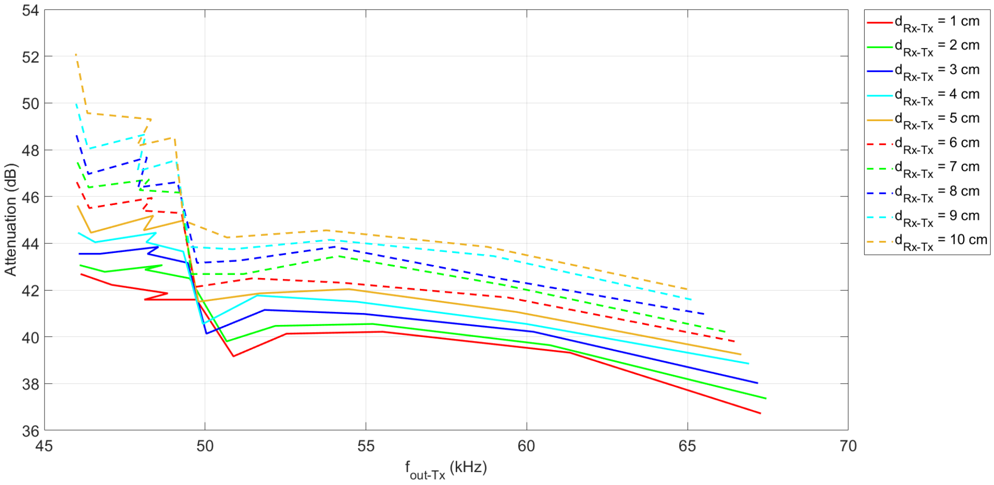

Figure 3.84: Trend of the attenuation the receiver-related input signal is subjected to in terms of the output frequency of the transmitter f_{out-Tx} varying the relative distance d_{Rx-Tx} over the plant stem length.

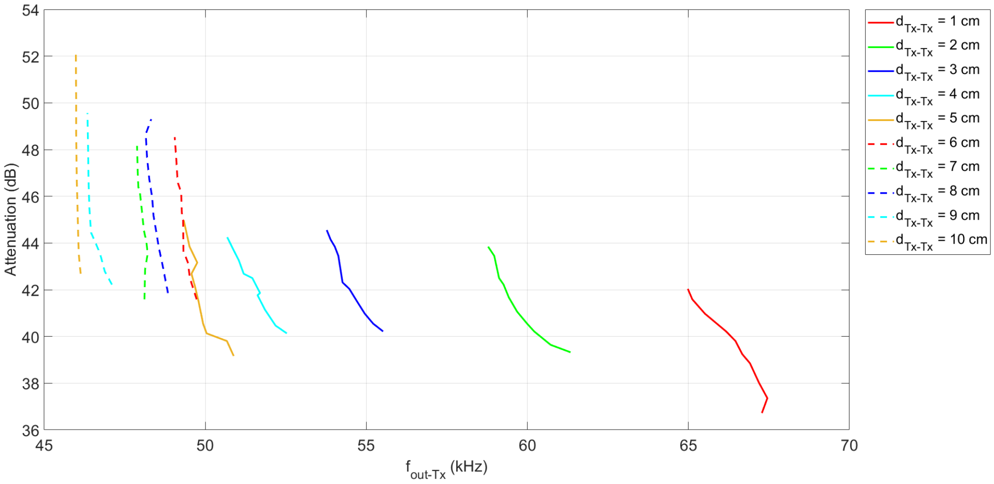

Figure 3.85: Trend of the attenuation the receiver-related input signal is subjected to in terms of the output frequency of the transmitter f_{out-Tx} varying the relative distance d_{Tx-Tx} over the plant stem length.

In addition, the attenuation seen by the input signal upstream the receiver moving through the plant stem has been put in relation with the electrical impedance values registered by using the 4294A precision impedance analyzer [52] during this third characterization and the results in response to relative distances d_{Rx-Tx} and d_{Tx-Tx} variations over the stem length have been depicted in Figure 3.86, Figure 3.87, Figure 3.88, Figure 3.89, Figure 3.90, and Figure 3.91 where the electrical impedance considered is the receiver-specific one Z_{Rx}, while in Figure 3.92, Figure 3.93, Figure 3.94, Figure 3.95, Figure 3.96, and Figure 3.97 where instead the electrical impedance considered is the transmitter-specific one Z_{Tx}: as expected, these curves represent a further justification for the previously done in this third section discussion.

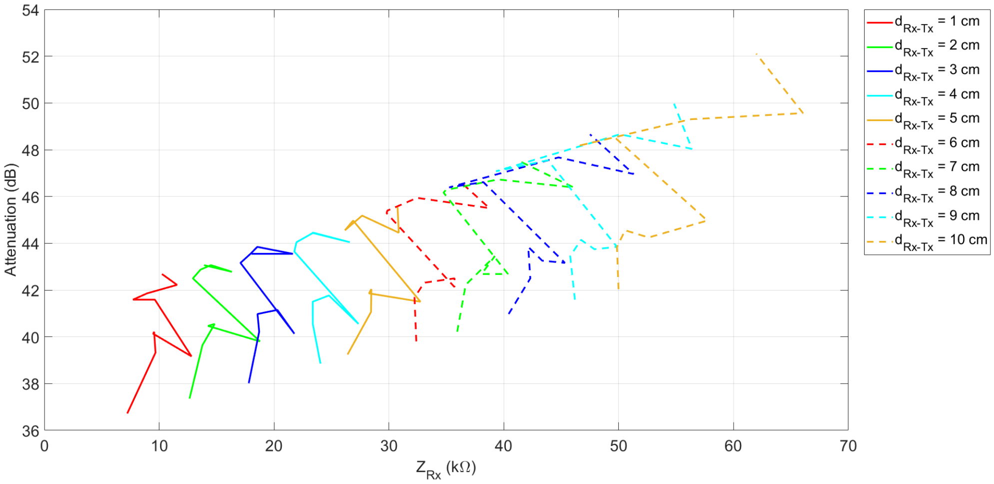

Figure 3.86: Evolution of the attenuation the receiver-related input signal is subjected to in relation with the receiver-related electrical impedance Z_{Rx} evaluated at 1 kHz and varying the relative distance d_{Rx-Tx} over the plant stem length.

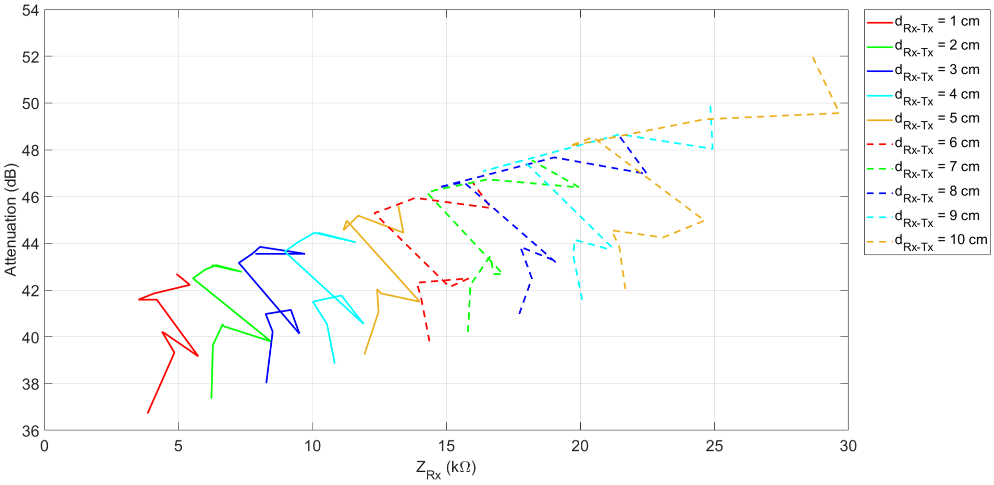

Figure 3.87: Evolution of the attenuation the receiver-related input signal is subjected to in relation with the receiver-related electrical impedance Z_{Rx} evaluated at 10 kHz and varying the relative distance d_{Rx-Tx} over the plant stem length.

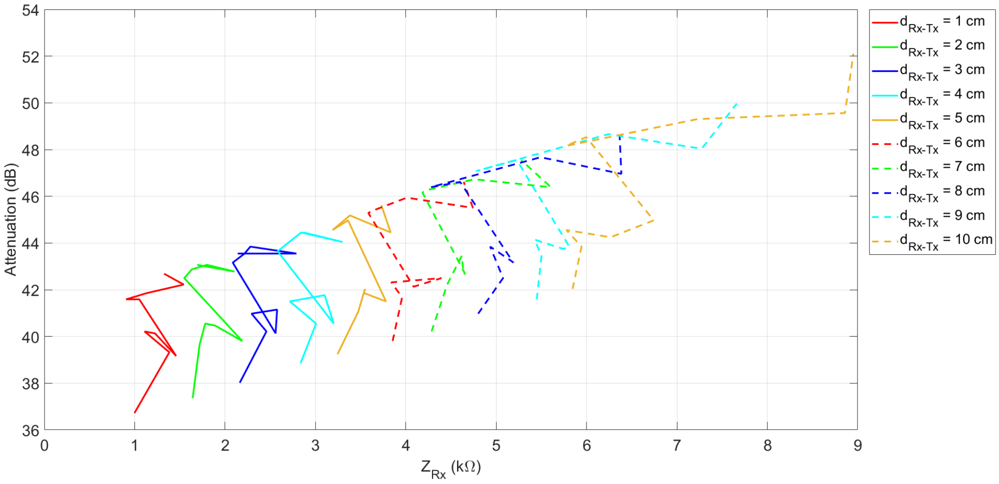

Figure 3.88: Evolution of the attenuation the receiver-related input signal is subjected to in relation with the receiver-related electrical impedance Z_{Rx} evaluated at 100 kHz and varying the relative distance d_{Rx-Tx} over the plant stem length.

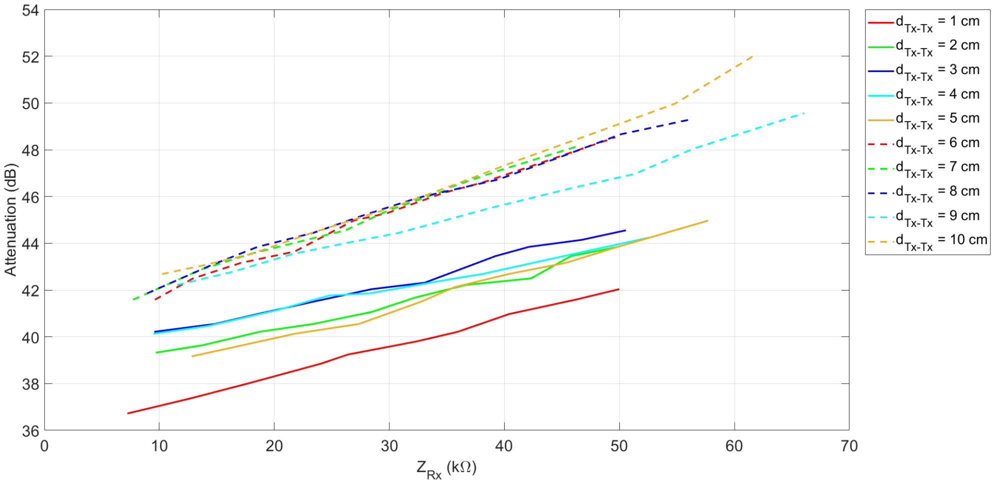

Figure 3.89: Evolution of the attenuation the receiver-related input signal is subjected to in relation with the receiver-related electrical impedance Z_{Rx} evaluated at 1 kHz and varying the relative distance d_{Tx-Tx} over the plant stem length.

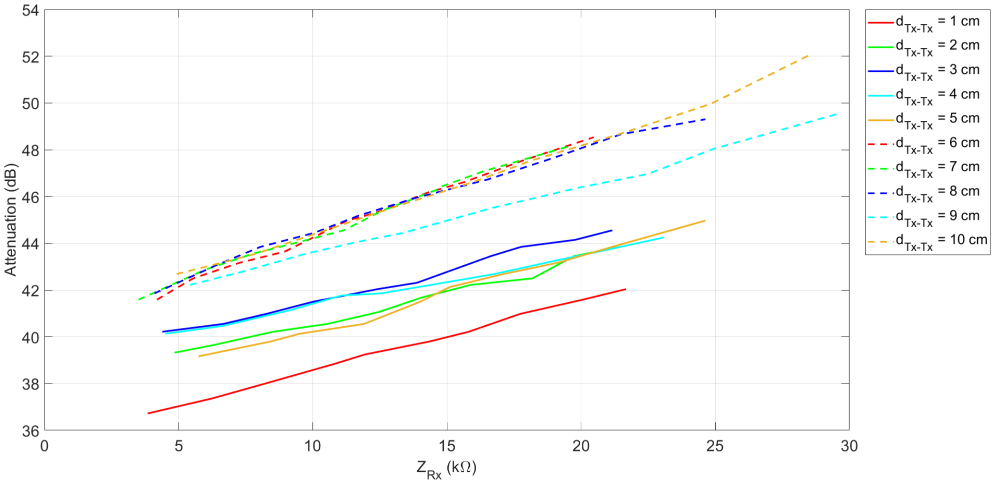

Figure 3.90: Evolution of the attenuation the receiver-related input signal is subjected to in relation with the receiver-related electrical impedance Z_{Rx} evaluated at 10 kHz and varying the relative distance d_{Tx-Tx} over the plant stem length.

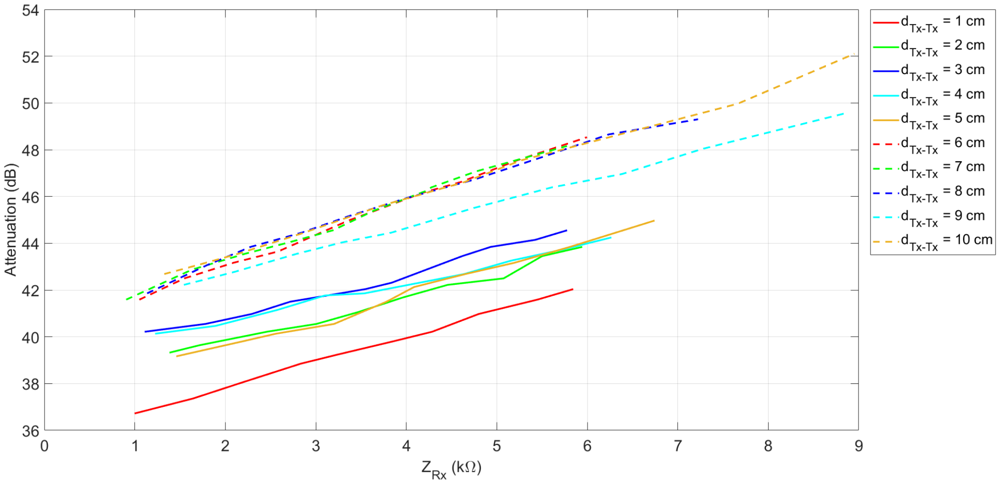

Figure 3.91: Evolution of the attenuation the receiver-related input signal is subjected to in relation with the receiver-related impedance Z_{Rx} evaluated at 100 kHz and varying the relative distance d_{Tx-Tx} over the plant stem length.

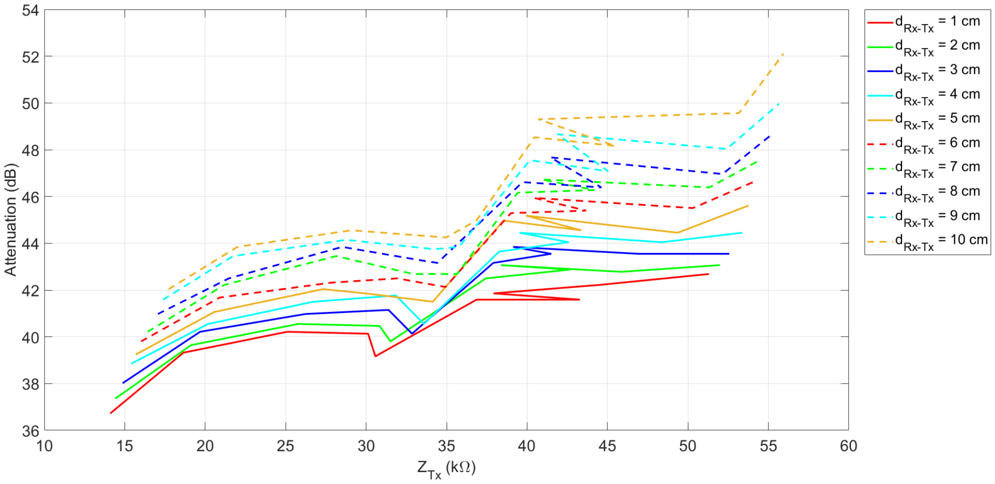

Figure 3.92: Evolution of the attenuation the receiver-related input signal is subjected to in relation with the transmitter-related electrical impedance Z_{Tx} evaluated at 1 kHz and varying the relative distance d_{Rx-Tx} over the plant stem length.

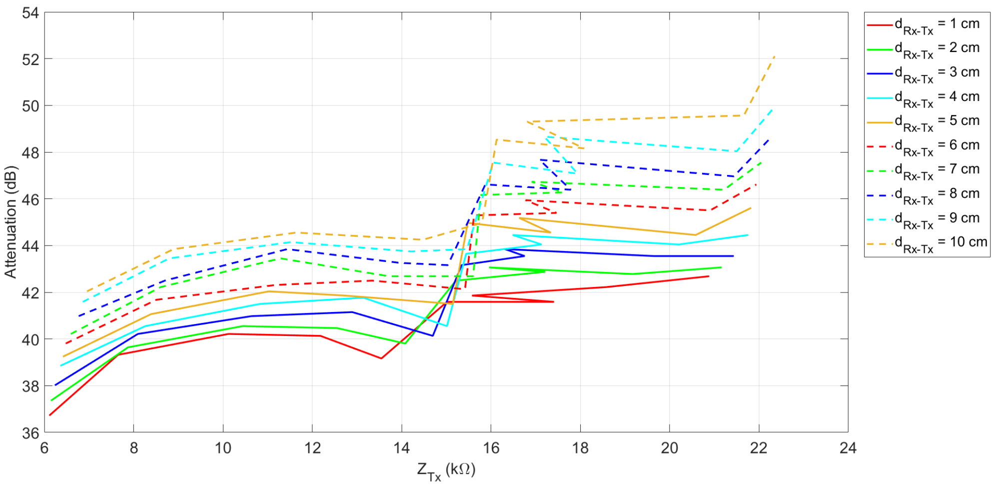

Figure 3.93: Evolution of the attenuation the receiver-related input signal is subjected to in relation with the transmitter-related impedance Z_{Tx} evaluated at 10 kHz and varying the relative distance d_{Rx-Tx} over the plant stem length.

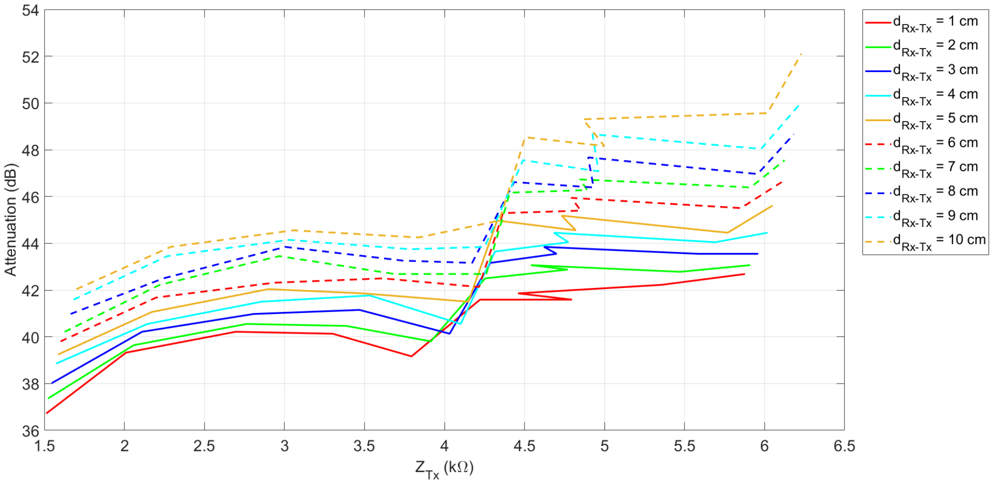

Figure 3.94: Evolution of the attenuation the receiver-related input signal is subjected to in relation with the transmitter-related electrical impedance Z_{Tx} evaluated at 100 kHz and varying the relative distance d_{Rx-Tx} over the plant stem length.

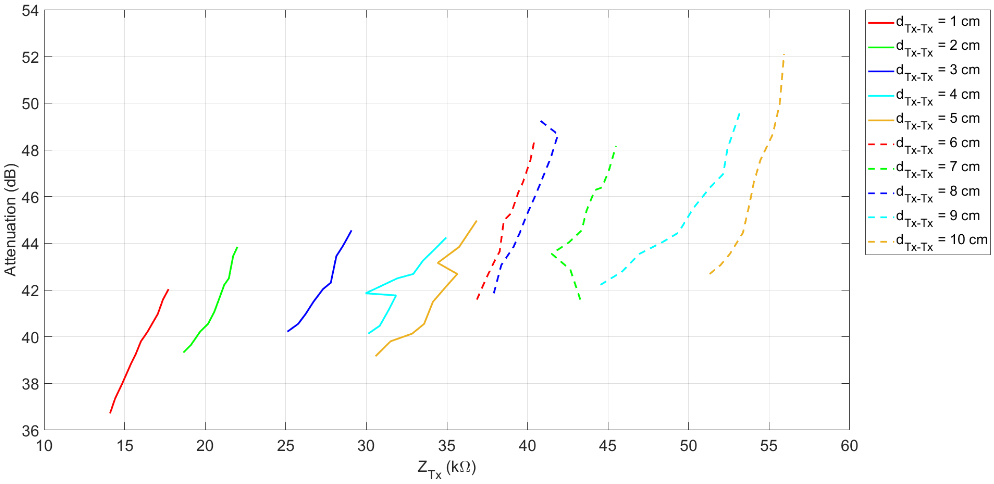

Figure 3.95: Evolution of the attenuation the receiver-related input signal is subjected to in relation with the transmitter-related electrical impedance Z_{Tx} evaluated at 1 kHz and varying the relative distance d_{Tx-Tx} over the plant stem length.

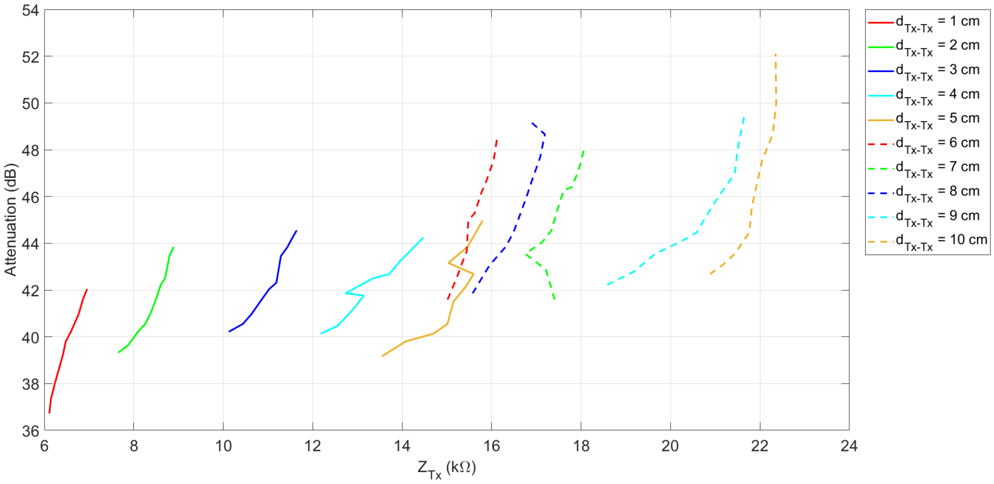

Figure 3.96: Evolution of the attenuation the receiver-related input signal is subjected to in relation with the transmitter-related electrical impedance Z_{Tx} evaluated at 10 kHz and varying the relative distance d_{Tx-Tx} over the plant stem length.

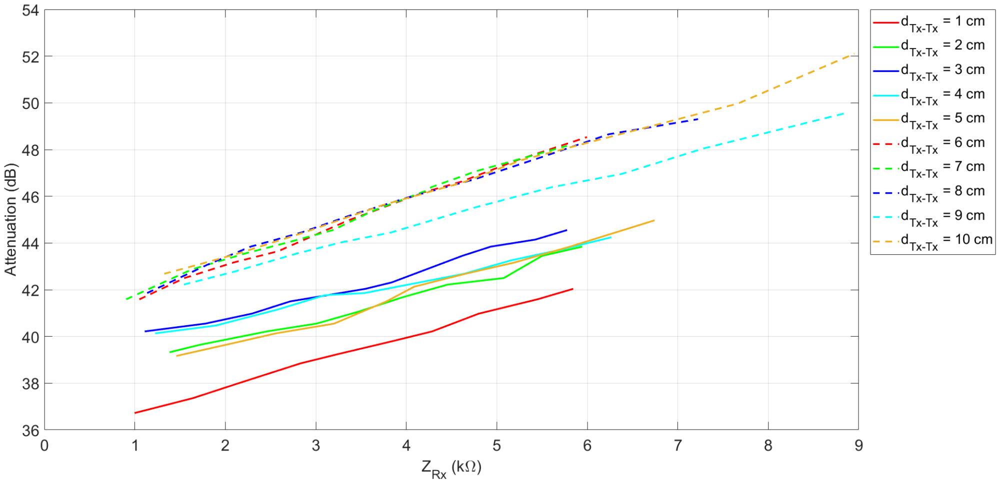

Figure 3.97: Evolution of the attenuation the receiver-related input signal is subjected to in relation with the transmitter-related electrical impedance Z_{Tx} evaluated at 100 kHz and varying the relative distance d_{Tx-Tx} over the plant stem length.

3.5 Conclusions

In the previous Section 3.4, the results of the several characterizations exploited to study the behavior of the system developed under the constraints exposed in Section 3.2 and Section 3.3 have been analyzed and several assumptions have been hypothesized to justify the plotted trends.

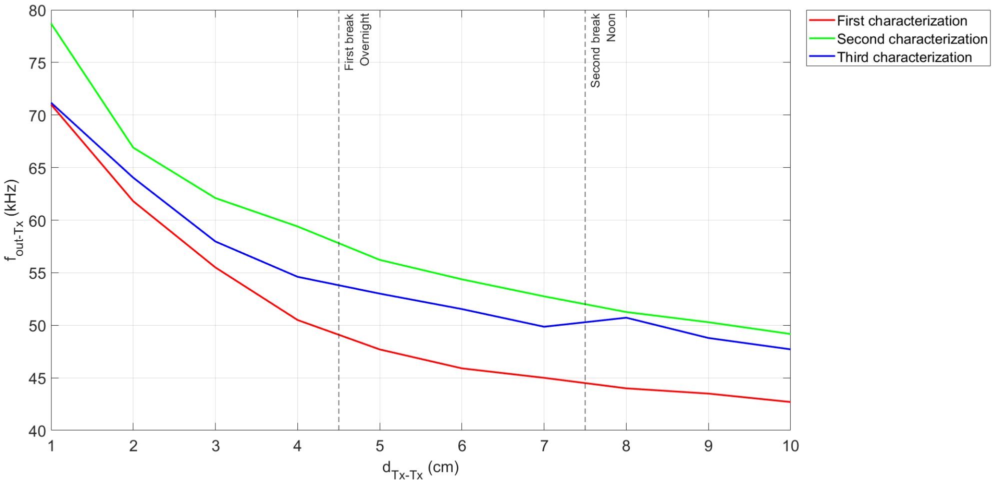

Figure 3.98: Comparison of the three-characterization-produced results in terms of transmitter output frequency without considering the receiver in the experimental setup f_{no-Rx} over the relative distance d_{Tx-Tx}.

Regarding the transmitter module, few formerly-done assumptions may be confirmed such as:

- As expected, even by considering the Equation 3.1, the output frequency of the transmitter follows an inverse proportional trend over the relative distance d_{Tx-Tx} variation over the stem length, all the more justified considering the evolution of the transmitter-related electrical impedance Z_{Tx} over the same relative distance d_{Tx-Tx} depicted in Figure 3.51.
- Remembering the employed plant conditions of each characterization and thereafter inspecting Figure 3.98, it can be evidenced a relation between the overall plant health status and its stem-specific output frequency (without considering the receiver installed in the experimental setup) f_{no-Rx}: in fact, the near-to-end tobacco plant transmitter-related curve exploited in the first characterization process presents a lower frequency range than both the second-characterization-related and the third-characterization-related results, where the employed plant was healthier than the first one and moreover the

third-characterization curve turns out to be even lower than the second one confirming the assumption by which a healthy plant presents an overall higher transmitter-related frequency than the one produced by a damaged plant (as in the third characterization case) and a near-to-end plant (as in the first characterization case).

- Strictly consequent to the previous point, analyzing the third characterization curve it can be noticed a local peak frequency just after the second break reinforcing the just-cited relation between overall plant condition in terms of stress and damages and the transmitter output frequency: even a short period of relaxation may imply an increase in the transmitter-related output frequency, especially during daytime (probably due to the plant circadian cycle and the effect of the sunlight).

However, a straightforward explicit relation of the transmitter-produced output frequency and the electrical impedance seen between the two transmitter-related surgical needles Z_{Tx} (or considering only its real part R_{plant}) can not be easily extrapolated since, taking into account the Equation 3.1, the transmitter-related output frequency is inversely proportional to the plant-stem-linked resistance R_{plant}, thus requiring a self-consistency algorithm to explicitly solve the desired relationship.

In the matter of the receiver-related output frequency f_{out-Rx}, a growing trend in turn to an increase of the relative distance d_{Rx-Tx} is expected since the signal injected by the transmitter and thereafter detected by the receiver is previously attenuated proportionally to the d_{Rx-Tx}-related electrical impedance Z_{Rx} thus to the relative distance d_{Rx-Tx}: this expected behavior has been verified and furthermore confirmed by inspecting both the receiver-related electrical impedance Z_{Rx} and the receiver-produced output frequency f_{out-Rx}. Within this framework, considering the relationship between the electrical impedance Z_{Rx} and the relative distance d_{Rx-Tx} described in Figure 3.65, Figure 3.66 and Figure 3.67, it seems possible to identify a one-to-one linear-like link between these two variables especially for small d_{Rx-Tx} values: by inspecting a specific arbitrary-selected d_{Tx-Tx}-related curve, it may be possible to estimate a mean receiver-related electrical impedance Z_{Rx} value per unit volume exploiting the relative distance d_{Rx-Tx} and the plant-stem diameter. However, this latter relation has not been further investigated in this thesis work due to the lack of other likely-to-be-useful information to estimate it, such as the level of freshness inside the stem, various environment-related factors, and other influences not considered during the characterization process: the same considerations are still valid considering the retrieval of an explicit unambiguous relation between the electrical impedance Z_{Rx} and the receiver output frequency

f_{out-Rx} as noticeable in Section 3.4.5. For thoroughness, an overview of the scatter plots depicting the receiver output frequency f_{out-Rx} in turn to the electrical impedance Z_{Rx} measured at different frequencies (1 kHz, 10 kHz, and 100 kHz) has been reported in Figure 3.99.

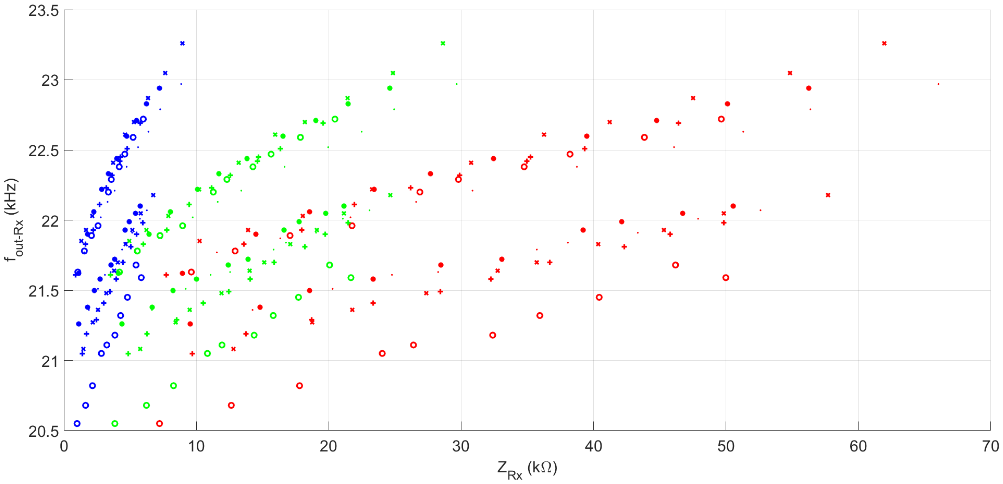

Figure 3.99: Comparison of the three scatter plots related respectively to the electrical impedance Z_{Rx} at 1 kHz (red results), the electrical impedance Z_{Rx} at 10 kHz (green plots) and the electrical impedance Z_{Rx} at 100 kHz (blue measurements) in relation with the receiver-related output frequency f_{out-Rx}.

However, the goal of the system developed in Chapter 3 is to permit the estimation of the plant stem electrical impedance through the analysis of the receiver-related output frequency f_{out-Rx} and in order to justify the exploitation of a peak-detector-based receiver system, few correlations can be noticed: in particular, it is evident the parallelism in terms of curves' behavior between Figure 3.80 and Figure 3.84 and between Figure 3.81 and Figure 3.85. The same considerations can be repeated while considering for instance the similarities of Figure 3.75 results compared to Figure 3.87 curves and noticing the analogies in terms of curves trend in Figure 3.78 and Figure 3.78 (this assumptions can be extended even to the plots which consider the electrical impedance Z_{Rx} evaluated at different frequencies than 10 kHz): therefore, in the end, thanks to all these aforementioned graphical parallelisms between the receiver output frequency f_{out-Rx} and the plant stem electrical impedance Z_{Rx} passing through its related attenuation value, it can be stated that due to this thesis-related developed system it is possible to evaluate the plant stem electrical impedance Z_{Rx} through the examination of the receiver-specific output frequency f_{out-Rx}.

In conclusion, summarizing the considerations made in Section 3.4.2, it may be a useful reminder to adjust the developed system to work primarily with more minor input frequencies and then lower peak-to-peak-amplitude input signals in order to reduce measurements errors related to the employed components' behavior as aforementioned in Figure 3.17 relative discussion reported in Section 3.4.2.

Chapter 4

Microcontroller Unit Implementation

4.1 Overview

In the previous Chapter 3, the design stage and the characterization of both the transmitter and receiver components have been studied and reported: as highlighted in Section 3.1, the microcontroller (MCU) employed in this thesis project is the ultra-low-power Sub-GHz MCU STM32WL55JC1 [40] developed by STMicroelectronics and reported in Figure 4.1 and Figure 4.2.

It is made up of two processors:

- ARM Cortex-M4
- ARM Cortex-M0+

The ARM Cortex-M4 is a 32-bit RISC (Reduced Instruction Set Computer) CPU from ARM for embedded systems characterized by high performances and code efficiency, while the ARM Cortex-M0+ is a 32-bit RISC entry-level processor from ARM for embedded systems mainly characterized by ultra-low power consumption in the memory size usually associated with 8-bit and 16-bit devices [40]. Both of the processors are mounted on a NUCLEO-WL55JC1 STM32WL Nucleo-64 development board manufactured by STMicroelectronics and implement an independent memory protection unit (MPU) to improve the application security [40, 53].

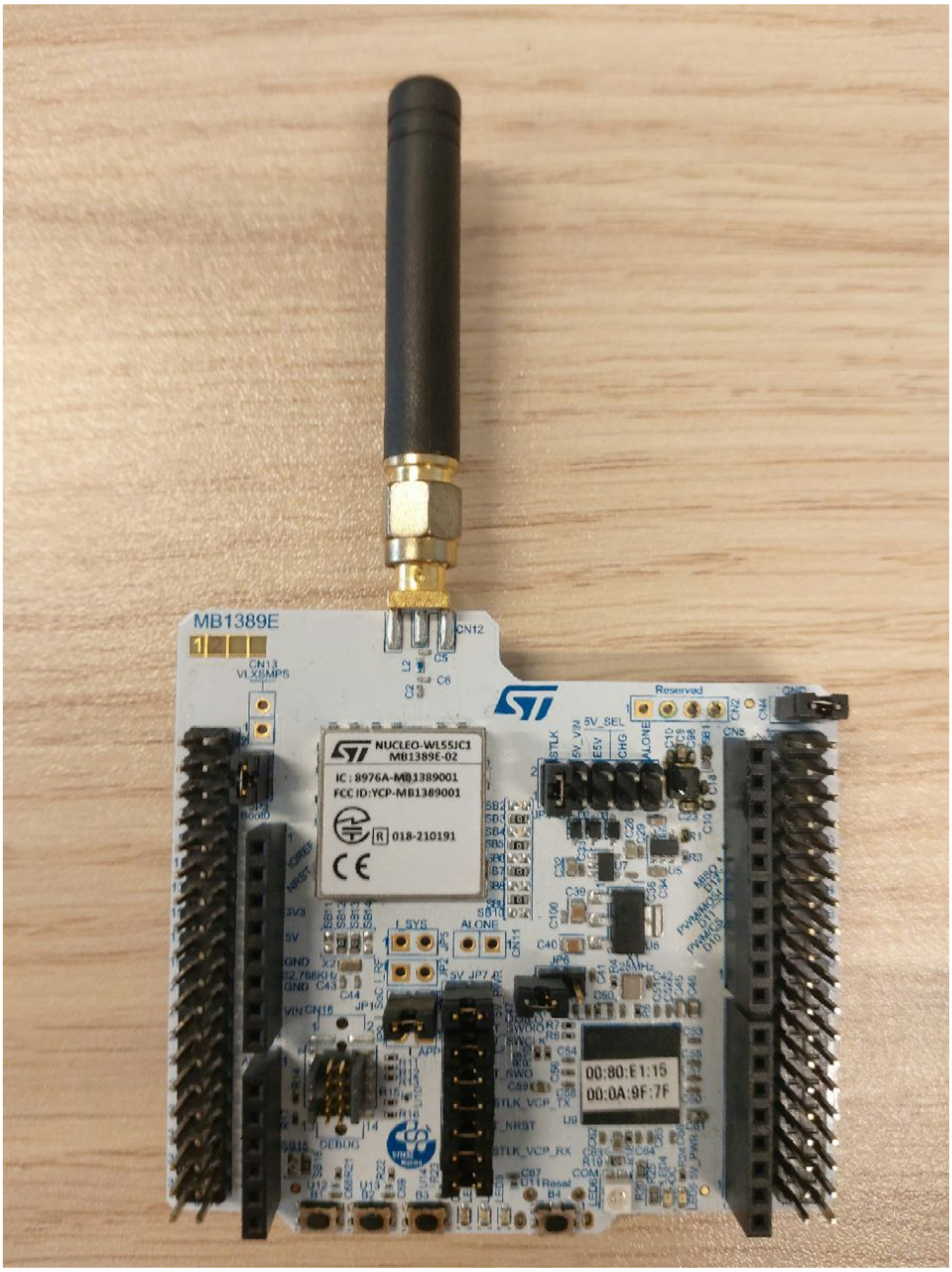

Figure 4.1: Top view of the STM32WL55JC1 development board.

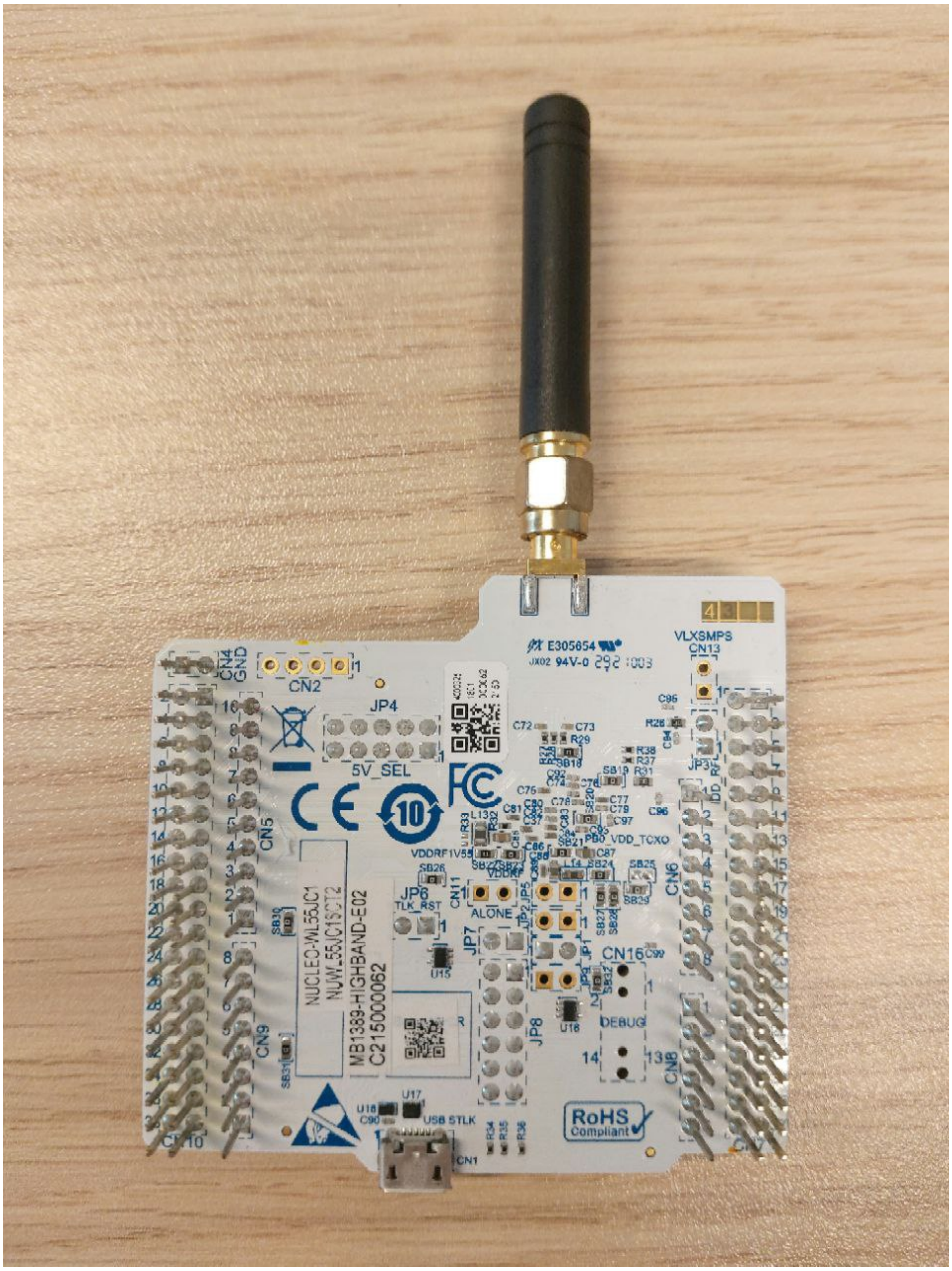

Figure 4.2: Bottom view of the STM32WL55JC1 development board.

This microcontroller can operate up to a maximum 48 MHz CPU frequency exploiting a 256-KB flash memory, a 64-KB SRAM (Static Random Access Memory), and a range of power supply swinging from 1.8 V to 3.6 V [40].

The STM32WL55JC1 [40] microcontroller can be connected through a USB-type-A-to-Micro-B-USB cable to a host PC which, in this case, will also be in charge of the board's power supply: in fact, this connection set-up is also employed to develop the code which manages the expected behavior of the system. In particular, STM32CubeIDE is an STMicroelectronics-proprietary integrated development environment (IDE) mainly utilized to configure the board's peripherals and to generate, compile, and debug the developed C/C++ code [53, 54].

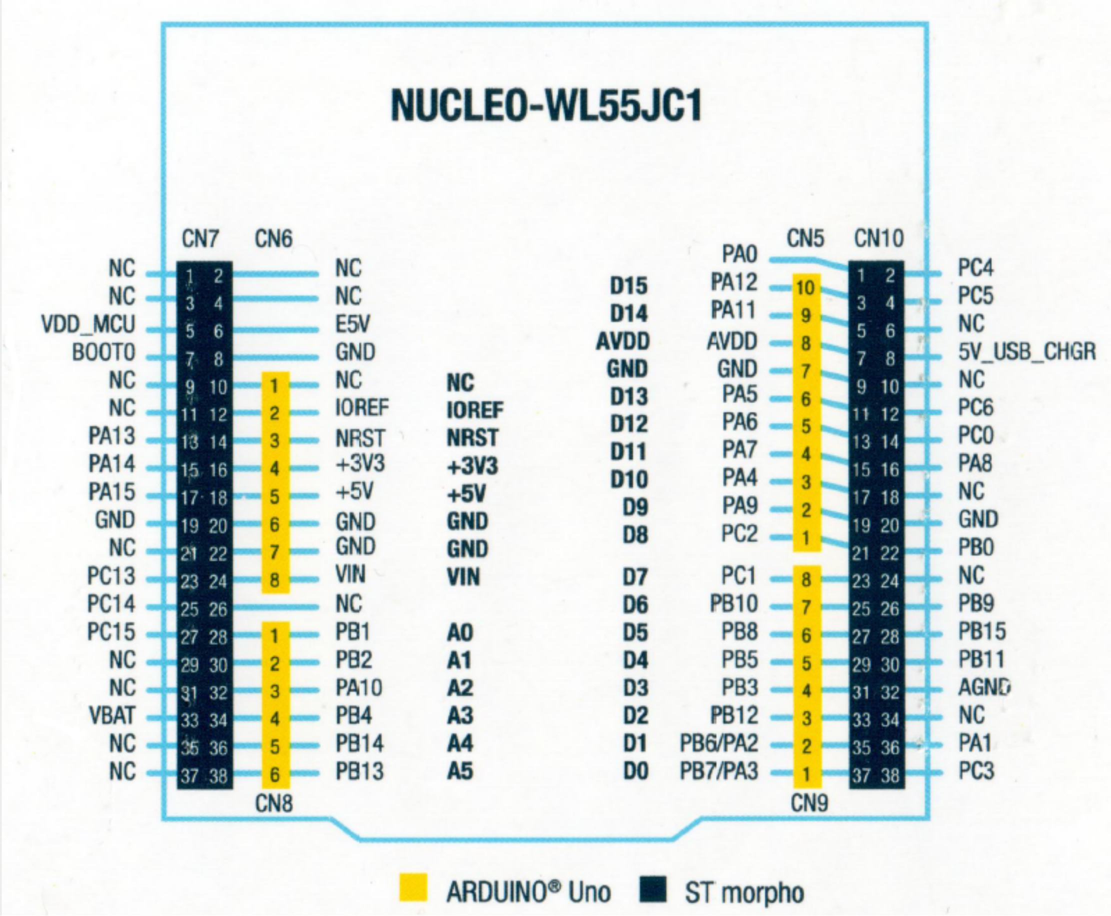

Figure 4.3: Scan of the pinout of the STM32WL55JC1 Nucleo-64 development board from its leaflet comprised in the commercial package [55].

In Figure 4.3, the two supported extension types are depicted: more in detail, the ST morpho connector (CN7 and CN10) and Arduino Uno V3 connectors (CN5, CN6, CN8 and CN9). Three ports (A, B, and C) characterized by 16 pins each are noticeable [40, 54, 55].

The STM32WL55JC1 belongs to the STM32WL wireless series, which is suitable for long-range connectivity: in particular, it supports the LoRa modulation since it complies with the physical layer requirements of LoRaWAN specifications released by the LoRa Alliance (more information about LoRa modulation and LoRaWAN protocol will be exposed in Section 4.1.1).

In order to achieve the best compromise between low-power consumption, short startup time, available peripherals, and available wake-up sources, several low-power modes are supported by this device and can be selected by the user [40, 53]:

- Sleep mode
- Low-power run mode (LPRun)
- Low-power sleep mode (LPSleep)
- Stop 0, Stop 1 and Stop 2 modes
- Standby mode
- Shutdown mode

In Sleep mode, the cores are off (since the CPU clock is off), while all the peripherals are kept running and triggered in turn to an interrupt or an event. In LPRun mode, the system clock frequency is reduced below 2 MHz, and the regulator is set to operate in low-power mode to reduce power consumption, while the LPSleep mode corresponds to the Sleep mode in relation to the default Run mode (default mode after a system or a power-on reset) from the LPRun mode. In the Stop modes, the lowest power consumption is achieved while retaining the content of the SRAMs and all the registers. In Standby mode, the programmable voltage detector (PVD) employed to monitor the supply voltage and compare it to a configured threshold selects its lowest level. In contrast, in Shutdown mode, the supply voltage monitoring is disabled, and the product behavior is not guaranteed in case of a power voltage drop [40]. In order to manage the actual running mode, an interrupt and/or an event are used to trigger the entering into and exiting from these low-power modes.

For completeness, the system developed in this thesis project is programmed to switch and enter into Stop 2 mode in turn to a trigger based on one of the low-power timers employed by the microcontroller when it is not running to reduce overall power consumption.

4.1.1 LoRa modulation and LoRaWAN protocol

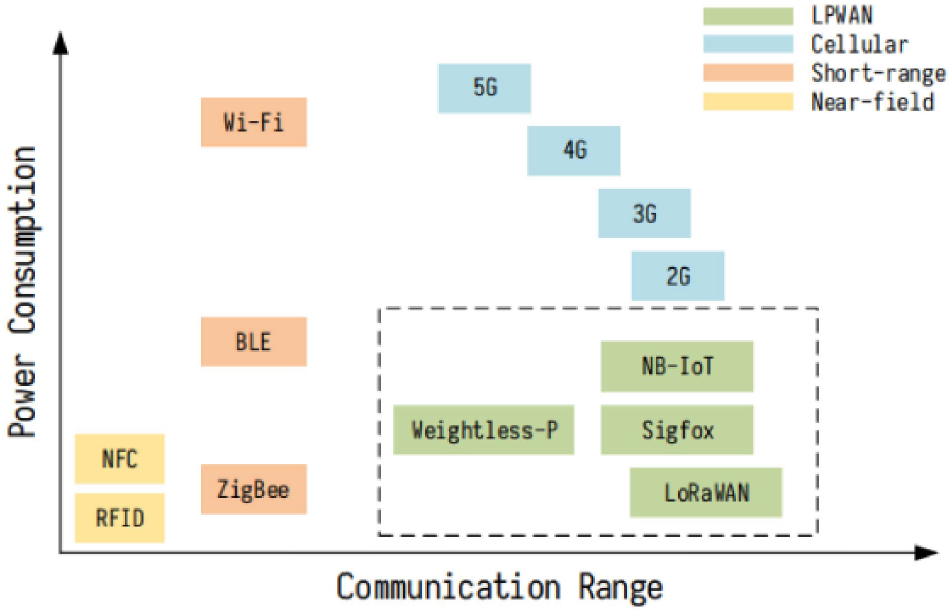

Figure 4.4: Classification in terms of power consumption and communication range of several wireless technologies [56].

LoRa (which stands for Long Range) is a proprietary physical-layer spread-spectrum-modulation-based radio communication technique developed by Cycleo and later patented and acquired by Semtech. It exploits license-free Sub-GHz RF bands (such as 868 MHz in Europe and 915 MHz in North America, to mention some examples), permitting long-range wireless transmissions with low-power consumption with respect to other wireless technologies [56] as reported in Figure 4.4. In order to improve communication reliability and resilience against interference, a Forward Error Correction (FEC) code is exploited: it is a code employed for error-detection-and-correction situations. As stated in the LoRa Development Portal by Semtech Corporation [57] and in the results of the studies conducted by Liando et al. [58], the LoRa technology is able to communicate over 4 km in urban areas and over 10 km or more in rural areas and in under line-of-sight environments. However, under non-line-of-sight environments, several kinds of obstructions, such as buildings and vegetation, severely affect its performance [58].

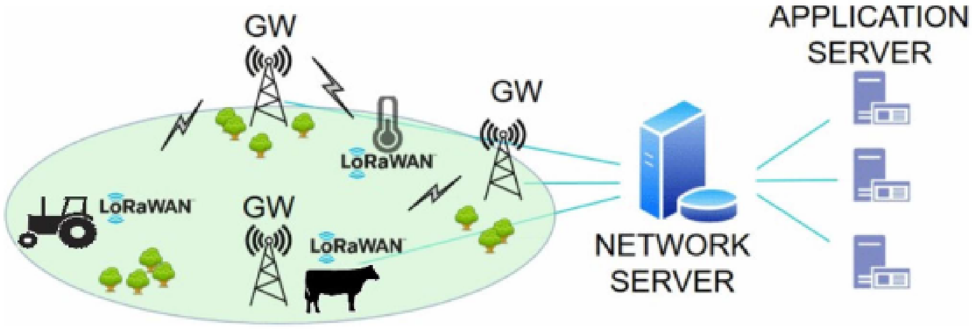

Figure 4.5: Representation of the typical LoRaWAN architecture [56].

LoRaWAN (which stands for Long Range Wide Area Network) is one of the communication protocols established by the LoRa Alliance and implemented to define upper network layers: in fact, according to the ISO/OSI conceptual model, LoRa modulation technology identifies just the physical layer, while upper layers are related to the LoRaWAN protocol [56]. LoRaWAN is a MAC-layer protocol but mainly implemented as network layer routing protocol in order to manage and route the communication between LPWAN (Low Power Wide Area Network) gateways and end-node devices.

The LoRa technology, alongside the LoRaWAN protocol, implements an LPWAN protocol that permits and manages the wireless interconnection between several energetically self-sufficient devices and up-to-global networks meeting Internet of Things (IoT) requirements such as bi-directional communication, end-to-end security, mobility, and localization services. Furthermore, the LoRa communication technology's LPWAN permits the reduction of power consumption with respect to a standard wireless WAN.

4.1.2 The Things Network

In order to deal with the LoRa communication technique and LoRaWAN network protocol, a cloud platform where to register and test LoRa-based devices and applications is required. Within this framework, The Things Network (TTN) is a global collaborative Internet of Things (IoT) ecosystem employed to realize, for instance, networks using LoRaWAN where registered devices can be utilized, monitored, and tested.

After choosing the network cluster related to the geographical position where the device is deployed, The Things Network's portal permits to develop and/or manage several applications and gateways, which, for instance, the LoRa-based devices can be added to and can rely on for their operations and evaluation. In particular, the data provided from the end device to the TTN exploited server (uplink operation) and vice-versa (downlink operation) can be handled, for example, according to a customizable user-developed JavaScript code enhancing flexibility and user-friendliness in the data manipulation and evaluation.

4.2 Firmware Implementation

As previously mentioned in Section 4.1, the design stage and the characterization of both the transmitter and receiver components have been considered in Chapter 3. From now on, the firmware implementation of the employed STM32WL55JC1 MCU in order to evaluate the receiver's output frequency and to send the acquired data through a LoRa communication will be presented in this section.

In addition to what has been depicted in Chapter 3, the actual entire system reported in Figure 4.6 also comprehends:

- A SIP switch to control the turn-on and the turn-off of the transmitter device in order to reduce the overall power consumption.
- A SIP switch to control the turn-on and the turn-off of the receiver module in order to reduce the overall power consumption.

Since both the transmitter and the receiver are born to be integrated with a previously developed system which already takes into account a soil humidity evaluation sensor from-now-on labeled as watermark, another SIP (Single In-Line Package) switch has been exploited to manage the turn-on and the turn-off of the watermark sensor to reduce the overall power consumption: in particular, the implemented SIP switches are SIP32431 [59] produced by Vishay and characterized by a low on-resistance and a 1.5-V-to-5.5-V input voltage range. These employed SIP switches are pass-transistor-based switches exploited to cut up the power supply of the powered devices (in this case, receiver, transmitter, and watermark sensor) in turn to an input control signal provided, for instance, by the microcontroller.

For the sake of completeness, even an air-humidity sensor, a light intensity sensor and a temperature sensor have been considered in the previously developed system, therefore in Appendix D they will be cited since integral part of the studied system.

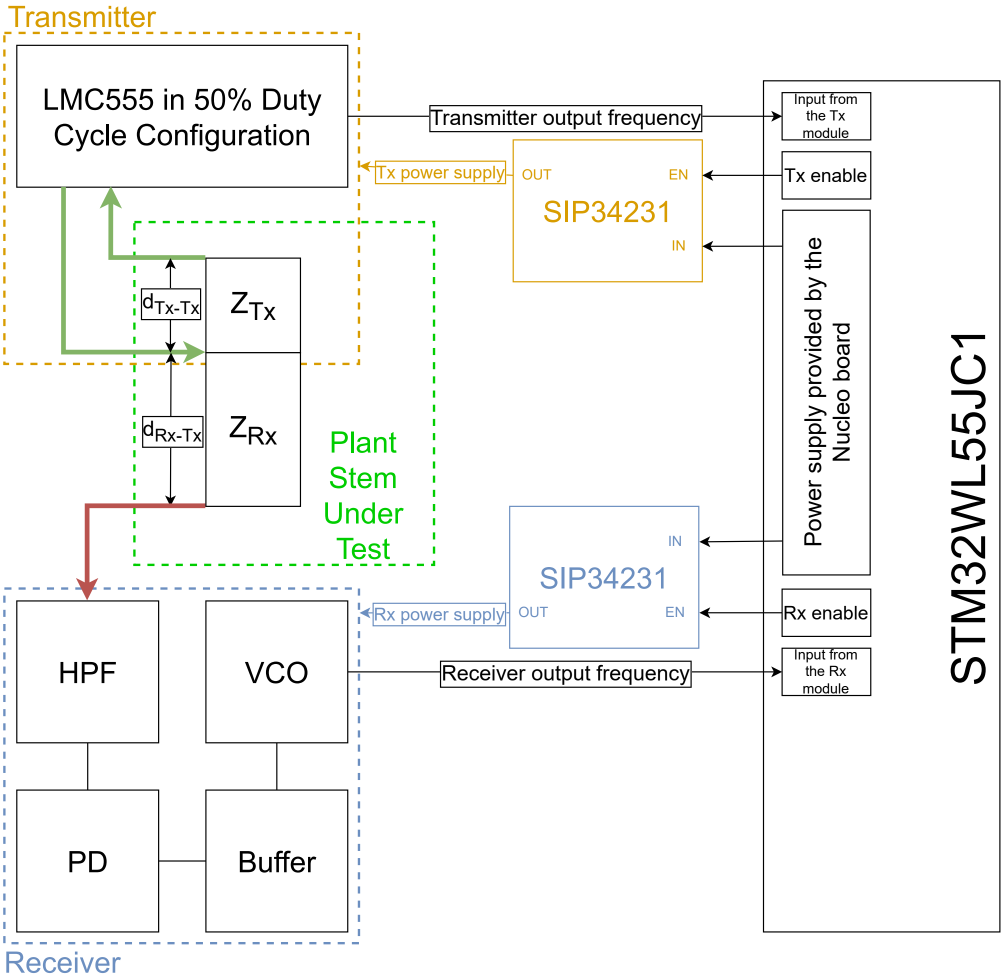

Figure 4.6: Schematic block diagram of the complete system: in particular, the transmitter, the receiver, the green and red surgical needles (as depicted in Figure 3.3) and their relative distances, the SIP switches and the Nucleo-64 Development Board are highlighted.

In order to generate the code to manage the entire system, the integrated development environment STM32CubeIDE has been utilized to set the required configuration of the peripherals accordingly and to produce the correspondent code.

The firmware has been developed exploiting two built-in timers:

- Advanced-control timer TIM1
- General-purpose timer TIM2

TIM1 is a 16-bit 6-channel advanced-control timer that relies on an auto-reload counter and a 16-bit programmable prescaler [53]. The latter has been configured to make the microcontroller count at 2 MHz, while the auto-reload register (ARR) has been adjusted to the maximum applicable value to reduce the number of overflows. In addition, in TIM1's NVIC (Nested Vectored Interrupt Controller) Settings tab, TIM1 break interrupt, TIM1 update interrupt, and TIM1 trigger and communication interrupt have been enabled to work exploiting interrupts. Moreover, three out of its six employable channels have been all used in Input Capture (IC) mode to sense the input signals coming from the transmitting module, the receiving device, and the watermark sensor and to accordingly trigger the correspondent IC callback in turn to an incoming rising edge: in particular, channel 1 (TIM1_CH1) has been associated to the measurement of the signal coming from the transmitter, while channel 2 (TIM1_CH2) has been related to the evaluation of the signal originating from the watermark sensor and channel 3 (TIM1_CH3) has been associated to the measurement of the signal sourced from the receiver, as also depicted in Figure 4.6.

On the other hand, TIM2 is a 32-bit 4-channel general-purpose timer that consists of an auto-reload counter and a 16-bit programmable prescaler [53]: the required working frequency for the only TIM2 channel employed (TIM2_CH1) is 10 kHz, while the auto-reload register has again been adjusted to the maximum applicable value to reduce the number of overflows. In addition, TIM2 global interrupt has been enabled to work exploiting interrupts. The only TIM2 channel used (TIM2_CH1) has been activated in Output Compare (OC) mode to accordingly trigger the respective OC callback in turn to a 1-second-long time interval elapsed after channel activation.

Therefore, for what concerns the configured pinout, three more GPIO pins (apart from the utilized TIM1 channels' ones configured in input mode) have been exploited in output mode to properly control independently the SIP switches employed to section and decouple the provided supply voltage and each device-specific supply voltage due to power consumption requirements.

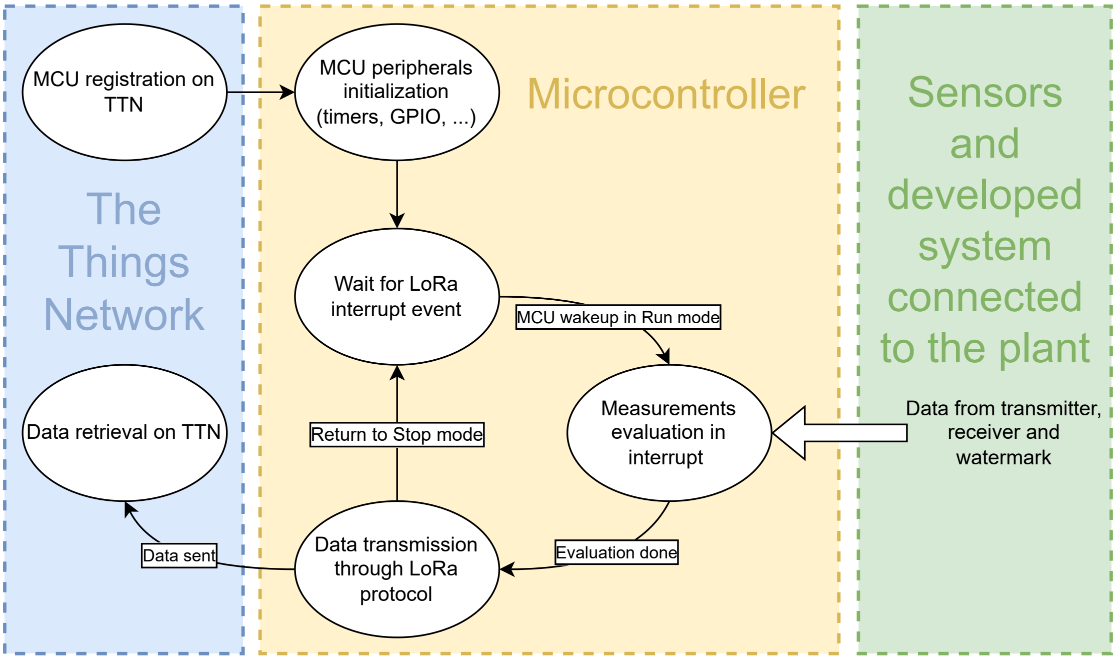

Figure 4.7: Schematic flowchart of the behavior of the developed setup.

According to Figure 4.7 where the flow of the operations performed in the setup have been cited, after the first stage of device registration on The Things Network and peripherals initialization, the microcontroller enters its working loop by waiting for an interrupt event related to the LoRa implementation and data transmission control. At this stage, the microcontroller is in Stop 2 mode. When a LoRa interrupt event occurs, the microcontroller starts to operate in Run mode and evaluates the data retrieved from the transmitter, receiver, and watermark sensor mounted on the employed plant. Once the measurements are done, the microcontroller sends the resulting information to The Things Network through LoRa communication protocol and sets itself in Stop 2 mode, waiting for the next LoRa-related interrupt event. The data sent to The Things Network are properly received and formatted to make them easier to be read on The Things Network application-specific suite. The look of the application-specific data log has been reported in Figure 4.8.

The time elapsed from two consecutive data sent (thus, for instance, from two successive LoRa-related interrupt events) has been arbitrarily set to 20 minutes due to the low rate of variations over time in plant stem parameters, as evidenced in Calvo et al. work [42] and previously underlined in Chapter 3.

For further insights about the firmware implementation and the microcontroller developed C code, consult the Appendix D.

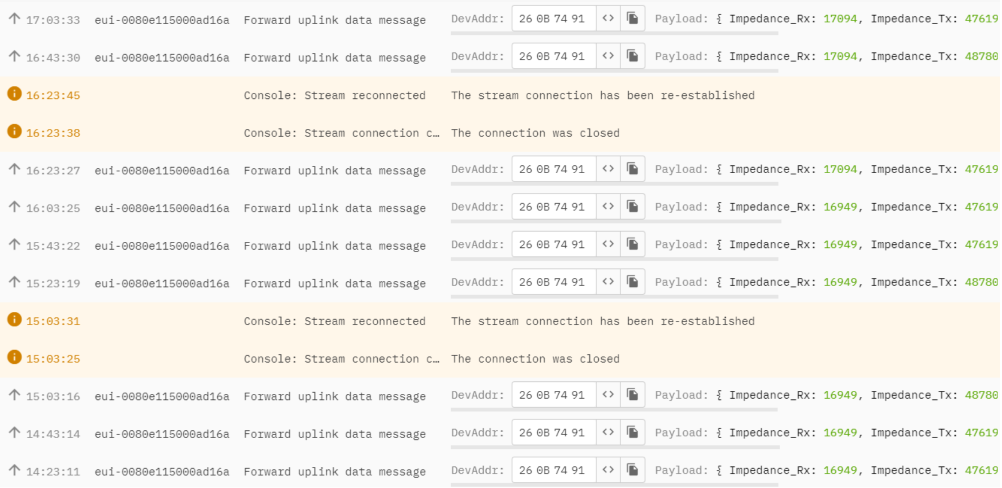

```
↑ 17:03:33  eui-0080e115000ad16a  Forward uplink data message    DevAddr:  26 0B 74 91  <>  Payload: { Impedance_Rx: 17094, Impedance_Tx: 47619
↑ 16:43:30  eui-0080e115000ad16a  Forward uplink data message    DevAddr:  26 0B 74 91  <>  Payload: { Impedance_Rx: 17094, Impedance_Tx: 48780
ⓘ 16:23:45                        Console: Stream reconnected    The stream connection has been re-established
ⓘ 16:23:38                        Console: Stream connection c…  The connection was closed
↑ 16:23:27  eui-0080e115000ad16a  Forward uplink data message    DevAddr:  26 0B 74 91  <>  Payload: { Impedance_Rx: 17094, Impedance_Tx: 47619
↑ 16:03:25  eui-0080e115000ad16a  Forward uplink data message    DevAddr:  26 0B 74 91  <>  Payload: { Impedance_Rx: 16949, Impedance_Tx: 47619
↑ 15:43:22  eui-0080e115000ad16a  Forward uplink data message    DevAddr:  26 0B 74 91  <>  Payload: { Impedance_Rx: 16949, Impedance_Tx: 47619
↑ 15:23:19  eui-0080e115000ad16a  Forward uplink data message    DevAddr:  26 0B 74 91  <>  Payload: { Impedance_Rx: 16949, Impedance_Tx: 48780
ⓘ 15:03:31                        Console: Stream reconnected    The stream connection has been re-established
ⓘ 15:03:25                        Console: Stream connection c…  The connection was closed
↑ 15:03:16  eui-0080e115000ad16a  Forward uplink data message    DevAddr:  26 0B 74 91  <>  Payload: { Impedance_Rx: 16949, Impedance_Tx: 48780
↑ 14:43:14  eui-0080e115000ad16a  Forward uplink data message    DevAddr:  26 0B 74 91  <>  Payload: { Impedance_Rx: 16949, Impedance_Tx: 47619
↑ 14:23:11  eui-0080e115000ad16a  Forward uplink data message    DevAddr:  26 0B 74 91  <>  Payload: { Impedance_Rx: 16949, Impedance_Tx: 47619
```

Figure 4.8: Application-specific data log displayed in The Things Network's "Live Data" tab.

4.3 Conclusions

In this chapter, a brief overview of the employed STM32WL55JC1 development board [40, 53, 54, 55] and LoRa-based communication have been reported in Section 4.1. Successively, the motivations that have guided the design of the system, the adopted solutions, and the consequent implementation of the employed firmware loaded on and off the board have been highlighted in Section 4.2 and in Appendix D: in particular, the developed functions and their behavior have been described and analyzed in Section D.0.1, while in Section D.0.2 the JavaScript code deployed on The Things Network portal and useful for decoding the device-sourced data packets has been pointed out.

Chapter 5

Implementation on the actual plant

5.1 Overview

The design phase and the subsequent characterization and microcontroller implementation stage have been exposed in detail and analyzed in the previous Chapter 3 and Chapter 4. Therefore, the previously developed system produced measurements will be underlined and further studied.

The experimental setup consists in:

- Transmitter module
- Receiver module
- STM32WL55JC1 Nucleo development board as the exploited MCU
- Tobacco plant under test

In order to collect even more information and thereafter to try to identify some correlation between different data types, a LoRa-based system from-now-on recalled as WAPPSEN previously developed by Barezzi et al. [60].

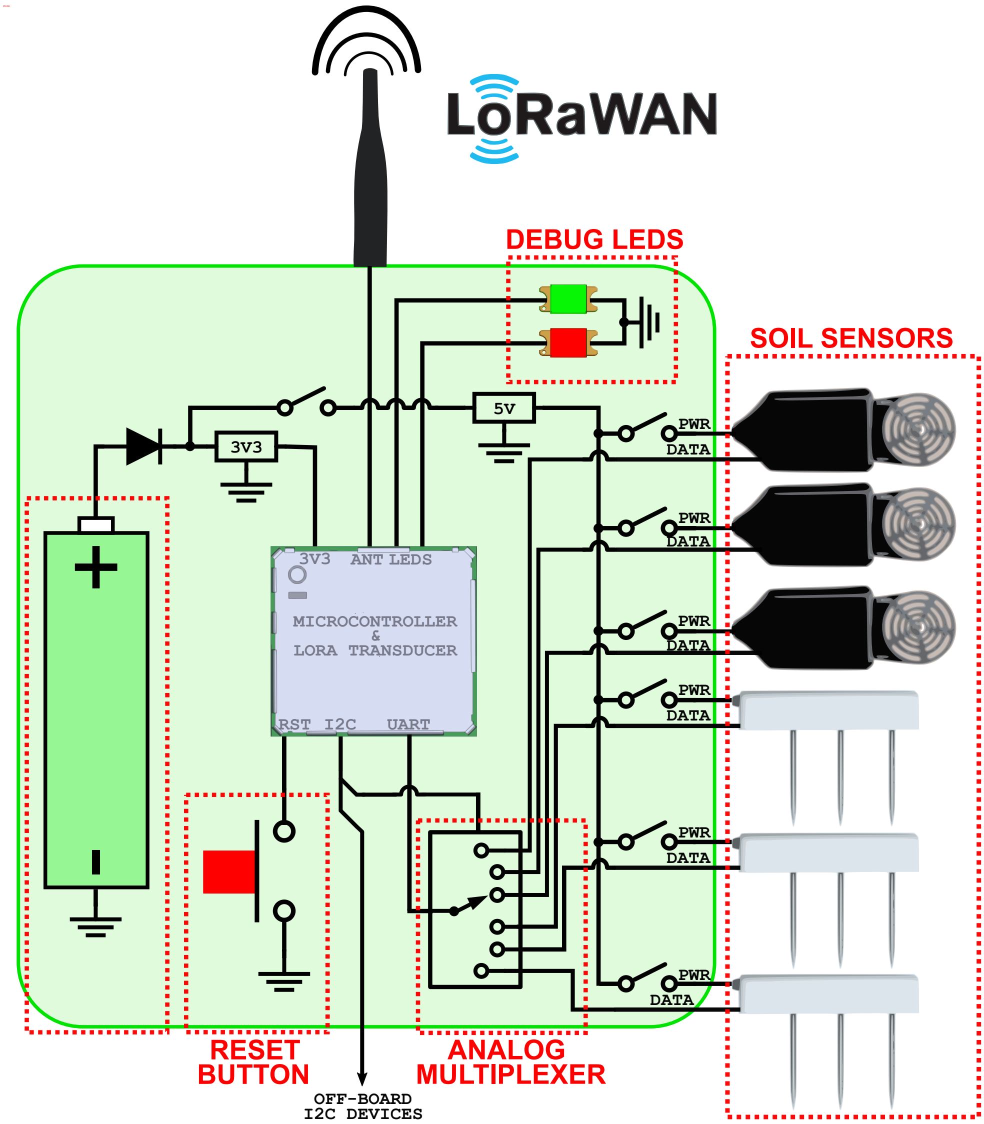

Figure 5.1: LoRa-based WAPPSEN sensor end node block scheme [60].

In more detail, the WAPPSEN developed system is a standalone system based on a four-layer PCB accordingly designed to support 868 MHz (LoRa-employed center frequency in Europe) radiofrequency LoRa communications and assembled exploiting a CMWX1ZZABZ-078 LoRaWAN module [61] from Murata which block scheme is depicted in Figure 5.2. To provide power supply, a non-rechargeable LS14500 AA-sized battery [62] produced by SAFT has been utilized due to its technical characteristics very suitable for agricultural applications, while a I^2C-protocol-properly-configured MAX4562 integrated circuit (IC) [63] manufactured by Maxim as analogical multiplexing stage has been realized.

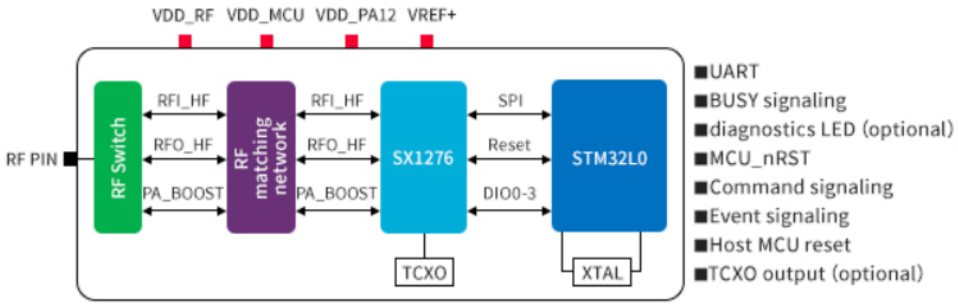

Figure 5.2: CMWX1ZZABZ-078 LoRaWAN module block scheme [61].

For what concerns the sensors connected to the aforementioned system, a TEROS 21 soil moisture and temperature sensor commercially-produced by METER Group, Inc. USA [64, 65, 66] has been exploited: in particular, TEROS 21 Gen 2 Soil Water Potential Sensor is a dielectric water potential sensor in natural systems or other drier systems used to measure water potential and temperature with a resolution respectively equal to 0.1 kPa and 0.1 °C [65]. In particular, a soil water potential measurement is exploited to evaluate the soil moisture level. In fact, soil water potential (SWP) is a measure of the energy required to remove water from the soil [67], exploiting zero as a standard environment-specific water potential reference value. Thus, this sensor can collect information about the moisture level and the temperature of the soil where the plant has grown.

The experiment took place in the PIC4SeR thesis students' room from January 19th, 2024 to March 19th, 2024 over a 60-day-long test period using the tobacco plant exploited for the second and third characterizations in Section 3.4 as the plant under investigation and the CPX200D as the bench-type power supply unit [48] configured to provide a 1.8-V output. Moreover, a BK Precision 891 LCR meter [68, 69] produced by B&K Precision Corporation has been exploited to further estimate stem-related electrical impedance values Z_{Tx} and Z_{Rx} and to validate the developed system performance. For this purpose, the results registered by the Tx-plant-Rx developed system will be compared to the electrical impedance value retrieved from the BK Precision 891 LCR meter [68, 69] spectroscopic analysis at an arbitrarily chosen reference frequency f_{BK}.

In Figure 5.3 and Figure 5.4, the experimental setup located in the PIC4SeR employed room has been reported, while in Table 5.1, the test apparatus parameters have been reported, such as the adopted values of the relative distances d_{Tx-Tx} and d_{Rx-Tx} over the plant-stem length and the reference frequency f_{BK} at which both the electrical impedance Z_{Tx} and Z_{Rx} have been evaluated. In particular, the relative distances have been arbitrarily chosen according to the considerations made up and reported in Section 3.5.

Parameter	Value
d_{Tx-Tx}	10 cm
d_{Rx-Tx}	5 cm
f_{BK}	10 kHz

Table 5.1: Exploited parameters of the experimental setup.

Figure 5.3: Experimental setup located in the PIC4SeR thesis students' room.

Figure 5.4: Zoom on the experimental setup which comprehends the WAPPSEN system (comprising the TEROS 21 Gen 2 sensor properly installed into the soil in the plant pot [64, 66]) on the leftmost part of the rack (in the red circle) and the CPX200D bench-type power supply unit [48] on its rightmost part (in the brown circle), while this latter is connected to this thesis developed system on its left (in the green circle), which in turn is mounted on the tobacco plant previously exploited in Section 3.4.4 and Section 3.4.5.

5.2 Experimental results

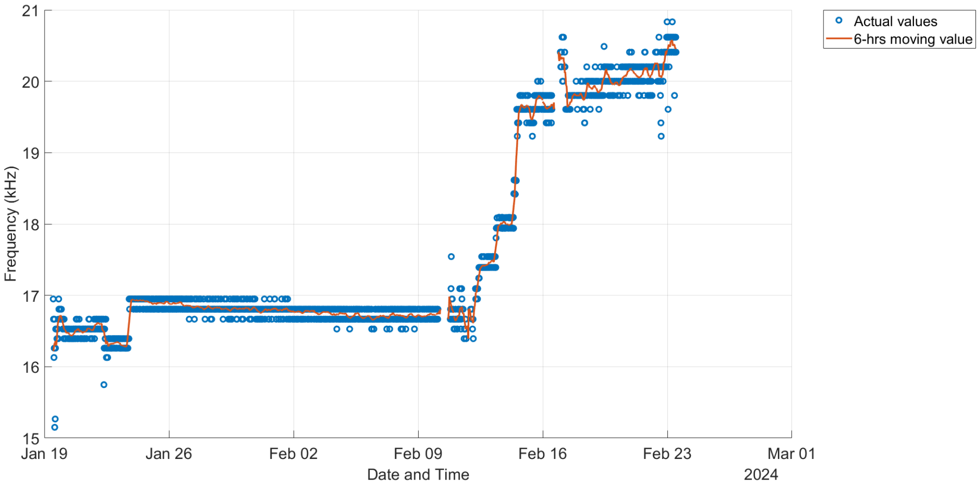

Figure 5.5: Receiver-related output evolution from January 19th, 2024 to February 23rd, 2024.

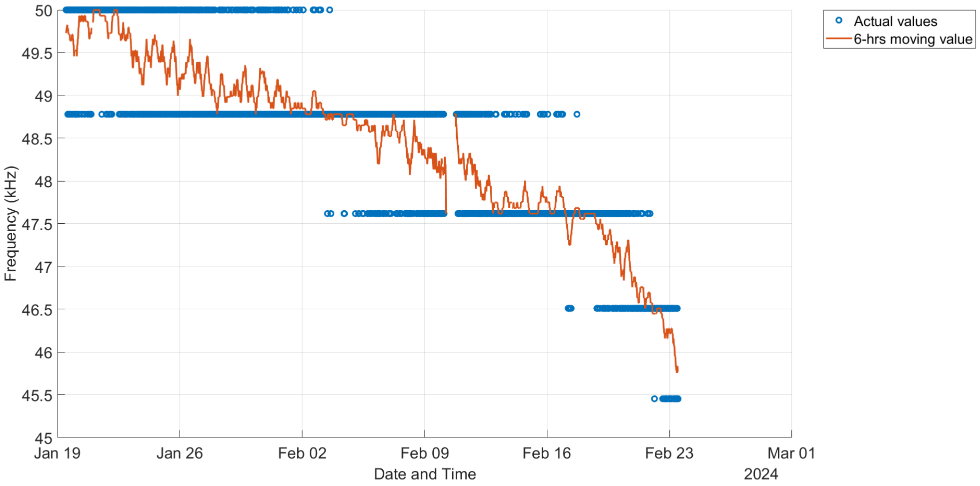

Figure 5.6: Transmitter-related output evolution from January 19th, 2024 to February 23rd, 2024.

In Figure 5.5, Figure 5.6, Figure 5.7, and Figure 5.8, the evolution of the receiver-related output frequency, the transmitter-related output frequency, the soil water potential, and soil temperature. Within this framework, a 35-day-long monitoring period from January 19th, 2024 to February 23rd, 2024, during which the plant has not been irrigated since the preparation process of the experimental setup on January 19th, 2024 in the morning.

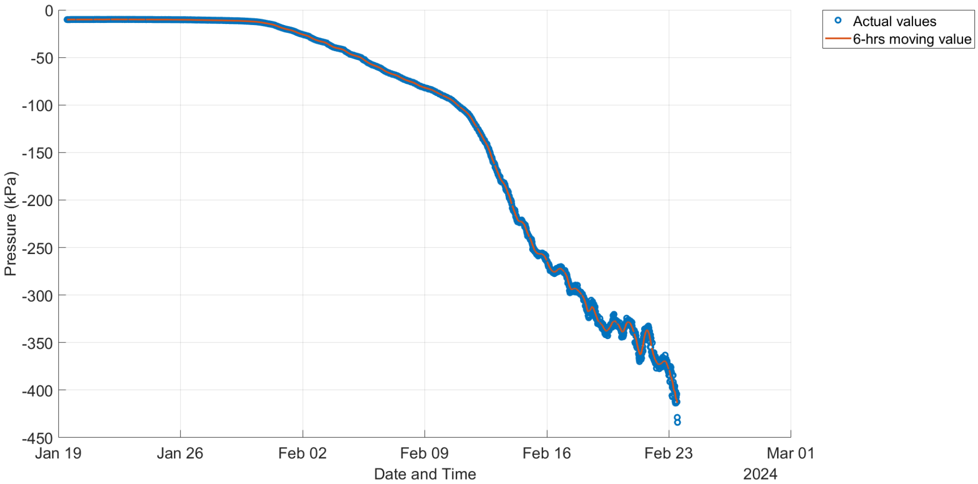

Figure 5.7: Soil water potential evolution from January 19th, 2024 to February 23rd, 2024.

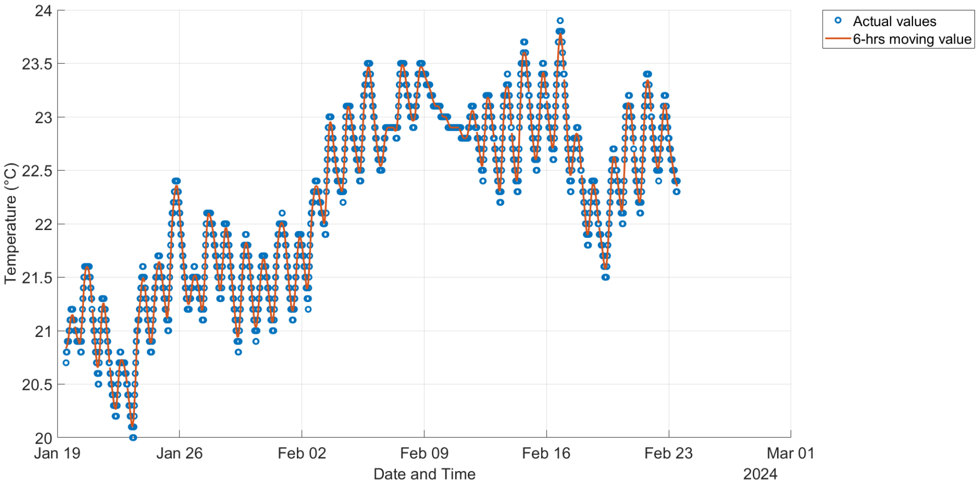

Figure 5.8: Soil temperature evolution from January 19th, 2024 to February 23rd, 2024.

An evident correlation between soil water potential and receiver-specific and transmitter-specific outputs can be underlined. A lowering trend of the SWP-related value implies a growing transmitter-related output and a decreasing receiver-related output, and vice-versa, coherently to the Section 3.4 results. The day-and-night cycle can be noticed by inspecting the receiver-specific and transmitter-specific outputs and the temperature measurement oscillations. However, according to the retrieved results, a relationship between temperature and both the receiver and transmitter output frequencies may not be assumed.

For thoroughness, watering influence can be further highlighted in Figure 5.9, Figure 5.10, and Figure 5.11. The relationship mentioned above between the receiver and transmitter output results and soil water potential can be evidenced, particularly from January 20th, 2024 to January 23rd, 2024. After that, the watering event influence has been depleted since January 24th, 2024. Thus, both transmitter output and soil water potential start to decrease, while an increase in receiver output can be evidenced. As mentioned before, no significant variations can be associated with the soil temperature effect within this framework as reported in Figure 5.12.

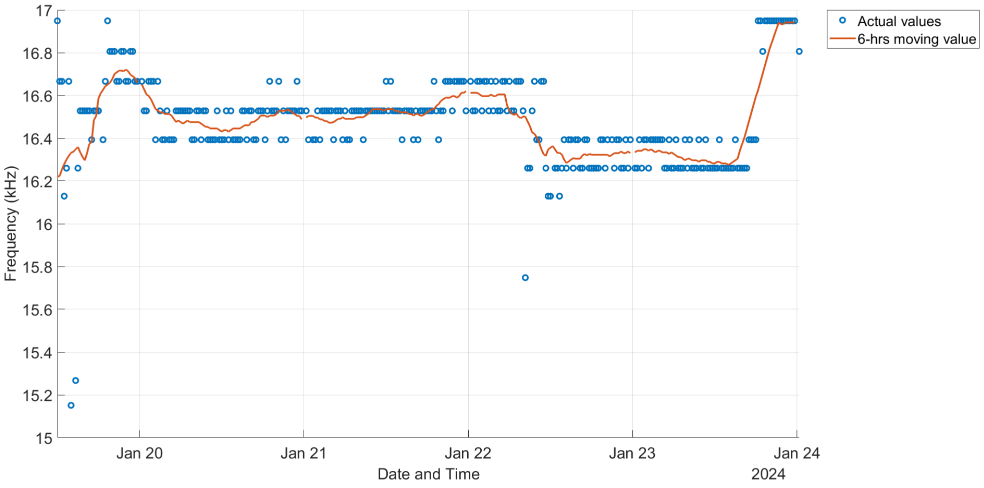

Figure 5.9: Zoom on the watering effect on receiver-related output evolution.

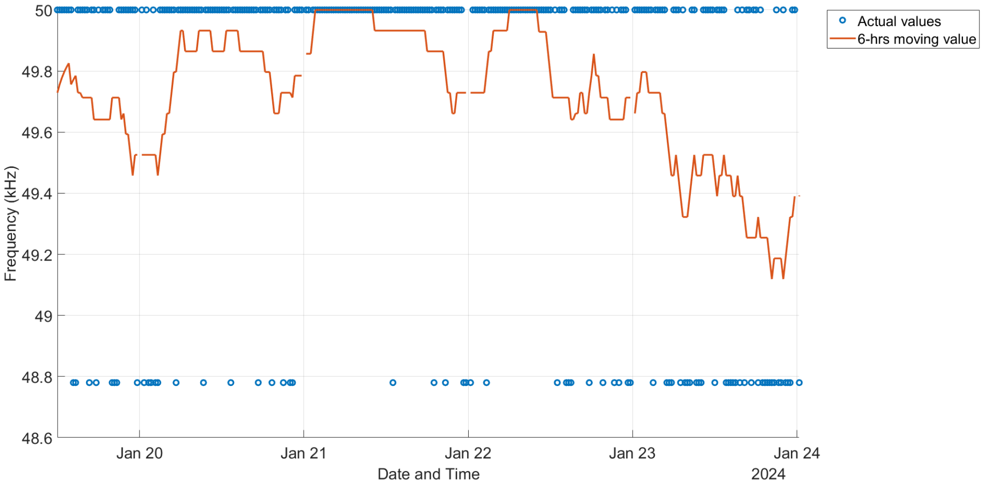

Figure 5.10: Zoom on the watering effect on transmitter-related output evolution.

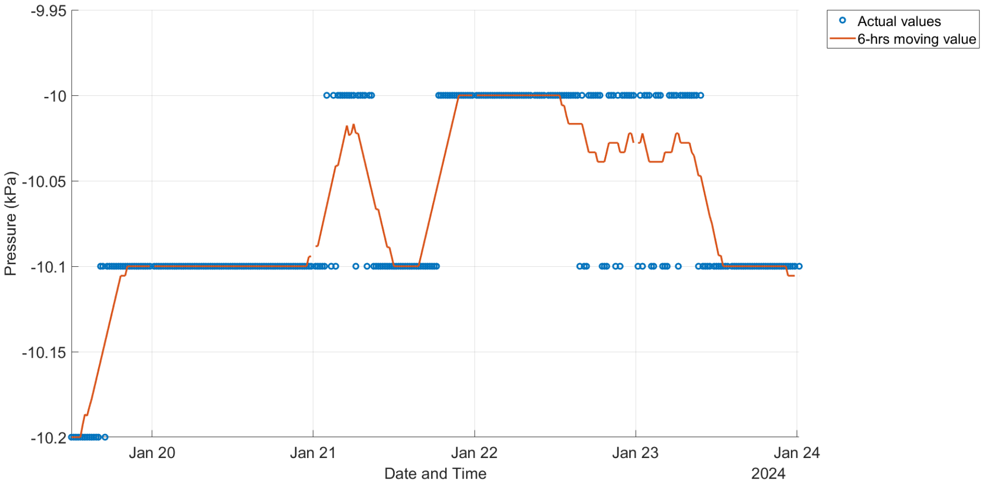

Figure 5.11: Zoom on the watering effect on soil water potential evolution.

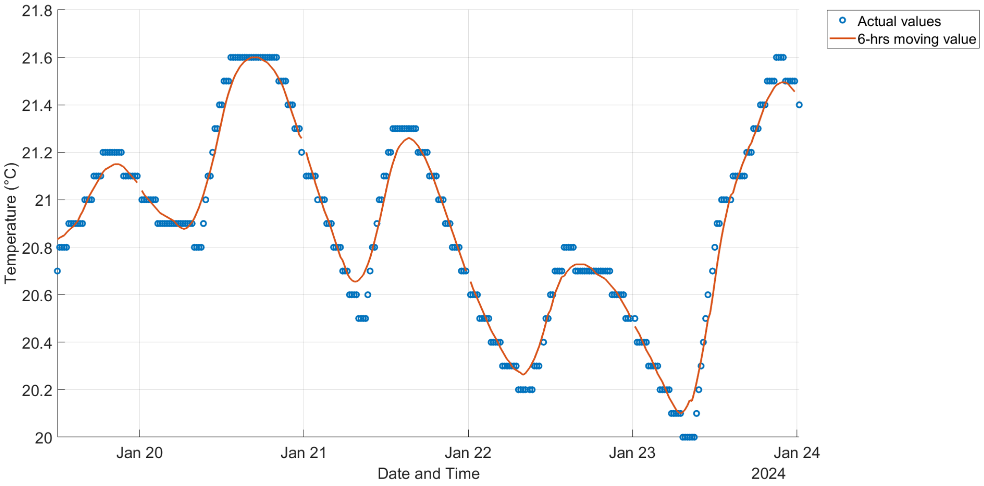

Figure 5.12: Zoom on the watering effect on soil temperature evolution.

Figure 5.13: Employed plant condition after the 35-day-long monitoring period from January 19th, 2024 to February 23rd, 2024.

Furthermore, after this 35-day-long monitoring period from January 19th, 2024 to February 23rd, 2024, the exploited plant was watered on February 26th, 2024, and a few days after the plant has seemed to be rejuvenated by only one watering event.

Figure 5.14: Employed plant condition four days after the watering event performed on February 26th, 2024 (thus on March 1st, 2024).

In parallel, both the Z_{Tx} and Z_{Rx} electrical impedance modulus values have been retrieved using the BK Precision 891 LCR meter [68, 69] before the watering event occurred on February 26th, 2024. The same electrical impedance measurement process has been repeated on March 1st, 2024, reporting Z_{Tx} and Z_{Rx} electrical impedance modulus variations with respect to the values retrieved before the watering event on February 26th, 2024 around at the same time (for instance, 3-5 kΩ lower than the before-watering-event values at 10 kHz for both Z_{Tx} and Z_{Rx} electrical impedance modulus). Thus, a more punctual analysis was performed on March 4th, 2024, considering only the 10 kHz measurements. Meanwhile, the Tx-plant-Rx system developed in this thesis project has been utilized to retrieve data from the plant in the experimental framework previously described in Section 5.2. The results have been depicted in Table 5.2 and reported in Figure 5.15 and Figure 5.16. To perform the electrical impedance modulus measurements, the WAPPSEN system has been disconnected during the evaluation process exploiting the BK Precision 891 LCR meter [68, 69].

Inspecting the results reported in Figure 5.15 and Figure 5.16, the possibility of estimating plant-stem-related electrical impedance modulus values through the analysis of this thesis' developed system, particularly Z_{Rx} and Z_{Tx} exploiting respectively receiver and transmitter output, has been verified. Variations on measurements retrieved using the BK Precision 891 LCR meter [68, 69] seem to be correlated to the variations of the developed Tx-plant-Rx system actual outputs.

Date	March 4th, 2024	
Time (hh:mm)	$\lvert Z_{Tx}\rvert$ $(k\Omega)$	$\lvert Z_{Rx}\rvert$ $(k\Omega)$
8:10	25.43	16.38
9:10	25.18	16.20
10:10	24.98	16.13
11:10	24.81	16.03
12:10	24.76	16.01
13:10	24.82	16.08
14:10	24.82	16.08
15:10	24.91	16.11

Table 5.2: Electrical impedance modulus values (Z_{Tx} and Z_{Rx}) retrieved using the BK Precision 891 LCR meter [68, 69] on March 4th, 2024.

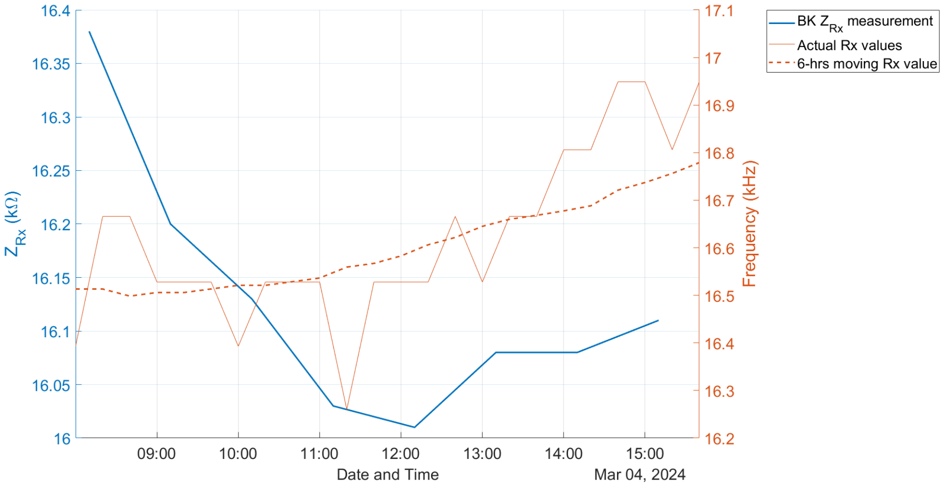

Figure 5.15: Comparison between the receiver-related output retrieved from this thesis' developed system and the receiver-related electrical impedance modulus values Z_{Rx} evaluated exploiting the BK Precision 891 LCR meter [68, 69].

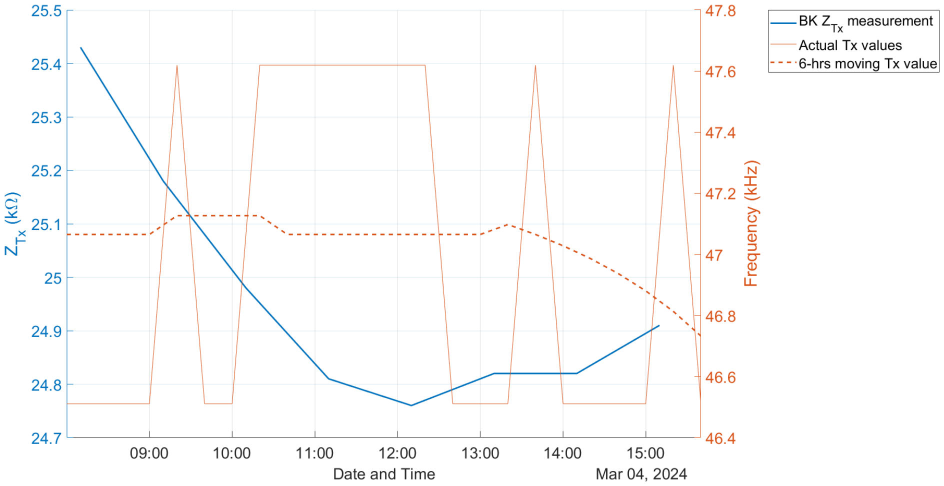

Figure 5.16: Comparison between the transmitter-related output retrieved from this thesis' developed system and the transmitter-related electrical impedance modulus values Z_{Tx} evaluated exploiting the BK Precision 891 LCR meter [68, 69].

For the sake of completeness, a further 11-day-long monitoring process exploiting the experimental setup previously described has been performed from March 8th, 2024 to March 19th, 2024. The experimentally obtained results have been collected and reported in Figure 5.17, Figure 5.18, Figure 5.19, and Figure 5.20. Inspecting the reported outcomes, all the considerations made above in this section have been validated.

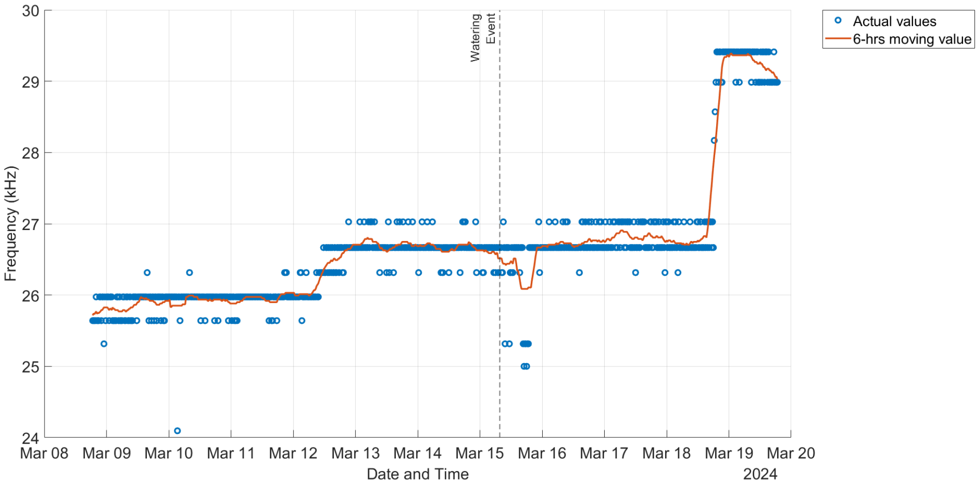

Figure 5.17: Receiver-related output evolution from March 8th, 2024 to March 19th, 2024.

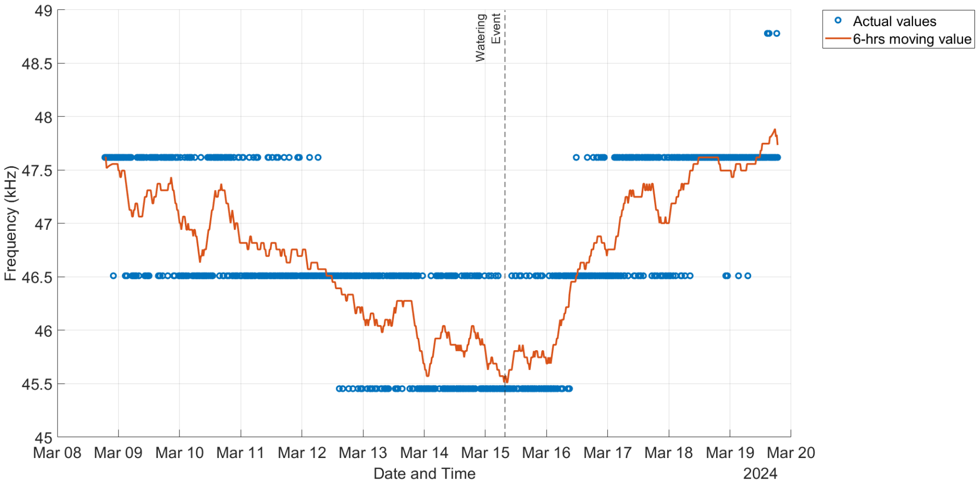

Figure 5.18: Transmitter-related output evolution from March 8th, 2024 to March 19th, 2024.

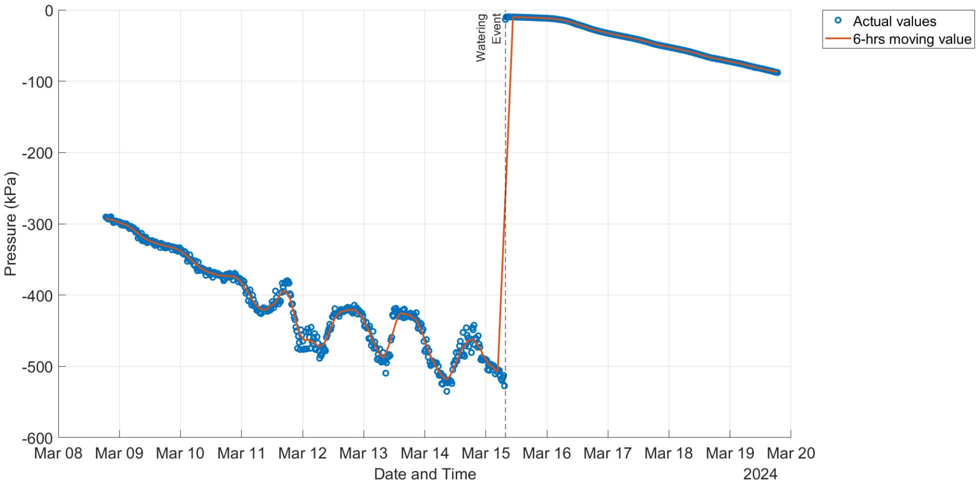

Figure 5.19: Soil water potential evolution from March 8th, 2024 to March 19th, 2024.

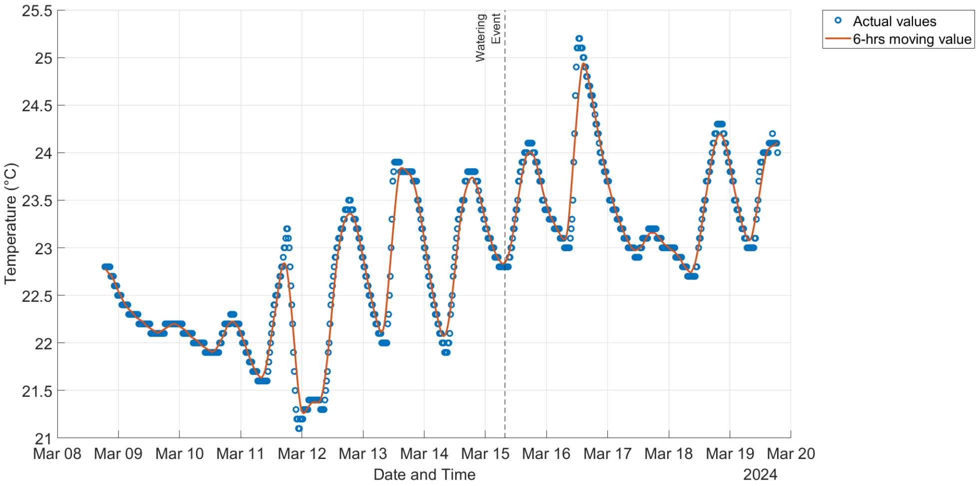

Figure 5.20: Soil water potential evolution from March 8th, 2024 to March 19th, 2024.

Focusing on the results in close temporal proximity of the watering event performed at 7:37 AM on March 15$^{\text{th}}$, 2024, it can be highlighted a relationship between some of the experimental setup outputs (for instance, receiver, transmitter, and soil water potential sensor produced values) and a watering event, coherently to what has been described before in this section. In particular, a watering event reduces the stem-related electrical impedance, forcing the receiver-related output frequency to reduce and the transmitter-related one to increase. Again, according to the experimentally obtained results, no significant variations can be associated with the soil temperature effect within this framework. The just-mentioned results have been depicted in Figure 5.21, Figure 5.22, Figure 5.23, and Figure 5.24, while in Figure 5.25 and Figure 5.26 employed plant conditions before and after the watering event occurred on March 15$^{\text{th}}$, 2024 have been reported.

For thoroughness, the power consumption of the developed monitoring system has been evaluated to estimate the number of monitoring operations allowed considering a 0.47-F supercapacitor. The considered supercapacitor is the one exploited in the multi-source power management system described in Altug's thesis work [18] and chosen as power supply for the developed Tx-plant-Rx system. As previously described in Chapter 2, a Zinc-Copper-based Plant Microbial Fuel Cell (PMFC) has been selected as the most suitable power supply in tandem with solar cells for this thesis-specific application in terms of power generation. The PMFC and the photovoltaic system have been designed to be employed as input for the multi-source power management system described in Altug's thesis work [18]. The energy-related worst situation is the one in case of absence of light (thus during the night or bad weather conditions) where the solar-cells-based system is unable to provide enough energy to accordingly charge the supercapacitor and therefore to supply the Tx-plant-Rx system energetically. To estimate the number of monitoring operations allowed considering the 0.47-F supercapacitor initially fully charged (as at the end of the day) and neglecting the contribution of the photovoltaic system (as during the night in the previously mentioned worst situation), only the best-performing PMFC (the Zinc-Copper configuration of PMFC 2 reported in Chapter 2 able to provide up to 51.050 μW) has been considered as input for the multi-source power management system described in Altug's thesis work [18]. According to the experimental setup and the timing-related choices reported in Chapter 4, a single monitoring operation is made up of 20 minutes of low-power microcontroller-specific operation (for instance, in Stop 2 with a measured 2.9 μA current consumption), followed by a 1-second LoRa communication of the retrieved results (with an estimated 42 mA current consumption). The relative current consumptions have been registered exploiting a 34401A bench-type multimeter from Agilent Technologies Inc. (now Keysight) [34] as employed multimeter. Within this framework, the supercapacitor initially stores 0.7167 J, while a 0.020604-J net energy consumption is associated with a single monitoring operation since 0.081864 J and 0.06126 J are, respectively, the energy consumed through a single monitoring operation and the energy provided by the employed PMFC during the same time frame (for instance, 20 minutes). Thus, almost 12 hours and 20 minutes of Tx-plant-Rx system monitoring operation can be accomplished considering the chosen PMFC as the only energy supply of the system.

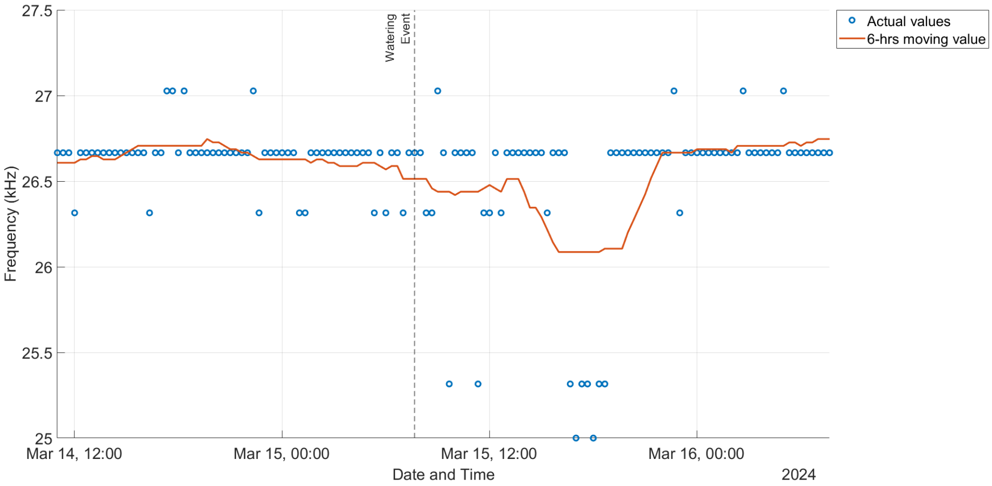

Figure 5.21: Zoom on the watering effect on receiver-related output evolution.

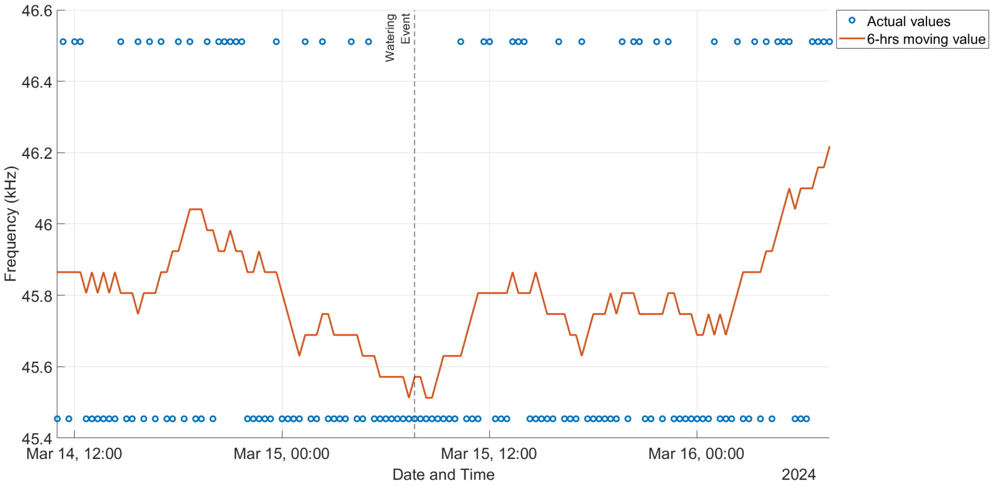

Figure 5.22: Zoom on the watering effect on transmitter-related output evolution.

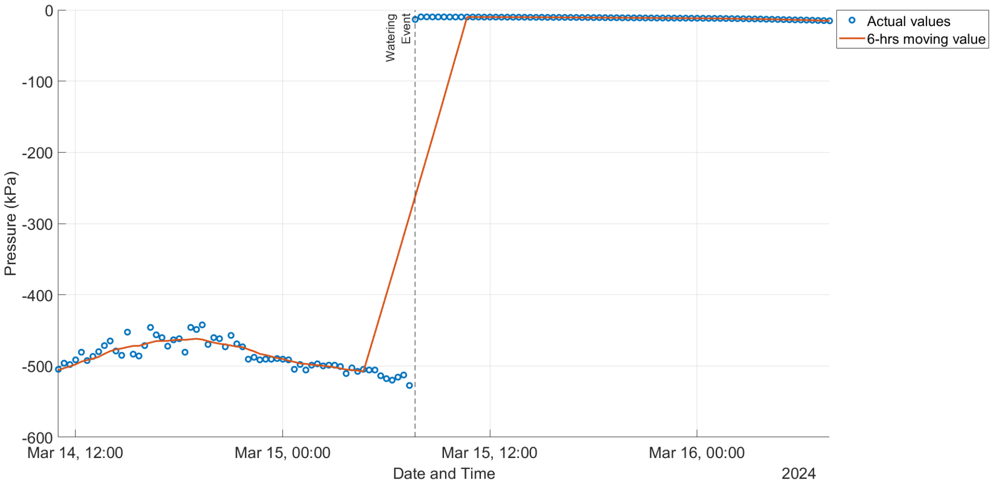

Figure 5.23: Zoom on the watering effect on soil water potential evolution.

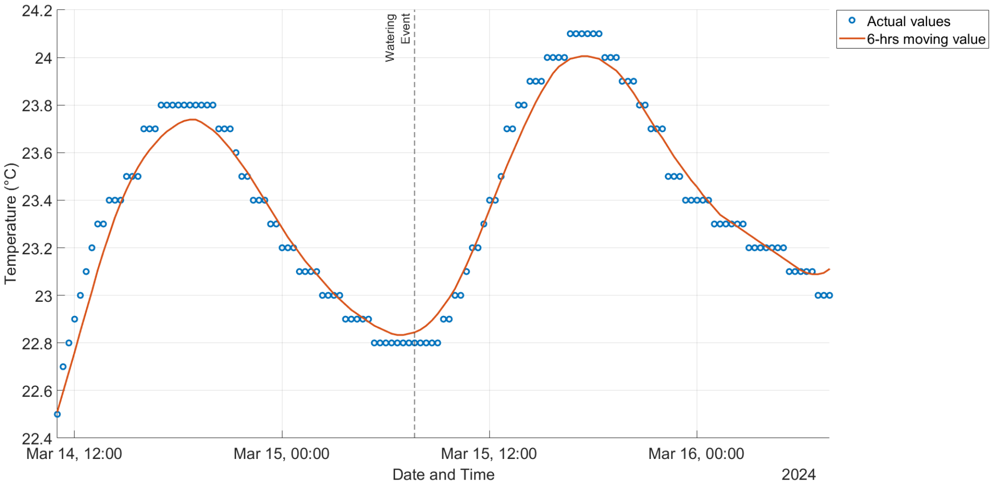

Figure 5.24: Zoom on the watering effect on soil temperature evolution.

Figure 5.25: Employed plant condition just few moments before the watering event performed on March 15th, 2024.

Figure 5.26: Employed plant condition three days after the watering event performed on March 15th, 2024 (thus on March 18th, 2024).

5.3 Conclusions

In this Chapter 5, the Tx-plant-RX system previously projected and characterized in Chapter 3 and Chapter 4 has been discussed and verified. The results retrieved in this chapter's dissertation have confirmed the validity of exploiting the developed monitoring system to evaluate plant-stem-specific electrical impedance modulus variations and their relationship with soil water potential and temperature, thus estimating the plant's overall health condition thanks to this thesis' developed system. In the end, the integration of the developed system with the best-performing Plant Microbial Fuel Cell (PMFC) studied in Chapter 2 has provided a more-than-interesting outcome.

Chapter 6

Conclusions

In this thesis project, an energetically self-sufficient measurement system able to evaluate the plant stem electrical bio-impedance has been developed. After a brief overview of the state-of-the-art in Chapter 1, the focus of Chapter 2 has been moved onto the performance inspection and characterization of several electrode materials combinations employed in a Plant Microbial Fuel Cell (PMFC) to work with photovoltaic (PV) cells as energy supply, further justifying the Zinc-Copper choice done in previous studies. However, aluminum plates may have positively affected the Zinc-Copper electrode configuration performance, while the Zinc-Aluminum electrode pair has provided strong results. In this regard, the influence of aluminum presence in Zinc-Copper-electrodes-based PMFCs may need to be further inspected in future works. In Chapter 3, the developed system used to estimate the plant stem electrical impedance has been designed and characterized: further implementation may include the PCB integration of the developed system, which firmware has been described in Chapter 4. In the end, in Chapter 5, the transmitter-plant-receiver system developed in this dissertation has been mounted on a tobacco plant, reporting strong and promising experimental results that have been further discussed. In the Appendix, more detailed data and information have been reported.

Appendix A

Power supply versus output frequency range

One of the goals required to be achieved through the design of this thesis project system consists in developing a low-power plant monitoring system.

Within this framework, a huge impact in overall power consumption is related to the selection of the most suitable power supply: in fact, it has to be both satisfactorily low to minimize power consumption and high enough to permit the smooth operation of all the components of the developed system.

Therefore, at design stage, the selection of the power supply has been performed exploiting a LTSpice simulation of the "50% Duty Cycle Oscillator" configuration reported at page 16 of the LMC555 datasheet [39]: in particular, the LTSpice simulated schematic reported in Figure A.1 has been studied exploiting a Linear Technology equivalent model of the LMC555 component (this latter produced by Texas Instruments) due to the default models of the Analog Devices and Linear Technology components present in the LTspice suite. Moreover, for the type of analysis performed at this design stage, the equivalent NE555 timer model is more than fair and proper.

In order to retrieve the output frequency range f_{out-Rx} results, the power supply level V_{supply} of the LTspice model in Figure A.1 has been modified from time to time ranging from 1.8 V to 3.3 V by a 0.1-V step. Considering the receiver structure discussed in Section 3.3, a square-wave signal $V_{pp-input}$ put as input of the receiver is firstly filtered and up-drifted with a $\frac{V_{supply}}{2}$ DC offset value V_{offset} thanks to

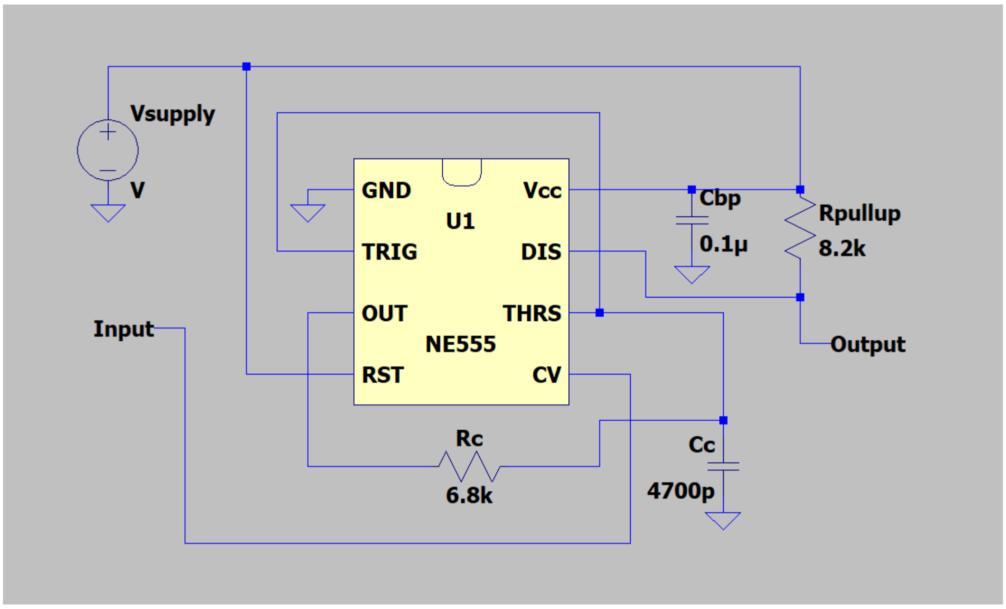

Figure A.1: Exploited LTspice model according to the developed receiver (see Section 3.3).

the input highpass filtering action (note Section 3.3.1), thereafter its peak value $V_{max-out}$ is detected by the peak detector (see Section 3.3.2) and finally presented as control input of the receiver-related voltage-controlled oscillator (note Section 3.3.4). The peak-to-peak input voltage $V_{pp-input}$ value ranges from 50 mV to 600 mV according to the receiver-specific input voltage ranges registered and reported in Chiarillo's work [20].

In Figure A.2 and Figure A.3, the results have been plotted: it is evident that the 1.8-V power supply case provide an higher output frequency range as well as lower power consumption than the other V_{supply} cases.

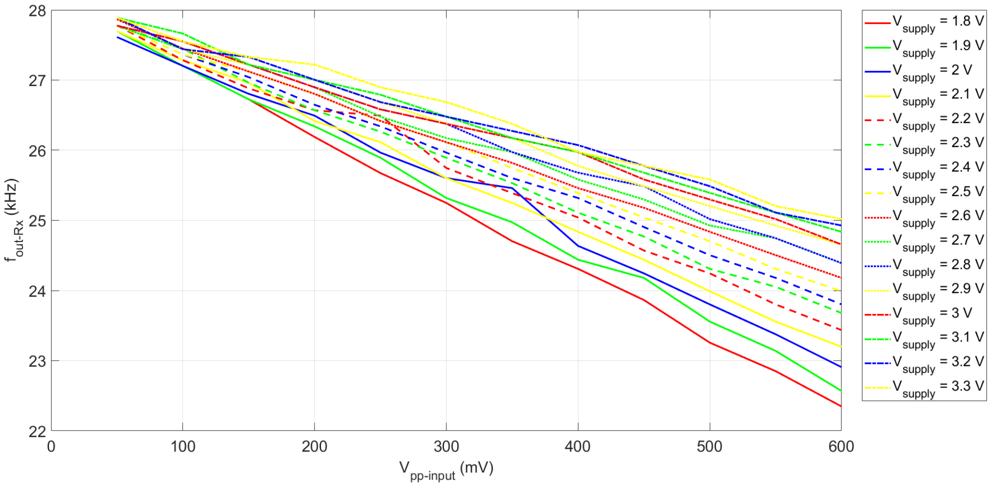

Figure A.2: Plot of the output frequency f_{out-Rx} for each power supply studied levels V_{supply}.

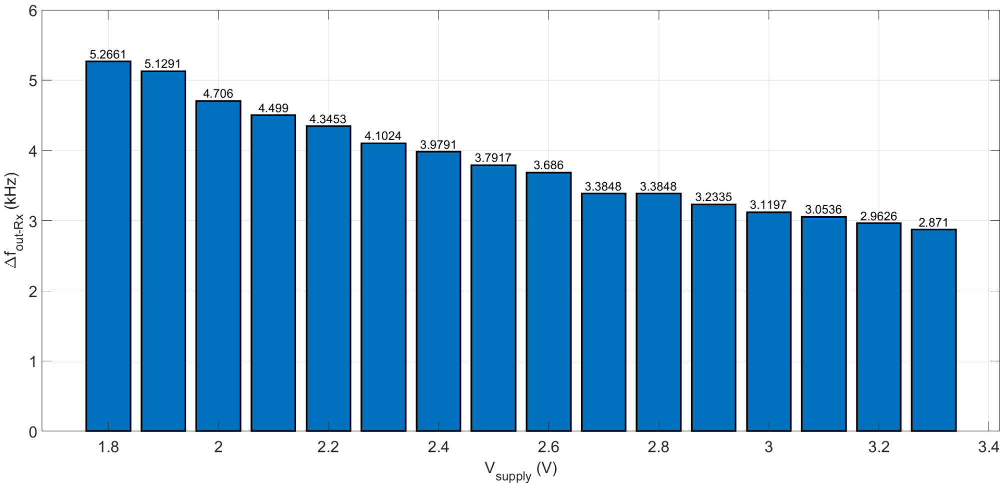

Figure A.3: Bar plot of the output frequency ranges for each power supply studied levels V_{supply}.

Appendix B

PMFCs registered data

In order to retrieve more information about the employed plant microbial fuel cells (PMFCs) and to have knowledge of their behaviour over time exploiting a tobacco plant (Nicotiana tabacum L.) and different electrode materials (Zinc, Aluminum and Copper), several characterization processes have been held as detailed in Chapter 2: in the following Section B.1, Section B.2, Section B.3 and Section B.4 the retrieved data have been organized and reported.

B.1 Characterization data of the Zinc-Copper PMFC 1

Plant number	PMFC 1		
Electrode materials	Zinc and Copper		
Characterization	#1		
Measurement day	02/11/2023		
Measurement start time	14:15		
Measurement end time	14:57		
Open circuit voltage	729 mV		
Resistance (Ω)	Voltage (mV)	Current (μA)	Power (μW)
120	11	91.67	1.008
180	14	77.78	1.089
270	19	70.37	1.337
390	25	64.10	1.603
560	32	57.14	1.829
820	44	53.66	2.361
1200	59	49.17	2.901
1800	80	44.44	3.556
2700	106	39.26	4.161
3900	136	34.87	4.743
5600	169	30.18	5.100
8200	205	25.00	5.125
12000	249	20.75	5.167
18000	296	16.44	4.868
27000	353	13.07	4.615
39000	423	10.85	4.588
56000	479	8.55	4.097
82000	536	6.54	3.504
120000	580	4.83	2.803
180000	613	3.41	2.088
270000	640	2.37	1.517
390000	659	1.69	1.114
560000	676	1.21	0.816
820000	674	0.82	0.554
1000000	691	0.69	0.477

Table B.1: Registered data of the 1^{st} characterization of the Zinc-Copper configuration of PMFC 1.

Plant number	PMFC 1		
Electrode materials	Zinc and Copper		
Characterization	#2		
Measurement day	15/11/2023		
Measurement start time	11:08		
Measurement end time	11:56		
Open circuit voltage	754 mV		
Resistance (Ω)	Voltage (mV)	Current (μA)	Power (μW)
120	10.2	85.00	0.867
180	12	66.67	0.800
270	17	62.96	1.070
390	24	61.54	1.477
560	32	57.14	1.829
820	45.5	55.49	2.525
1200	64.3	53.58	3.445
1800	87.8	48.78	4.283
2700	117.5	43.52	5.113
3900	148.4	38.05	5.647
5600	181.3	32.38	5.870
8200	220.9	26.94	5.951
12000	266.8	22.23	5.932
18000	318.1	17.67	5.622
27000	378.5	14.02	5.306
39000	442	11.33	5.009
56000	508.6	9.08	4.619
82000	536.8	6.55	3.514
120000	576.1	4.80	2.766
180000	601.8	3.34	2.012
270000	627.6	2.32	1.459
390000	642.8	1.65	1.059
560000	653.1	1.17	0.762
820000	667	0.81	0.543
1000000	673	0.67	0.453

Table B.2: Registered data of the 2nd characterization of the Zinc-Copper configuration of PMFC 1.

Plant number	PMFC 1		
Electrode materials	Zinc and Copper		
Characterization	#3		
Measurement day	28/11/2023		
Measurement start time	14:15		
Measurement end time	14:52		
Open circuit voltage	732 mV		
Resistance (Ω)	Voltage (mV)	Current (μA)	Power (μW)
120	7.5	62.50	0.469
180	11.2	62.22	0.697
270	16.1	59.63	0.960
390	23	58.97	1.356
560	31.7	56.61	1.794
820	44.3	54.02	2.393
1200	61.2	51.00	3.121
1800	84.8	47.11	3.995
2700	112.3	41.59	4.671
3900	144.8	37.13	5.376
5600	179.8	32.11	5.773
8200	219.5	26.77	5.876
12000	265.9	22.16	5.892
18000	314.5	17.47	5.495
27000	367.2	13.60	4.994
39000	427.8	10.97	4.693
56000	470.6	8.40	3.955
82000	514.1	6.27	3.223
120000	544.7	4.54	2.472
180000	588.4	3.27	1.923
270000	610.8	2.26	1.382
390000	625.3	1.60	1.003
560000	634.6	1.13	0.719
820000	645.9	0.79	0.509
1000000	650.2	0.65	0.423

Table B.3: Registered data of the 3$^{\text{rd}}$ characterization of the Zinc-Copper configuration of PMFC 1.

Plant number	PMFC 1		
Electrode materials	Zinc and Copper		
Characterization	#4		
Measurement day	13/12/2023		
Measurement start time	09:05		
Measurement end time	09:42		
Open circuit voltage	746 mV		
Resistance (Ω)	Voltage (mV)	Current (μA)	Power (μW)
120	15	125.00	1.875
180	21.2	117.78	2.497
270	29.6	109.63	3.245
390	40.5	103.85	4.206
560	54.2	96.79	5.246
820	72.6	88.54	6.428
1200	95.7	79.75	7.632
1800	123.8	68.78	8.515
2700	158.2	58.59	9.269
3900	193.4	49.59	9.591
5600	232.4	41.50	9.645
8200	277.4	33.83	9.384
12000	318.3	26.53	8.443
18000	369	20.50	7.565
27000	422.5	15.65	6.611
39000	528.4	13.55	7.159
56000	566	10.11	5.721
82000	603.7	7.36	4.445
120000	631.7	5.26	3.325
180000	649.5	3.61	2.344
270000	668	2.47	1.653
390000	682	1.75	1.193
560000	688	1.23	0.845
820000	693	0.85	0.586
1000000	696	0.70	0.484

Table B.4: Registered data of the 4th characterization of the Zinc-Copper configuration of PMFC 1.

Plant number	PMFC 1		
Electrode materials	Zinc and Copper		
Characterization	#5		
Measurement day	11/01/2024		
Measurement start time	13:05		
Measurement end time	13:43		
Open circuit voltage	740 mV		
Resistance (Ω)	Voltage (mV)	Current (μA)	Power (μW)
120	19.3	160.83	3.104
180	27.5	152.78	4.201
270	38.8	143.70	5.576
390	52.7	135.13	7.121
560	69.4	123.93	8.601
820	91.6	111.71	10.232
1200	119.1	99.25	11.821
1800	153.6	85.33	13.107
2700	193.1	71.52	13.810
3900	233.2	59.79	13.944
5600	272.7	48.70	13.280
8200	325.7	39.72	12.937
12000	366.2	30.52	11.175
18000	416.6	23.14	9.642
27000	472.6	17.50	8.272
39000	561.1	14.39	8.073
56000	600.5	10.72	6.439
82000	638.7	7.79	4.975
120000	661	5.51	3.641
180000	676	3.76	2.539
270000	688	2.55	1.753
390000	696	1.78	1.242
560000	702	1.25	0.880
820000	708	0.86	0.611
1000000	711	0.71	0.506

Table B.5: Registered data of the 5th characterization of the Zinc-Copper configuration of PMFC 1.

Plant number	PMFC 1		
Electrode materials	Zinc and Copper		
Characterization	#6		
Measurement day	25/01/2024		
Measurement start time	08:38		
Measurement end time	09:19		
Open circuit voltage	762 mV		
Resistance (Ω)	Voltage (mV)	Current (μA)	Power (μW)
120	15.3	127.50	1.951
180	20.8	115.56	2.404
270	29.6	109.63	3.245
390	40.6	104.10	4.227
560	55.3	98.75	5.461
820	73.9	90.12	6.660
1200	98.2	81.83	8.036
1800	129.7	72.06	9.346
2700	168.8	62.52	10.553
3900	207.7	53.26	11.061
5600	248.5	44.38	11.027
8200	295.9	36.09	10.678
12000	347.1	28.93	10.040
18000	400.7	22.26	8.920
27000	464.3	17.20	7.984
39000	543.4	13.93	7.571
56000	611.5	10.92	6.677
82000	647.9	7.90	5.119
120000	670	5.58	3.741
180000	685	3.81	2.607
270000	703	2.60	1.830
390000	708	1.82	1.285
560000	714	1.28	0.910
820000	718	0.88	0.629
1000000	721	0.72	0.520

Table B.6: Registered data of the 6th characterization of the Zinc-Copper configuration of PMFC 1.

Plant number	PMFC 1		
Electrode materials	Zinc and Copper		
Characterization	#7		
Measurement day	08/02/2024		
Measurement start time	08:14		
Measurement end time	09:04		
Open circuit voltage	790 mV		
Resistance (Ω)	Voltage (mV)	Current (μA)	Power (μW)
120	12.5	104.17	1.302
180	16.3	90.56	1.476
270	23.2	85.93	1.993
390	32.4	83.08	2.692
560	44.6	79.64	3.552
820	61.8	75.37	4.658
1200	83.9	69.92	5.866
1800	113.1	62.83	7.106
2700	148.8	55.11	8.201
3900	186.6	47.85	8.928
5600	228.3	40.77	9.307
8200	279.2	34.05	9.506
12000	342.1	28.51	9.753
18000	416.2	23.12	9.623
27000	487	18.04	8.784
39000	550.8	14.12	7.779
56000	593.2	10.59	6.284
82000	629.6	7.68	4.834
120000	653.6	5.45	3.560
180000	675	3.75	2.531
270000	687	2.54	1.748
390000	698	1.79	1.249
560000	705	1.26	0.888
820000	711	0.87	0.616
1000000	716	0.72	0.513

Table B.7: Registered data of the 7th characterization of the Zinc-Copper configuration of PMFC 1.

Plant number	PMFC 1		
Electrode materials	Zinc and Copper		
Characterization	#8		
Measurement day	21/02/2024		
Measurement start time	08:28		
Measurement end time	09:09		
Open circuit voltage	850 mV		
Resistance (Ω)	Voltage (mV)	Current (μA)	Power (μW)
120	12.2	101.67	1.240
180	17.3	96.11	1.663
270	25.1	92.96	2.333
390	35.3	90.51	3.195
560	49.9	89.11	4.446
820	69.4	84.63	5.874
1200	94.7	78.92	7.473
1800	128.2	71.22	9.131
2700	169.5	62.78	10.641
3900	210.8	54.05	11.394
5600	256	45.71	11.703
8200	309.1	37.70	11.652
12000	376.8	31.4	11.832
18000	456.1	25.34	11.557
27000	537	19.89	10.680
39000	602.3	15.44	9.302
56000	648.6	11.58	7.512
82000	689	8.40	5.789
120000	709	5.91	4.189
180000	728	4.04	2.944
270000	744	2.76	2.050
390000	757	1.94	1.469
560000	768	1.37	1.053
820000	778	0.95	0.738
1000000	780	0.78	0.608

Table B.8: Registered data of the 8th characterization of the Zinc-Copper configuration of PMFC 1.

Plant number	PMFC 1		
Electrode materials	Zinc and Copper		
Characterization	#9		
Measurement day	06/03/2024		
Measurement start time	08:32		
Measurement end time	09:17		
Open circuit voltage	826 mV		
Resistance (Ω)	Voltage (mV)	Current (μA)	Power (μW)
120	16.5	137.50	2.269
180	23.5	130.56	3.068
270	34	125.93	4.281
390	47.6	122.05	5.810
560	65.7	117.32	7.708
820	90.9	110.85	10.077
1200	123.9	103.25	12.793
1800	167.9	93.28	15.661
2700	224	82.96	18.584
3900	283.5	72.69	20.608
5600	350	62.50	21.875
8200	426.9	52.06	22.225
12000	579.6	48.30	27.995
18000	639.7	35.54	22.734
27000	687	25.44	17.480
39000	721	18.49	13.329
56000	744	13.29	9.885
82000	767	9.35	7.174
120000	775	6.46	5.005
180000	781	4.34	3.389
270000	798	2.96	2.359
390000	805	2.06	1.662
560000	811	1.45	1.175
820000	818	1.00	0.816
1000000	821	0.82	0.674

Table B.9: Registered data of the 9$^{\text{th}}$ characterization of the Zinc-Copper configuration of PMFC 1.

B.2 Characterization data of the Zinc-Copper PMFC 2

Plant number	PMFC 2		
Electrode materials	Zinc and Copper		
Characterization	#1		
Measurement day	02/11/2023		
Measurement start time	14:57		
Measurement end time	15:35		
Open circuit voltage	585 mV		
Resistance (Ω)	Voltage (mV)	Current (μA)	Power (μW)
120	0.9	7.50	0.007
180	1.2	6.67	0.008
270	1.7	6.30	0.011
390	2.3	5.90	0.014
560	3.1	5.54	0.017
820	4.5	5.49	0.025
1200	6.4	5.33	0.034
1800	9.5	5.28	0.050
2700	13.7	5.07	0.070
3900	18.8	4.82	0.091
5600	25.6	4.57	0.117
8200	36.2	4.41	0.160
12000	51.8	4.32	0.224
18000	71.7	3.98	0.286
27000	96.8	3.59	0.347
39000	126.6	3.25	0.411
56000	159.7	2.85	0.455
82000	200.3	2.44	0.489
120000	242	2.02	0.488
180000	292.1	1.62	0.474
270000	337.3	1.25	0.421
390000	385.6	0.99	0.381
560000	431.3	0.77	0.332
820000	491.8	0.60	0.295
1000000	500	0.50	0.250

Table B.10: Registered data of the 1^{st} characterization of the Zinc-Copper configuration of PMFC 2.

Plant number	PMFC 2		
Electrode materials	Zinc and Copper		
Characterization	#2		
Measurement day	15/11/2023		
Measurement start time	11:56		
Measurement end time	12:41		
Open circuit voltage	614 mV		
Resistance (Ω)	Voltage (mV)	Current (μA)	Power (μW)
120	1.5	12.50	0.019
180	1.8	10.00	0.018
270	2.2	8.15	0.018
390	2.8	7.18	0.020
560	3.7	6.61	0.024
820	4.9	5.98	0.029
1200	6.8	5.67	0.039
1800	9.6	5.33	0.051
2700	14	5.19	0.073
3900	19.1	4.90	0.094
5600	25.9	4.63	0.120
8200	35.6	4.34	0.155
12000	48.2	4.02	0.194
18000	64.7	3.59	0.233
27000	85.8	3.18	0.273
39000	108.1	2.77	0.300
56000	134.2	2.40	0.322
82000	167.4	2.04	0.342
120000	202.5	1.69	0.342
180000	244.8	1.36	0.333
270000	288.6	1.07	0.308
390000	322.7	0.83	0.267
560000	352.2	0.63	0.222
820000	390.8	0.48	0.186
1000000	403.1	0.40	0.162

Table B.11: Registered data of the 2$^{\text{nd}}$ characterization of the Zinc-Copper configuration of PMFC 2.

Plant number	PMFC 2		
Electrode materials	Zinc and Copper		
Characterization	#3		
Measurement day	28/11/2023		
Measurement start time	14:52		
Measurement end time	15:27		
Open circuit voltage	778 mV		
Resistance (Ω)	Voltage (mV)	Current (μA)	Power (μW)
120	4.2	35.00	0.147
180	5.8	32.22	0.187
270	8.1	30.00	0.243
390	10.6	27.18	0.288
560	13.4	23.93	0.321
820	17.8	21.71	0.386
1200	22.2	18.50	0.411
1800	29.8	16.56	0.493
2700	39	14.44	0.563
3900	50.8	13.03	0.662
5600	64.2	11.46	0.736
8200	85.9	10.48	0.900
12000	110.8	9.23	1.023
18000	144.8	8.04	1.165
27000	186.6	6.91	1.290
39000	231.9	5.95	1.379
56000	275.6	4.92	1.356
82000	324.1	3.95	1.281
120000	380.4	3.17	1.206
180000	434.9	2.42	1.051
270000	480.2	1.78	0.854
390000	512.8	1.31	0.674
560000	545.7	0.97	0.532
820000	574	0.70	0.402
1000000	586.6	0.59	0.344

Table B.12: Registered data of the 3rd characterization of the Zinc-Copper configuration of PMFC 2.

Plant number	PMFC 2		
Electrode materials	Zinc and Copper		
Characterization	#4		
Measurement day	13/12/2023		
Measurement start time	09:42		
Measurement end time	10:24		
Open circuit voltage	675 mV		
Resistance (Ω)	Voltage (mV)	Current (μA)	Power (μW)
120	1.4	11.67	0.016
180	1.8	10.00	0.018
270	2.6	9.63	0.025
390	3.6	9.23	0.033
560	4.9	8.75	0.043
820	6.4	7.80	0.050
1200	9.2	7.67	0.071
1800	13.1	7.28	0.095
2700	19.1	7.07	0.135
3900	26.5	6.79	0.180
5600	36.2	6.46	0.234
8200	49.3	6.01	0.296
12000	63.2	5.27	0.333
18000	86.5	4.81	0.416
27000	120.1	4.45	0.534
39000	151.6	3.89	0.589
56000	188.9	3.37	0.637
82000	235.4	2.87	0.676
120000	290.1	2.42	0.701
180000	338.3	1.88	0.636
270000	395.9	1.47	0.581
390000	442.9	1.14	0.503
560000	484.5	0.87	0.419
820000	531.2	0.65	0.344
1000000	546.5	0.55	0.299

Table B.13: Registered data of the 4th characterization of the Zinc-Copper configuration of PMFC 2.

Plant number	PMFC 2		
Electrode materials	Zinc and Copper		
Characterization	#5		
Measurement day	11/01/2024		
Measurement start time	13:43		
Measurement end time	14:21		
Open circuit voltage	800 mV		
Resistance (Ω)	Voltage (mV)	Current (μA)	Power (μW)
120	9.5	79.17	0.752
180	11.7	65.00	0.761
270	15	55.56	0.833
390	18.9	48.46	0.916
560	25.3	45.18	1.143
820	34.7	42.32	1.468
1200	47.8	39.83	1.904
1800	65.3	36.28	2.369
2700	90.4	33.48	3.027
3900	120.8	30.97	3.742
5600	153.5	27.41	4.208
8200	201.3	24.55	4.942
12000	251.7	20.98	5.279
18000	312.2	17.34	5.415
27000	377.3	13.97	5.272
39000	440.4	11.29	4.973
56000	496.8	8.87	4.407
82000	556.3	6.78	3.774
120000	609.1	5.08	3.092
180000	654	3.63	2.376
270000	690	2.56	1.763
390000	711	1.82	1.296
560000	728	1.30	0.946
820000	741	0.90	0.670
1000000	747	0.75	0.558

Table B.14: Registered data of the 5th characterization of the Zinc-Copper configuration of PMFC 2.

Plant number	PMFC 2		
Electrode materials	Zinc and Copper		
Characterization	#6		
Measurement day	25/01/2024		
Measurement start time	09:19		
Measurement end time	10:01		
Open circuit voltage	964 mV		
Resistance (Ω)	Voltage (mV)	Current (μA)	Power (μW)
120	14.1	117.5	1.657
180	22.9	127.22	2.913
270	33.1	122.59	4.058
390	46.8	120	5.616
560	67.3	120.18	8.088
820	100.5	122.56	12.317
1200	125.4	104.5	13.104
1800	184	102.22	18.809
2700	247.3	91.59	22.651
3900	296.7	76.08	22.572
5600	331.6	59.21	19.635
8200	382.6	46.66	17.852
12000	432.2	36.02	15.566
18000	487.7	27.09	13.214
27000	546.1	20.23	11.045
39000	600.6	15.40	9.249
56000	651.7	11.64	7.584
82000	700	8.54	5.976
120000	731	6.09	4.453
180000	754	4.19	3.158
270000	777	2.88	2.236
390000	788	2.02	1.592
560000	797	1.42	1.134
820000	808	0.99	0.796
1000000	814	0.81	0.663

Table B.15: Registered data of the 6th characterization of the Zinc-Copper configuration of PMFC 2.

Plant number	PMFC 2		
Electrode materials	Zinc and Copper		
Characterization	#7		
Measurement day	08/02/2024		
Measurement start time	09:04		
Measurement end time	09:58		
Open circuit voltage	952 mV		
Resistance (Ω)	Voltage (mV)	Current (μA)	Power (μW)
120	12.1	100.83	1.220
180	16.6	92.22	1.531
270	26.2	97.04	2.542
390	39.2	100.51	3.940
560	57.6	102.86	5.925
820	83.5	101.83	8.503
1200	115.7	96.42	11.155
1800	157	87.22	13.694
2700	206	76.30	15.717
3900	254.2	65.18	16.569
5600	303.3	54.16	16.427
8200	360.2	43.93	15.822
12000	413.5	34.46	14.249
18000	470.5	26.14	12.298
27000	531.7	19.69	10.471
39000	592.8	15.20	9.011
56000	644.8	11.51	7.424
82000	689	8.40	5.789
120000	721	6.01	4.332
180000	741	4.12	3.050
270000	758	2.81	2.128
390000	773	1.98	1.532
560000	797	1.42	1.134
820000	807	0.98	0.794
1000000	814	0.81	0.663

Table B.16: Registered data of the 7th characterization of the Zinc-Copper configuration of PMFC 2.

Plant number	PMFC 2		
Electrode materials	Zinc and Copper		
Characterization	#8		
Measurement day	21/02/2024		
Measurement start time	09:09		
Measurement end time	09:40		
Open circuit voltage	875 mV		
Resistance (Ω)	Voltage (mV)	Current (μA)	Power (μW)
120	27.3	227.50	6.211
180	39.8	221.11	8.800
270	57.8	214.07	12.373
390	80.3	205.90	16.534
560	109.6	195.71	21.450
820	150.8	183.90	27.732
1200	201.8	168.17	33.936
1800	270.5	150.28	40.650
2700	349.8	129.56	45.319
3900	427.6	109.64	46.883
5600	504.8	90.14	45.504
8200	581.9	70.96	41.294
12000	652.4	54.37	35.469
18000	707	39.28	27.769
27000	751	27.81	20.889
39000	780	20.00	15.600
56000	801	14.30	11.457
82000	819	9.99	8.180
120000	834	6.95	5.796
180000	845	4.69	3.967
270000	853	3.16	2.695
390000	859	2.20	1.892
560000	864	1.54	1.333
820000	867	1.06	0.917
1000000	871	0.87	0.759

Table B.17: Registered data of the 8th characterization of the Zinc-Copper configuration of PMFC 2.

Plant number	PMFC 2		
Electrode materials	Zinc and Copper		
Characterization	#9		
Measurement day	06/03/2024		
Measurement start time	09:19		
Measurement end time	09:55		
Open circuit voltage	884 mV		
Resistance (Ω)	Voltage (mV)	Current (μA)	Power (μW)
120	28.8	240.00	6.912
180	41.8	232.22	9.707
270	61	225.93	13.781
390	85.1	218.21	18.569
560	116.3	207.68	24.153
820	159.7	194.76	31.103
1200	214.2	178.50	38.235
1800	284.1	157.83	44.840
2700	366.3	135.67	49.695
3900	446.2	114.41	51.050
5600	523.8	93.54	48.994
8200	600.4	73.22	43.961
12000	667	55.58	37.074
18000	718	39.89	28.640
27000	758	28.07	21.280
39000	788	20.21	15.922
56000	812	14.50	11.774
82000	828	10.10	8.361
120000	842	7.02	5.908
180000	853	4.74	4.042
270000	865	3.20	2.771
390000	871	2.23	1.945
560000	875	1.56	1.367
820000	880	1.07	0.944
1000000	882	0.88	0.778

Table B.18: Registered data of the 9th characterization of the Zinc-Copper configuration of PMFC 2.

B.3 Characterization data of the Zinc-Aluminum PMFC 2

Plant number	PMFC 2		
Electrode materials	Zinc and Aluminum		
Characterization	#1		
Measurement day	02/11/2023		
Measurement start time	15:35		
Measurement end time	16:09		
Open circuit voltage	167 mV		
Resistance (Ω)	Voltage (mV)	Current (μA)	Power (μW)
120	0.2	1.67	0.0003
180	0.3	1.67	0.0005
270	0.4	1.48	0.0006
390	0.6	1.54	0.0009
560	0.9	1.61	0.0014
820	1.2	1.46	0.0018
1200	1.8	1.50	0.0027
1800	2.5	1.39	0.0035
2700	3.7	1.37	0.0051
3900	5.5	1.41	0.0078
5600	7.6	1.36	0.010
8200	10.9	1.33	0.014
12000	15.1	1.26	0.019
18000	21.1	1.17	0.025
27000	29.2	1.08	0.032
39000	38.9	1.00	0.039
56000	50.2	0.90	0.045
82000	62.9	0.77	0.048
120000	76.7	0.64	0.049
180000	92.2	0.51	0.047
270000	106.4	0.39	0.042
390000	118	0.30	0.036
560000	129.6	0.23	0.030
820000	139.8	0.17	0.024
1000000	143.5	0.14	0.021

Table B.19: Registered data of the 1^{st} characterization of the Zinc-Aluminum configuration of PMFC 2.

Plant number	PMFC 2		
Electrode materials	Zinc and Aluminum		
Characterization	#2		
Measurement day	15/11/2023		
Measurement start time	12:41		
Measurement end time	13:19		
Open circuit voltage	124.2 mV		
Resistance (Ω)	Voltage (mV)	Current (μA)	Power (μW)
120	0.1	0.83	0.0001
180	0.1	0.56	0.0001
270	0.2	0.74	0.0001
390	0.3	0.77	0.0002
560	0.4	0.71	0.0003
820	0.6	0.73	0.0004
1200	0.8	0.67	0.0005
1800	1.2	0.67	0.0008
2700	1.8	0.67	0.0012
3900	2.5	0.64	0.0016
5600	3.6	0.64	0.0023
8200	5.1	0.62	0.0032
12000	7.2	0.60	0.0043
18000	10	0.56	0.0056
27000	14.1	0.52	0.0074
39000	19.4	0.50	0.0097
56000	25.5	0.46	0.012
82000	32.4	0.40	0.013
120000	42.2	0.35	0.015
180000	52.4	0.29	0.015
270000	61.7	0.23	0.014
390000	70.8	0.18	0.013
560000	78.4	0.14	0.011
820000	83.9	0.10	0.0086
1000000	98.4	0.10	0.0097

Table B.20: Registered data of the 2$^{\text{nd}}$ characterization of the Zinc-Aluminum configuration of PMFC 2.

Plant number	PMFC 2		
Electrode materials	Zinc and Aluminum		
Characterization	#3		
Measurement day	28/11/2023		
Measurement start time	15:27		
Measurement end time	15:55		
Open circuit voltage	276 mV		
Resistance (Ω)	Voltage (mV)	Current (μA)	Power (μW)
120	1.7	14.17	0.024
180	2.1	11.67	0.025
270	3.1	11.48	0.036
390	4.4	11.28	0.050
560	6.2	11.07	0.069
820	8.8	10.73	0.094
1200	12.7	10.58	0.134
1800	17.6	9.78	0.172
2700	24.7	9.15	0.226
3900	32.4	8.31	0.269
5600	41.3	7.38	0.305
8200	52.9	6.45	0.341
12000	66.3	5.53	0.366
18000	81.9	4.55	0.373
27000	99.2	3.67	0.364
39000	117.6	3.02	0.355
56000	136.4	2.44	0.332
82000	160.5	1.96	0.314
120000	178.6	1.49	0.266
180000	209.6	1.16	0.244
270000	224.8	0.83	0.187
390000	241.2	0.62	0.149
560000	252.6	0.45	0.114
820000	264.6	0.32	0.085
1000000	270.2	0.27	0.073

Table B.21: Registered data of the 3$^{\text{rd}}$ characterization of the Zinc-Aluminum configuration of PMFC 2.

Plant number	PMFC 2		
Electrode materials	Zinc and Aluminum		
Characterization	#4		
Measurement day	13/12/2023		
Measurement start time	10:24		
Measurement end time	11:00		
Open circuit voltage	352 mV		
Resistance (Ω)	Voltage (mV)	Current (μA)	Power (μW)
120	3.1	25.83	0.080
180	4.8	26.67	0.128
270	7.2	26.67	0.192
390	10.4	26.67	0.277
560	14.6	26.07	0.381
820	20.7	25.24	0.523
1200	28.6	23.83	0.682
1800	39.5	21.94	0.867
2700	52.7	19.52	1.029
3900	66.8	17.13	1.144
5600	81.8	14.61	1.195
8200	99.2	12.10	1.200
12000	117.3	9.78	1.147
18000	136.6	7.59	1.037
27000	156.6	5.80	0.908
39000	174.8	4.48	0.783
56000	191.7	3.42	0.656
82000	209.7	2.56	0.536
120000	230.6	1.92	0.443
180000	246.9	1.37	0.339
270000	264.5	0.98	0.259
390000	277.3	0.71	0.197
560000	295.8	0.53	0.156
820000	306.1	0.37	0.114
1000000	327.4	0.33	0.107

Table B.22: Registered data of the 4th characterization of the Zinc-Aluminum configuration of PMFC 2.

Plant number	PMFC 2		
Electrode materials	Zinc and Aluminum		
Characterization	#5		
Measurement day	11/01/2024		
Measurement start time	14:21		
Measurement end time	15:00		
Open circuit voltage	353.4 mV		
Resistance (Ω)	Voltage (mV)	Current (μA)	Power (μW)
120	8.6	71.67	0.616
180	12.9	71.67	0.925
270	19.1	70.74	1.351
390	26.7	68.46	1.828
560	36.5	65.18	2.379
820	50.1	61.10	3.061
1200	66.7	55.58	3.707
1800	88.5	49.17	4.351
2700	112.7	41.74	4.704
3900	136.2	34.92	4.757
5600	158.9	28.38	4.509
8200	184.5	22.50	4.151
12000	207.6	17.30	3.591
18000	229.5	12.75	2.926
27000	249.8	9.25	2.311
39000	265.9	6.82	1.813
56000	280.6	5.01	1.406
82000	292.7	3.57	1.045
120000	305.2	2.54	0.776
180000	313.1	1.74	0.545
270000	320.9	1.19	0.381
390000	325.5	0.83	0.272
560000	328.6	0.59	0.193
820000	331.8	0.40	0.134
1000000	332.4	0.33	0.110

Table B.23: Registered data of the 5th characterization of the Zinc-Aluminum configuration of PMFC 2.

Plant number	PMFC 2		
Electrode materials	Zinc and Aluminum		
Characterization	#6		
Measurement day	25/01/2024		
Measurement start time	10:01		
Measurement end time	10:47		
Open circuit voltage	493.1 mV		
Resistance (Ω)	Voltage (mV)	Current (μA)	Power (μW)
120	20.9	174.17	3.640
180	30.6	170.00	5.202
270	42.1	155.93	6.564
390	57.1	146.41	8.360
560	76.4	136.43	10.423
820	102.3	124.76	12.763
1200	133.2	111.00	14.785
1800	171.9	95.50	16.416
2700	214.7	79.52	17.073
3900	255.5	65.51	16.739
5600	295.7	52.80	15.614
8200	336.6	41.05	13.817
12000	373.1	31.09	11.600
18000	410.3	22.79	9.353
27000	435.2	16.12	7.015
39000	453.8	11.64	5.280
56000	467.2	8.34	3.898
82000	478.5	5.84	2.792
120000	485.9	4.05	1.967
180000	492.3	2.74	1.346
270000	496.6	1.84	0.913
390000	500.1	1.28	0.641
560000	501.1	0.89	0.448
820000	501.7	0.61	0.307
1000000	501.9	0.50	0.252

Table B.24: Registered data of the 6$^{\text{th}}$ characterization of the Zinc-Aluminum configuration of PMFC 2.

Plant number	PMFC 2		
Electrode materials	Zinc and Aluminum		
Characterization	#7		
Measurement day	08/02/2024		
Measurement start time	09:58		
Measurement end time	10:43		
Open circuit voltage	476.7 mV		
Resistance (Ω)	Voltage (mV)	Current (μA)	Power (μW)
120	19.4	161.67	3.136
180	27.1	150.56	4.080
270	39.1	144.81	5.662
390	53	135.90	7.203
560	71.1	126.96	9.027
820	95.9	116.95	11.216
1200	125.8	104.83	13.188
1800	163.1	90.61	14.779
2700	205.3	76.04	15.610
3900	245.2	62.87	15.416
5600	284.6	50.82	14.464
8200	328.7	40.09	13.176
12000	361.8	30.15	10.908
18000	391.6	21.76	8.519
27000	416	15.41	6.409
39000	434.6	11.14	4.843
56000	446.3	7.97	3.557
82000	457.1	5.57	2.548
120000	462.8	3.86	1.785
180000	468.2	2.60	1.218
270000	472.5	1.75	0.827
390000	475	1.22	0.579
560000	476.4	0.85	0.405
820000	477.6	0.58	0.278
1000000	480	0.48	0.230

Table B.25: Registered data of the 7^{th} characterization of the Zinc-Aluminum configuration of PMFC 2.

B.4 Characterization data of the Copper-Aluminum PMFC 2

Plant number	PMFC 2		
Electrode materials	Copper and Aluminum		
Characterization	#1		
Measurement day	02/11/2023		
Measurement start time	16:09		
Measurement end time	17:17		
Open circuit voltage	435 mV		
Resistance (Ω)	Voltage (mV)	Current (μA)	Power (μW)
120	1.8	15.00	0.027
180	2.2	12.22	0.027
270	2.9	10.74	0.031
390	4.1	10.51	0.043
560	5.6	10.00	0.056
820	7.8	9.51	0.074
1200	11.2	9.33	0.105
1800	15.5	8.61	0.133
2700	22.2	8.22	0.183
3900	31	7.95	0.246
5600	41.8	7.46	0.312
8200	57.9	7.06	0.409
12000	79.6	6.63	0.528
18000	103.9	5.77	0.600
27000	133.3	4.94	0.658
39000	170.3	4.37	0.744
56000	199.2	3.56	0.709
82000	237.8	2.90	0.690
120000	271.9	2.27	0.616
180000	300	1.67	0.500
270000	327.9	1.21	0.398
390000	345.1	0.88	0.305
560000	371.1	0.66	0.246
820000	381.5	0.47	0.177
1000000	391.1	0.39	0.153

Table B.26: Registered data of the 1^{st} characterization of the Copper-Aluminum configuration of PMFC 2.

Plant number	PMFC 2		
Electrode materials	Copper and Aluminum		
Characterization	#2		
Measurement day	15/11/2023		
Measurement start time	13:19		
Measurement end time	14:03		
Open circuit voltage	414.3 mV		
Resistance (Ω)	Voltage (mV)	Current (μA)	Power (μW)
120	2.7	22.50	0.061
180	3.2	17.78	0.057
270	4.5	16.67	0.075
390	6.3	16.15	0.102
560	7.9	14.11	0.111
820	10.7	13.05	0.140
1200	14.8	12.33	0.183
1800	20.1	11.17	0.224
2700	27.5	10.19	0.280
3900	35.8	9.18	0.329
5600	47.5	8.48	0.403
8200	61.5	7.50	0.461
12000	80.2	6.68	0.536
18000	108.2	6.01	0.650
27000	139.9	5.18	0.725
39000	175.6	4.50	0.791
56000	208.8	3.73	0.779
82000	244.5	2.98	0.729
120000	271.5	2.26	0.614
180000	298.4	1.66	0.495
270000	335.2	1.24	0.416
390000	346.9	0.89	0.309
560000	367.2	0.66	0.241
820000	375.4	0.46	0.172
1000000	380.3	0.38	0.145

Table B.27: Registered data of the 2$^{\text{nd}}$ characterization of the Copper-Aluminum configuration of PMFC 2.

Plant number	PMFC 2		
Electrode materials	Copper and Aluminum		
Characterization	#3		
Measurement day	28/11/2023		
Measurement start time	15:55		
Measurement end time	16:43		
Open circuit voltage	402.3 mV		
Resistance (Ω)	Voltage (mV)	Current (μA)	Power (μW)
120	2.1	17.50	0.037
180	2.6	14.44	0.038
270	3.5	12.96	0.045
390	4.9	12.56	0.062
560	6.3	11.25	0.071
820	8.4	10.24	0.086
1200	11.9	9.92	0.118
1800	17.1	9.50	0.162
2700	22.8	8.44	0.193
3900	29.5	7.56	0.223
5600	39.9	7.13	0.284
8200	54.8	6.68	0.366
12000	76.8	6.40	0.492
18000	102.4	5.69	0.583
27000	133	4.93	0.655
39000	162.6	4.17	0.678
56000	195.7	3.49	0.684
82000	230.1	2.81	0.646
120000	255.8	2.13	0.545
180000	277.5	1.54	0.428
270000	293.2	1.09	0.318
390000	306.8	0.79	0.241
560000	317.1	0.57	0.180
820000	336.5	0.41	0.138
1000000	350.2	0.35	0.123

Table B.28: Registered data of the 3rd characterization of the Copper-Aluminum configuration of PMFC 2.

Plant number	PMFC 2		
Electrode materials	Copper and Aluminum		
Characterization	#4		
Measurement day	13/12/2023		
Measurement start time	11:00		
Measurement end time	11:38		
Open circuit voltage	339.7 mV		
Resistance (Ω)	Voltage (mV)	Current (μA)	Power (μW)
120	1	8.33	0.008
180	1	5.56	0.006
270	1.3	4.81	0.006
390	1.7	4.36	0.007
560	2.3	4.11	0.009
820	3.1	3.78	0.012
1200	4.4	3.67	0.016
1800	6.3	3.50	0.022
2700	9.2	3.41	0.031
3900	13.1	3.36	0.044
5600	18	3.21	0.058
8200	25.5	3.11	0.079
12000	35.3	2.94	0.104
18000	48.7	2.71	0.132
27000	66.9	2.48	0.166
39000	90.5	2.32	0.210
56000	111.8	2.00	0.223
82000	139.3	1.70	0.237
120000	165.4	1.38	0.228
180000	196.4	1.09	0.214
270000	215.5	0.80	0.172
390000	236	0.61	0.143
560000	247.6	0.44	0.109
820000	256.9	0.31	0.080
1000000	282.2	0.28	0.080

Table B.29: Registered data of the 4th characterization of the Copper-Aluminum configuration of PMFC 2.

Plant number	PMFC 2		
Electrode materials	Copper and Aluminum		
Characterization	#5		
Measurement day	11/01/2024		
Measurement start time	15:00		
Measurement end time	15:40		
Open circuit voltage	455.4 mV		
Resistance (Ω)	Voltage (mV)	Current (μA)	Power (μW)
120	4	33.33	0.133
180	5.1	28.33	0.145
270	7.1	26.30	0.187
390	9.1	23.33	0.212
560	12.2	21.79	0.266
820	16.9	20.61	0.348
1200	23.6	19.67	0.464
1800	33.9	18.83	0.638
2700	48.3	17.89	0.864
3900	66.1	16.95	1.120
5600	89.7	16.02	1.437
8200	114.9	14.01	1.610
12000	146.3	12.19	1.784
18000	181.6	10.09	1.832
27000	222.3	8.23	1.830
39000	262.3	6.73	1.764
56000	296.8	5.30	1.573
82000	336.5	4.10	1.381
120000	362.4	3.02	1.094
180000	384.3	2.14	0.820
270000	398.7	1.48	0.589
390000	408.4	1.05	0.428
560000	413.4	0.74	0.305
820000	421.7	0.51	0.217
1000000	427.8	0.43	0.183

Table B.30: Registered data of the 5$^{\text{th}}$ characterization of the Copper-Aluminum configuration of PMFC 2.

Plant number	PMFC 2		
Electrode materials	Copper and Aluminum		
Characterization	#6		
Measurement day	25/01/2024		
Measurement start time	10:47		
Measurement end time	11:27		
Open circuit voltage	397.5 mV		
Resistance (Ω)	Voltage (mV)	Current (μA)	Power (μW)
120	1.7	14.17	0.024
180	2.3	12.78	0.029
270	3.3	12.22	0.040
390	4.7	12.05	0.057
560	6.7	11.96	0.080
820	9.7	11.83	0.115
1200	14.2	11.83	0.168
1800	21.5	11.94	0.257
2700	30.6	11.33	0.347
3900	42.8	10.97	0.470
5600	58.5	10.45	0.611
8200	81.6	9.95	0.812
12000	108.5	9.04	0.981
18000	143	7.94	1.136
27000	181.5	6.72	1.220
39000	222.5	5.71	1.269
56000	247.6	4.42	1.095
82000	270.1	3.29	0.890
120000	291.7	2.43	0.709
180000	313.6	1.74	0.546
270000	329.8	1.22	0.403
390000	337.3	0.86	0.292
560000	343.3	0.61	0.210
820000	348.5	0.43	0.148
1000000	355.6	0.36	0.126

Table B.31: Registered data of the 6th characterization of the Copper-Aluminum configuration of PMFC 2.

Plant number	PMFC 2		
Electrode materials	Copper and Aluminum		
Characterization	#7		
Measurement day	08/02/2024		
Measurement start time	10:43		
Measurement end time	11:19		
Open circuit voltage	409.2 mV		
Resistance (Ω)	Voltage (mV)	Current (μA)	Power (μW)
120	2	16.67	0.033
180	2.7	15	0.041
270	3.9	14.44	0.056
390	5.4	13.85	0.075
560	7.6	13.57	0.103
820	10.9	13.29	0.145
1200	15.7	13.08	0.205
1800	23.2	12.89	0.299
2700	34.2	12.67	0.433
3900	47.6	12.21	0.581
5600	65.2	11.64	0.759
8200	89	10.85	0.966
12000	120.4	10.03	1.208
18000	157.8	8.77	1.383
27000	197	7.30	1.437
39000	232.1	5.95	1.381
56000	262.5	4.69	1.230
82000	290.8	3.55	1.031
120000	312.7	2.61	0.815
180000	331.5	1.84	0.611
270000	346.6	1.28	0.445
390000	357.9	0.92	0.328
560000	366.5	0.65	0.240
820000	372.7	0.45	0.169
1000000	381.3	0.38	0.145

Table B.32: Registered data of the 7th characterization of the Copper-Aluminum configuration of PMFC 2.

Appendix C

Developed system characterization data

C.1 Receiver characterization without plant data

$f_{in-instr} = 1$ kHz				
$V_{pp-in-instr}$ (mV)	V_{pp-in} (mV)	V_{max-in} (mV)	$V_{max-out}$ (mV)	f_{out-Rx} (kHz)
100	24.41	904.6	906.7	25.57
110	25.58	905.8	906.7	25.55
120	26.74	906.9	908.9	25.54
130	27.9	906.9	910	25.52
140	27.9	908.1	911.1	25.52
150	29.07	908.1	912.2	25.51
160	30.23	908.1	912.2	25.5
170	31.39	908.1	912.2	25.49
180	31.39	909.3	912.2	25.49
190	32.55	909.3	912.2	25.47
200	34.88	910.4	913.3	25.47

Table C.1: Results of the plant-less instrumentation-only receiver-related characterization process exploiting an input 1-kHz sine waveform with peak-to-peak amplitude ranging from 100 mV to 200 mV.

$f_{in-instr} = 1$ kHz				
$V_{pp-in-instr}$ (mV)	V_{pp-in} (mV)	V_{max-in} (mV)	$V_{max-out}$ (mV)	f_{out-Rx} (kHz)
210	34.88	910.4	913.3	25.46
220	36.04	911.6	913.3	25.46
230	36.04	911.6	913.3	25.41
240	37.2	912.7	913.3	25.39
250	38.37	912.7	914.4	25.38
260	39.53	913.9	917.7	25.38
270	39.53	913.9	917.7	25.39
280	40.69	915.1	917.7	25.39
290	41.86	915.1	917.7	25.38
300	43.02	916.2	918.8	25.37
310	44.18	916.2	918.8	25.37
320	45.34	917.4	921	25.37
330	46.51	917.4	921	25.36
340	46.51	917.4	921	25.36
350	48.83	918.6	922.1	25.35
360	48.83	918.6	923.2	25.35
370	48.83	918.6	923.2	25.34
380	51.16	920.9	923.2	25.3
390	51.16	920.9	923.2	25.29
400	52.32	920.9	924.3	25.3
410	53.48	920.9	924.3	25.27
420	54.65	920.9	924.3	25.25
430	55.81	922.1	925.4	25.24
440	56.97	922.1	925.4	25.25
450	56.97	923.2	925.4	25.24
460	58.14	923.2	925.4	25.23
470	59.3	924.4	925.4	25.23
480	60.46	925.5	926.5	25.22
490	61.62	925.5	926.5	25.21
500	62.79	926.7	927.6	25.2

Table C.2: Results of the plant-less instrumentation-only receiver-related characterization process exploiting an input 1-kHz sine waveform with peak-to-peak amplitude ranging from 210 mV to 500 mV.

$f_{in-instr}$ = 10 kHz				
$V_{pp-in-instr}$ (mV)	V_{pp-in} (mV)	V_{max-in} (mV)	$V_{max-out}$ (mV)	f_{out-Rx} (kHz)
100	138.3	948.5	955.9	25.01
110	138.3	948.5	955.9	24.95
120	138.3	948.5	955.9	24.91
130	158	968.3	975	24.86
140	158	968.3	975	24.81
150	177.8	968.3	975	24.76
160	177.8	968.3	975	24.71
170	177.8	968.3	975	24.65
180	197.6	988	994.1	24.6
190	197.6	988	994.1	24.54
200	197.6	988	994.1	24.48
210	217.3	988	994.1	24.43
220	217.3	988	994.1	24.39
230	217.3	988	994.1	24.32
240	237.1	1007	1013	24.28
250	237.1	1007	1013	24.23
260	237.1	1007	1013	24.18
270	256.9	1007	1013	24.12
280	256.9	1007	1013	24.06
290	256.9	1007	1013	24.01
300	276.6	1027	1032	23.95

Table C.3: Results of the plant-less instrumentation-only receiver-related characterization process exploiting an input 10-kHz sine waveform with peak-to-peak amplitude ranging from 100 mV to 300 mV.

$f_{in-instr} = 10$ kHz				
$V_{pp-in-instr}$ (mV)	V_{pp-in} (mV)	V_{max-in} (mV)	$V_{max-out}$ (mV)	f_{out-Rx} (kHz)
310	276.6	1027	1032	23.9
320	276.6	1027	1032	23.84
330	296.4	1027	1032	23.78
340	296.4	1027	1032	23.73
350	316.1	1027	1032	23.67
360	316.1	1027	1051	23.62
370	316.1	1027	1051	23.56
380	316.1	1027	1051	23.51
390	335.9	1047	1051	23.45
400	335.9	1047	1051	23.4
410	355.7	1047	1070	23.33
420	355.7	1047	1070	23.27
430	355.7	1047	1070	23.22
440	375.4	1047	1070	23.16
450	375.4	1047	1070	23.1
460	395.2	1067	1070	23.02
470	395.2	1067	1070	22.96
480	395.2	1067	1089	22.9
490	414.9	1067	1089	22.83
500	414.9	1067	1089	22.78

Table C.4: Results of the plant-less instrumentation-only receiver-related characterization process exploiting an input 10-kHz sine waveform with peak-to-peak amplitude ranging from 310 mV to 500 mV.

$f_{in-instr}$ = 50 kHz				
$V_{pp-in-instr}$ (mV)	V_{pp-in} (mV)	V_{max-in} (mV)	$V_{max-out}$ (mV)	f_{out-Rx} (kHz)
100	118.6	933.1	918.8	25.29
110	118.6	933.1	926.4	25.22
120	134.4	941	926.4	25.15
130	134.4	941	934	25.07
140	150.2	949	941.6	24.99
150	158.1	949	941.6	24.92
160	166	956.9	949.2	24.87
170	173.9	956.9	949.2	24.8
180	181.8	964.8	956.8	24.72
190	197.7	972.7	956.8	24.65
200	197.7	972.7	964.4	24.57
210	213.5	980.6	964.4	24.5
220	221.4	988.5	972	24.43
230	229.3	988.5	972	24.36
240	245.1	996.4	979.6	24.29
250	245.1	996.4	987.2	24.22
260	260.9	1004	987.2	24.15
270	268.8	1012	994.8	24.07
280	276.7	1012	994.8	24
290	292.6	1020	1002	23.93
300	292.6	1020	1002	23.85

Table C.5: Results of the plant-less instrumentation-only receiver-related characterization process exploiting an input 50-kHz sine waveform with peak-to-peak amplitude ranging from 100 mV to 300 mV.

$f_{in-instr} = 50$ kHz				
$V_{pp-in-instr}$ (mV)	V_{pp-in} (mV)	V_{max-in} (mV)	$V_{max-out}$ (mV)	f_{out-Rx} (kHz)
310	308.4	1028	1010	23.77
320	308.4	1036	1017	23.7
330	324.2	1036	1017	23.64
340	332.1	1043	1025	23.56
350	340	1043	1025	23.49
360	347.9	1051	1025	23.41
370	363.7	1059	1032	23.34
380	363.7	1059	1040	23.26
390	379.6	1067	1040	23.18
400	387.5	1067	1047	23.11
410	395.4	1075	1047	23.08
420	411.2	1083	1055	23
430	411.2	1083	1055	22.92
440	427	1091	1063	22.84
450	434.9	1091	1063	22.77
460	442.8	1099	1070	22.57
470	458.6	1107	1078	22.48
480	466.5	1115	1085	22.4
490	474.5	1115	1085	22.32
500	490.3	1122	1093	22.26

Table C.6: Results of the plant-less instrumentation-only receiver-related characterization process exploiting an input 50-kHz sine waveform with peak-to-peak amplitude ranging from 310 mV to 500 mV.

$f_{in-instr} = 100$ kHz				
$V_{pp-in-instr}$ (mV)	V_{pp-in} (mV)	V_{max-in} (mV)	$V_{max-out}$ (mV)	f_{out-Rx} (kHz)
100	118.6	933.1	911.2	25.32
110	126.5	941	918.8	25.27
120	134.4	941	918.8	25.22
130	142.3	949	926.4	25.16
140	150.2	949	926.4	25.08
150	166	956.9	934	25.01
160	166	956.9	934	24.99
170	181.8	964.8	941.6	24.99
180	189.8	972.7	941.6	24.84
190	197.7	980.6	949.2	24.75
200	205.6	980.6	949.2	24.68
210	221.4	988.5	956.8	24.61
220	229.3	988.5	956.8	24.55
230	237.2	996.4	964.4	24.49
240	245.1	996.4	964.4	24.42
250	253	1004	972	24.35
260	268.8	1012	979.6	24.29
270	268.8	1012	979.6	24.24
280	284.7	1020	987.2	24.17
290	292.6	1020	987.2	24.1
300	300.5	1028	994.8	24.03

Table C.7: Results of the plant-less instrumentation-only receiver-related characterization process exploiting an input 100-kHz sine waveform with peak-to-peak amplitude ranging from 100 mV to 300 mV.

$f_{in-instr}$ = 100 kHz				
$V_{pp-in-instr}$ (mV)	V_{pp-in} (mV)	V_{max-in} (mV)	$V_{max-out}$ (mV)	f_{out-Rx} (kHz)
310	308.4	1036	994.8	23.98
320	316.3	1036	1002	23.91
330	332.1	1043	1002	23.85
340	340	1051	1010	23.78
350	347.9	1051	1010	23.71
360	363.7	1059	1017	23.65
370	371.6	1059	1017	23.58
380	379.6	1067	1025	23.53
390	387.5	1075	1025	23.47
400	393.4	1075	1025	23.41
410	403.3	1083	1032	23.36
420	411.2	1083	1032	23.3
430	427	1091	1040	23.24
440	434.9	1099	1040	23.19
450	442.8	1099	1047	23.11
460	458.6	1107	1047	23.04
470	458.6	1107	1055	22.97
480	474.5	1115	1055	22.89
490	482.4	1122	1055	22.83
500	490.3	1122	1063	22.76

Table C.8: Results of the plant-less instrumentation-only receiver-related characterization process exploiting an input 100-kHz sine waveform with peak-to-peak amplitude ranging from 310 mV to 500 mV.

$f_{in-instr} = 150$ kHz				
$V_{pp-in-instr}$ (mV)	V_{pp-in} (mV)	V_{max-in} (mV)	$V_{max-out}$ (mV)	f_{out-Rx} (kHz)
100	118.6	933.1	903.6	25.4
110	126.5	941	903.6	25.35
120	134.4	941	911.2	25.28
130	142.3	949	911.2	25.22
140	150.2	949	918.8	25.16
150	166	956.9	918.8	25.11
160	166	964.8	926.4	25
170	181.8	964.8	926.4	24.99
180	189.8	972.7	934	24.99
190	197.7	972.7	941.6	24.92
200	205.6	980.6	941.6	24.85
210	213.5	980.6	941.6	24.8
220	221.4	988.5	949.2	24.76
230	237.2	996.4	949.2	24.7
240	245.1	996.4	956.8	24.65
250	253	1004	964.4	24.59
260	260.9	1004	964.4	24.54
270	276.7	1012	964.4	24.49
280	284.7	1020	964.4	24.41
290	292.6	1020	972	24.35
300	300.5	1028	972	24.3

Table C.9: Results of the plant-less instrumentation-only receiver-related characterization process exploiting an input 150-kHz sine waveform with peak-to-peak amplitude ranging from 100 mV to 300 mV.

$f_{in-instr}$ = 150 kHz				
$V_{pp-in-instr}$ (mV)	V_{pp-in} (mV)	V_{max-in} (mV)	$V_{max-out}$ (mV)	f_{out-Rx} (kHz)
310	308.4	1028	972	24.24
320	316.3	1036	979.6	24.2
330	332.1	1043	979.6	24.15
340	340	1043	979.6	24.1
350	347.9	1051	987.2	24.05
360	355.8	1059	987.2	23.98
370	363.7	1059	994.8	23.94
380	379.6	1067	994.8	23.89
390	387.5	1067	1002	23.86
400	395.4	1075	1002	23.82
410	403.3	1075	1002	23.77
420	419.1	1083	1002	23.71
430	427	1091	1010	23.67
440	434.9	1099	1010	23.64
450	442.8	1099	1017	23.6
460	450.7	1099	1017	23.55
470	458.6	1107	1017	23.5
480	474.5	1115	1025	23.46
490	482.4	1115	1025	23.42
500	490.3	1122	1025	23.39

Table C.10: Results of the plant-less instrumentation-only receiver-related characterization process exploiting an input 150-kHz sine waveform with peak-to-peak amplitude ranging from 310 mV to 500 mV.

C.2 Transmitter characterization without plant data

R_{plant} (Ω)	$f_{datasheet}$ (Hz)	f_{out-Tx} (Hz)	Absolute error (Hz)	Relative error (%)
120	181745.8124	112400	69345.81244	38.15538389
180	174846.19	109900	64946.18999	37.14475563
270	165719.1304	106200	59519.13037	35.91566661
390	155388.2619	101900	53488.26192	34.42233104
560	143473.5477	96760	46713.54773	32.55899674
820	129556.3606	90190	39366.36056	30.38550974
1200	115133.0939	82940	32193.09386	27.9616336
1800	100330.2675	74970	25360.2675	25.27678649
2700	87127.7467	67240	19887.7467	22.8259624
3900	77068.68323	61030	16038.68323	20.81089563
5600	69079.85631	55910	13169.85631	19.064684
8200	62572.33362	51500	11072.33362	17.6952544
12000	57743.67476	48150	9593.674765	16.61424356
18000	54051.95775	45560	8491.957747	15.71073112
27000	51480.94054	43690	7790.940539	15.13364064
39000	49852.62964	42500	7352.62964	14.74872979
56000	48719.47761	41670	7049.477611	14.46952627
82000	47884.26988	41040	6844.269879	14.2933575
120000	47309.23493	40630	6679.23493	14.11824761
180000	46892.8822	40320	6572.882205	14.01680148
270000	46614.03342	40110	6504.033424	13.95295139
390000	46441.92216	39980	6461.922156	13.91398516
560000	46324.13894	39900	6424.13894	13.8678
820000	46238.348	39830	6408.347998	13.85937923
1000000	46205.0614	39810	6395.061403	13.84060795

Table C.11: Results of the plant-less instrumentation-only transmitter-related characterization process.

C.3 Registered data of the first characterization with the tobacco plant

Relative distances		$d_{Tx-Tx} = 1$ cm		
		f_{out-Tx} (kHz)	f_{out-Rx} (kHz)	Peak value (V)
d_{Rx-Tx}	Rx absent	71	-	-
	1 cm	68.5 (Average Value)	17.1	1.41
	2 cm		17.8	1.39
	3 cm		18.6	1.33
	4 cm		19.3	1.31
	5 cm		19.8	1.27
	6 cm		20.3	1.24
	7 cm		20.8	1.21
	8 cm		21.1	1.2
	9 cm		21.5	1.19
	10 cm		21.7	1.17

Table C.12: Results of the 1st characterization process with the tobacco plant and setting d_{Tx-Tx} to 1 cm.

Relative distances		$d_{Tx-Tx} = 2$ cm		
		f_{out-Tx} (kHz)	f_{out-Rx} (kHz)	Peak value (V)
d_{Rx-Tx}	Rx absent	61.8	-	-
	1 cm	58.8 (Average Value)	16.3	1.44
	2 cm		17.2	1.4
	3 cm		18.2	1.35
	4 cm		18.9	1.33
	5 cm		19.5	1.3
	6 cm		20.2	1.26
	7 cm		20.5	1.24
	8 cm		20.8	1.22
	9 cm		21	1.2
	10 cm		21.3	1.19

Table C.13: Results of the 1st characterization process with the tobacco plant and setting d_{Tx-Tx} to 2 cm.

Relative distances		$d_{Tx-Tx} = 3$ cm		
		f_{out-Tx} (kHz)	f_{out-Rx} (kHz)	Peak value (V)
d_{Rx-Tx}	Rx absent	55.5	-	-
	1 cm	53.8 (Average Value)	15.8	1.47
	2 cm		16.9	1.43
	3 cm		17.8	1.38
	4 cm		18.4	1.35
	5 cm		19.1	1.32
	6 cm		19.5	1.3
	7 cm		19.9	1.27
	8 cm		20.5	1.25
	9 cm		20.8	1.23
	10 cm		21	1.22

Table C.14: Results of the 1st characterization process with the tobacco plant and setting d_{Tx-Tx} to 3 cm.

Relative distances		$d_{Tx-Tx} = 4$ cm		
		f_{out-Tx} (kHz)	f_{out-Rx} (kHz)	Peak value (V)
d_{Rx-Tx}	Rx absent	50.5	-	-
	1 cm	47.9 (Average Value)	16	1.48
	2 cm		17	1.44
	3 cm		17.7	1.39
	4 cm		18.5	1.35
	5 cm		19.1	1.33
	6 cm		19.5	1.31
	7 cm		19.9	1.27
	8 cm		20.4	1.25
	9 cm		20.8	1.23
	10 cm		21	1.21

Table C.15: Results of the 1st characterization process with the tobacco plant and setting d_{Tx-Tx} to 4 cm.

Relative distances		$d_{Tx-Tx} = 5$ cm		
		f_{out-Tx} (kHz)	f_{out-Rx} (kHz)	Peak value (V)
d_{Rx-Tx}	Rx absent	47.7	-	-
	1 cm	45.9 (Average Value)	15.4	1.51
	2 cm		16.3	1.46
	3 cm		17.4	1.42
	4 cm		18.1	1.38
	5 cm		18.6	1.35
	6 cm		19.2	1.32
	7 cm		19.7	1.29
	8 cm		20	1.26
	9 cm		20.5	1.24
	10 cm		20.8	1.22

Table C.16: Results of the 1st characterization process with the tobacco plant and setting d_{Tx-Tx} to 5 cm.

Relative distances		$d_{Tx-Tx} = 6$ cm		
		f_{out-Tx} (kHz)	f_{out-Rx} (kHz)	Peak value (V)
d_{Rx-Tx}	Rx absent	45.9	-	-
	1 cm	45 (Average Value)	15.1	1.52
	2 cm		16	1.48
	3 cm		16.9	1.43
	4 cm		17.7	1.39
	5 cm		18.2	1.35
	6 cm		18.9	1.32
	7 cm		19.4	1.3
	8 cm		19.8	1.28
	9 cm		20.2	1.25
	10 cm		20.5	1.24

Table C.17: Results of the 1st characterization process with the tobacco plant and setting d_{Tx-Tx} to 6 cm.

Relative distances		$d_{Tx-Tx} = 7$ cm		
		f_{out-Tx} (kHz)	f_{out-Rx} (kHz)	Peak value (V)
d_{Rx-Tx}	Rx absent	45	-	-
	1 cm	44.2 (Average Value)	14.8	1.54
	2 cm		15.6	1.49
	3 cm		16.7	1.45
	4 cm		17.4	1.41
	5 cm		18.1	1.36
	6 cm		18.6	1.34
	7 cm		19.2	1.31
	8 cm		19.7	1.29
	9 cm		20.1	1.26
	10 cm		20.3	1.24

Table C.18: Results of the 1st characterization process with the tobacco plant and setting d_{Tx-Tx} to 7 cm.

Relative distances		$d_{Tx-Tx} = 8$ cm		
		f_{out-Tx} (kHz)	f_{out-Rx} (kHz)	Peak value (V)
d_{Rx-Tx}	Rx absent	44	-	-
	1 cm	43.5 (Average Value)	14.4	1.57
	2 cm		15.4	1.52
	3 cm		16.3	1.45
	4 cm		17.4	1.42
	5 cm		17.8	1.38
	6 cm		18.6	1.34
	7 cm		19.2	1.31
	8 cm		19.6	1.29
	9 cm		19.8	1.28
	10 cm		20.1	1.27

Table C.19: Results of the 1st characterization process with the tobacco plant and setting d_{Tx-Tx} to 8 cm.

Relative distances		$d_{Tx-Tx} = 9$ cm		
		f_{out-Tx} (kHz)	f_{out-Rx} (kHz)	Peak value (V)
d_{Rx-Tx}	Rx absent	43.5	-	-
	1 cm	42.8 (Average Value)	14.6	1.55
	2 cm		15.8	1.48
	3 cm		16.8	1.43
	4 cm		17.5	1.4
	5 cm		18.4	1.35
	6 cm		18.8	1.33
	7 cm		19.2	1.31
	8 cm		19.5	1.29
	9 cm		19.8	1.28
	10 cm		20.1	1.26

Table C.20: Results of the 1^{st} characterization process with the tobacco plant and setting d_{Tx-Tx} to 9 cm.

Relative distances		$d_{Tx-Tx} = 10$ cm		
		f_{out-Tx} (kHz)	f_{out-Rx} (kHz)	Peak value (V)
d_{Rx-Tx}	Rx absent	42.7	-	-
	1 cm	42.1 (Average Value)	14	1.6
	2 cm		15.3	1.52
	3 cm		16.1	1.48
	4 cm		17.4	1.42
	5 cm		18	1.38
	6 cm		18.6	1.34
	7 cm		18.8	1.32
	8 cm		19.2	1.3
	9 cm		19.6	1.29
	10 cm		19.8	1.28

Table C.21: Results of the 1^{st} characterization process with the tobacco plant and setting d_{Tx-Tx} to 10 cm.

C.4 Registered data of the second characterization with the tobacco plant

Relative distances		$d_{Tx-Tx} = 1$ cm		
		f_{out-Tx} (kHz)	f_{out-Rx} (kHz)	Peak value (V)
d_{Rx-Tx}	Rx absent	78.71	-	-
	1 cm	76.3 (Average Value)	16.1	1.43
	2 cm		16.4	1.4
	3 cm		16.7	1.39
	4 cm		17	1.37
	5 cm		17.5	1.36
	6 cm		17.9	1.35
	7 cm		18	1.34
	8 cm		18.3	1.32
	9 cm		18.8	1.31
	10 cm		19.1	1.3

Table C.22: Results of the 2nd characterization process with the tobacco plant and setting d_{Tx-Tx} to 1 cm.

Relative distances		$d_{Tx-Tx} = 2$ cm		
		f_{out-Tx} (kHz)	f_{out-Rx} (kHz)	Peak value (V)
d_{Rx-Tx}	Rx absent	66.9	-	-
	1 cm	64.4 (Average Value)	16	1.5
	2 cm		16.1	1.49
	3 cm		16.2	1.47
	4 cm		16.2	1.46
	5 cm		16.9	1.44
	6 cm		17.4	1.43
	7 cm		17.8	1.42
	8 cm		18.2	1.4
	9 cm		18.6	1.38
	10 cm		18.7	1.37

Table C.23: Results of the 2nd characterization process with the tobacco plant and setting d_{Tx-Tx} to 2 cm.

Relative distances		$d_{Tx-Tx} = 3$ cm		
		f_{out-Tx} (kHz)	f_{out-Rx} (kHz)	Peak value (V)
d_{Rx-Tx}	Rx absent	62.1	-	-
	1 cm	60.1 (Average Value)	14.9	1.54
	2 cm		15	1.52
	3 cm		15.1	1.51
	4 cm		15.4	1.5
	5 cm		15.9	1.48
	6 cm		16.3	1.46
	7 cm		17.1	1.44
	8 cm		17.4	1.43
	9 cm		17.8	1.42
	10 cm		17.9	1.41

Table C.24: Results of the 2nd characterization process with the tobacco plant and setting d_{Tx-Tx} to 3 cm.

Relative distances		$d_{Tx-Tx} = 4$ cm		
		f_{out-Tx} (kHz)	f_{out-Rx} (kHz)	Peak value (V)
d_{Rx-Tx}	Rx absent	59.4	-	-
	1 cm	58.2 (Average Value)	14.3	1.55
	2 cm		14.4	1.54
	3 cm		15.1	1.52
	4 cm		15.7	1.51
	5 cm		16.2	1.48
	6 cm		16.5	1.46
	7 cm		16.7	1.47
	8 cm		17	1.45
	9 cm		17.3	1.44
	10 cm		17.8	1.42

Table C.25: Results of the 2nd characterization process with the tobacco plant and setting d_{Tx-Tx} to 4 cm.

Relative distances		$d_{Tx-Tx} = 5$ cm		
		f_{out-Tx} (kHz)	f_{out-Rx} (kHz)	Peak value (V)
d_{Rx-Tx}	Rx absent	56.22	-	-
	1 cm	54.7 (Average Value)	14	1.57
	2 cm		14.5	1.55
	3 cm		15.2	1.53
	4 cm		15.5	1.52
	5 cm		15.8	1.51
	6 cm		16.1	1.49
	7 cm		16.5	1.48
	8 cm		16.8	1.47
	9 cm		17.1	1.46
	10 cm		17.6	1.44

Table C.26: Results of the 2^{nd} characterization process with the tobacco plant and setting d_{Tx-Tx} to 5 cm.

Relative distances		$d_{Tx-Tx} = 6$ cm		
		f_{out-Tx} (kHz)	f_{out-Rx} (kHz)	Peak value (V)
d_{Rx-Tx}	Rx absent	54.37	-	-
	1 cm	52.5 (Average Value)	13.9	1.59
	2 cm		14.4	1.58
	3 cm		14.9	1.55
	4 cm		15.2	1.54
	5 cm		15.4	1.53
	6 cm		15.8	1.51
	7 cm		16.1	1.5
	8 cm		16.5	1.49
	9 cm		17.4	1.46
	10 cm		17.6	1.45

Table C.27: Results of the 2^{nd} characterization process with the tobacco plant and setting d_{Tx-Tx} to 6 cm.

Relative distances		$d_{Tx-Tx} = 7$ cm		
		f_{out-Tx} (kHz)	f_{out-Rx} (kHz)	Peak value (V)
d_{Rx-Tx}	Rx absent	52.75	-	-
	1 cm	51.3 (Average Value)	14.1	1.6
	2 cm		14.5	1.57
	3 cm		14.7	1.56
	4 cm		14.9	1.55
	5 cm		15.3	1.53
	6 cm		15.6	1.52
	7 cm		16.1	1.51
	8 cm		16.9	1.48
	9 cm		17	1.46
	10 cm		17.1	1.45

Table C.28: Results of the 2^{nd} characterization process with the tobacco plant and setting d_{Tx-Tx} to 7 cm.

Relative distances		$d_{Tx-Tx} = 8$ cm		
		f_{out-Tx} (kHz)	f_{out-Rx} (kHz)	Peak value (V)
d_{Rx-Tx}	Rx absent	51.26	-	-
	1 cm	50.5 (Average Value)	14.1	1.61
	2 cm		14.2	1.59
	3 cm		14.4	1.58
	4 cm		14.9	1.56
	5 cm		15.1	1.54
	6 cm		15.4	1.53
	7 cm		16.5	1.5
	8 cm		16.6	1.49
	9 cm		16.7	1.47
	10 cm		16.7	1.46

Table C.29: Results of the 2^{nd} characterization process with the tobacco plant and setting d_{Tx-Tx} to 8 cm.

Relative distances		$d_{Tx-Tx} = 9$ cm		
		f_{out-Tx} (kHz)	f_{out-Rx} (kHz)	Peak value (V)
d_{Rx-Tx}	Rx absent	50.29	-	-
	1 cm	48.8 (Average Value)	14	1.61
	2 cm		14.1	1.6
	3 cm		14.3	1.58
	4 cm		14.7	1.56
	5 cm		14.8	1.55
	6 cm		15.3	1.53
	7 cm		16.3	1.5
	8 cm		16.5	1.49
	9 cm		16.8	1.47
	10 cm		16.8	1.47

Table C.30: Results of the 2^{nd} characterization process with the tobacco plant and setting d_{Tx-Tx} to 9 cm.

Relative distances		$d_{Tx-Tx} = 10$ cm		
		f_{out-Tx} (kHz)	f_{out-Rx} (kHz)	Peak value (V)
d_{Rx-Tx}	Rx absent	49.17	-	-
	1 cm	47.7 (Average Value)	13.8	1.64
	2 cm		13.9	1.63
	3 cm		14.1	1.61
	4 cm		14.3	1.59
	5 cm		14.7	1.56
	6 cm		15.2	1.54
	7 cm		15.9	1.52
	8 cm		16.4	1.5
	9 cm		16.7	1.48
	10 cm		17	1.47

Table C.31: Results of the 2^{nd} characterization process with the tobacco plant and setting d_{Tx-Tx} to 10 cm.

C.5 Registered data of the third characterization with the tobacco plant

Relative distances		$d_{Tx-Tx} = 1$ cm		
		f_{out-Tx} (kHz)	f_{out-Rx} (kHz)	Peak value (V)
d_{Rx-Tx}	Rx absent	71.17	-	-
	1 cm	67.28	20.55	1.187
	2 cm	67.45	20.68	1.178
	3 cm	67.19	20.82	1.169
	4 cm	66.91	21.05	1.158
	5 cm	66.67	21.11	1.153
	6 cm	66.46	21.18	1.146
	7 cm	66.17	21.32	1.141
	8 cm	65.51	21.45	1.132
	9 cm	65.12	21.68	1.125
	10 cm	64.98	21.59	1.12

Table C.32: Frequencies and peak voltage results of the 3$^{\text{rd}}$ characterization process with the tobacco plant and setting d_{Tx-Tx} to 1 cm.

Relative distances		$d_{Tx-Tx} = 1$ cm					
		Z_{Tx} at 1 kHz (Ω)	Z_{Tx} at 10 kHz (Ω)	Z_{Tx} at 100 kHz (Ω)	Z_{Rx} at 1 kHz (Ω)	Z_{Rx} at 10 kHz (Ω)	Z_{Rx} at 100 kHz (Ω)
d_{Rx-Tx}	Rx absent	13204.45	5582.83	1436.17	-	-	-
	1 cm	14095.47	6112.68	1512.23	7222.17	3851.41	997.73
	2 cm	14412.66	6149.65	1522.62	12643.58	6235.77	1641.46
	3 cm	14865.87	6238.35	1545.99	17797.71	8282.03	2162.32
	4 cm	15399.77	6360.98	1572.86	24041.92	10840.91	2834.91
	5 cm	15681.72	6418.39	1585.76	26398.22	11942.48	3244.65
	6 cm	16015.07	6479.37	1601.54	32381.09	14369.53	3853.8
	7 cm	16424.62	6594.58	1627.07	35941.93	15810.16	4284.78
	8 cm	17060.59	6769.58	1664.37	40423.17	17719.11	4800.51
	9 cm	17379.15	6861.28	1683.24	46185.53	20065.04	5448.39
	10 cm	17729.53	6955.95	1701.18	49984.34	21676.37	5844.59

Table C.33: Electrical impedance module results of the 3$^{\text{rd}}$ characterization process with the tobacco plant and setting d_{Tx-Tx} to 1 cm.

Relative distances		d_{Tx-Tx} = 2 cm		
		f_{out-Tx} (kHz)	f_{out-Rx} (kHz)	Peak value (V)
d_{Rx-Tx}	Rx absent	64.04	-	-
	1 cm	61.34	21.05	1.152
	2 cm	60.72	21.19	1.148
	3 cm	60.21	21.29	1.141
	4 cm	59.99	21.41	1.137
	5 cm	59.68	21.49	1.131
	6 cm	59.42	21.58	1.124
	7 cm	59.26	21.7	1.118
	8 cm	59.12	21.81	1.115
	9 cm	58.97	21.9	1.105
	10 cm	58.78	21.98	1.101

Table C.34: Frequencies and peak voltage results of the 3rd characterization process with the tobacco plant and setting d_{Tx-Tx} to 2 cm.

Relative distances		d_{Tx-Tx} = 2 cm					
		Z_{Tx} at 1 kHz (Ω)	Z_{Tx} at 10 kHz (Ω)	Z_{Tx} at 100 kHz (Ω)	Z_{Rx} at 1 kHz (Ω)	Z_{Rx} at 10 kHz (Ω)	Z_{Rx} at 100 kHz (Ω)
d_{Rx-Tx}	Rx absent	18022.78	7195.39	1955.08	-	-	-
	1 cm	18645.65	7652.93	2010.51	9681.23	4854.58	1383.39
	2 cm	19112.2	7873.59	2058.96	13766.2	6289.74	1717.73
	3 cm	19684.02	8093.75	2110.95	18705.92	8520.53	2457.53
	4 cm	20179.52	8258.8	2143.75	23371.55	10544.83	3006.97
	5 cm	20564.62	8388.74	2172.28	28441.8	12470.62	3473.97
	6 cm	20895.39	8510.07	2198.65	32227.67	14057.39	3959.09
	7 cm	21184.76	8604.57	2221.09	36678.29	15895.48	4457.12
	8 cm	21469.23	8699.75	2243.69	42305.08	18189.32	5075.65
	9 cm	21733.89	8797.02	2268.5	45779.24	19737.81	5501.25
	10 cm	22003.02	8891.53	2289.19	49848.24	21450.72	5944.16

Table C.35: Electrical impedance module results of the 3rd characterization process with the tobacco plant and setting d_{Tx-Tx} to 2 cm.

Relative distances		$d_{Tx-Tx} = 3$ cm		
		f_{out-Tx} (kHz)	f_{out-Rx} (kHz)	Peak value (V)
d_{Rx-Tx}	Rx absent	57.97	-	-
	1 cm	55.52	21.26	1.141
	2 cm	55.21	21.38	1.137
	3 cm	54.95	21.5	1.132
	4 cm	54.71	21.58	1.126
	5 cm	54.47	21.68	1.12
	6 cm	54.26	21.72	1.117
	7 cm	54.13	21.93	1.105
	8 cm	54.02	21.99	1.101
	9 cm	53.89	22.05	1.098
	10 cm	53.77	22.1	1.094

Table C.36: Frequencies and peak voltage results of the 3rd characterization process with the tobacco plant and setting d_{Tx-Tx} to 3 cm.

Relative distances		$d_{Tx-Tx} = 3$ cm					
		Z_{Tx} at 1 kHz (Ω)	Z_{Tx} at 10 kHz (Ω)	Z_{Tx} at 100 kHz (Ω)	Z_{Rx} at 1 kHz (Ω)	Z_{Rx} at 10 kHz (Ω)	Z_{Rx} at 100 kHz (Ω)
d_{Rx-Tx}	Rx absent	24186.54	9468.33	2628.36	-	-	-
	1 cm	25101.41	10123.5	2695.34	9560.91	4394.18	1108.91
	2 cm	25770.93	10439.2	2763.92	14827.32	6661.42	1779.71
	3 cm	26237.9	10634.32	2808.06	18560.45	8259.67	2292.85
	4 cm	26724.78	10826	2855.76	23367.38	10017.69	2716.82
	5 cm	27314.14	11026.34	2899.04	28469.5	12415.4	3548.02
	6 cm	27796.94	11188.67	2935.81	33065.58	13892.41	3838.65
	7 cm	28141.51	11288.88	2967.86	39221.37	16638.63	4618.29
	8 cm	28511.81	11437.42	3005.46	42124.39	17762.8	4932.96
	9 cm	28760.09	11520.91	3028.83	46716.51	19778.52	5424.4
	10 cm	29084.12	11642.53	3055.07	50559.77	21163.83	5776.71

Table C.37: Electrical impedance module results of the 3rd characterization process with the tobacco plant and setting d_{Tx-Tx} to 3 cm.

Relative distances		$d_{Tx-Tx} = 4$ cm		
		f_{out-Tx} (kHz)	f_{out-Rx} (kHz)	Peak value (V)
d_{Rx-Tx}	Rx absent	54.61	-	-
	1 cm	52.53	21.26	1.142
	2 cm	52.18	21.36	1.138
	3 cm	51.85	21.51	1.13
	4 cm	51.62	21.61	1.123
	5 cm	51.7	21.63	1.122
	6 cm	51.46	21.79	1.115
	7 cm	51.19	21.84	1.113
	8 cm	51.04	21.91	1.107
	9 cm	50.86	22.01	1.102
	10 cm	50.68	22.07	1.097

Table C.38: Frequencies and peak voltage results of the 3$^{\text{rd}}$ characterization process with the tobacco plant and setting d_{Tx-Tx} to 4 cm.

Relative distances		$d_{Tx-Tx} = 4$ cm					
		Z_{Tx} at 1 kHz (Ω)	Z_{Tx} at 10 kHz (Ω)	Z_{Tx} at 100 kHz (Ω)	Z_{Rx} at 1 kHz (Ω)	Z_{Rx} at 10 kHz (Ω)	Z_{Rx} at 100 kHz (Ω)
d_{Rx-Tx}	Rx absent	29708.44	11556.81	3249.49	-	-	-
	1 cm	30122.35	12181.74	3301.5	9479.84	4512.86	1224.4
	2 cm	30831.84	12554.82	3386.99	14247.43	6650.72	1891.22
	3 cm	31391.82	12894.31	3469.48	20292.12	9200.02	2575.89
	4 cm	31848.83	13143.3	3533.06	24775.14	11081.69	3101.91
	5 cm	29955.21	12729.26	3490.88	28263.64	12554.29	3547.49
	6 cm	31923.06	13344.3	3614.42	35712.54	15837.5	4394.42
	7 cm	32914.76	13713.28	3688.35	38060.69	16771.08	4639.43
	8 cm	33518.6	13962.47	3741.7	43338.94	19044.12	5157.64
	9 cm	34247.39	14217.37	3783.83	47891.72	21068.14	5743.4
	10 cm	34964.65	14473.91	3837.73	52605.13	23078.37	6265.54

Table C.39: Electrical impedance module results of the 3$^{\text{rd}}$ characterization process with the tobacco plant and setting d_{Tx-Tx} to 4 cm.

Relative distances		d_{Tx-Tx} = 5 cm		
		f_{out-Tx} (kHz)	f_{out-Rx} (kHz)	Peak value (V)
d_{Rx-Tx}	Rx absent	53.01	-	-
	1 cm	50.88	21.08	1.154
	2 cm	50.67	21.27	1.146
	3 cm	50.04	21.36	1.142
	4 cm	49.93	21.48	1.137
	5 cm	49.79	21.64	1.126
	6 cm	49.68	21.7	1.119
	7 cm	49.57	21.83	1.113
	8 cm	49.75	21.93	1.108
	9 cm	49.51	22.05	1.101
	10 cm	49.33	22.18	1.09

Table C.40: Frequencies and peak voltage results of the 3rd characterization process with the tobacco plant and setting d_{Tx-Tx} to 5 cm.

Relative distances		d_{Tx-Tx} = 5 cm					
		Z_{Tx} at 1 kHz (Ω)	Z_{Tx} at 10 kHz (Ω)	Z_{Tx} at 100 kHz (Ω)	Z_{Rx} at 1 kHz (Ω)	Z_{Rx} at 10 kHz (Ω)	Z_{Rx} at 100 kHz (Ω)
d_{Rx-Tx}	Rx absent	29769.53	12432.56	3664.42	-	-	-
	1 cm	30572.32	13546.2	3793.9	12813.2	5747.34	1458.5
	2 cm	31509.23	14080.82	3914.47	18768.43	8455.39	2190.5
	3 cm	32851.01	14696.53	4032.27	21771.85	9518.83	2558.81
	4 cm	33588.46	15013.99	4101	27353.44	11913.66	3202.27
	5 cm	34141.18	15144.02	4149.45	32746.23	14008.19	3780.66
	6 cm	34931.19	15416.34	4215.57	35703.57	15116.61	4086.62
	7 cm	35645.72	15599.58	4261.13	40363.42	17108.65	4654.74
	8 cm	34429.81	15033.16	4172.38	45317.01	19105.23	5189.91
	9 cm	35764.13	15462.14	4250.94	49851.81	21159.26	5808.95
	10 cm	36855.51	15799.4	4342.62	57715.45	24632.2	6743.14

Table C.41: Electrical impedance module results of the 3rd characterization process with the tobacco plant and setting d_{Tx-Tx} to 5 cm.

Relative distances		$d_{Tx-Tx} = 6$ cm		
		f_{out-Tx} (kHz)	f_{out-Rx} (kHz)	Peak value (V)
d_{Rx-Tx}	Rx absent	51.54	-	-
	1 cm	49.73	21.63	1.125
	2 cm	49.52	21.78	1.115
	3 cm	49.46	21.89	1.108
	4 cm	49.32	21.96	1.103
	5 cm	49.31	22.2	1.09
	6 cm	49.27	22.29	1.087
	7 cm	49.25	22.38	1.079
	8 cm	49.14	22.47	1.075
	9 cm	49.1	22.59	1.067
	10 cm	49.05	22.72	1.059

Table C.42: Frequencies and peak voltage results of the 3$^{\text{rd}}$ characterization process with the tobacco plant and setting d_{Tx-Tx} to 6 cm.

Relative distances		$d_{Tx-Tx} = 6$ cm					
		Z_{Tx} at 1 kHz (Ω)	Z_{Tx} at 10 kHz (Ω)	Z_{Tx} at 100 kHz (Ω)	Z_{Rx} at 1 kHz (Ω)	Z_{Rx} at 10 kHz (Ω)	Z_{Rx} at 100 kHz (Ω)
d_{Rx-Tx}	Rx absent	36291.56	14350.19	4177.36	-	-	-
	1 cm	36863.97	15014.39	4221.99	9622.92	4196.77	1050.54
	2 cm	37440.51	15214.58	4253.89	12933.08	5547.32	1548.05
	3 cm	37902.38	15341.7	4286	17078.4	7258.24	2085.08
	4 cm	38276.84	15443.49	4315.51	21759.98	8966.96	2581.98
	5 cm	38534.43	15477.93	4329.11	26883.21	11284.07	3360.3
	6 cm	38996.22	15620.91	4364.81	29798.86	12312.23	3584.37
	7 cm	39425.83	15770.71	4408.2	34758.85	14276.98	4183.65
	8 cm	39723.75	15873.4	4434.8	38219.62	15647.48	4600.19
	9 cm	40182.26	16045.44	4490.32	43836.65	17863.43	5227.97
	10 cm	40468.49	16125.18	4503.37	49643.55	20469.11	5995.92

Table C.43: Electrical impedance module results of the 3$^{\text{rd}}$ characterization process with the tobacco plant and setting d_{Tx-Tx} to 6 cm.

Relative distances		$d_{Tx-Tx} = 7$ cm		
		f_{out-Tx} (kHz)	f_{out-Rx} (kHz)	Peak value (V)
d_{Rx-Tx}	Rx absent	49.86	-	-
	1 cm	48.11	21.61	1.125
	2 cm	48.13	21.83	1.111
	3 cm	48.21	21.93	1.104
	4 cm	48.17	22.11	1.099
	5 cm	48.09	22.23	1.094
	6 cm	48.03	22.32	1.086
	7 cm	47.96	22.42	1.078
	8 cm	47.92	22.45	1.077
	9 cm	47.9	22.51	1.071
	10 cm	47.88	22.69	1.062

Table C.44: Frequencies and peak voltage results of the 3$^{\text{rd}}$ characterization process with the tobacco plant and setting d_{Tx-Tx} to 7 cm.

Relative distances		$d_{Tx-Tx} = 7$ cm					
		Z_{Tx} at 1 kHz (Ω)	Z_{Tx} at 10 kHz (Ω)	Z_{Tx} at 100 kHz (Ω)	Z_{Rx} at 1 kHz (Ω)	Z_{Rx} at 10 kHz (Ω)	Z_{Rx} at 100 kHz (Ω)
d_{Rx-Tx}	Rx absent	42879.5	16669.76	4765.88	-	-	-
	1 cm	43282.08	17409.81	4795.97	7717.49	3514.98	904.42
	2 cm	42661.54	17212.4	4769.26	13603.1	6002.3	1633.47
	3 cm	41504.68	16752.68	4700.29	17949.98	7756.12	2215.58
	4 cm	42587.85	17129.9	4774.26	21955.36	9465.02	2709.86
	5 cm	43369.53	17338.48	4819.94	26168.46	11158.05	3189.22
	6 cm	43671.42	17463.65	4851.67	29865.71	12589.67	3642.02
	7 cm	44184.25	17613.4	4892.43	34942.49	14603.55	4243.71
	8 cm	44619.99	17784.3	4931.03	35234.01	14707.52	4274.99
	9 cm	45039.01	17939.15	4962.22	39322.34	16359.06	4775.36
	10 cm	45493.34	18084.41	4998.59	46421.21	19593.06	5775.15

Table C.45: Electrical impedance module results of the 3$^{\text{rd}}$ characterization process with the tobacco plant and setting d_{Tx-Tx} to 7 cm.

Relative distances		$d_{Tx-Tx} = 8$ cm		
		f_{out-Tx} (kHz)	f_{out-Rx} (kHz)	Peak value (V)
d_{Rx-Tx}	Rx absent	50.72	-	-
	1 cm	48.84	21.62	1.122
	2 cm	48.67	21.9	1.109
	3 cm	48.55	22.06	1.101
	4 cm	48.48	22.22	1.095
	5 cm	48.39	22.33	1.088
	6 cm	48.35	22.44	1.081
	7 cm	48.26	22.6	1.074
	8 cm	48.19	22.71	1.066
	9 cm	48.15	22.83	1.058
	10 cm	48.32	22.94	1.053

Table C.46: Frequencies and peak voltage results of the 3$^{\text{rd}}$ characterization process with the tobacco plant and setting d_{Tx-Tx} to 8 cm.

Relative distances		$d_{Tx-Tx} = 8$ cm					
		Z_{Tx} at 1 kHz (Ω)	Z_{Tx} at 10 kHz (Ω)	Z_{Tx} at 100 kHz (Ω)	Z_{Rx} at 1 kHz (Ω)	Z_{Rx} at 10 kHz (Ω)	Z_{Rx} at 100 kHz (Ω)
d_{Rx-Tx}	Rx absent	36877.5	14670.91	4364.83	-	-	-
	1 cm	37914.8	15574.64	4459.7	8944.86	4104.21	1135.89
	2 cm	38376.74	15955.85	4539.92	14512.03	6415.55	1798.81
	3 cm	39138.5	16312.64	4621.26	18540.25	8051.34	2279.67
	4 cm	39529.11	16484.4	4682.41	23419.07	10075.09	2842.45
	5 cm	39936.84	16627.91	4731.21	27666.92	11713.47	3382.01
	6 cm	40429.61	16772.26	4792.57	32444.53	13836.98	4011.15
	7 cm	40901.74	16909.28	4844.91	39485.83	16526.49	4756.81
	8 cm	41454.07	17084.23	4897.62	44759.82	19025.2	5490.98
	9 cm	41898.79	17191.42	4924.32	50104.54	21481.51	6241.35
	10 cm	40699.12	16809.14	4864.72	56241.44	24631.77	7223.96

Table C.47: Electrical impedance module results of the 3$^{\text{rd}}$ characterization process with the tobacco plant and setting d_{Tx-Tx} to 8 cm.

Relative distances		d_{Tx-Tx} = 9 cm		
		f_{out-Tx} (kHz)	f_{out-Rx} (kHz)	Peak value (V)
d_{Rx-Tx}	Rx absent	48.79	-	-
	1 cm	47.1	21.77	1.118
	2 cm	46.88	21.87	1.112
	3 cm	46.73	22.02	1.104
	4 cm	46.58	22.13	1.099
	5 cm	46.45	22.21	1.095
	6 cm	46.4	22.38	1.085
	7 cm	46.38	22.52	1.077
	8 cm	46.37	22.63	1.072
	9 cm	46.36	22.79	1.063
	10 cm	46.34	22.97	1.051

Table C.48: Frequencies and peak voltage results of the 3$^{\text{rd}}$ characterization process with the tobacco plant and setting d_{Tx-Tx} to 9 cm.

Relative distances		d_{Tx-Tx} = 9 cm					
		Z_{Tx} at 1 kHz (Ω)	Z_{Tx} at 10 kHz (Ω)	Z_{Tx} at 100 kHz (Ω)	Z_{Rx} at 1 kHz (Ω)	Z_{Rx} at 10 kHz (Ω)	Z_{Rx} at 100 kHz (Ω)
d_{Rx-Tx}	Rx absent	43646.75	17505.22	5233.37	-	-	-
	1 cm	44532.96	18584.03	5354.76	11554.06	5429.15	1541.94
	2 cm	45862.56	19170.83	5470.86	16340.41	7368.8	2104.28
	3 cm	46953.27	19654	5584.04	21641.42	9729.26	2789.15
	4 cm	48371.06	20202	5690.9	26601.8	11615.92	3300.22
	5 cm	49369.72	20581.12	5769.07	30857.1	13396.12	3832.02
	6 cm	50300.11	20904.26	5851.39	38739.48	16667.89	4741.99
	7 cm	51331.88	21213.62	5911.81	46077.63	19958.86	5605.66
	8 cm	52147.55	21434.84	5955.93	51299.39	22487.55	6384.63
	9 cm	52412.36	21500.37	5978.05	56372.02	24933.36	7273.38
	10 cm	53166.7	21659.35	6016.8	66044.16	29663.04	8858.76

Table C.49: Electrical impedance module results of the 3$^{\text{rd}}$ characterization process with the tobacco plant and setting d_{Tx-Tx} to 9 cm.

Relative distances		$d_{Tx-Tx} = 10$ cm		
		f_{out-Tx} (kHz)	f_{out-Rx} (kHz)	Peak value (V)
d_{Rx-Tx}	Rx absent	47.71	-	-
	1 cm	46.13	21.85	1.113
	2 cm	46.1	21.93	1.109
	3 cm	46.07	22.03	1.104
	4 cm	46.05	22.22	1.095
	5 cm	46.03	22.41	1.084
	6 cm	46.01	22.61	1.075
	7 cm	46	22.7	1.067
	8 cm	45.99	22.87	1.058
	9 cm	45.99	23.05	1.048
	10 cm	45.98	23.26	1.033

Table C.50: Frequencies and peak voltage results of the 3rd characterization process with the tobacco plant and setting d_{Tx-Tx} to 10 cm.

Relative distances		$d_{Tx-Tx} = 10$ cm					
		Z_{Tx} at 1 kHz (Ω)	Z_{Tx} at 10 kHz (Ω)	Z_{Tx} at 100 kHz (Ω)	Z_{Rx} at 1 kHz (Ω)	Z_{Rx} at 10 kHz (Ω)	Z_{Rx} at 100 kHz (Ω)
d_{Rx-Tx}	Rx absent	50618.38	19863.84	5833	-	-	-
	1 cm	51307.83	20883.45	5877.06	10242.11	4933.35	1326.03
	2 cm	51982.26	21162.91	5909.74	13905.84	6251.99	1691.84
	3 cm	52569.34	21434.31	5959.44	18033.57	7875.46	2140.28
	4 cm	53376.35	21756.87	6018.54	23292.96	10212.78	2869.22
	5 cm	53761.8	21822.71	6048.93	30743.78	13204.83	3729.4
	6 cm	54054.13	21938.37	6106.23	36245.03	15974.58	4640.78
	7 cm	54453.93	22048.19	6124.48	41207.33	18186.56	5275.14
	8 cm	55222.68	22282.25	6181.38	47496.49	21405.89	6364.58
	9 cm	55658.4	22362.01	6221.46	54817.45	24843.82	7661.67
	10 cm	55929.96	22347.09	6229.6	61971.44	28608.13	8951.99

Table C.51: Electrical impedance module results of the 3rd characterization process with the tobacco plant and setting d_{Tx-Tx} to 10 cm.

Appendix D

MCU firmware implementation

In order to generate the code to manage the entire system, the integrated development environment STM32CubeIDE has been utilized to set the required configuration of the peripherals accordingly and to produce the correspondent code as reported in Figure D.1.

The firmware has been developed exploiting two built-in timers:

- Advanced-control timer TIM1
- General-purpose timer TIM2

TIM1 is a 16-bit 6-channel advanced-control timer that relies on an up, down, up-down auto-reload counter and a 16-bit programmable prescaler [53]. The latter has been configured to make the microcontroller count at 2 MHz, thus it has been set to 23 since 48 MHz is the maximum base CPU frequency exploited by the STM32WL55JC1 [40], while the auto-reload register (ARR) has been adjusted to the maximum applicable value to reduce the number of overflows, therefore, since it is a 16-bit counter, it has been set to 65535. In addition, in TIM1's NVIC (Nested Vectored Interrupt Controller) Settings tab, TIM1 break interrupt, TIM1 update interrupt, and TIM1 trigger and communication interrupt have been enabled with preemption priority set to 0, while TIM1 capture compare interrupt has been enabled with preemption priority set to 1. Three out of its six employable channels have been all exploited in Input Capture (IC) mode (in particular, IC Direct mode since the default IC-related pin of each channel has been utilized) to sense the input signals coming from the Tx module, the Rx device and the watermark sensor and to accordingly trigger the correspondent IC callback in turn to an incoming rising edge as will be further explained in Section D.0.1: in particular, channel 1 (TIM1_CH1) has been associated to the measurement of the signal coming from the transmitter, while channel 2 (TIM1_CH2) has been related to the evaluation of the signal originating from the watermark sensor and channel 3 (TIM1_CH3) has been associated to the measurement of the signal sourced from the receiver, as also depicted in Figure 4.6.

On the other hand, TIM2 is a 32-bit 4-channel general-purpose timer that consists of an up, down, up-down auto-reload counter and a 16-bit programmable prescaler [53]: the required working frequency for the only TIM2 channel employed (TIM2_CH1) is 10 kHz thus the prescaler has been set to 4799 since the internal 48-MHz clock [40] is exploited as TIM2 clock source as previously done in TIM1, while the 32-bit auto-reload register has been adjusted to the maximum applicable value to reduce the number of overflows, therefore, in this case, it has been set to 4294967295. In addition, TIM2 global interrupt has been enabled with preemption priority set to 0. The only TIM2 channel exploited (TIM2_CH1) has been activated in Output Compare (OC) mode (in the present case, OC No Output mode since no signal is required to be generated as output) to accordingly trigger the respective OC callback in turn to a 1-second-long time interval elapsed after channel activation: to achieve this elapsed time value, in the 32-bit register associated to the Pulse field of TIM2_CH1 a 10000 value has been forced therefore an interrupt event will be triggered after a 1-second-long elapsed time interval, as will be further explained in Section D.0.1.

For what concerns the configured pinout, the exploited pins, their location on the mounted connectors, their associated signal, and their customized GPIO mode are summarized in Table D.1.

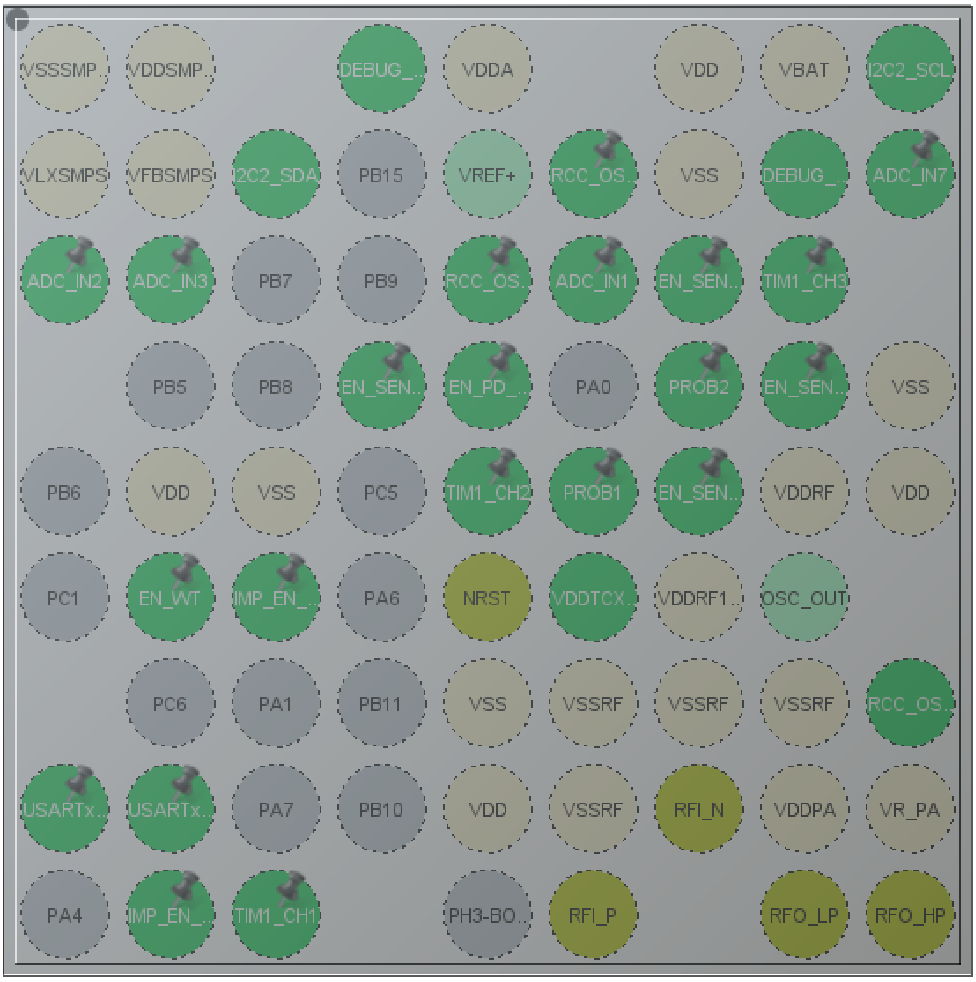

Figure D.1: Exploited STM32WL55JC1 pins in the integrated development environment STM32CubeIDE [53, 54].

Pin	Connector	Actual signal	GPIO mode
PA5	CN5/CN10	IMP_EN_TX	Output Push Pull
PA8	CN10	TIM1_CH1	Alternate Function Push Pull
PA9	CN5/CN10	TIM1_CH2	Alternate Function Push Pull
PA10	CN7/CN8	TIM1_CH3	Alternate Function Push Pull
PC0	CN10	EN_WT	Output Push Pull
PC3	CN10	EN_PD_DISCH	Output Push Pull
PC4	CN10	IMP_EN_RX	Output Push Pull

Table D.1: Summary of the exploited pins on the employed NUCLEO-WL55JC1 STM32WL Nucleo-64 development board [40, 53, 54, 55].

Referencing Table D.1 and Figure D.1, each pin is associated with a specific function. In particular:

- PA5 is related to the IMP_EN_TX output signal which is responsible for the control of the SIP switch exploited in order to section and decouple the provided supply voltage and the transmitter-specific supply voltage due to power consumption requirements: for instance, when PA5 is in its default reset state (for instance, low) the transmitter-related SIP switch is disabled, while if it is forced in its set state (for instance, high) the SIP switch is then enabled providing the supply voltage generated by the autonomous-energy system cited in Chapter 2 from upstream the switch to downstream (in this case, the transmitter module supply voltage input).

- PC4 is related to the IMP_EN_RX output signal which is in charge of the control of the SIP switch exploited in order to section and decouple the provided supply voltage and the receiver-specific supply voltage due to power consumption requirements: in particular, when PC4 is in its default reset state (for instance, low) the receiver-related SIP switch is disabled, while if it is forced in its set state (for instance, high) the SIP switch is then enabled providing the supply voltage generated by the autonomous-energy system cited in Chapter 2 from upstream the switch to downstream (in this case, the receiver device supply voltage input).

- PC0 is related to the EN_WT output signal which is in charge of the control of the SIP switch exploited in order to section and decouple the provided supply voltage and the watermark-specific supply voltage due to power consumption requirements: as also highlighted for PA5 and PC4, when PC0 is in its default reset state (for instance, low) the SIP switch is disabled, while if it is forced in its set state (for instance, high) the SIP switch is then enabled providing the supply voltage generated by the autonomous-energy system from upstream the switch to downstream (in this case, the transmitter module supply voltage).

- PC3 is related to the EN_PD_DISCH output signal responsible for the peak detector output capacitor discharge: in the case of activated PC3, the PD capacitor C_{PD} will be discharged. However, as reported in Section 3.3.2, no component has been actually employed to discharge the peak detector output capacitor C_{PD} due to the very low retention of ceramic capacitor utilized as output capacitor C_{PD}: this output signal has been predisposed (even in the application code) for eventual future implementations.

- Other exploited pins as depicted in Figure D.1 (but not reported in Table D.1 since not utilized in this thesis project's developed system) are PA11, PB3, PB4, PB14, PB1, PB2, PC2, PC13, PB12 and PB13 respectively related to the built-in analog-to-digital converter (ADC) inputs (ADC_IN7, ADC_IN2, ADC_IN3, and ADC_IN1), the ADC enable output signals (PB1, PB2, PC2, and PC13) and to the internal SPI LoRa-related signals (PROB1 and PROB2).

D.0.1 Application code

As previously stated in Section 4.2, it is important to remember that this thesis project firmware has been integrated and loaded on a pre-existent microcontroller application on the STM32WL55JC1 [40], therefore in the upcoming listings few lines are related to the previous firmware: however, those will be highlighted in the discussion.

In this thesis work, HAL (Hardware Abstract Layer) software routines have been employed to access hardware resources through API (Application Programming Interface) without requiring an accurate knowledge of the specific hardware resource utilized on behalf of the program and simplifying the code generation.

Initialization functions

The initialization functions reported in Listing D.1 from line 6 to line 16 are responsible for the correct configuration of the Nucleo board. For instance, HAL drivers have been initialized at line 6, while at line 9 the system clock has been configured. Then, from line 12 to line 16, the peripherals have been initialized: for what concerns only the application developed in this thesis project, the GPIO peripherals (GPIOA and GPIOC in the selected configurations previously explained in Section 4.2) have been initialized by the line 12, while the timers' initialization has been taken into account by the instruction at line 15 and line 16 respectively for TIM1 in IC and for TIM2 in OC as reported in Section 4.2. Lastly, the LoRaWAN peripheral has been initialized at line 13.

It is important to notice that the I2C peripheral has been configured at line 14: the initialization of this peripheral has been required since it permits the communication with three sensors aforementioned in Section 4.2, for instance, an air-humidity sensor, a light intensity sensor, and the temperature sensor, already implemented in the system that is going to be integrated with this thesis project's newly-developed components.

```
 1 int main(void)
 2 {
 3     /* MCU Configuration */
 4 
 5     /* Reset of all peripherals, Initializes the Flash interface and
       the Systick. */
 6     HAL_Init();
 7 
 8     /* Configure the system clock */
 9     SystemClock_Config();
10 
11     /* Initialize all configured peripherals */
12     MX_GPIO_Init();
13     MX_LoRaWAN_Init();
14     MX_I2C2_Init();
15     MX_TIM1_Init();
16     MX_TIM2_Init();
17     HAL_TIM_Base_MspDeInit(&htim1);
18     htim1.State = HAL_TIM_STATE_RESET;
19     HAL_I2C_MspDeInit(&hi2c2);
20 
21     /* Set the employed pins to default and known values */
22     HAL_GPIO_WritePin(GPIOB, EN_SEN_3_Pin, GPIO_PIN_RESET);
23     HAL_GPIO_WritePin(GPIOC, EN_SEN_1_Pin, GPIO_PIN_RESET);
24     HAL_GPIO_WritePin(GPIOC, EN_SEN_4_Pin, GPIO_PIN_RESET);
25     HAL_GPIO_WritePin(GPIOB, EN_SEN_2_Pin, GPIO_PIN_RESET);
26     HAL_GPIO_WritePin(GPIOA, IMP_EN_TX_Pin, GPIO_PIN_RESET);
27     HAL_GPIO_WritePin(GPIOC, IMP_EN_RX_Pin, GPIO_PIN_RESET);
28     HAL_GPIO_WritePin(GPIOC, EN_WT_Pin, GPIO_PIN_RESET);
29     HAL_GPIO_WritePin(GPIOC, EN_PD_DISCH_Pin, GPIO_PIN_RESET);
30     HAL_I2C_MspInit(&hi2c2);
31 
32     /* Infinite loop */
33     while (1)
34     {
35         MX_LoRaWAN_Process();
36     }
37 }
```

Listing D.1: Initialization functions in main.c.

Then, from line 22 to line 30 of Listing D.1, all the pins employed in the application have been set on default values accordingly to their role in the system: in particular, the exploited pins that are significant for this thesis project have been set from line 26 to line 29 where the GPIO pins reported in Table D.1 (for instance, PA5, PC0, PC3, and PC4) have been set to their reset state, thus to low value since their activation implies an high output as previously explained in Section 4.2.

For the same reason aforementioned in the first part of this section, the I2C peripheral has been prepared and set ready to be used at line 30.

In the end, the whole LoRaWAN process has been launched and performed inside the while loop at line 35 of Listing D.1.

Interrupt callbacks

In this thesis project, the implemented firmware has been developed in order to work in response to interrupt events, therefore correspondent interrupt callbacks have been written as reported in Listing D.2 and Listing D.3 for timers employed respectively in IC mode and in OC mode.

```
void HAL_TIM_IC_CaptureCallback(TIM_HandleTypeDef *htim)
{
    if (htim -> Channel == HAL_TIM_ACTIVE_CHANNEL_1)
    {
        old_capture = new_capture;
        new_capture = TIM1 -> CCR1; // Tx case
    }
    if (htim -> Channel == HAL_TIM_ACTIVE_CHANNEL_2)
    {
        old_capture = new_capture;
        new_capture = TIM1 -> CCR2; // Watermark case
    }
    if (htim -> Channel == HAL_TIM_ACTIVE_CHANNEL_3)
    {
        old_capture = new_capture;
        new_capture = TIM1 -> CCR3; // Rx case
    }
}
```

Listing D.2: Interrupt callback for timers in Input Capture (IC) mode.

As previously explained in Section 4.2, three out of the six channels (CH1, CH2, and CH3) of the advanced-control timer TIM1 have been configured in Input Capture mode to respond in turn to the rising edge of the input signals respectively coming from the transmitter, the watermark sensor and the receiving module through the correspondent pins (PA8, PA9, and PA10) reported in Table D.1: in fact, since each of the employed channels is dedicated to a specific input, three independent not-exclusive if structures similar to each other have been utilized to be able to respond to any interrupt event from each possible source.

For each exploited if structure, two unsigned short external auxiliary variables *new_capture* and *old_capture* have been employed: in particular, the value assessed in previous measurements is stored in *old_capture* from the *new_capture* variable and then the value in the Capture Compare register (CCR) of the correspondent TIM1's channel related to the respective input signal is stored in *new_capture*. The evaluation of the frequency coming from each source is then estimated in a specific code explained in Section D.0.1 and reported in Listing D.4.

```c
1 void HAL_TIM_OC_DelayElapsedCallback(TIM_HandleTypeDef *htim)
2 {
3     if (htim -> Channel == HAL_TIM_ACTIVE_CHANNEL_1)
4     {
5         flag_meas = 1;
6         HAL_TIM_IC_Stop_IT(&htim1, TIM_CHANNEL_1); // Stop TIM1 CH1 in IC with Interrupt for Tx case
7         HAL_TIM_IC_Stop_IT(&htim1, TIM_CHANNEL_3); // Stop TIM1 CH2 in IC with Interrupt for Rx case
8     }
9 }
```

Listing D.3: Interrupt callback for timers in Output Compare (OC) mode.

Moreover, the Output-Compare-mode-related interrupt callback is reported in Listing D.3: since only one channel (TIM2_CH1) has been exploited in OC mode, after a check on which channel the interrupt event is sourced from in the mode reported in Section 4.2 (thus after a 1-second elapsed time interval since the OC channel activation), a flag variable *flag_meas* (also present in Listing D.5 set to 0) is set to 1 in order to overcome the busy-waiting while loop exploited in Listing D.5 utilized to wait for the completion of the measurements of the input signals. Thereafter, at line 6 and line 7 the Input Capture of both the transmitter and receiver cases are stopped.

Frequency measurement routine

In Listing D.4, the routine employed to evaluate the frequency of the captured signals is reported: it relies on the values stored in *new_capture* and *old_capture* and previously modified by IC callback shown in Listing D.2.

```
 1 uint32_t eval_freq()
 2 {
 3     uint32_t freq = 0;
 4     float fr_tmp;
 5 
 6     if (old_capture != new_capture)
 7     {
 8         if (new_capture > old_capture)
 9         {
10             diffCapture = new_capture - old_capture;
11             fr_tmp = 2000000 / diffCapture;
12             freq = (uint32_t) fr_tmp;
13         }
14         else
15         {
16             diffCapture = 65535 - old_capture + new_capture;
17             fr_tmp = 2000000 / diffCapture;
18             freq = (uint32_t) fr_tmp;
19         }
20     }
21 
22     return freq;
23 }
```

Listing D.4: Frequency measurement exploited code.

By relying on two local variables ($freq$ and fr_temp) and a global variable ($diffCapture$), the retrieval of the frequency starts from the actual values stored in the variables *new_capture* and *old_capture* then according to them, the resulting frequency is returned to the calling function. It is important to notice that in line 11 and line 17, the temporary frequency value fr_tmp has been evaluated considering the chosen working frequency of TIM1, which in this thesis project is set equal to 2 MHz.

Data evaluation and LoRa transmission

In Listing D.5, data evaluation and LoRa transmission instructions are present in the $SendTxData$ function: in particular, the evaluation of output coming from the transmitter, the receiver, and the watermark is paced by the instruction written from line 2 to line 79, while thereafter the LoRa-transmission-related code is reported until the $SendTxData$ routine end.

```c
static void SendTxData(void)
{
    ...

    // Temperature, air-humidity and light intensity measurements
    temp_int = hdc2080_readtemp();
    rh_int = hdc2080_readrh();
    if (read_devid() == 12289) // Checks if the opt3001 is actually connected
    {
        opt_ok = opt3001_init();
        if (opt_ok == 1)
        {
            lux_int = opt3001_readdata();
        }
    }
    else
    {
        lux_int = 0;
    }

    // Tx measurement
    flag_meas = 0;
    new_capture = 0;
    old_capture = 0;
    TIM2 -> CNT = 0; // Reset TIM2 Counter
    TIM1 -> CNT = 0; // Reset TIM1 Counter
    HAL_TIM_IC_Init(&htim1); // Initialize TIM1
    HAL_TIM_OC_Init(&htim2); // Initialize TIM2
    HAL_TIM_IC_Start_IT(&htim1, TIM_CHANNEL_1); // Start TIM1 CH1 in IC with Interrupt
    HAL_TIM_OC_Start_IT(&htim2, TIM_CHANNEL_1); // Start TIM2 CH1 in OC with Interrupt
    HAL_GPIO_WritePin(GPIOA, IMP_EN_TX_Pin, GPIO_PIN_SET); // Start Impedance Modulus for Tx side
    while (flag_meas == 0)
    {

    }
    HAL_TIM_OC_Stop_IT(&htim2, TIM_CHANNEL_1); // Stop TIM2 CH1 in OC with Interrupt
    impedance_Tx = eval_freq(); // Evaluate the frequency relative to stem impedance modulus for Tx side

    // Rx measurement
    flag_meas = 0;
    new_capture = 0;
    old_capture = 0;
```

```
    TIM2 -> CNT = 0; // Reset TIM2 Counter
    TIM1 -> CNT = 0; // Reset TIM1 Counter
    HAL_TIM_IC_Start_IT(&htim1, TIM_CHANNEL_3); // Start TIM1 CH3 in IC with Interrupt
    HAL_TIM_OC_Start_IT(&htim2, TIM_CHANNEL_1); // Start TIM2 CH1 in OC with Interrupt
    HAL_GPIO_WritePin(GPIOC, IMP_EN_RX_Pin, GPIO_PIN_SET); // Start Impedance Modulus for Rx side
    while (flag_meas == 0)
    {

    }
    HAL_GPIO_WritePin(GPIOC, IMP_EN_RX_Pin, GPIO_PIN_RESET); // Stop Impedance Modulus for Rx side
    HAL_TIM_OC_Stop_IT(&htim2, TIM_CHANNEL_1); // Stop TIM2 CH1 in OC with Interrupt
    HAL_GPIO_WritePin(GPIOA, IMP_EN_TX_Pin, GPIO_PIN_RESET); // Stop Impedance Modulus for Tx side
    impedance_Rx = eval_freq(); // Evaluate the frequency relative to stem impedance modulus for Rx side

    // Predisposition for eventual future implementation of the discharging process of the peak detector output capacitor of the receiver side
    /*
    HAL_GPIO_WritePin(GPIOC, EN_PD_DISCH_Pin, GPIO_PIN_SET); // Start PD discharge
    HAL_Delay(200);
    HAL_GPIO_WritePin(GPIOC, EN_PD_DISCH_Pin, GPIO_PIN_RESET); // Stop PD discharge
    */


    // Watermark measurement
    flag_meas = 0;
    TIM1 -> CNT = 0; // Reset TIM1 counter
    TIM2 -> CNT = 0; // Reset TIM2 counter
    new_capture = 0;
    old_capture = 0;
    HAL_GPIO_WritePin(GPIOC, EN_WT_Pin, GPIO_PIN_SET); // Start Watermark Measurement
    HAL_TIM_IC_Start_IT(&htim1, TIM_CHANNEL_2); // Start TIM1 CH2 in IC with Interrupt
    HAL_Delay(200);
    HAL_TIM_IC_Stop_IT(&htim1, TIM_CHANNEL_2); // Stop TIM1 CH2 in IC with Interrupt
    HAL_GPIO_WritePin(GPIOC, EN_WT_Pin, GPIO_PIN_RESET); // Stop Watermark Measurement
    watermark = (uint16_t) (eval_freq());
```

```

    TIM1 -> CNT = 0; // Reset TIM1 counter
    TIM2 -> CNT = 0; // Reset TIM2 counter

    ...

    LmHandlerErrorStatus_t status = LORAMAC_HANDLER_ERROR;
    UTIL_TIMER_Time_t nextTxIn = 0;
    if (LmHandlerIsBusy() == false)
    {

        ...

        #ifdef CAYENNE_LPP

            ...

        #else /* not CAYENNE_LPP */
            if ((LmHandlerParams.ActiveRegion == LORAMAC_REGION_US915) || (LmHandlerParams.ActiveRegion == LORAMAC_REGION_AU915) || (LmHandlerParams.ActiveRegion == LORAMAC_REGION_AS923))
            {

            }
            else
            {
                AppData.Buffer[i++] = (uint8_t)((rh_int >> 8) & 0xFF);
                AppData.Buffer[i++] = (uint8_t)(rh_int & 0xFF);

                AppData.Buffer[i++] = (uint8_t)((lux_int >> 8) & 0xFF);
                AppData.Buffer[i++] = (uint8_t)(lux_int & 0xFF);

                AppData.Buffer[i++] = (uint8_t)((temp_int >> 8) & 0xFF);
                AppData.Buffer[i++] = (uint8_t)(temp_int & 0xFF);

                AppData.Buffer[i++] = (uint8_t)((impedance_Tx >> 16) & 0xFF);
                AppData.Buffer[i++] = (uint8_t)((impedance_Tx >> 8) & 0xFF);
                AppData.Buffer[i++] = (uint8_t)(impedance_Tx & 0xFF);

                AppData.Buffer[i++] = (uint8_t)((impedance_Rx >> 16) & 0xFF);
                AppData.Buffer[i++] = (uint8_t)((impedance_Rx >> 8) & 0xFF);
                AppData.Buffer[i++] = (uint8_t)(impedance_Rx & 0xFF);
```

```
117
118                 AppData.Buffer[i++] = (uint8_t)((watermark >> 8) & 0xFF);
119                 AppData.Buffer[i++] = (uint8_t)(watermark & 0xFF);
120
121                 ...
122
123             }
124             AppData.BufferSize = i;
125         #endif /* CAYENNE_LPP */
126
127         ...
128
129     }
130
131     ...
132
133 }
```

Listing D.5: Data evaluation and LoRa transmission code.

For what concerns the data evaluation part, it can be described as follows:

- From line 22 to line 79 the transmitter-related code is reported.
    - From line 22 to line 24, the employed variables $flag\_meas$, *new_capture*, and *old_capture* are set to 0 in order to work with a known default value.
    - At line 25 and line 26, the counters of both TIM1 and TIM2 is reset.
    - In correspondence of line 27 and line 28, the exploited timers are initialized in the correspondent mode (Input Capture or Output Compare).
    - From line 29 to line 30, the timer channels are configured enabling the respective interrupt: in this case, the considered channels are TIM1_CH1 in IC mode and TIM2_CH1 in OC mode.
    - In order to perform the Tx-related frequency measurement, the transmitter has to be powered through the correspondent SIP switch, therefore the pin IMP_EN_TX previously reported in Table D.1 is set to its high value at line 31.
    - From line 32 to line 35, the busy-waiting while loop (previously mentioned in Listing D.3) depending on the variable $flag\_meas$ is reported.

  - The timer channel TIM2_CH1 related to the evaluation of the transmitter-sourced signal is then stopped at line 36.

  - Finally, the resulting value of the frequency estimated by the frequency measurement routine $eval\_freq()$ (see Listing D.4) is returned and then stored in the variable $impedance\_Tx$ at line 37.

- From line 40 to line 61 the receiver-related code is reported remembering that the transmitter module should still be powered on in order to perform the Rx-related frequency evaluation.

  - From line 40 to line 46, the same instructions exploited from line 6 to line 14 are reported accordingly to the channels of the timers employed in the receiver evaluation: in this case, the considered channels are TIM1_CH3 in IC mode and TIM2_CH1 in OC mode.

  - The receiver has to be powered through the correspondent SIP switch to be able to perform the Rx-related frequency measurement, thus the pin IMP_EN_RX previously reported in Table D.1 is set to its high value at line 47.

  - From line 48 to line 51, the busy-waiting while loop (previously mentioned in Listing D.3) depending on the variable $flag\_meas$ is reported.

  - The frequency measurement of the receiver-sourced signal has to be stopped by the instruction at line 52 which disable the SIP switch related to the receiving module.

  - The timer channel TIM2_CH1 related to the evaluation of the receiver-sourced signal is stopped at line 53.

  - At line 54, the transmitting device is powered off through the correspondent SIP switch since the evaluation of both the Tx side and the Rx part is concluded.

  - Finally, the resulting value of the frequency measurement routine $eval\_freq()$ (see Listing D.4) is returned and then stored in the variable $impedance\_Rx$ at line 55.

  - As reported in Section 3.3.2, the presence of an element exploited to discharge the peak detector output capacitor when it is not used has been removed due to the characteristics of the actual employed ceramic capacitor C_{PD}: however, from line 59 to line 61, the discharge process code utilizing the EN_PD_DISCH pin (previously reported in Table D.1) has been implemented for eventual future implementations.

- In the end, from line 66 to line 76, the watermark-related code is reported.
  - From line 66 to line 72, the same instructions exploited for both the transmitter and the receiver cases, but powering on the watermark-related SIP switch in order to allow the watermark measurement through the activation of the correspondent pin EN_WT previously reported in Table D.1 at line 71 and accordingly changing the employed timer channel TIM_CH2 in IC mode at line 72.
  - After a 200-ms software delay at line 73 useful to permit the watermark sensor output evaluation, the measurement is ended by stopping the timer channel TIM2_CH1 related to the watermark-related signal at line 74 and by turning off the sensor through the EN_WT pin deactivation which controls the watermark power supply at line 75.
  - Lastly, the code reported in Listing D.4 is then exploited in order to evaluate the frequency of the signal sourced from the watermark sensor and storing it in the watermark variable at line 76.
- Before the LoRa-transmission-related code, both the employed timers TIM1 and TIM2 are set to 0 as default in correspondence of line 78 and line 79.

In the matter of the LoRa-related code, after several error checks on the LoRa configuration regarding, for example, the geographical area where the application is employed (see line 95 of Listing D.5) from line 101 to line 119, the buffer $AppData.Buffer$ containing the data that needs to be sent through the LoRaWAN protocol as explained in Section 4.1.1. In particular, since the data transmission is performed by sending an 8-bit-sized packet at a time, each line of the buffer has to be filled by 8-bit right-shifting the more-than-8-bit-sized data to be sent (after applying a bit mask) as highlighted from line 101 to line 119 of Listing D.5. As mentioned in Section 4.1.2, after the buffer loading, the evaluated data is finally sent by the developed device and thereafter received and accordingly decoded by the uplink payload formatter algorithm loaded on The Things Network (further explained in Section D.0.2).

D.0.2 The Things Network algorithm

In order to accordingly decode the data evaluated and thereafter sent through the LoRa-based communication system by the developed device, a JavaScript code has been implemented on The Things Network's suite as uplink payload formatter algorithm reported in the following Listing D.6.

```javascript
function Decoder(bytes, port)
{
    // Decode an uplink message from a buffer (array) of bytes to an object of fields.
    // TEST PAYLOAD_DATA
    var decoded = {};
    if (port==2)
    {
        // Relative humidity sensor
        decoded.RH = (((bytes[0] << 8) | bytes[1]) * 100) / 65535;
        // Light intensity sensor
        decoded.Light = (bytes[2] << 8) | bytes[3];
        // Temperature sensor
        decoded.Temperature = ((((bytes[4] << 8) | bytes[5]) * 165) / 65535) - 40.5;
        // Transmitter-related impedance
        decoded.Impedance_Tx = (bytes[6] << 16) | (bytes[7] << 8) | bytes[8];
        // Receiver-related impedance
        decoded.Impedance_Rx = (bytes[9] << 16) | (bytes[10] << 8) | bytes[11];
        // Watermark sensor
        decoded.Watermark = (bytes[12] << 8) | bytes[13];
    }

    return decoded;
}
```

Listing D.6: The Things Network uplink exploited algorithm.

In Listing D.6, the exploited uplink-related code has been written according to the organization and the order of the *AppData.Buffer* previously managed and thereafter sent in the form of a 8-bit packet through a LoRa-based communication by the *SendTxData* routine previously highlighted in Listing D.5: in particular, the first data sent (for instance, *rh_int* in Listing D.5) is then the first data decoded by the The Things Network uplink payload formatter code and, since the data from the device have been 8-bit right-shifted in order to accordingly fill the buffer to be sent, the decoder has to eventually 8-bit left-shift its input when it is required before properly appending the data retrieved from different 8-bit packets.

From line 6 to line 20 in Listing D.6, after a check on the port where retrieve the data from (for instance, port 2 since it is the default one in STM-provided LoRa-related examples), the measurements related to each sensor are properly managed according to the type of the specific sensor exploited and to the output produced by the microcontroller. In the end, at line 22, the appropriately decoded data are finally returned.

Bibliography

[1] World Meteorological Organization (WMO). *State of the Global Climate 2022.* WMO, Apr. 2023. ISBN: 978-92-63-11316-0. URL: `https://library.wmo.int/idurl/4/66214` (cit. on pp. 1–3).

[2] Internal Displacement Monitoring Centre (IDMC). *Global Report on Internal Displacemnet 2023 (GRID 2023).* Apr. 2023. URL: `https://www.internal-displacement.org/global-report/grid2023/` (cit. on pp. 1, 4).

[3] Food and Agriculture Organization of the United Nations (FAO). *FAOSTAT.* Dec. 2023. URL: `https://www.fao.org/faostat/en/#data` (cit. on pp. 5, 6, 9).

[4] Joseph Poore and Tomas Nemecek. «Reducing food's environmental impacts through producers and consumers». In: *Science* 360.6392 (June 2018), pp. 987–992. DOI: `10.1126/science.aaq0216`. eprint: `https://www.science.org/doi/pdf/10.1126/science.aaq0216`. URL: `https://www.science.org/doi/abs/10.1126/science.aaq0216` (cit. on pp. 5, 7).

[5] «Erratum for the Research Article "Reducing food's environmental impacts through producers and consumers" by J. Poore and T. Nemecek». In: *Science* 363.6429 (Feb. 2019), eaaw9908. DOI: `10.1126/science.aaw9908`. eprint: `https://www.science.org/doi/pdf/10.1126/science.aaw9908`. URL: `https://www.science.org/doi/abs/10.1126/science.aaw9908` (cit. on pp. 5, 7).

[6] Hannah Ritchie, Pablo Rosado, and Max Roser. *Environmental Impacts of Food Production.* 2022. URL: `https://ourworldindata.org/environmental-impacts-of-food` (cit. on pp. 5, 7, 8).

[7] Hannah Ritchie, Lucas Rodés-Guirao, Edouard Mathieu, Marcel Gerber, Esteban Ortiz-Ospina, Joe Hasell, and Max Roser. *Population Growth.* 2023. URL: `https://ourworldindata.org/population-growth` (cit. on pp. 6, 9).

[8] Dunia Abas Gzar, Ali Majeed Mahmood, and Maythem Kamal Abbas Al-Adilee. «Recent trends of smart agricultural systems based on Internet of Things technology: A survey». In: *Computers & Electrical Engineering* 104 (Nov. 2022), p. 108453. ISSN: 0045-7906. DOI: `https://doi.org/10.1016/j.compeleceng.2022.108453`. URL: `https://www.sciencedirect.com/science/article/pii/S0045790622006681` (cit. on pp. 6, 7).

[9] Chander Prakash, Lakhwinder Pal Singh, Ajay Gupta, and Shiv Kumar Lohan. «Advancements in smart farming: A comprehensive review of IoT, wireless communication, sensors, and hardware for agricultural automation». In: *Sensors and Actuators A: Physical* 362 (Aug. 2023), p. 114605. ISSN: 0924-4247. DOI: `https://doi.org/10.1016/j.sna.2023.114605`. URL: `https://www.sciencedirect.com/science/article/pii/S0924424723004545` (cit. on pp. 6, 7, 10, 11).

[10] Monish Sai Krishna Namana, Gudikandhula Narasimha Rao, Prasanthi Rathnala, Srinivasa Rao Sura, Pradeep Patnaik, and Vasudeva Naidu. «Internet of Things for Smart Agriculture: State of the Art and Challenges». In: *Ecological Engineering & Environmental Technology* 23.6 (Aug. 2022), pp. 147–160. DOI: `10.12912/27197050/152916`. URL: `https://doi.org/10.12912/27197050/152916` (cit. on p. 11).

[11] Umberto Garlando, Stefano Calvo, Mattia Barezzi, Alessandro Sanginario, Paolo Motto Ros, and Danilo Demarchi. «Ask the plants directly: Understanding plant needs using electrical impedance measurements». In: *Computers and Electronics in Agriculture* 193 (Feb. 2022), p. 106707. ISSN: 0168-1699. DOI: `https://doi.org/10.1016/j.compag.2022.106707`. URL: `https://www.sciencedirect.com/science/article/pii/S0168169922000242` (cit. on pp. 12, 45, 49, 50).

[12] Umberto Garlando, Stefano Calvo, Mattia Barezzi, Alessandro Sanginario, Paolo Motto Ros, and Danilo Demarchi. «A "Plant-Wearable System" for Its Health Monitoring by Intra- and Interplant Communication». In: *IEEE Transactions on AgriFood Electronics* 1.2 (Dec. 2023), pp. 60–70. DOI: `10.1109/TAFE.2023.3284563` (cit. on pp. 12, 45, 47, 49, 51).

[13] Umberto Garlando, Lee Bar-On, Paolo Motto Ros, Alessandro Sanginario, Sebastian Peradotto, Yosi Shacham-Diamand, Adi Avni, Maurizio Martina, and Danilo Demarchi. «Towards Optimal Green Plant Irrigation: Watering and Body Electrical Impedance». In: *2020 IEEE International Symposium on Circuits and Systems (ISCAS)*. IEEE, Sept. 2020, pp. 1–5. DOI: `10.1109/ISCAS45731.2020.9181290` (cit. on pp. 12, 46, 49).

[14] Umberto Garlando, Lee Bar-On, Paolo Motto Ros, Alessandro Sanginario, Stefano Calvo, Maurizio Martina, Adi Avni, Yosi Shacham-Diamand, and Danilo Demarchi. «Analysis of in Vivo Plant Stem Impedance Variations in Relation with External Conditions Daily Cycle». In: *2021 IEEE International Symposium on Circuits and Systems (ISCAS)*. IEEE, May 2021, pp. 1–5. DOI: `10.1109/ISCAS51556.2021.9401242` (cit. on pp. 12, 46, 49).

[15] Lee Bar-On, Umberto Garlando, Marios Sophocleous, Aakash Jog, Paolo Motto Ros, Nir Sade, Adi Avni, Yosi Shacham-Diamand, and Danilo Demarchi. «Electrical Modelling of In-Vivo Impedance Spectroscopy of Nicotiana tabacum Plants». In: *Frontiers in Electronics* 2 (Sept. 2021). ISSN: 2673-5857. DOI: `10.3389/felec.2021.753145`. URL: `https://www.frontiersin.org/articles/10.3389/felec.2021.753145` (cit. on pp. 12, 46, 49).

[16] Elisabeth Borges, A.P. Matos, J.M. Cardoso, C. Correia, T. Vasconcelos, and N. Gomes. «Early detection and monitoring of plant diseases by Bioelectric Impedance Spectroscopy». In: *2012 IEEE 2nd Portuguese Meeting in Bioengineering (ENBENG)*. IEEE, Oct. 2012, pp. 1–4. DOI: `10.1109/ENBENG.2012.6331377` (cit. on pp. 12, 46).

[17] Athil S. Al-Ezzi and Mohamed Nainar M. Ansari. «Photovoltaic Solar Cells: A Review». In: *Applied System Innovation* 5.4 (2022). ISSN: 2571-5577. DOI: `10.3390/asi5040067`. URL: `https://www.mdpi.com/2571-5577/5/4/67` (cit. on p. 13).

[18] Burc Arda Altug. *Design and Implementation of a Multi-Source Energy Harvesting System for Smart Agriculture Applications*. Apr. 2023. URL: `http://webthesis.biblio.polito.it/id/eprint/26760` (cit. on pp. 13–17, 19, 156).

[19] Stefano Calvo. *An energy autonomous electronic transmitting system for green plant sensing applications*. Dec. 2020. URL: `http://webthesis.biblio.polito.it/id/eprint/16781` (cit. on pp. 13–15, 45).

[20] Marta Chiarillo. *Design of an indirect bio-impedance measurement system for plant health monitoring*. 2022. URL: `http://webthesis.biblio.polito.it/id/eprint/25753` (cit. on pp. 14, 45–49, 55, 58, 164).

[21] Wenxuan Zhu, Chaosheng Hu, Maoyi Zhang, Tao Jiang, Chris R. Bowen, Xiaojing Mu, and Ya Yang. «Multi-Effects Coupled Nanogenerators for Simultaneously Harvesting Solar, Thermal, and Mechanical Energies». In: *Advanced Materials Technologies* 9.16 (Apr. 2023), p. 2300212. DOI: `https://doi.org/10.1002/admt.202300212` (cit. on pp. 14, 16).

[22] Yuan Wang, Min Hong, Jeffrey Venezuela, Ting Liu, and Matthew Dargusch. «Expedient secondary functions of flexible piezoelectrics for biomedical energy harvesting». In: *Bioactive Materials* 22 (Apr. 2023), pp. 291–311. ISSN: 2452-199X. DOI: `10.1016/j.bioactmat.2022.10.003`. URL: `https://www.sciencedirect.com/science/article/pii/S2452199X22004273` (cit. on pp. 14, 15).

[23] Aisha B. Rahman and Md. Fazlul Kader. «A new energy harvesting scheme for multi-relay cooperative networks». In: *Digital Signal Processing* 133 (Mar. 2023), p. 103846. ISSN: 1051-2004. DOI: `https://doi.org/10.1016/j.dsp.2022.103846`. URL: `https://www.sciencedirect.com/science/article/pii/S1051200422004638` (cit. on p. 14).

[24] Wouter A. Serdijn, Andre Luis R. Mansano, and Mark Stoopman. «Chapter 4.2 - Introduction to RF Energy Harvesting». In: *Wearable Sensors*. Ed. by Edward Sazonov and Michael R. Neuman. Oxford: Academic Press, 2014, pp. 299–322. ISBN: 978-0-12-418662-0. DOI: `https://doi.org/10.1016/B978-0-12-418662-0.00019-2`. URL: `https://www.sciencedirect.com/science/article/pii/B9780124186620000192` (cit. on p. 14).

[25] Malek Teib, Alexandre Malherbe, and Edith Kussener. «Multi-harvesting smart solution for self-powered wearable objects: System-level model and transistor-level design». In: *Integration* 91 (2023), pp. 165–172. ISSN: 0167-9260. DOI: `https://doi.org/10.1016/j.vlsi.2023.03.010`. URL: `https://www.sciencedirect.com/science/article/pii/S0167926023000548` (cit. on pp. 14, 15).

[26] Jeffrey G. Snyder. «Thermoelectric Energy Harvesting». In: *Energy Harvesting Technologies*. Ed. by Shashank Priya and Daniel J. Inman. Boston, MA: Springer US, 2009, pp. 325–336. ISBN: 978-0-387-76464-1. DOI: `10.1007/978-0-387-76464-1_11`. URL: `https://doi.org/10.1007/978-0-387-76464-1_11` (cit. on pp. 15, 16).

[27] Francesca Angelini. *Development of an autonomous plant monitoring system based on Plant Microbial Fuel Cells*. Dec. 2021. URL: `http://webthesis.biblio.polito.it/id/eprint/21028` (cit. on pp. 16, 25, 26, 32, 34).

[28] Edith Osorio-de-la-Rosa, Javier Vàsquez-Castillo, Alejandro Castillo-Atoche, Julio Heredia-Lozano, Andrea Castillo-Atoche, Guillermo Becerra-Nuñez, and Romeli Barbosa. «Arrays of Plant Microbial Fuel Cells for Implementing Self-Sustainable Wireless Sensor Networks». In: *IEEE Sensors Journal* 21.2 (Jan. 2021), pp. 1965–1974. DOI: `10.1109/JSEN.2020.3019986` (cit. on pp. 16, 17).

[29] Korneel Rabaey and Willy Verstraete. «Microbial fuel cells: novel biotechnology for energy generation». In: *Trends in Biotechnology* 23.6 (June 2005), pp. 291–298. DOI: `https://doi.org/10.1016/j.tibtech.2005.04.008` (cit. on p. 16).

[30] Felix Tetteh Kabutey, Qingliang Zhao, Liangliang Wei, Jing Ding, Philip Antwi, Frank Koblah Quashie, and Weiye Wang. «An overview of plant microbial fuel cells (PMFCs): Configurations and applications». In: *Renewable and Sustainable Energy Reviews* 110 (2019), pp. 402–414. ISSN: 1364-0321. DOI: `https://doi.org/10.1016/j.rser.2019.05.016`. URL: `https://www.sciencedirect.com/science/article/pii/S1364032119303223` (cit. on pp. 17, 18).

[31] Antonella Fatica et al. «Study on analytical characteristics of Nicotiana tabacum L., cv. Solaris biomass for potential uses in nutrition and biomethane production». In: *Scientific Reports* 9 (Nov. 2019), p. 16828. ISSN: 2045-2322. DOI: `10.1038/s41598-019-53237-8`. URL: `https://doi.org/10.1038/s41598-019-53237-8` (cit. on p. 19).

[32] Fluke. *Fluke 114, 115, 116 and 117 Digital Multimeters datasheet.* URL: `https://dam-assets.fluke.com/s3fs-public/flk-2793260b-en-117-extended-specs-ds-w.pdf?iK8zKhZCoPI2YuKIQ1lk.0RIAeEbd76T` (cit. on pp. 23, 37, 38).

[33] Agilent. *34410A and 34411A Multimeters datasheet.* URL: `https://www.keysight.com/us/en/assets/7018-01326/data-sheets/5989-3738.pdf` (cit. on pp. 37, 38).

[34] Agilent. *34401A Digital Multimeter datasheet.* URL: `https://www.keysight.com/us/en/assets/7018-06774/data-sheets/5968-0162.pdf` (cit. on pp. 38, 156).

[35] Paolo Motto Ros, Enrico Macrelli, Alessandro Sanginario, Yosi Shacham-Diamand, and Danilo Demarchi. «Electronic System for Signal Transmission Inside Green Plant Body». In: *2019 IEEE International Symposium on Circuits and Systems (ISCAS).* IEEE, May 2019, pp. 1–5. DOI: `10.1109/ISCAS.2019.8702577` (cit. on pp. 45, 46).

[36] Texas Instruments. *TLV701x and TLV702x Small-Size, Low-Power, Low-Voltage Comparators.* URL: `https://www.ti.com/lit/ds/symlink/tlv7011.pdf?ts=1704124549721&ref_url=https%253A%252F%252Fwww.ti.com%252Fproduct%252FTLV7011` (cit. on p. 46).

[37] Analog Devices. *AD5272/AD5274 datasheet.* URL: `https://www.analog.com/media/en/technical-documentation/data-sheets/ad5272_5274.pdf` (cit. on p. 46).

[38] STMicroelectronics. *STM32F401RE datasheet and documentation*. URL: https://www.st.com/resource/en/datasheet/stm32f401re.pdf (cit. on pp. 46, 48).

[39] Texas Instruments. *LMC555 CMOS Timer*. URL: https://www.ti.com/lit/ds/symlink/lmc555.pdf?ts=1697102063287&ref_url=https%253A%252F%252Fwww.ti.com%252Fproduct%252FLMC555%253Futm_source%253Dgoogle%2526utm_medium%253Dcpc%2526utm_campaign%253Dasc-null-null-GPN_EN-cpc-pf-google-eu%2526utm_content%253DLMC555%2526ds_k%253DLMC555%2BDatasheet%2526DCM%253Dyes%2526gclid%253DEAIaIQobChMI9IKm6ZXwgQMVXJRoCR0ZCgGzEAAYASAAEgLm0_D_BwE%2526gclsrc%253Daw.ds (cit. on pp. 47, 49, 50, 58–61, 65, 66, 78, 89, 108, 163).

[40] STMicroelectronics. *STM32WL55JC1 datasheet and documentation*. URL: https://www.st.com/resource/en/datasheet/stm32wl55cc.pdf (cit. on pp. 48, 129, 132, 133, 140, 230–232, 234).

[41] Hassan Kelley and Gabino Alonso. *LTC6244 High Speed Peak Detector*. URL: https://www.analog.com/en/technical-articles/ltc6244-high-speed-peak-detector.html (cit. on p. 56).

[42] Stefano Calvo, Mattia Barezzi, Danilo Demarchi, and Umberto Garlando. «In-vivo proximal monitoring system for plant water stress and biological activity based on stem electrical impedance». In: *2023 9th International Workshop on Advances in Sensors and Interfaces (IWASI)*. IEEE, June 2023, pp. 80–85. DOI: 10.1109/IWASI58316.2023.10164553 (cit. on pp. 57, 139).

[43] Texas Instruments. *TLV904x 1.2-V Ultra Low Voltage, 10µA Micro-Power RRIO Amplifier for Power Conscious Applications*. URL: https://www.ti.com/lit/ds/symlink/tlv9041.pdf?ts=1704195958012 (cit. on p. 57).

[44] Texas Instruments. *TLVx387 High Precision, Zero-Drift, Low-Input-Bias-Current Op Amps*. URL: https://www.ti.com/lit/ds/symlink/tlv387.pdf?ts=1698334788091&ref_url=https%253A%252F%252Fwww.ti.com%252Famplifier-circuit%252Fop-amps%252Fprecision%252Fproducts.html (cit. on pp. 57–59).

[45] Vishay. *SD103A, SD103B, SD103C Small Signal Schottky Diodes*. URL: https://www.vishay.com/docs/85754/sd103a.pdf (cit. on pp. 57, 58).

[46] Diodes Incorporated. *1N4148/1N4448 Fast Switching Diode*. URL: https://www.diodes.com/assets/Datasheets/ds12019.pdf (cit. on p. 58).

[47] Keysight. *Keysight 33220A datasheet*. URL: https://www.keysight.com/us/en/assets/7018-01144/data-sheets/5988-8544.pdf (cit. on pp. 65, 67–70).

[48] Aim-TTi Instruments. *Aim-TTi CPX200D datasheet.* URL: `https://www.farnell.com/datasheets/3674411.pdf` (cit. on pp. 65, 74, 143, 145).

[49] Rigol. *DS1104Z-S Plus digital oscilloscope datasheet.* URL: `https://cdn.shopify.com/s/files/1/1618/2733/files/MSO1000Z_Datasheet_d67f8cf5-ad75-4564-8968-d8e2e0b05620.pdf?134` (cit. on pp. 65, 74).

[50] Rigol. *DP800 series datasheet.* URL: `https://cdn.shopify.com/s/files/1/1618/2733/files/DP800_datasheet_e7bfcb80-fa39-48f8-a488-3eac159072e1.pdf?v=1636389163` (cit. on pp. 83, 94).

[51] Rigol. *MSO5000 series datasheet.* URL: `https://cdn.shopify.com/s/files/1/1618/2733/files/MSO5000_datasheet.pdf?127` (cit. on pp. 83, 94).

[52] Agilent. *Agilent 4294A Precision Impedance Analyzer.* URL: `https://www.bellnw.com/cdn/shop/files/PDF-KTA-4294A.pdf?v=7082112840516713773` (cit. on pp. 94, 96, 118).

[53] STMicroelectronics. *STM32WL5x Reference Manual.* URL: `https://www.st.com/resource/en/reference_manual/rm0453-stm32wl5x-advanced-armbased-32bit-mcus-with-subghz-radio-solution-stmicroelectronics.pdf` (cit. on pp. 129, 132, 133, 138, 140, 230–232).

[54] STMicroelectronics. *STM32WL series User Manual.* URL: `https://www.st.com/resource/en/user_manual/um3191-stm32wl-series-ulcsaiec-607301603351-selftest-library-user-guide-stmicroelectronics.pdf` (cit. on pp. 132, 133, 140, 232).

[55] STMicroelectronics. *STM32WL Nucleo-64 board (MB1389) User Manual.* URL: `https://www.st.com/resource/en/user_manual/um2592-stm32wl-nucleo64-board-mb1389-stmicroelectronics.pdf` (cit. on pp. 132, 133, 140, 232).

[56] Antonino Pagano, Daniele Croce, Ilenia Tinnirello, and Gianpaolo Vitale. «A Survey on LoRa for Smart Agriculture: Current Trends and Future Perspectives». In: *IEEE Internet of Things Journal* 10.4 (Feb. 2023), pp. 3664–3679. DOI: `10.1109/JIOT.2022.3230505` (cit. on pp. 134, 135).

[57] Semtech Corporation. *LoRa and LoRaWAN: A Technical Overview.* Dec. 2019. URL: `https://lora-developers.semtech.com/uploads/documents/files/LoRa_and_LoRaWAN-A_Tech_Overview-Downloadable.pdf` (cit. on p. 134).

[58] Jansen C. Liando, Amalinda Gamage, Agustinus W. Tengourtius, and Mo Li. «Known and Unknown Facts of LoRa: Experiences from a Large-scale Measurement Study». In: *ACM Transactions on Sensor Networks* 15.2 (Feb. 2019). ISSN: 1550-4859. DOI: `10.1145/3293534`. URL: `https://doi.org/10.1145/3293534` (cit. on p. 134).

[59] Vishay. *SIP32431 10 pA, Ultra Low Leakage and Quiescent Current, Load Switch with Reverse Blocking.* URL: `https://www.vishay.com/docs/66597/sip32431.pdf` (cit. on p. 136).

[60] Mattia Barezzi, Umberto Garlando, Francesca Pettiti, Luca Nari, Davide Gisolo, Davide Canone, and Danilo Demarchi. «Long-Range Low-Power Soil Water Content Monitoring System for Precision Agriculture». In: *2022 IEEE 13th Latin America Symposium on Circuits and System (LASCAS).* IEEE, 2022, pp. 1–4. DOI: `10.1109/LASCAS53948.2022.9789070` (cit. on pp. 141, 142).

[61] Murata. *CMWX1ZZABZ-078 datasheet.* URL: `https://www.mouser.com/catalog/specsheets/Murata_CMWX1ZZABZ-078.pdf?_gl=1*1k2lvc8*_ga*MjA2ODk4MjI2NC4xNzA2MjkxMTYy*_ga_15W4STQT4T*MTcwNjI5MTE2Mi4xLjEuMTcwNjI5MTE2Ny41NS4wLjA.*_ga_1KQLCYKRX3*MTcwNjI5MTE2Mi4xLjEuMTcwNjI5MTE2Ny4wLjAuMA..` (cit. on pp. 142, 143).

[62] SAFT. *Primary lithium battery LS14500 datasheet.* URL: `https://www.mouser.com/datasheet/2/101/LS%2014500_0408_revised_0908.58ecd0c2-6b62-44ca-8c7e-2392.pdf` (cit. on p. 142).

[63] Maxim. *MAX4562/MAX4563 datasheet.* URL: `https://www.analog.com/media/en/technical-documentation/data-sheets/MAX4562-MAX4563.pdf` (cit. on p. 142).

[64] METER Group Inc. USA. *TEROS 21 Quick Start.* URL: `https://library.metergroup.com/Quick%20Start%20Guides/14536_TEROS21_Web.pdf` (cit. on pp. 143, 145).

[65] METER Group Inc. USA. *TEROS 21 Gen 2 Integrator Guide.* URL: `https://library.metergroup.com/Integrator%20Guide/18407%20TEROS%2021%20Gen2%20Integrator%20Guide.pdf` (cit. on p. 143).

[66] METER Group Inc. USA. *TEROS 21 Gen 2 Manual.* URL: `https://library.metergroup.com/Manuals/20854_TEROS21_Gen2_Manual_Web.pdf` (cit. on pp. 143, 145).

[67] M.S.A. Blackwell, P.C. Brookes, N. de la Fuente-Martinez, H. Gordon, P.J. Murray, K.E. Snars, J.K. Williams, R. Bol, and P.M. Haygarth. «Chapter 1 - Phosphorus Solubilization and Potential Transfer to Surface Waters from the Soil Microbial Biomass Following Drying–Rewetting and Freezing–Thawing». In: *Advances in Agronomy v106*. Ed. by Donald L. Sparks. Vol. 106. Advances in Agronomy. Academic Press, 2010, pp. 1–35. DOI: `https://doi.org/10.1016/S0065-2113(10)06001-3`. URL: `https://www.sciencedirect.com/science/article/pii/S0065211310060013` (cit. on p. 143).

[68] B&K Precision Corporation. *300 kHz Bench LCR Meter User Manual*. URL: `https://bkpmedia.s3.us-west-1.amazonaws.com/downloads/manuals/en-us/891_manual.pdf` (cit. on pp. 143, 152, 153).

[69] B&K Precision Corporation. *300 kHz Bench LCR Meter datasheet*. URL: `https://bkpmedia.s3.us-west-1.amazonaws.com/downloads/datasheets/en-us/891_datasheet.pdf` (cit. on pp. 143, 152, 153).